# Water vapor transport in snowpacks

## Mahdi JAFARI

Knowledge is power.
— Firdowsi Tusi

,

To my family...

# Acknowledgments

During around four years, many people helped me for the accomplishment of this thesis. It is almost impossible to thank everyone who provided help for both my education and development as a person – and I am not an exception to this.

I would like to reserve the first big expression of gratitude to the most important ones in my life, i.e., my beloved family.

I would like to thank all the colleagues from the CRYOS laboratory (along with the colleagues at SLF), who are also members of a well-known group as "Mahdi's best friend". Special thanks to Shokoufeh who really supported me during my difficult times. I am so grateful to many friends whom I had the chance to meet in EPFL and Lausanne: All the GR building and our great neighbours SBER, WIRE, and ECOL.

As my supervisor, Michael Lehning, I think that he deserves an extra note of thanks for: (1) all his support specially during my first year when I was sick, (2) his openness and flexibility at work, and (3) his grasp of issues and how quickly he could get the point and propose ideas when we had a scientific discussion. I am always grateful for all his supports. Likewise, I would like to thank the members of my dissertation committee for their time and efforts towards improving the dissertation.

I have to thank OpenFOAM, the best open-source CFD package ever. OpenFOAM is the subtle art of OOP programming in C++.

*Lausanne, February 2021*                                               Mahdi Jafari

# Abstract

This thesis is an in-depth treatment of water vapor transport in snowpacks and its impacts on snow structure. The aim is to better understand this transport process and to lay the basis for a model representation in physics-based multi-layer snow models. Overall the process should improve the representation of the impact of snow in diverse environments from mountains, ice sheets to sea ice.

The vertical diffusion of water vapor in the snow cover is investigated first by solving a one-dimensional transient diffusion equation in the SNOWPACK model. The implications on the snow layering of this vertical diffusive flux are analyzed for four different regions: Alpine, Subarctic, Arctic, and Antarctic sea ice. The largest impact of diffusion is observed in snow on sea ice in the Weddell Sea and the shallow Arctic snowpack. The simulations show significant density reductions at the base of the snow cover upon inclusion of diffusive water vapor transport.

Diffusion may in some snow covers have a small effect and it is the convection often invoked to explain observed density profiles e.g. of thin tundra snowpacks. The effects of convection on snowpack structure have never been studied systematically by looking at the thermal and phase change regimes for different snowpack conditions. Therefore, this thesis presents for the first time a numerical investigation for convection of water vapor in idealized snowpacks using an Eulerian–Eulerian two-phase approach. We find considerable impact of the natural convection on the snow density distribution with a layer of significantly lower density at the bottom of the snowpack and a layer of higher density located near the surface. We observe that emergent heterogeneity in the snow porosity results in a feedback effect on the spatial organization of convection cells causing their horizontal displacement. We additionally find that the thermal equilibrium assumption is not valid in our idealized system.

Natural convection is rather not likely to have a large impact in typical Alpine or sub-arctic snow covers if conditions are horizontally homogeneous. Therefore, this thesis also studies numerically the potential impact of heterogeneity induced by shrubs or rocks on convection of water vapor in snowpacks. We find that the convection cells are formed even with sub-critical Rayleigh number as low as 5 due to heterogeneity induced in snow density. We show that contributions of diffusive and convective flux divergence on snow density change show strong

## Abstract

variations. We further find that the strongest effect of convection is not for very thin or thick snow covers but for snow covers in between, which allow the formation of convection cells with a scale of 0.5 m.

Among different snow covers, significant convection events are numerically observed by SNOWPACK-OpenFOAM coupling for a herb tundra permafrost at Bylot Island. We find that significant sublimation in downward flow generates a low-density base in the snow cover. We further observe a strong footprint of convection on snow density and temperature with significant lateral variations up to 80 $\mathrm{kg\,m^{-3}}$ and 6.5 K respectively. This effect of convection on the snow density profile, namely a low density foot and high density top, corresponds qualitatively to observations. Further work is required to adapt physical parameterizations in conventional snow models to represent this effect and its interaction with snow settling and metamorphism.

**Keywords** water vapor transport, diffusive vapor flux, phase change, convection

# Résumé

Cette thèse présente une étude approfondi du transport de la vapeur d'eau dans la neige ainsi que de ses impacts sur la structure du manteau neigeux. L'objectif est de mieux comprendre les processus de transport et de jeter les bases d'une représentation dans des modèles de neige multicouches basés sur la physique. Globalement, le processus devrait améliorer la représentation de l'impact de la neige dans divers environnements, des montagnes à la banquise en passant par les calottes glaciaires.

La diffusion verticale de la vapeur induite par la chaleur dans le manteau neigeux est d'abord étudiée en résolvant une équation de diffusion transitoire unidimensionnelle dans le modèle SNOWPACK. Les implications de ce flux diffusif vertical sur les différentes couches de neige sont analysées pour quatre régions différentes échantillonnant l'espace de variabilité naturelle du manteau neigeux : Alpine, Subarctique, Arctique, et la banquise de l'Antarctique. L'impact le plus important du transport diffusif de la vapeur est observé dans la neige de la banquise dans la mer de Weddell et dans le manteau neigeux arctique peu profond. Les simulations montrent des réductions significatives de la densité à la base de du manteau neigeux lors de l'inclusion dans le model du transport diffusif de la vapeur d'eau.

Dans certains manteaux neigeux, la diffusion peut avoir un faible effet seulement et la convection est souvent invoquée pour expliquer les profils de densité observés, par exemple dans les minces couches de neige de la toundra. Les effets de la convection sur la structure du manteau neigeux n'ont jamais été étudiés systématiquement en examinant les régimes thermiques et de changement de phase pour différentes conditions du manteau neigeux. Cette thèse présente donc pour la première fois une étude numérique de la convection de la vapeur d'eau dans des manteaux neigeux idéalisés en utilisant une approche biphasée Eulerienne-Eulerienne. Nous trouvons un impact considérable de la convection naturelle sur la distribution de la densité de la neige avec une couche de densité significativement plus faible au bas du manteau neigeux et une couche de densité plus élevée située proche de la surface. Nous observons que l'hétérogénéité émergente dans la porosité de la neige entraîne un effet de rétroaction sur l'organisation spatiale des cellules de convection, provoquant leur déplacement horizontal. Nous constatons en outre que l'hypothèse de l'équilibre thermique n'est pas valable dans notre système idéalisé.

**Résumé**

La convection naturelle est plutôt peu susceptible d'avoir un impact important dans les couvertures neigeuses typiques des Alpes ou des régions sub-arctiques si les conditions sont horizontalement homogènes. Par conséquent, cette thèse étudie également numériquement l'impact potentiel de l'hétérogénéité induite par les arbustes ou les rochers sur la convection de la vapeur d'eau dans les couches de neige. Nous constatons que les cellules de convection se forment même avec un nombre de Rayleigh sous-critique aussi bas que 5 en raison de l'hétérogénéité induite dans la densité de la neige. Nous montrons que les contributions de la divergence des flux diffusifs et convectifs sur le changement de densité de la neige présentent de fortes variations. Nous constatons en outre que l'effet le plus important de la convection ne concerne pas les couvertures neigeuse très fines ou très épaisses, mais les couvertures neigeuse intermédiaires, qui permettent la formation de cellules de convection à l'échelle de 0,5 mètre.

Parmi les différents manteaux neigeux, des événements de convection significatifs sont observés numériquement par le couplage SNOWPACK-OpenFOAM pour un pergélisol de toundra herbacée sur l'île de Bylot. Nous constatons qu'une sublimation importante dans le flux descendant génère une base de faible densité dans le manteau neigeux. Nous observons en outre une forte empreinte de la convection sur la densité et la température de la neige avec des variations latérales significatives allant jusqu'à 90 kg m$^{-3}$ et 6,5 K respectivement. Cet effet de la convection sur le profil de densité de la neige, à savoir une base de faible densité et des chouches supprieures de haute densité, correspond qualitativement aux observations. Des travaux supplémentaires sont nécessaires pour adapter les paramétrisations physiques dans les modèles de neige conventionnels afin de représenter cet effet et son interaction avec le tassement de la neige et le métamorphisme.

# Contents

# Introduction

## Motivation and research objectives

Accurate modeling of the snowpack properties, especially vertical profiles of snow density and temperature, is vital in many applications, e.g. as input and validation data for climate models, hydrological models for irrigation and hydroelectricity (Bavay et al., 2013), etc. Water vapor transport within the snow and between snow cover and its environment is a significant process in different aspects such as snow metamorphism (Sturm and Benson, 1997; Pfeffer and Mrugala, 2002), thermal implications for climate applications (Slater et al., 2001; Callaghan et al., 2011), and snowpack stability and avalanches (Woo, 2012; Pfeffer and Mrugala, 2002). The typical density profile and micro-structural properties of many - in particular Arctic - snow covers cannot be fully understood or explained with current snow models because they omit an accurate description of water vapor transport. Furthermore, snow density change due to water vapor transport has a direct feedback on other physical properties or processes like snow thermal conductivity, snow viscosity, and snow compaction. In the presence of strong convective motions within the snowpack, lateral heterogeneity in snow density, the thermal regime and temperature profile are likely to be significantly different in comparison to situations without convection. Hence, the main goal of this thesis is to introduce this important transport process, which has been neglected thus far, to build the basis for a model representation in physics-based multi-layer snow models. To achieve this purpose, a novel implementation of heat and mass transfer processes in porous media, including the effects of internal phase change is developed in a computational fluid dynamics (CFD) framework to simulate convective motions occurring within the snowpack. This new model is then used to explore the impact of vapor transport on snow density in idealized snowpacks and also on snow profiles in deep and shallow snow covers and on sea ice. In summary, the research objective of the thesis is to understand and quantify the effect of convection on subsurface snow dynamics as well as develop a framework for model representation.

## State of the art

### The impact of water vapor transport on snow covers

Water vapor transport has been shown as a key player in shaping the snowpack structure, and of importance for issues ranging from snowpack stability and avalanches (Woo, 2012; Pfeffer and Mrugala, 2002) to the thermal implications for climate applications (Slater et al., 2001; Callaghan et al., 2011). For layers at the bottom of thin snow covers, an observed density decrease of more than 100 kg m$^{-3}$ (Trabant and Benson, 1972; Sturm and Benson, 1997; Domine et al., 2016b) was suggested to be a result of ice mass transfer due to water vapor flux. The "near-total disappearance of the basal depth hoar" at some measurement sites (Domine et al., 2016b) hinted at significant amount of water vapor transport which cannot be explained from purely diffusive fluxes. From measurements by Domine et al. (2016b), it was further found that increased snow density in the wind slabs may be explained by deposition of upward water vapor flux.

Strong temperature gradients (i.e low surface temperatures and comparably high base temperatures) in the snowpack also produce strong gradients in water vapor density. Cold air temperature and shallow snow depths result in sufficient vertical temperature gradients to develop a snow cover with a significant fraction of depth hoar layers (Derksen et al., 2009; Sturm and Benson, 1997; Taillandier et al., 2006; Domine et al., 2015). However, growth of depth hoar is an evidence of local inter-particle vapor fluxes (Gubler, 1985) that don't necessarily imply movement of vapor between snow layers nor result in change in layer density. Albert et al. (2004) have highlighted that due to temperature gradients, the snow and firn is affected by persistent vapor diffusion, causing sustained metamorphism over many years. Birkeland (1998); Birkeland et al. (1998) also connected the strong near-surface temperature gradients (strong vapor pressure gradients) to the formation of near-surface faceted crystals.

Arctic and subarctic snowpacks are frequently in direct contact with permafrost, which effects vapor transport. The measurements (Trabant and Benson, 1972; Alley et al., 1990; Sturm and Benson, 1997) suggest a continuous vapor flux from the soil into the basal snow layers, which are then losing vapor to upper layers. Sturm and Benson (1997) suggest that water vapor fluxes between snow layers result in mass change over finite distances and also change in layer density. They calculated the averaged net layer-to-layer vapor fluxes from end-of-winter density profiles of Subarctic snowpacks to be on the order of $10^{-7}$ kg m$^{-2}$ s$^{-1}$.

A deeper understanding of Arctic and subarctic snow characteristics is crucial for hydrology and ecology (Gouttevin et al., 2018). Domine et al. (2016b) have underlined the difficulties of existing snowpack models to accurately simulate Subarctic snowpack layering (e.g high density on top and lower density in the bottom). The explicit modeling of layer to layer diffusive vapor transport in this type of snowpack may constitute the lower limit for total water vapor transport but it is not sufficient for a correct representation of snow density profiles. Recently, Touzeau et al. (2018) have studied vapor diffusion in polar firn and how it may

affect the isotopic composition, which is critical for ice-core analysis and paleo-climatological studies.

Natural convection, in addition to diffusion, is another mechanism for vapor transport in snowpacks under strong temperature gradients, such as the Arctic and Subarctic ones (Trabant and Benson, 1972; Johnson and Bens, 1987; Alley et al., 1990; Sturm and Johnson, 1991; Domine et al., 2016b, 2018). From the measured rates of densification and density changes for snow in Fairbanks, Trabant and Benson (1972) concluded that convection must occur to explain measured vapor fluxes, which are an order of magnitude higher than calculated diffusive vapor fluxes. On the contrary, Akitaya (1974) found that convection did not occur in his experimental studies of depth hoar formation in Hokkaido. Observed temporal and lateral variations in temperature, strong horizontal thermal gradients, and half of the total heat transfer all were attributed to convective circulation in the Fairbanks subarctic snowpack by Sturm and Johnson (1991). Domine et al. (2016b) suggested convection as the possible explanation for the near-total disappearance of basal depth hoar at Bylot Island and concluded that water vapor diffusion could not be sufficient alone. Additionally, almost no depth hoar was observed by Domine et al. (2018) at Ward Hunt Island (Canadian high Arctic) despite favorable thermal conditions. Hard wind slabs of low permeability formed by high winds was suggested as a reason to prevent convection and as a factor delaying depth hoar formation.

Observations cannot distinguish between different types of vapor transport and represent a mixture of effects such as snow settling, vapor transport and wind compaction (Sommer et al., 2018). Therefore, a sound modeling of water vapor transport needs to take into account the natural convection as a possible mechanism of density change and observations need to be explained by modeling. Previous studies for natural convection in snowpacks only focused on the thermal regime without explicitly considering water vapor transport and its effects on porosity change and mass redistribution (Klever, 1985; Powers et al., 1985). More recently, Calonne et al. (2014, 2015) compared fine-scale modeling with its macroscopic equivalent approach for a small snow layer either for diffusion or with different advective flow velocities imposed at the bottom. However, they did not consider the porosity change and consequently mass redistribution and snow density change due to advective vapor transport. We also note that simulations were only carried out for an idealized small snow sample not for a typical snow cover. As reviewed by Jafari et al. (2020), previous attempts to numerically study water vapor transport in snow and its effects on snow properties consider diffusion only.

## Achievements, outcomes, and structure of the thesis

This thesis is made of two published articles and two chapters which have not been published yet. A detailed description of the published articles and the doctoral candidate's contribution is given on the first page of each chapter.

As a first step, we focused on modelling of purely diffusive water vapor transport, which constitutes the lower limit for total water vapor transport. The diffusive water vapor transport

has been implemented in SNOWPACK and its results have been analysed and presented in chapter 1 based on a postprint version of a published paper as Jafari et al. (2020). This study served as a useful exercise to establish the current state of the art and expose the shortcomings of a diffusive only approach for vapor transport.

For natural convection as a potential main mechanism of the vapor transport in snowpacks, it is not possible to explicitly model it with phase change in a one-dimensional snow model. Thus, the convective vapor transport has been numerically investigated in an idealized snowpack, using the Eulerian–Eulerian two-phase model in a new solver developed in OpenFOAM in chapter 2. In this two-phase system, sublimation and deposition produce significant gradients in snow density that alter the permeability structure and cause convection cells to migrate laterally. The thermal equilibrium assumption is often used for heat transfer in porous media e.g. as assumed by Calonne et al. (2014, 2015) for an idealized small snow sample without snow density change. However as stated in Faghri and Zhang (2006); Nield and Bejan (2017), for some situations this assumption is not locally valid such as for sufficiently large Rayleigh numbers, widely different thermal properties between phases, and also for rapid transient problems. As discussed in chapter 2, the relative magnitude of heat transfer between phases is not negligible and the temperature difference between phases can locally reach up to 5 K. Therefore, our system of governing equations treats temperature in the solid and pore phase separately. Chapter 2 is written based on a postprint version of a published paper as Jafari et al. (2022).

After studying the convection of water vapor in idealized snowpacks, it is realized that a potential heterogeneity in the initial snow density profile significantly impacts the water vapor distribution and consequently the snow density change. Therefore, in chapter 3, we introduce heterogeneity in the snow density at the bottom of snowpack for example caused by thee presence of herbs and shrubs. We observe that even with sub-critical Rayleigh number, the convection cells are formed in the domain and it considerably increases the phase change rate compared to the homogeneous snowpack.

As a straightforward solution to improve the one-dimensional physics-based multi-layer snow model, a C++ interface (dynamic library) is implemented for a tight coupling between SNOWPACK and OpenFOAM. In summary, in this coupling SNOWPACK takes into account all important processes for snow dynamics such as settling, metamorphism, and melting-refreezing while OpenFOAM only solves two-dimensional natural convection to update phase change rate due to vapor transport. The coupled model is applied for different snow covers and the results for the most significant cases are analyzed and discussed in chapter 4. Notably, it is found that early season snowpacks already develop convective motions that seem to persist throughout the winter season. The SNOWPACK-OpenFOAM coupling builds a first step to take into account the effects of convection in real snow covers. To reach this goal, several physical and numerical assumptions and simplifications had still to be taken. These include: (1) the choice of classical grain size for porosity and permeability calculations which induces higher flow velocities than using the optical grain size; (2) the neglect of dispersion effects on

the thermal and mass transport regime; and (3) the effects of wind compaction on surface snow. To limit computational burden, we also used a "flow freezing" assumption, which may not be valid in all cases.

# 1 The impact of diffusive water vapor transport on snow profiles in deep and shallow snow covers and on sea ice

This chapter is based on a postprint version of a published paper in the Journal of Frontiers in Earth Science as:

MC has started the project, but the first author, MJ, continued the project by implementing the diffusive vapor transport in SNOWPACK and performing the simulations. MJ prepared the manuscript with contributions from all co-authors.

**Chapter 1. The impact of diffusive water vapor transport on snow profiles in deep and shallow snow covers and on sea ice**

## Abstract

Water vapor transport has been highlighted as a critical process in Arctic snowpacks, shaping the snow cover structure in terms of density, thermal conductivity, and temperature profile among others. Here, we present an attempt to describe the thermally-induced vertical diffusion of water vapor in the snow cover and its effects of the snowpack structure using the SNOWPACK model. Convection, that may also constitute a significant part of vapor transport, is not addressed. Assuming saturated conditions at the upper boundary of the snowpack and as initial condition, the vapor flux between snow layers is expressed by a 1-dimensional transient diffusion equation, which is solved with a finite difference routine. The implications on the snowpack of this vertical diffusive flux, are analyzed using metrics such as the cumulative density change due to diffusive vapor transport, the degree of over- or undersaturation, the instantaneous snow density change rate, and the percentage of snow density change. We present results for four different regions sampling the space of natural snow cover variability: Alpine, Subarctic, Arctic, and Antarctic sea ice. The largest impact of diffusive water vapor transport is observed in snow on sea ice in the Weddell Sea and the shallow Arctic snowpack. The simulations show significant density reductions upon inclusion of diffusive water vapor transport: cumulative density changes from diffusive vapor transport can reach -62 and -66 kg m$^{-3}$ for the bottom layer in the shallow Arctic snowpack and snow on sea ice respectively. For comparison, in deeper snow covers, they rarely exceed -40 kg m$^{-3}$. This leads to changes in density for shallow snowpacks at the soil-snow interface in the range of -5% to -21%. Mirroring the density decease at depth is a thicker deposition layer above it with increase in density around 7.5%. Similarly, for the sea ice, the density decreased at the sea ice-snow interface by -20%. We acknowledge that vapor transport by diffusion may in some snow covers - such as in thin tundra snow - be small compared to convective transport, which will have to be addressed in future work.

## 1.1  Introduction

As a crucial player in snow metamorphism, water vapor transport has been proven to be a very significant process in shaping the snowpack structure (Sturm and Benson, 1997; Pfeffer and Mrugala, 2002). It is important for issues such as snowpack stability and avalanches (Woo, 2012; Pfeffer and Mrugala, 2002) but also thermal conductivity e.g. in the context of climate studies (Slater et al., 2001; Callaghan et al., 2011).

In dry snow and particularly under strong temperature gradients, metamorphism is essentially driven by water vapor transport, whereby temperature gradients induce gradients in saturation water vapor density and pressure that result in diffusion (Sturm and Benson, 1997; Pfeffer and Mrugala, 2002). Both microscopic exchange of vapor between grains, and macroscopic vapor flux between snow layers over the entire snowpack, occur as a result of these gradients.

This process is especially active in Arctic and sub-arctic snowpacks, where shallow snow

depth and strong temperature differences between soil and atmosphere lead to significant kinetic metamorphism, rapidly creating snow layers composed of depth hoar crystals, which are coarse grained, typically vertically-oriented and cup-shaped (Pinzer et al., 2012). Depth hoar has been seen to be dominant in sub-arctic snowpacks (Derksen et al., 2009; Sturm and Benson, 1997; Taillandier et al., 2006; Domine et al., 2015). Arctic, and to some extent subarctic snowpacks, are sometimes in direct contact with permafrost, which influences the vapor transport. Significant amounts of mass transferred from one layer to another, and from the soil into the basal snow layers, have been observed in these snowpacks (Trabant and Benson, 1972; Alley et al., 1990). Also, as an evidence of ice mass transfer due to water vapor flux, observations by Trabant and Benson (1972); Sturm and Benson (1997); Domine et al. (2016b) indicate a density decrease of more than $100\,\mathrm{kg\,m^{-3}}$ for layers close to the ground in thin snow covers. Domine et al. (2016b) also report in some places about the "near-total disappearance of the basal depth hoar" due to a possible extreme impact of water vapor transport other than purely diffusive fluxes. From their measurements, Domine et al. (2016b) also found that density increases in the wind slabs overlying the depth hoar, which may be attributed to upward water vapor transfer and its deposition. Sturm and Benson (1997) estimated that the magnitude of the averaged net layer-to-layer vapor flux from end-of-winter subarctic snowpacks is in the order of $10^{-7}\,\mathrm{kg\,m^{-2}\,s^{-1}}$.

As it results notably in the formation of thick depth hoar layers that generally exhibit a low thermal conductivity, water vapor transport in high latitude snowpacks carries significant thermal implications: the ground thermal regime below the snow, including the permafrost thermal dynamics, is in great part governed by the thermal insulation of the snowpack (Zhang et al., 1996; Gouttevin et al., 2012, 2018), with consequences for ecology (Domine et al., 2018), geo-engineering, snow-atmosphere heat exchange (Domine et al., 2019) and global climate feedbacks (Schneider von Deimling et al., 2012). Note that the range of thermal conductivities of depth hoar snow types is still not well known and that local values are influenced by local conditions (Domine et al., 2016b; Calonne et al., 2014; Gouttevin et al., 2018).

In alpine snowpacks, temperature gradients that can result from the meteorological conditions over the course of the winter or early snowfall on unfrozen grounds are responsible for the formation of faceted snow layers of moderate cohesion. When covered by more cohesive snow types, faceted crystals form weak layers in the snowpack, which increases the avalanche risk.

For all these reasons, modelling the vapor transport within most types of snow covers, and its effects on the properties of the snow, appears to be of high importance. Some attempts to study the water vapor transport in snow columns have been done. The Snow Thermal model, SNTHERM (Jordan, 1991), includes vapor transport in snow (but not soil). In this model, saturation was assumed in snow such that the water vapor flux divergence in each layer was considered to be compensated by phase gains (deposition) and losses (sublimation) within the medium. Bartelt et al. (2004) studied the diffusive mass conservation of the water vapor with interfacial mass transfer term applying the atmospheric relative humidity as the top boundary condition. Calonne et al. (2014) applied the macroscopic equivalent model for

heat conduction and vapor diffusion including the phase change source term. They concluded that for the large temperature gradient, the impact of these mass and energy source terms due to phase change cannot be neglected. Recently, Touzeau et al. (2018) have looked at vapor diffusion in polar firn and its potential influence on the isotopic composition.

Depending on the snowpack, soil, and meteorological conditions, water vapor transport may occur through both diffusion and convection (Trabant and Benson, 1972; Johnson and Bens, 1987; Alley et al., 1990; Sturm and Johnson, 1991; Domine et al., 2016b, 2018). Trabant and Benson (1972) found from the measured rates of densification and density changes for snow in Fairbanks that significant convection must occur to explain differences with respect to vapor fluxes calculated from pure diffusion models. On the contrary, Akitaya (1974) found that convection did not occur in his experimental studies of depth hoar formation in Hokkaido. In the Fairbanks subarctic snowpack, Sturm and Johnson (1991) interpreted significant horizontal thermal gradients and incoherent temporal variations of horizontal temperature patterns, as a sign of convective circulation. They estimated that about half of the total heat transfer at their study site, and for the 3 years with measurements, were caused by convection. Domine et al. (2016b) concluded that the near-total disappearance of basal depth hoar at Bylot Island could not be caused by just water vapor diffusion alone and also suggested convection as the possible explanation. Additionally, Domine et al. (2018) observed almost no depth hoar at Ward Hunt Island (Canadian high Arctic) in spring 2016 despite favorable thermal conditions. He proposed that high winds, which formed hard wind slabs of low permeability, prevented convection and would be a factor delaying depth hoar formation.

These seminal works suggest that both convection and diffusion have to be accounted for if a sound modelling of water vapor transport within the snowpack is to be achieved. As a first step in this process, we focus here on the modelling of water transport through diffusion only, which constitutes the lower limit for total water vapor transport. It is furthermore not possible to explicitly model convection in a one-dimensional model, so that a different, maybe stochastic approach, should be undertaken for this purpose. As will be shown, the results from the diffusion vapor model do not contradict most of the relevant observations from the field. For instance, diffusion vapor transport alone already reproduces lower densities at the base of the snowpack in some cases.

## 1.2 Methods

### 1.2.1 SNOWPACK model

SNOWPACK is a 1D physics-based model predicting snowpack settling, layering, surface energy exchange and mass balance. It is based on a Lagrangian finite element coordinate system implementation and governed by the one-dimensional, mass, energy and momentum conservation equations taking into account phase change in the snowpack. The Lagrangian coordinate system allows the snowpack mesh to evolve over time, i.e keeping track of the

layer identities when snow deposition (snowfall, wind drift) or removal (erosion, sublimation, melt) events occur. Snow is modeled as a three-component (ice, water, air) porous material for which phase changes between the components are simulated. For each layer, several core variables such as snow bulk temperature, density as well as liquid water content are calculated.

SNOWPACK requires at minimum 6 parameters: air temperature, relative humidity, wind speed, incoming shortwave radiation (or reflected shortwave radiation), incoming long wave radiation (or surface temperature). The amount of new snow added to the mesh is obtained from either measured precipitation rates or measured snow depth (from which snow precipitation rates are then derived via calculated settling rates) (Lehning et al., 1999a).

Atmospheric forcing governs the development of the snow cover throughout the season, dictating mass and energy exchanges at the snow surface. As a result, it determines upper boundary conditions for e.g. temperature and relative humidity, at the top node of the snowpack using either Dirichlet or Neumann formulations. Usage of Dirichlet boundary conditions imposes measured temperatures at the snowpack surface, whereas Neumann prescribes the net snowpack surface energy flux (including long wave radiation, sensible and latent heat exchange and energy from rain) (Lehning et al., 2002a). At the snowpack-ground interface, the lower thermal boundary conditions are either set to a constant ground temperature or, if soil layers are specified, calculated from soil properties to which a constant heat flux is applied at the bottom.

Two particularly important and nonlinear features of the model are thermal conductivity and creep viscosity, governing respectively energy transport and snow settlement. They are formulated as constitutive relations at both macroscopic and microscopic scales (Lehning et al., 2002c). To model liquid water flow through the snowpack, the model solves Richards Equation which describes liquid water movement in variably saturated porous media. This method is hence able to better reproduce the formation of capillary barriers (Richards, 1931; Wever et al., 2014, 2015). Snow microstructure plays a key role in determining the bulk characteristics in the snowpack such as temperature distribution, settling rate as well as mechanical and optical properties. Its representation in SNOWPACK model is done by determining several microscopic properties including ice grain size, shape (dendricity, sphericity) and bondings (bond radius, coordination number) (Lehning et al., 2002c).

Adding explicit vapor transport as described below changes the SNOWPACK dynamics and affects the non-linearities discussed above. For example, changes in local density will strongly impact creep viscosity and thermal conductivity. However, parameterizations for viscosity or thermal conductivity have been physically or empirically adjusted for the SNOWPACK model without explicit vapor transport. At this stage, we chose not to adjust these formulations to the changes in model behaviour ensuing from the new explicit diffusive vapor transport. Indeed, as the present study will reveal, the effect of the new diffusive water vapor transport on e.g. density, is rather small for most snowpacks, so that effects of inconsistencies will be limited. Furthermore, adjusting paramaterizations requires major efforts and should be done as soon

as also convective transport is implemented, which is expected to yield more substantial changes in e.g. snowpack density.

## 1.2.2 Diffusive water vapor transport in snow and soils

### 1.2.2.1 General equations

Layer-to-layer vapor transport is implemented by considering mass conservation of the water vapor component in the snow or soil, resulting in a transient diffusion equation written as:

$$\theta_a \frac{\partial \rho_v}{\partial t} + \frac{\partial}{\partial z}(\theta_a J_v) = M_{mm} \tag{1.1a}$$

$$J_v = -D_{\text{eff},a} \frac{\partial \rho_v}{\partial z} \tag{1.1b}$$

In Eqs. (1.1), $\rho_v$ (kg m$^{-3}$) is the water vapor density, $J_v$ (kg m$^{-2}$s$^{-1}$) is the diffusive water vapor flux (it is positive when is upward), $\theta_a$ is the air volume fraction in snow or soil, $M_{mm}$ (kg m$^{-3}$s$^{-1}$) is the mass source (or sink) term due to deviation of vapor pressure from the saturation condition, and finally $D_{\text{eff},a}$ (m$^2$s$^{-1}$) is the effective water vapor diffusivity in the air component of the snow or soil. As pointed out by Hansen and Foslien (2015), it is distinguished from the effective water vapor diffusivity in snow or soil by $D_{v,s} = \theta_a D_{\text{eff},a}$.

Following Albert and McGilvary (1992), $M_{mm}$ may be evaluated as:

$$M_{mm} = h_m a_s (\rho_{vs} - \rho_v) \tag{1.2}$$

In Eq. (1.2), $h_m$ (m s$^{-1}$) is the mass transfer coefficient, $a_s$ (m$^{-1}$) is the specific surface area of snow, and $\rho_{vs}$ (kg m$^{-3}$) is the saturation water vapor density at the local snow temperature. It should be noted that the heat source (or sink) term due to vapor transport, $-M_{mm}L_h$ , is added to the heat transfer equation in SNOWPACK, with $L_h$ (J kg$^{-1}$) being the latent heat of sublimation.

Choices of formulations for the mass transfer coefficient and the effective water vapor diffusivity in snow and soil, will be detailed in the next subsections.

#### 1.2.2.2 Mass transfer coefficient

Different formulations and quantifications for the mass transfer coefficient $h_m$ have been proposed in the literature. For spheres, $h_m$ may be evaluated as $h_m = \text{Sh} D_{v,a}/d_p$ (Bird et al., 1961), using the definition of the Sherwood number, Sh, and with $d_p$ (m), the sphere diameter, and $D_{v,a}$ (m$^2$s$^{-1}$), the water vapor diffusivity in air. Theory indicates that for Sh = 2, the mass transfer between sphere and fluid occurs only through diffusion in still fluids (Bird et al., 1961). Based on measurements, Thorpe and Mason (1966) proposed a formulation of Sh for an ice sphere, Sh$_i$, when the sphere is in a moving fluid:

$$\text{Sh}_i = 1.88 + 0.66 \text{Re}^{1/2} \text{Sc}^{1/3} \tag{1.3}$$

with Re the Reynolds number of the flow based the sphere diameter and Sc is the Schmidt number. Eq. (1.3) is a simple sum of the mass transfer contribution from the diffusive flow (the first term) and from the advective flow (the second term). For the range of particle diameters between 0.1 mm and 1 mm, which are reasonable for snow, both formulations yield mass transfer coefficients in the range between 0.04 to 0.4 m s$^{-1}$ for the diffusion process only.

However, based on a similar formulation for the advective flow contribution, Albert and McGilvary (1992) quantified $h_m$ for the diffusion process, to values as low as 0.09 m s$^{-1}$. Combining measurements of specific surface area and mass changes in an air-flow experiment, Neumann et al. (2009) inferred from Eq. (1.2) also low values for $h_m$, between $7.5 \times 10^{-5}$ and $8 \times 10^{-3}$ m s$^{-1}$ and proposed the following formulation in which advection is also accounted for:

$$h_m = (0.5 \text{Re} + 0.075) \times 10^{-3} \tag{1.4}$$

It should be noted that the factor $10^{-3}$ in the text of their paper is missing, however in the plots for $h_m$ versus Re, the factor $10^{-3}$ is correctly represented.

Calonne et al. (2014) and Ebner et al. (2015) respectively proposed and relied on another formulation for $h_m$:

$$h_m = \frac{\rho_i}{\beta \rho_{v,s}} \tag{1.5}$$

where $\beta$ is the interface kinetic growth coefficient in units of s m$^{-1}$. Based on experiments of sublimation and deposition on the ice structure for one case without advective flow and three cases with different possible rates of advective flows, Ebner et al. (2015) inferred $\beta = 9.7 \times 10^9$ s m$^{-1}$ with an average normalized root-mean-square error less than 9.7 %. This means an $h_m$ value around $8.07 \times 10^{-5}$ m s$^{-1}$.

As a result, there is a clear discrepancy in order of magnitude between the $h_m$ values inferred by Neumann et al. (2009) and Ebner et al. (2015) on the one hand (that lie in the range of $7.5 \times 10^{-5}$ and $8 \times 10^{-3}$ m s$^{-1}$), and the theoretical original estimations from Bird et al. (1961) and Thorpe and Mason (1966) that reach values from 0.04 to 0.4 m s$^{-1}$. A plausible explanation for this apparent contradiction is the fact that part of the snow grains' specific surface area may be not active for mass transfer, hence inducing much lower estimations of $h_m$ in the approaches of Neumann et al. (2009) and Ebner et al. (2015). They considered all specific surface area is active for mass transport which may not be the case (Kunii and Levenspiel, 1991). This is analogous to Crowe (2005) who explained that for a bed of small particles with low Re (low velocities), due to very large specific surface area, the gas phase gets saturated already before penetrating further into the bed of particles.

We made use of both theoretical mass transfer coefficient $h_{m,t}$ based on Sh$_i = 2.0$, and experimental or numerical estimations of $h_m$, $h_{m,e}$, by Ebner et al. (2015), to infer the actually active specific surface area, $a_{s,a}$, to be used in Eq. (1.2) instead of $a_s$ :

$$a_{s,a} = \frac{a_s h_{m,e}}{h_{m,t}} \tag{1.6}$$

Eq. (1.2) now has the form:

$$M_{mm} = h_{m,t} a_{s,a} (\rho_{vs} - \rho_v) \tag{1.7}$$

### 1.2.2.3   Specific surface area in snow and soils

The specific surface area of a dry snow layer (or in general a porous material layer), $a_s$, is defined as the total surface area of the snow - pore interface per volume of snow layer. Assuming the dry snow layer is composed of the spherical grains with average diameter of $d_p$ (m), the specific surface area is evaluated as :

$$a_s = \frac{6\theta_i}{d_p} \tag{1.8}$$

For wet snow, we use the approximation applied by Gallet et al. (2014), that wet snow consists of ice cores with radius $r_i$ covered by a water film with outer radius of $r_w$ such that the ice core is not in contact with air. Similarly, for a frozen soil layer which may have some liquid water, the soil grain with radius $r_s$ is assumed to be covered first by an ice shell with the outer radius of $r_i$ and then covered by a water film with the outer radius of $r_w$ if liquid water is present. Hence, the diameter used in Eq. (1.8) should be updated as the diameter of the last

shell which can be: (1) water for wet snow, (2) either water for the wet-frozen soil or the ice for the completely-frozen soil. According to the Appendix of Gallet et al. (2014), the diameter of the last shell may be evaluated as:

$$\text{dry snow:} \rightarrow d_p = 2r_i \rightarrow a_s = \frac{6\theta_i}{d_p} \tag{1.9a}$$

$$\text{wet snow:} \rightarrow d_p = 2r_i[\frac{\theta_w}{\theta_i} + 1]^{1/3} \rightarrow a_s = \frac{6(\theta_w + \theta_i)}{d_p} \tag{1.9b}$$

$$\text{completely-frozen soil:} \rightarrow d_p = 2r_s[\frac{\theta_i}{\theta_s} + 1]^{1/3} \rightarrow a_s = \frac{6(\theta_i + \theta_s)}{d_p} \tag{1.9c}$$

$$\text{wet-frozen soil:} \rightarrow d_p = 2r_s[\frac{\theta_w + \theta_i}{\theta_s} + 1]^{1/3} \rightarrow a_s = \frac{6(\theta_w + \theta_i + \theta_s)}{d_p} \tag{1.9d}$$

It should be noted that for dry and wet snow, the radius of the ice core, $r_i$, is selected as the optical grain size (Calonne et al., 2012). Obviously, in case there is just a dry soil layer, the mass source (or sink) term in Eq. (1.1a), $M_{mm}$, will be set to zero.

### 1.2.2.4 Effective water vapor diffusivity in snow and soils

The measured and calculated values of $D_{v,s}$, show an enhancement compared to the water vapor diffusion coefficient in air ($D_{v,a}$) (Yosida et al., 1955; Sommerfeld et al., 1987; Colbeck, 1993; Sokratov and Maeno, 2000). Yosida et al. (1955) have justified this enhancement by "hand-to-hand" way of water vapor transport which reduces the actual transport distance. Using a finite element model based on real snow microstructure, Pinzer et al. (2012) and Calonne et al. (2014) both calculated the effective water vapor diffusivity in snow in different ways. Based on results of Pinzer et al. (2012), an enhancement for the water vapor diffusivity in snow, compared to that in air, has been observed, ranging between 1.05-1.13. Results of Calonne et al. (2014) show a linear reduction of $D_{v,s}/D_{v,a}$ when the snow density increases to higher values. Hansen and Foslien (2015) extended an analytical model developed by Foslien (1994) for the effective water vapor diffusivity in snow, based on two possible snow microstructures: (1) "pore microstructure" in which the heat is transferred in parallel through the air and ice phases, (2) "layered microstructure" in which the heat is transferred in series through the air and ice layers. Hansen and Foslien (2015) justified in detail how they combined heat fluxes resulting from these two microstructures to derive the following parametrization for effective water vapor diffusivity in snow:

$$D_{v,s} = \theta_i \theta_a D_{v,a} + \theta_a \frac{k_i D_{v,a}}{\theta_i(k_a + L_h D_{v,a}\frac{d\rho_{vs}}{dT}) + \theta_a k_i} \tag{1.10}$$

## Chapter 1.  The impact of diffusive water vapor transport on snow profiles in deep and shallow snow covers and on sea ice

In Eq. (1.10), $k_i$ and $k_a$ (W m$^{-1}$K$^{-1}$), are the thermal conductivities for the air and ice component of the snow respectively, and $\theta_i$ is the volume fraction of the ice component in snow. Even though this model assumes homogeneous snow, we believe this model predicts $D_{v,s}$ with reliable accuracy because (1) it provides self-consistent values for $D_{v,s}$ for the limiting cases of ice and air, (2) the calculated values are in a very good agreement with values calculated by numerical finite element results on microscale by Christon et al. (1994) and Pinzer et al. (2012), (3) it has no empirical coefficients, as developed based on heat and mass conservation using simple assumptions on snow microstructures, (4) in this model, the density contribution is included explicitly through volume fractions of air and ice and temperature effects are considered implicitly by thermal conductivity for ice and air. With this formulation, for snow with different values of $\theta_a$ e.g. 0.2, 0.3 and 0.5, the effective water vapor diffusivity in snow are estimated as $D_{v,s} = 1.16D_{v,air}$, $1.21D_{v,air}$, and $1.25D_{v,air}$, respectively.

To estimate the effective water vapor diffusivity in the soil, we rely on a simple parameterization and standard parameters. We a posteriori justify this simplified description as a brief sensitivity study of our results show that soil parameters have a negligible influence (discussed in Sect. 1.3.6). Through the soil, the effective water vapor diffusivity is defined as $D_{v,soil} = \theta_a \tau D_{v,air}$, in which $D_{\text{eff},a} = \tau D_{v,air}$ is the effective water vapor diffusivity in the air component of the soil, $\theta_a$ is the air volume fraction, $\tau$ is the tortuosity factor defined by Millington and Quirk (1961) as $\tau = \theta_a^{7/3}/(1-\theta_s)^2$, $\theta_s$ is the soil volume fraction, and $D_{v,air} = 22.0 \times 10^{-6}$ m$^2$ s$^{-1}$ is the vapor diffusivity in air. We hence get the effective water vapor diffusivity in the soil as:

$$D_{v,soil} = \frac{\theta_a^{10/3}}{(1-\theta_s)^2} D_{v,air} \tag{1.11}$$

Similar to the effective diffusivity estimates made earlier for snow, we can use Eq. (1.11) to assess the effective diffusivity for soils, given our soil setup with $\theta_s = 0.625$ (see Sect. 1.2.4): Maximum water vapor diffusivity in soils is reached for maximum air content (e.g. completely dry soils), yielding $D_{v,soil,max} = 0.27D_{v,air}$. Minimum water vapor diffusivity in soil is reached in completely saturated soils and tends to zero. Based on the initial soil volumetric content, these estimates show that vapor diffusivity in snow is at least three orders of magnitude larger than in the soil.

### 1.2.2.5   Discretization

Applying a combination of the forward and backward Euler methods in time ($n$ is the time index) and the central difference scheme in space for an internal node ($i$ is space index) excluding the boundary nodes, the discretized form of Eq. (1.1a) has the form:

$$\theta_{a,i}^{n} \frac{\rho_{v,i}^{n+1} - \rho_{v,i}^{n}}{\Delta t}$$

$$-f \left[ \frac{2D_{i+1}^{n}\theta_{a,i+1}^{n}}{dz_{u}\left(dz_{u}+dz_{d}\right)}\rho_{v,i+1}^{n+1} - \frac{2D_{i}^{n}\theta_{a,i}^{n}}{dz_{u}dz_{d}}\rho_{v,i}^{n+1} + \frac{2D_{i-1}^{n}\theta_{a,i-1}^{n}}{dz_{d}\left(dz_{u}+dz_{d}\right)}\rho_{v,i-1}^{n+1} \right]$$

$$-\left(1-f\right)\left[ \frac{2D_{i+1}^{n}\theta_{a,i+1}^{n}}{dz_{u}\left(dz_{u}+dz_{d}\right)}\rho_{v,i+1}^{n} - \frac{2D_{i}^{n}\theta_{a,i}^{n}}{dz_{u}dz_{d}}\rho_{v,i}^{n} + \frac{2D_{i-1}^{n}\theta_{a,i-1}^{n}}{dz_{d}\left(dz_{u}+dz_{d}\right)}\rho_{v,i-1}^{n} \right]$$

$$-f\left[ h_{m,i}^{n}a_{s,i}^{n}\left(\rho_{v,i}^{n+1}-\rho_{vs,i}^{n}\right) \right] - \left(1-f\right)\left[ h_{m,i}^{n}a_{s,i}^{n}\left(\rho_{v,i}^{n}-\rho_{vs,i}^{n}\right) \right] = 0 \quad (1.12)$$

In Eq. (1.12), $\Delta t$ is the simulation time step, $dz_d = z_i - z_{i-1}$, and $dz_u = z_{i+1} - z_i$. Here, choosing $f = 1$, a fully implicit discretization is selected while $f = 0.5$ refers to the Crank-Nicolson scheme. Even though the Crank-Nicolson scheme is unconditionally stable as the fully implicit scheme, it suffers from numerical oscillations so that the simulation time step should be limited similar to the criterion applied for the stability of an explicit scheme as $v_d \Delta t / \Delta z < 1$ (Courant et al., 1928) (with $v_D = J_v / \rho_{vs}$ the diffusive water vapor velocity). The system of equations described by Eq. (1.12) forms a tridiagonal sparse matrix for which the sparse solvers from the `Eigen` C++ library are used (Guennebaud et al., 2010). For the upper boundary condition the saturation water vapor density at the snow surface temperature is used, and zero vapor flux is used for the bottom node of the soil as lower boundary condition. For the new snow layers added to snowpack due to snowfall, the water vapor density is initialized as saturation density based on the new snow temperature.

### 1.2.2.6   Diagnostic variable: The cumulative snow density change due to diffusive vapor transport

To quantify the effects that water vapor transport has on the snow layer, the cumulative snow density change due to vapor transport, $\Delta\rho_{cum}$, is introduced in Eq. (1.13). This is the summation of snow density change due to the sublimation and deposition of water vapor for each element over all time steps. This is an interesting diagnostic variable since density changes due to vapor transport will tend to be masked by the highly non-linear snow settling.

$$\Delta\rho_{cum}(t) = \int_{0}^{t} \frac{d\rho_{snow}}{dt}(t^*)dt^* \quad (1.13)$$

### 1.2.3   Study sites

The Arctic site is situated at Samoylov Island, Russia. This study site is located in a zone of continuous permafrost featuring polygonal tundra landscape in the delta of the Lena river, Siberia (Boike et al., 2013, 2018). Our simulation for the winter season 2010-2011 analyzed in Sect. 1.3.2 characterizes a polygon center as described in (Gouttevin et al., 2018), forcing data

are derived from observations (for snow depth) and reanalysis data for the other atmospheric variables. It should be noted that the simulation for the winter season of 2012-2013 is used for comparison with measured density profile at Samoylov described in Sect. 1.3.7.

The Subarctic site is situated in Sodankylä, Finland in a small clearing in pine plantation with sandy loam soil. The site has been one of the reference sites for snow studies in the past (Essery et al., 2016), whereby forcing data are derived from local meteorological measurements (incoming solar and longwave radiation, snowfall and rainfall rates, air temperature, humidity, wind speed and atmospheric pressure). Winter season of 2007-2008 is analyzed in this study. Simulated snow density profiles are compared with observation at Sodankylä for four winter seasons, 2009-2013, in Sect. 1.3.7.

The Alpine site, called Weissfluhjoch is located at an altitude of 2540 m in the Swiss Alps (Davos, Switzerland). It has been operated by the WSL Institute for Snow and Avalanche research (SLF) since 1936. The long time operation of the site results in a large amount of reliable data. Meteorological parameters are automatically measured ((Enescu et al., 2018) under doi: 10.16904/1) and forcing data were derived for them for the winter season 2001-2002 simulated in the present paper.

The SNOWPACK sea ice version introduced by Wever et al. (2020) has been tested for a point in the Weddell Sea with latitude -69.4672°and longitude -42.3728°. This point represents the starting location of Snow Buoy 2016S31, for which we here simulate the snowpack evolution from 16th January 2016 until 25th January 2017. Forcing data are taken from the ERA5 re-analysis except for snow depth which was observed at the buoy. The trajectory of Snow Buoy 2016S31 from 16th January 2016 until 25th January 2017 is presented at www.meereisportal.de (Nicolaus and Schwegmann, 2017).

### 1.2.4   Model configurations at sites

All the simulations performed here rely on the same setup for the SNOWPACK model. The only exception is the high-Arctic Samoylov simulation, where additional options were used, namely the adaptations of the SNOWPACK model developed by Gouttevin et al. (2018). These include a mechanically reduced compaction and an enhanced grain growth in basal snow layers, as well as enhanced wind densification close to the surface. They were shown by Gouttevin et al. (2018) to provide better agreement with e.g. density measurements at Samoylov.

To solve the diffusive vapor transport equation discretized in Eq. (1.12), the fully implicit scheme with a time step of 1 min is used, while the main simulation time step of SNOWPACK is 15 min. Note that the layer resolution of the simulations was increased from 2 cm to 0.1 cm for the thin Arctic snow cover. A general sensitivity analysis was conducted and it was found that a finer layer resolution did not qualitatively change the results. A small effect of stronger density decrease very close to the surface was observed for higher resolutions (not shown).

This, however, is anyway artificial as the true snow surface is rough and we therefore assume that the layer resolution of the order of cm is adequate in general.

For all snow covers over land, a soil column 3 m deep with the soil volume fraction of 0.625, the air volume fraction of 0.125, and water volume fraction of 0.25 has been considered except for the layers with sub-zero temperatures. For these layers, the water content was added to the ice content. Sensitivity tests regarding this configuration have been performed at Samoylov and are reported in the Results section. For the heat transfer equation, the Neumann boundary condition was used at the top surface of snowpack and a constant heat flux of $0.06 \, \text{Wm}^{-2}$ is applied at the bottom of soil layer.

For the sea ice site, initial snow conditions are derived from observations and assumptions in terms of brine salinity, temperature, and pore space as described in Wever et al. (2020): at the beginning of the simulation in January 2016, 2 cm of snow lies above 274 cm of sea-ice. The boundary conditions applied by Wever et al. (2020) are also used.

## 1.3   Results And Discussion

In this section, we first present some general features of the new model for diffusive water vapor transport. Then, we analyse the effects of diffusive water vapor transport in four diverse snow covers, ranging from polar to Alpine conditions. These effects are primarily investigated on the density profiles, via the cumulative snow density change due to vapor transport. The largest effects are obtained for the snowpack on sea ice in the Weddell sea, and for the most shallow snowpack at Samoylov.

### 1.3.1   General model behaviour

First, our simulations reveal that the temporal term in Eq. (1.1a), $\partial \rho_v / \partial t$, is very small compared to the other terms: Its magnitude rarely exceeds $5 \times 10^{-8} \, \text{kg m}^{-3} \, \text{s}^{-1}$ while the diffusion and source/sink terms reach values of $2 \times 10^{-5} \, \text{kg m}^{-3} \, \text{s}^{-1}$ at Samoylov for instance. This means that (i) departure from saturated conditions within the snowpack is always rather small when compared to the changes in water vapor content implied by inter-layer vapor fluxes, and (ii) that the source/sink term efficiently compensates for these inter-layer vapor fluxes. In other words, the sink/source term is generally not a limiting term for Eq. (1.1a).

As a next observation, the degree of over- or undersaturation, $\sigma = (\rho_v - \rho_{v,s})/\rho_v$, is very much related to the divergence of the vapor flux. It also drives snow density changes as an important player in sublimation/deposition processes (Eq. (1.2)). The degree of oversaturation is in general small over the whole depth of the snowpack (e.g. below 2%), except for situations with liquid water as discussed below.

### 1.3.2   Arctic snowpack - Samoylov Island

Over the 2010-2011 season investigated at Samoylov, the snowpack gradually developed from early October on, to reach an height of about 30 cm at maximum accumulation mid-April. The February and March snowpack only reached 20 cm. The snowpack melt started on April 20, with positive air temperature for a few days, then paused for about 15 days. There were renewed positive temperatures around May 5, and the final meltout phase started on May 15, steadily up to snow disappearance by the end of the month. Samoylov is characterized by very low temperatures and high wind speeds : over the 2010-2011 snow season, air temperatures were negative from October 4 to late April; they were very rarely above -20°C from late November to early April, with minimum values around -37°C reached late February and early April. Mean wind speed from October to late April was 4.6 m s$^{-1}$ with frequent winds above 10 m s$^{-1}$. Temperature gradients within the snowpack are strong and negative from October to end of February, as a result of shallow snow and extremely cold, arctic weather conditions, and polar night (Fig. 1.1a, to be compared to e.g. alpine conditions, Fig. 1.7a). These gradients result in a general upward flux of water vapor (Fig. 1.1b). After this period, temperature gradients at time reverse, leading also to downward vapor fluxes.

During the first part of the winter, the temperature gradients within snow and soil are strongest just above the soil, at the soil-snow interface: this may be due to the specific conditions at Samoylov, where snow and sedges are intertwined within the lowest centimeters of the snowpack, which leads to reduced density and hence thermal conductivity there, enhancing temperature gradients. As a result of these strong temperature gradients, vapor fluxes are considerable in these basal snow layers (e.g. Fig. 1.1b).

Fig. 1.2a also shows considerable undersaturation in the basal snow layers in the first part of the winter: this is an exception to the general model behaviour described above. We explain this by two processes : first, there is a sharp change of temperature gradient at the soil-snow interface, with the temperature gradient at the snow-side of the interface being larger around one order of magnitude than that at the soil-side. The gradient for the degree of undersaturation is dependent on the temperature gradient and can be given as:

$$\frac{d\sigma}{dz} = (1+\sigma)(\frac{1}{\rho_v}\frac{d\rho_v}{dz} - \frac{1}{\rho_{v,s}}\frac{d\rho_{v,s}}{dz}) = (1+\sigma)(\frac{1}{\rho_v}\frac{d\rho_v}{dz} - \frac{1}{\rho_{v,s}}\frac{d\rho_{v,s}}{dT}\frac{dT}{dz}) \qquad (1.14)$$

This means that the gradient of the saturation water vapor density, $d\rho_{v,s}/dz = d\rho_{v,s}/dT \times dT/dz$ (here, $d\rho_{v,s}/dT$ is always positive and decreases with temperature), changes one order of magnitude at the snow-soil interface, and can induce a significant change of $d\sigma/dz$ for the first element above the soil-snow interface. Second, the very low diffusivity of water vapor in the soil layers limits the contribution of the soil to reduce the water vapor undersaturation in the basal snow layers (cf. Sect. 1.2.2.4 ), and is a further explanation for undersaturation in these layers. Above the basal snow layers, e.g. above 3-4 cm height within the snowpack, the temperature gradients start to decrease and so does the magnitude of the water vapor diffusive

flux, resulting in local flux convergence. Slight oversaturation occurs there, fostering moderate deposition (Fig. 1.2). Similarly, a second sublimation layer occurs in the Samoylov snowpack around 7 cm height, concomitant to an increase in magnitude of temperature gradient there (Fig. 1.1a, inset). Until the top of the snowpack, the alternance of deposition and sublimation layers can be traced down to convergence or divergence of temperature gradients, as over and undersaturations remain very low.

In the second part of the winter, e.g. from early March on, temperature and vapor fluxes mainly reverse as described earlier, with exception of cold spells that can affect the thermal structure of the upper snowpack (like in late March-early April, Fig. 1.1a). Vapor fluxes in the lower half of the snowpack are mainly downward, and contrary to the first part of the winter, oversaturation and deposition occur in the basal layers of the snowpack : this is to be traced down to the same phenomena than during the first part of the winter, i.e. the much lower effective diffusivity of water vapor within the soil when compared to within the snow, that leads to oversaturation and deposition in the basal snow layers as vapor cannot be efficiently routed downward in the soil.

The cumulative density change profile introduced in Eq. (1.13) is shown in Fig. 1.3a. It is important to emphasize that the cumulative density change is basically the vapor flux divergence summed up for the individual layers over their full lifetime, showing the history of the snow density change over the winter season. This is different from an actual density difference between simulations with and without vapor transport, which will be discussed afterwards. Results at Samoylov show a considerable sublimation layer attached to the ground, with largest negative cumulative density changes around -62 kg m$^{-3}$. Since settling counteracts the decrease in density in a non-linear way, (Lehning et al., 2002c), SNOWPACK actually predicts a much smaller density difference. Above this layer, and according to the alternation of sublimation and deposition layers described above, there is a substantial deposition layer with maximum positive changes around 18 kg m$^{-3}$. We also note that the reversal of fluxes from March on, which is especially marked for the lower half of the snowpack, does not really change the characteristics of these sublimation and deposition layers, probably due to lower duration and magnitude of the involved fluxes.

To show how much the density has changed in the case of vapor transport, the snow density difference in percentage as, $(\rho_{vapor} - \rho_{no\ vapor})/\rho_{no\ vapor}$, is calculated. The snow density difference is shown in Fig. 1.3b. At the snowpack base (soil-snow interface), the density difference is negative and its magnitude starts to increase over the winter season till it reaches around -21%. Above this layer, the density difference is positive and it increases over the winter season to reach a value around 7.5%.

The diffusive latent heat flux at the snow surface may be calculated as $q_{l,D} = J_{v,top} \times L_h$, and be compared to the turbulent latent heat flux between atmosphere and the snow surface, $q_l$. Here, $J_{v,top}$ is the diffusive water vapor flux at the snow surface and $q_l$ is due to turbulent mixing over the snow surface and is calculated in SNOWPACK based on wind speed, relative

humidity and temperature in atmosphere. Larger fluxes are observed in autumn and spring and in particular during melt. Corresponding to the dynamics of the surface temperature gradient, there are mostly upward fluxes (here negative values). The averaged ratio of $|q_{l,D}/q_l|$ is 1.4%.

### 1.3.3 Subarctic snowpack- Sodankylä

Over the 2007-2008 snow season investigated at Sodankylä, the snowpack developed to a height of about 68 cm at peak accumulation. Two significant melt events from early December and early January, resulted in a quite thick melt-freeze crust in the lowest 15 cm of the snowpack that persisted until the melt season in the SNOWPACK simulations. Over most of the accumulation season the temperature gradient within the snowpack is negative but shows lower magnitude than at Samoylov (Fig. 1.4a). Especially, the temperature gradient has low magnitude in the basal snow layers (from 0 to -25 K m$^{-1}$) while it increases towards the upper layers to reach values up to -110 K m$^{-1}$ below the surface. This structure results from the modelled stratigraphy described above, where dense, conductive layers dominate the lowermost snowpack, while more recent and facetted snow crystals occupy the upper part with lower thermal conductivity. Contrary to Samoylov, there is no big change in temperature-gradient at the soil-snow interface at Sodankylä.

Accordingly, the vapor flux is also quite small at the soil-snow interface and in the lower part of the snowpack (Fig. 1.4b). Also, the generally smoother variations of the temperature gradient leads to less flux divergence and convergence (Fig. 1.5a and b). Hence in general, the degree of over- or undersaturation is small at Sodankylä compared to Samoylov, with values around -2% except for some events at the beginning of the winter season (Fig. 1.5a). Sublimation and deposition layers exhibit cumulative snow density changes of lower magnitude than at Samoylov: Most cumulative density changes are below 5 kg m$^{-3}$. Only at the bottom of snowpack, sublimation layers reach cumulative density changes between -15 and -40 kg m$^{-3}$ toward the end of the winter (Fig. 1.6a). Within the snow, SNOWPACK simulates only two main deposition layers at Sodankylä, with maximum positive changes around 1.3 kg m$^{-3}$, hence much smaller absolute changes than the negative ones and also smaller positive mass changes than simulated at Samoylov.

In the top layers of the snowpack however, the magnitude of the water vapor flux, its vertical change (flux divergence), and the degree of undersaturation, can reach large values, comparable or larger than at Samoylov (Fig. 1.1b). Towards the snowpack top at Sodankylä, the temperature gradient decreases at times very fast and reaches very low values similar to minimal values occurring at Samoylov and the higher temperatures at Sodankylä lead to higher diffusive fluxes.

The snow density difference between a simulation with and a simulation without diffusive vapor transport is shown in Fig. 1.6b. Some layers in the central, upper and basal parts of

Sodankylä snowpack exhibit a larger density (by a few percent) in the case of vapor transport, sometimes for layers that did not show a positive cumulative density change due to vapor transport (Fig. 1.6a). Actually, local sublimation and changes in density lead to complex feed-back effects affecting the final density of the snowpack. Lower density induced by sublimation does, for example, decrease the thermal conductivity, which may lead to higher temperatures and decreased viscosity, enhancing snowpack compaction. Viscosity is also directly sensitive to ice content. The melt-refreeze processes that occur at Sodankylä early in the winter season may also be affected by differences in snow density due to sublimation/deposition. This is especially visible for the layer between 5 and 10 cm, influenced by a melt-refreeze event in early January. In this layer, water vapor transport leads to a change in density of around -20 to -30%. In the end, not only the vapor transport changes the snow density by direct deposition and sublimation processes but it also leads to side effects on the temperature profile, snow viscosity (compaction rate), percolation, and the rate of melt-refreezing in a highly non-linear way, which may change the final density more significantly than just by direct deposition and sublimation.

The ratio of the diffusive latent heat flux at the snow surface to the turbulent latent heat flux between atmosphere and the snow surface, $|q_{l,D}/q_l|$, is calculated over the winter season for Sodankylä as 4% which is more significant than at Samoylov. As explained above, this is because the diffusive vapor flux of top layers for Sodankylä is larger than at Samoylov.

### 1.3.4  Alpine snowpack- Weissfluhjoch

The seasonal snowpack at Weissfluhjoch builds up to a height of 2 m reached in mid March, when it features a typical multi-layered structure of alpine, high altitude snowpack as shown in Figure S23 of Wever et al. (2015): the lower half features mainly an alternation of shallow depth hoar layers, and wider layers of faceted crystals with rounded grains still present. A small melt-freeze crust persists at about 50 cm height, from an early-winter melt event. In the upper half, layers of rounded grains are more present, intertwined with some very thin melt-freeze crusts from late February. More recent snow types can be found at the snowpack's top until early April.

The temperature gradient at Weissfluhjoch is shown in Fig. 1.7a. For most of the snowpack with exception of the uppermost layers, it takes moderate, negative values rarely reaching below -40 K m$^{-1}$. This gradient is considerably smaller than at Sodankylä and Samoylov, as the snow height for Weissfluhjoch is much higher and winter air temperature are also less extreme. The temperature gradient is larger at the beginning of the winter season, which corresponds to the coldest air temperatures at Weissfluhjoch for this snow-season. At this time the gradient is also stronger in the upper half of the snowpack, where more recent snow of low thermal conductivity dominates. The temperature gradient then decreases gradually in magnitude over the winter season to reach a value around zero in the melting period. However,

for top layers, its sign changes frequently based on the diurnal variations of the air and snow temperatures.

Fig. 1.7b shows the weekly time series of the water vapor flux. It follows perfectly the pattern of the temperature gradient in terms of magnitude and direction. As a matter of fact, the degree of undersaturation is very small at Weissfluhjoch (Fig. 1.8a): usually smaller than 0.1% except for a thin layer at the snowpack base and few elements on top, which are affected by the strong, cyclic temperature gradients mentioned above. As a result of lower temperature gradients than at Samoylov or Sodankylä (except close to the snow surface), the magnitude of the upward water vapor flux at Weissfluhjoch is also much lower, reaching only values comparable to Arctic or subarctic snowpacks in early winter when air temperature is the coldest, occasionally as low as -20°C. Later in the winter, between January and March, the upward vapor flux is much lower. This can be attributed both to milder air temperatures around -5°C for this period, and to the daily cycles of surface temperature under the Alpine climate which frequently changes the sign of the temperature gradient near the surface.

The snow density change rate, shown in Fig. 1.8b, has the same behavior as the degree of undersaturation (Fig. 1.8a). A small sublimation layer forms at the snowpack base, and so do a few deposition or sublimation layers close to the snowpack top, which exhibit quite significant density changes rates as a result of abrupt changes or inversions of the temperature gradients there. For the snowpack core, there are many small and less significant deposition or sublimation layers due to small changes in magnitude of the water vapor flux.

The cumulative density change for Weissfluhjoch is shown in Fig. 1.9a. Most density changes (positive and negative) are small and below 2.5 kg m$^{-3}$. For the snowpack base (soil-snow interface), the cumulative density change has a value around -5 to -26 kg m$^{-3}$, resulting from sustained temperature gradients there at the interface of a more isothermal soil of lower diffusivity. In the upper layers, density decrease can be stronger in the melting period amounting to 5 to 10 kg m$^{-3}$.

The density change in percentage for Weissfluhjoch 2001 in Fig. 1.9b confirms the dominance of density reduction, even though of low magnitude. For a few centimetres above the snowpack base (soil-snow interface), the density is decreased around 10 %.

For Weissfluhjoch, the averaged ratio of the diffusive to the turbulent heat flux over the the winter season, $|q_{l,D}/q_l|$, is 8.4% indicating that for the mass and energy balance of the snow surface, the diffusive latent heat flux is not negligible and should be considered.

### 1.3.5   Sea ice- Snow Buoy 2016S31 (Buoy S31)

Vapor transport in sea ice is expected to be important as (often) very low surface temperatures during the polar night generate large temperature gradients through the snow-ice pack, given that the liquid water at the ice base remains always close to -1.8°C. Density profiles that may

be affected by vapor transport, are crucial to understand specific sea-ice processes related to brine dynamics and salinity transport. It is therefore interesting to analyze the effect of macroscopic vapor transport for the density profiles of snow on sea ice.

The snowpack over sea ice at Buoy S31 is here followed over one full year, from January to January. The coldest part of the year occurs between March and September; air temperatures are steadily below -20°C from April to early July. From January to July, precipitation are also very low, resulting in a shallow snowpack (approx. 20 cm in July): very strong temperature gradients develop during this period (Fig. 1.10a), resulting in significant upward vapor fluxes (Fig. 1.10b) and temperature-gradient metamorphism. As a result, during this period, the snowpack features mostly depth-hoar overlain by faceted crystals in the SNOWPACK simulations (Figure 11 of Wever et al. (2020)). From August to early October, more precipitation occurs and the snowpack reaches 60 cm while air temperatures get milder, around -5°C on average. The temperature gradients within the snowpack reduce with respect to the previous period, being generally lower than 40 K m$^{-1}$ in magnitude (Fig. 1.10a) and so does the upward vapor flux (Fig. 1.10b). As presented in Figure 11 of Wever et al. (2020), the snowpack further builds up, with new layers rapidly transforming into faceted crystals or towards October, rounded grains. Sustained melt occurs from November until mid or late January.

The degree of undersaturation and the snow density change rate at Buoy S31 are shown in Fig. 1.11a and Fig. 1.11b, respectively. Similar to Samoylov, they are high at the base of the snowpack, i.e. for few centimetres above the sea ice-snow interface, from March until late July. Over this period the magnitude of temperature gradient through the ice underlying the snowpack is relatively constant and less than 10 K m$^{-1}$. Again similar to Samoylov, there is a sharp change of temperature gradient at the sea ice-snow interface. This sharp change, in association with a reduced diffusivity of water vapor in ice when compared to snow, creates the basal layer of undersaturation. The cumulative density change due to vapor transport for Buoy S31 is shown in Fig. 1.12a. Similar to Samoylov, there is a strong sublimation layer attached to the sea ice-snow interface with the largest negative change around -66 kg m$^{-3}$. Deposition layers occur in the Buoy S31 snowpack with a pattern close to the one of oversaturation. They are related to vertical variations in the temperature gradient that drive vapor flux convergence (Fig. 1.10b) and reach cumulative deposition around 11 kg m$^{-3}$ at most. This makes Buoy S31 the snow cover with the highest overall magnitude of cumulative density change as a result of water vapor transport.

The density profiles for Buoy S31 for the case of vapor transport and the case of no vapor transport are compared in Fig. 1.12b. As expected, due to the stronger effect of the vapor transport in the bottom layers above the sea ice, strongest differences can be seen in these snow layers, which are around -20% for the first sublimation layer and around 5% for the main deposition layer that develops from March to August. As for the other snow covers analyzed before, the differences in the density profiles for top layers in the accumulation period and also in general for all layers during the melting period, are not consistent with cumulative density changes due to diffusive water vapor fluxes. Therefore they are not the direct result of

sublimation/deposition from the water vapor transport, but are mainly due to side effects of diffusion on the compaction and melting-refreezing rates via changes in temperature, density and viscosity described above.

The averaged ratio of the diffusive to the turbulent latent heat flux over the season, $|q_{l,D}/q_l|$, is calculated as 6.8% for Buoy S31, hence being the second largest among our 4 study sites after Weissfluhjoch (8.4 %).

### 1.3.6  Sensitivity of diffusion effects to soil characteristics at Samoylov

Given the important role of soil in the formation of a basal sublimation layer, highlighted most strikingly at Samoylov, but also visible at Sodankylä and Weissfluhjoch, we evaluated the impact of the soil characteristics on the simulation results at Samoylov. The following sensitivity tests were performed:

(i) enhanced diffusion in the soil was considered by changing the tortuosity parameter $\tau$ to 1 and then 5. Indeed, diffusivity in the soil is debated in the literature with some authors suggesting significant enhancement (e.g. (Ho and Webb, 1998), (Shokri et al., 2009)). $\tau = 1$ means no enhancement but getting rid off the effect of tortuosity, which actually changes the effective water vapor diffusivity in the soil by a factor of 18 with respect to the original formulation of diffusion in soils described in Sect. 1.2.2.4.

(ii) the effect of the soil porosity was tested by setting a very porous (62.5 % of porosity) soil layer in the uppermost 5 cm of the soil while keeping the default water fraction. A very porous organic soil layer can indeed be found at the top of Arctic permafrost soils (e.g. (Boike et al., 2013)).

(iii) the effect of soil water content was tested by considering a saturated soil in the default setup, as low-centered polygons at Samoylov can be saturated at the beginning of the winter season ((Boike et al., 2013)).

The results of the tests were the following, using the example of Samoylov:

(i) the increase of soil effective diffusivity leads to enhanced vapor flux from the soil to the snow basal layer. Therefore the (negative) density change in the basal snow layers is reduced, from -62 to -54 and -40 kg m$^{-3}$ for cumulative density changes from default setup to enhanced setups with $\tau = 1$ and $\tau = 5$, respectively. The additional vapor flux is mainly deposited in the first deposition layer above the basal snow layer, which experiences an increase in its (positive) cumulative density change. This increase is of lower magnitude than the change in basal depletion. Overall we see a moderate sensitivity of snow density changes to diffusion enhancement in the soil with effects restricted to the lower half of the snowpack and mainly affecting basal depletion. Qualitatively, the results obtained with default setup remain valid for increased soil diffusivity.

(ii) a very porous uppermost soil layer has qualitatively and quantitatively an effect similar to the enhanced soil diffusivity tested in (i): vapor flux from the soil is increased, leading to less flux divergence in the basal snow layer and therefore less depletion there, while the soil is more depleted. Some enhanced deposition in the first deposition layer also occurs.

(iii) saturated soil conditions at Samoylov did not noticeably change the density changes induced by water vapor diffusion in the snowpack.

As a conclusion, the effects of water vapor diffusion in the snowpack can be quantitatively affected by porosity and diffusive properties in the soil, but the general behaviour depicted by our Samoylov simulations remains qualitatively valid.

### 1.3.7   Comparison with measured density profiles

Since Samoylov showed the strongest response of the density profile to vapor transport of all snow covers over land investigated, a limited comparison with measured density profile is presented in Fig. 1.13. This comparison is limited in the sense that few density profile data are available at the site, and they show a significant spatial variability which is in part linked to the local micro-topography. Fig. 1.13 compares our simulations with a density profile from a polygon center, that was selected as representative for the snow conditions in the centers of the tundra polygons (Gouttevin et al., 2018). The comparison confirms that vapor transport is helping to generate a low-density for the base of this Arctic snow cover. For the middle and upper part, the effect is still small compared to the general error between observations and model. The effect of diffusive vapor transport on density for deep snow covers is weak because of the lower temperature gradients compared to thin snow covers (Samoylov). This is shown in Fig. 1.14, which has a minor density reduction at the base due to diffusive vapor flux. The density reduction slightly improves the agreement between simulations and in-situ observations. These comparisons also show that vapor transport as simulated by the model is not a sufficient explanation for the observed density changes. This does not necessarily indicate an underestimation of diffusive vapor fluxes in the simulation, because other processes, such as fresh snow density and wind compaction also impact density profiles. However, our result is also in agreement with experimental studies (Domine et al., 2016b, 2018), pointing to the significance of convective transport. We conducted a Rayleigh number analysis for all snow covers investigated and found that for Samoylov, based on maximum ($Ra^* = 40$) and minimum ($Ra^* = 4$) critical Rayleigh numbers from literature (Palm and Tveitereid, 1979; Powers et al., 1985; Sturm and Johnson, 1991), the time for which free convection can occur over the winter season is 29.9% and 77.2%, respectively. The other snow covers are less susceptible to convection for minimum critical Rayleigh number but still show significant time fractions, over which convection is possible. Thus, other processes such as convective vapor transport but also (non-)settling of depth hoar need to be improved in SNOWPACK and other snow models. We will attempt a more complete

model validation against measured density profiles in future, after introducing convective transport in SNOWPACK.

## 1.4    Conclusions, limitations and outlook

In our analysis, the effects of diffusive vapor transport through four different types of snow covers, from thin Arctic and Antarctic (on sea ice) to thick Alpine, have been investigated numerically. To do so, a model to account for diffusive water vapor transport through soil and snow has been implemented in the detailed, multi-layered snowpack model SNOWPACK.

In the shallow Arctic snowpack at Samoylov, strong and sustained temperature gradients develop and the vapor transport has significant effects on the simulated density profile with a significant density decrease in the snowpack at the soil-snow interface that reaches a value of -21%. Above this layer, the density of the snowpack is generally increased up to around 7.5% by the end of season, as a result of deposition, which occurs over a larger depth of the snow cover.

At the other sites studied here, the highly non-linear side effects of original density changes induced by diffusion, on conductivity, temperature profiles, snow viscosity, compaction rate and melt-freeze processes, may change the final snowpack density more significantly than just by direct deposition and sublimation. At Sodankylä, typically, the density at the snowpack base is decreased by about 5% with dominating sublimation there, while other layers in the middle of snow cover feature a density decrease around -20 to -30%. At Weissfluhjoch, significant direct effects of diffusion happen near the surface or the base with moderate magnitude; they are even smaller in the core of the snowpack. For the sea ice, Snow Buoy 2016S31, it is found that the density decreased at the sea ice-snow interface by -20% while there is a deposition layer above it with increase in density around 5%. This result for the sea ice from Antarctic is qualitatively and quantitatively similar to Arctic snowpack at Samoylov as very low surface temperatures generate large temperature gradients through snowpack in both cases.

The simulations presented yield plausible results but validation against measurements is difficult. In general, the new simulations for thin snow covers reproduce the weak snow cover base often observed in Arctic environments better than the version without vapor transport (Gouttevin et al., 2012; Domine et al., 2016b; Sturm and Johnson, 1991; Barrere et al., 2017). Errors in the density measurements are typically larger than the effect of vapor transport on density, especially in close to ground depth hoar layers in Arctic snow covers (Proksch et al., 2016). Since the settling routines in SNOWPACK have been calibrated to reproduce observed densities at Weissfluhjoch (Lehning et al., 2002a) without vapor transport, future work should construct micro-structure based snow settling laws independent of vapor transport. It should be noted that we did not change the thermal conductivity calculation in SNOWPACK in case of vapor transport despite the fact that the parameterization contains a term for the heat effect of that transport (Lehning et al., 2002c). This will be done in the future but is expected to have a very small impact on results.

The effect of vapor transport on density as discussed here is considered to be conservative and expected to be significantly larger in reality as we do not consider convective motion of vapor in the pore space (Sturm and Johnson, 1991) and neglect also arising anisotropy (Loewe et al., 2013), both of which are expected to increase vapor flux as well as effects on density. In summary, we see that diffusive transport has more local effects than what we expect from observations. It changes snow density significantly in a thin layer above ground in thin snow covers and mostly adds mass to upper layers. It will be interesting to see, how this patterns changes if convection is considered.

Future work will therefore include attempts to quantify convection and improve microstructure modelling. This should generate a solid basis for assessing isotope dynamics in snow deposition and metamorphism (Ebner et al., 2017; Touzeau et al., 2018). This paper only looked at the density effects of diffusive water vapor transport and has shown that it can affect the density profile in particular in thin snow covers.

## Acknowledgements

Figure 1.1: The weekly time series for Samoylov 2010-2011, (a) the temperature gradient, (b) the diffusive water vapor flux. The insets in (a) and (b) show the vertical profiles on 13 December 2010 12:00:00. Black color refers to zero values.

Figure 1.2: The weekly time series for Samoylov 2010-2011, (a) the degree of undersaturation, (b) the snow density change rate due to water vapor transport. The insets in (a) and (b) show the vertical profiles on 13 December 2010 12:00:00.

Figure 1.3: The weekly time series for Samoylov 2010-2011, (a) the cumulative density change, (b) the snow density difference in percentage between the case of vapor transport and the case without vapor transport. The insets in (a) and (b) show the vertical profiles on 21 March 2010 12:00:00. Black color refers to zero values.
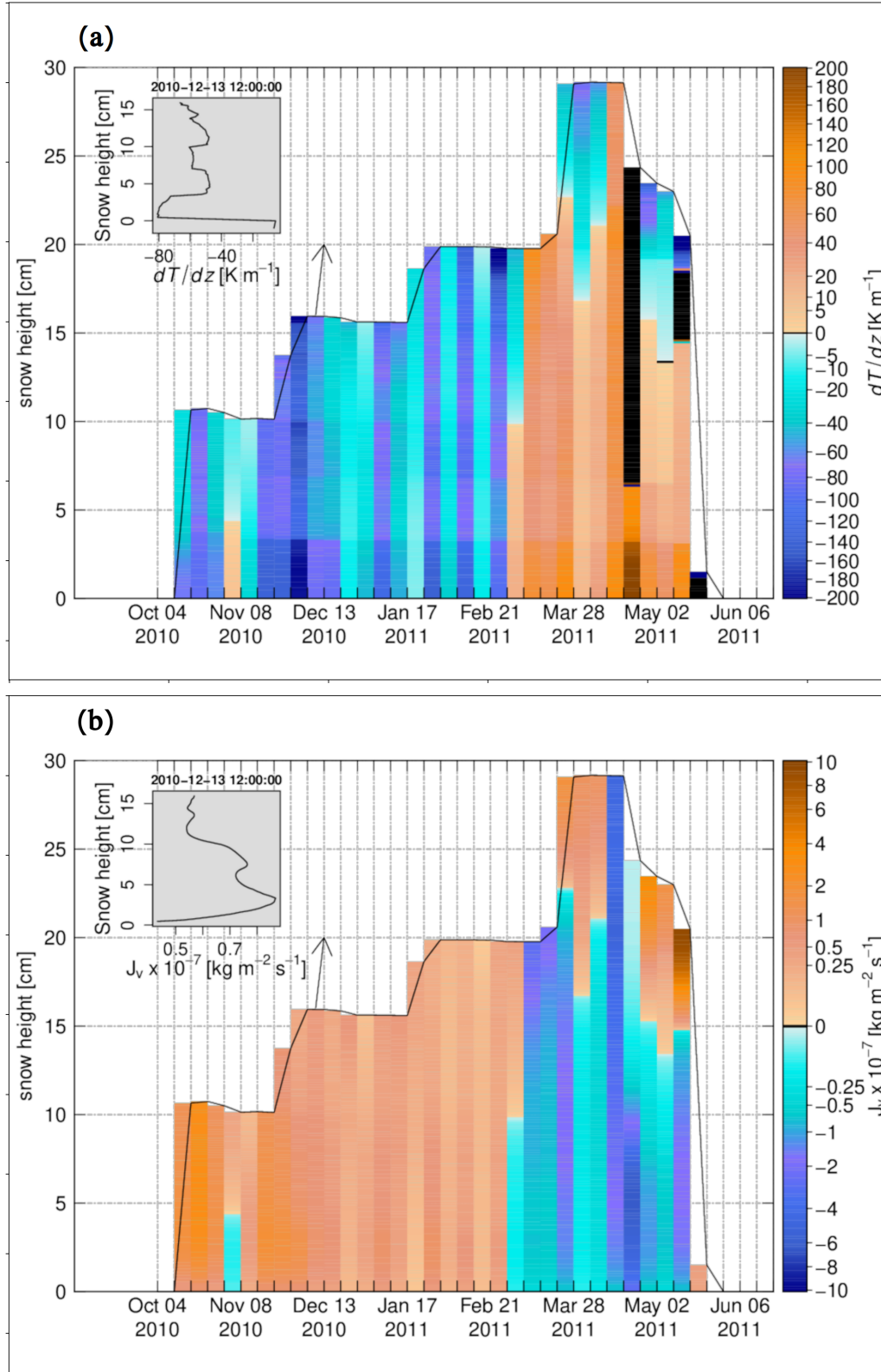
Figure 1.4: The weekly time series for Sodankylä 2007-2008, (a) the temperature gradient, (b) the diffusive water vapor flux. The insets in (a) and (b) show the vertical profiles on 28 January 2008 12:00:00. Black color refers to zero values.
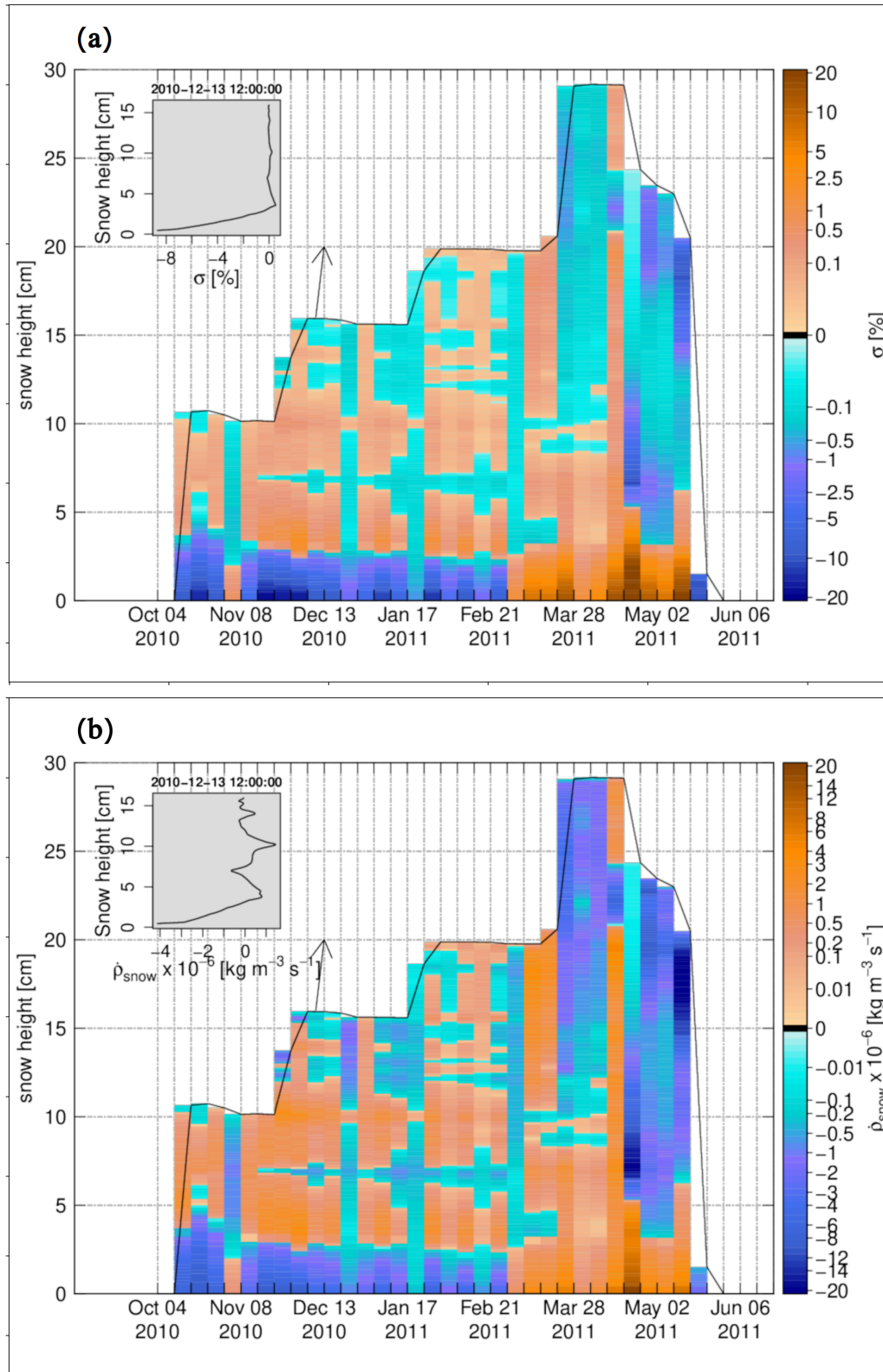
Figure 1.5: The weekly time series for Sodankylä 2007-2008, (a) the degree of undersaturation, (b) the snow density change rate due to water vapor transport. The insets in (a) and (b) show the vertical profiles on 28 January 2008 12:00:00. Black color refers to zero values.

Figure 1.6: The weekly time series for Sodankylä 2007-2008, (a) the cumulative density change, (b) the snow density difference in percentage between the case of vapor transport and the case without vapor transport. The insets in (a) and (b) show the vertical profiles on 3 March 2008 12:00:00. Black color refers to zero values.
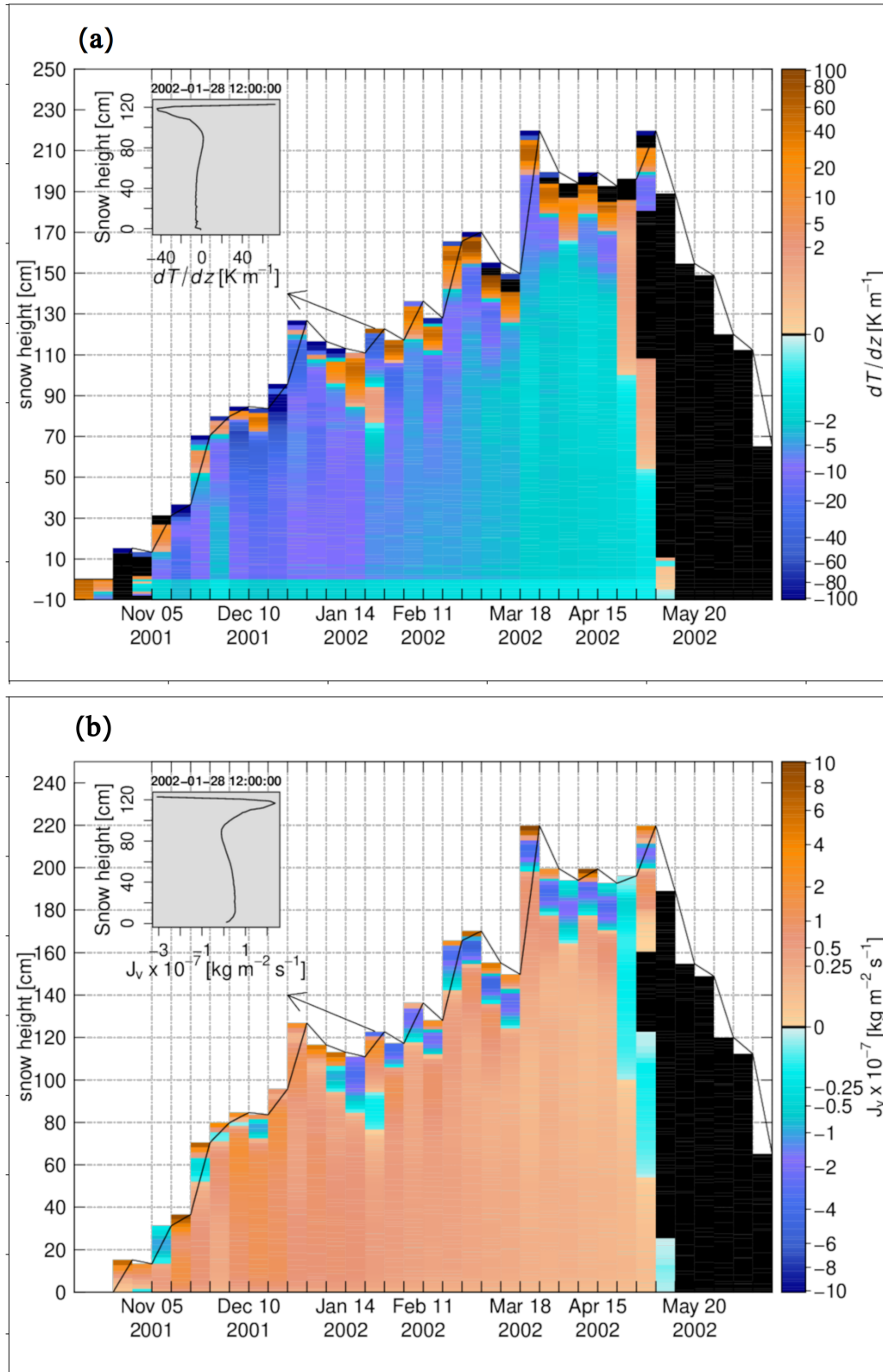
Figure 1.7: The weekly time series for Weissfluhjoch 2001-2002, (a) the temperature gradient, (b) the diffusive water vapor flux. The insets in (a) and (b) show the vertical profiles on 28 January 2002 12:00:00. Black color refers to zero values.
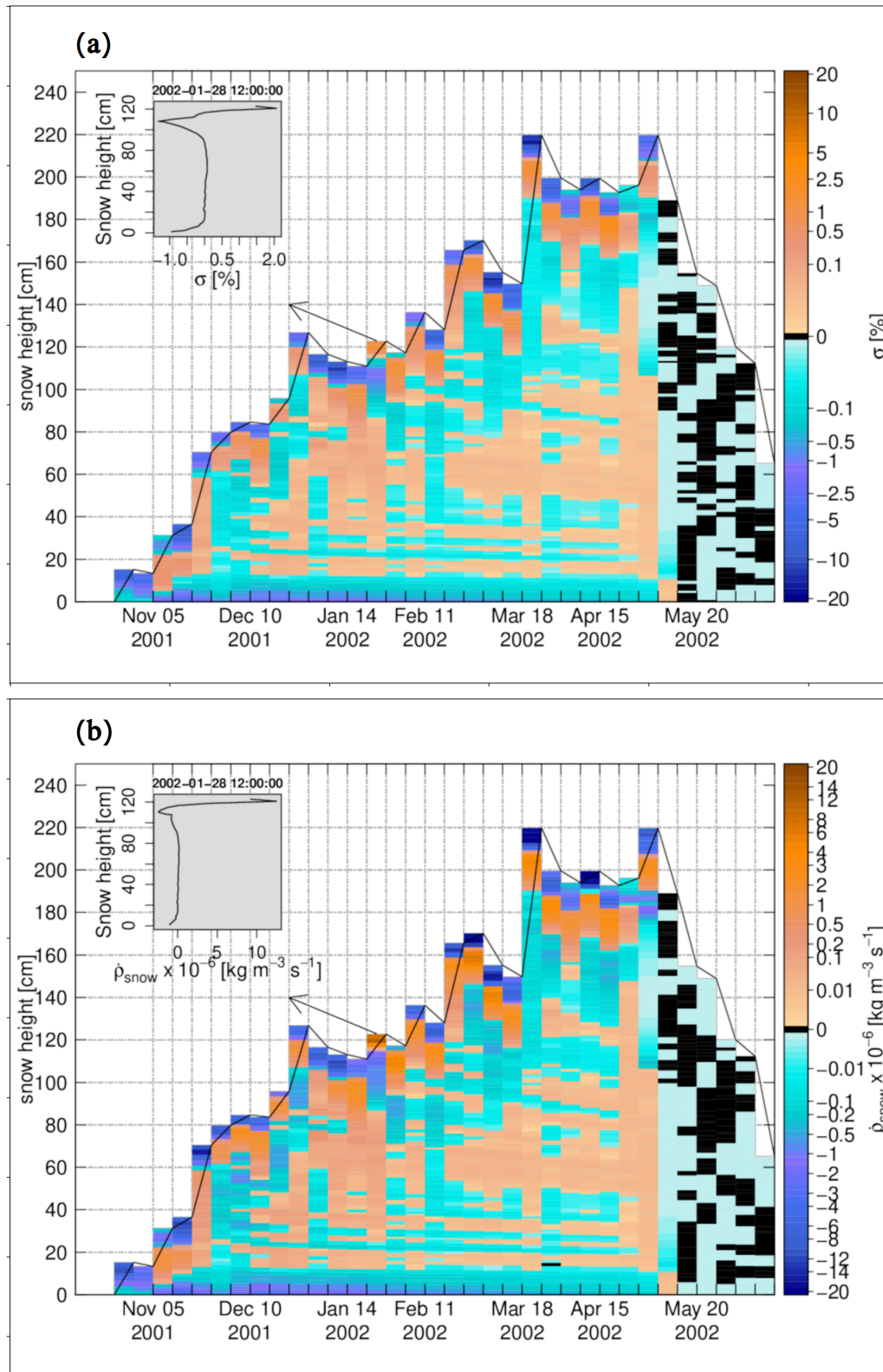
Figure 1.8: The weekly time series for Weissfluhjoch 2001-2002, (a) the degree of undersaturation, (b) the snow density change rate due to water vapor transport. The insets in (a) and (b) show the vertical profiles on 28 January 2002 12:00:00. Black color refers to zero values.
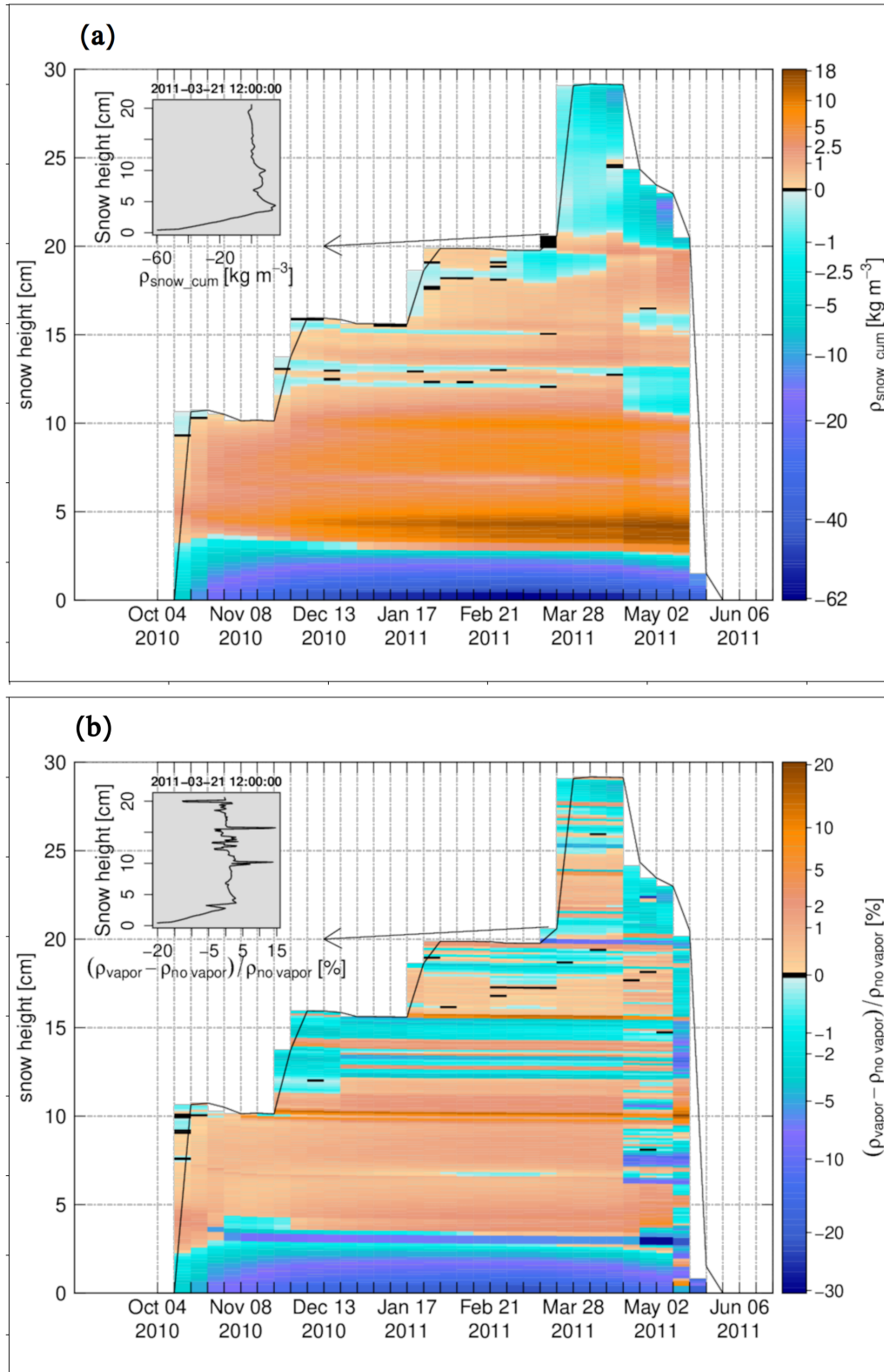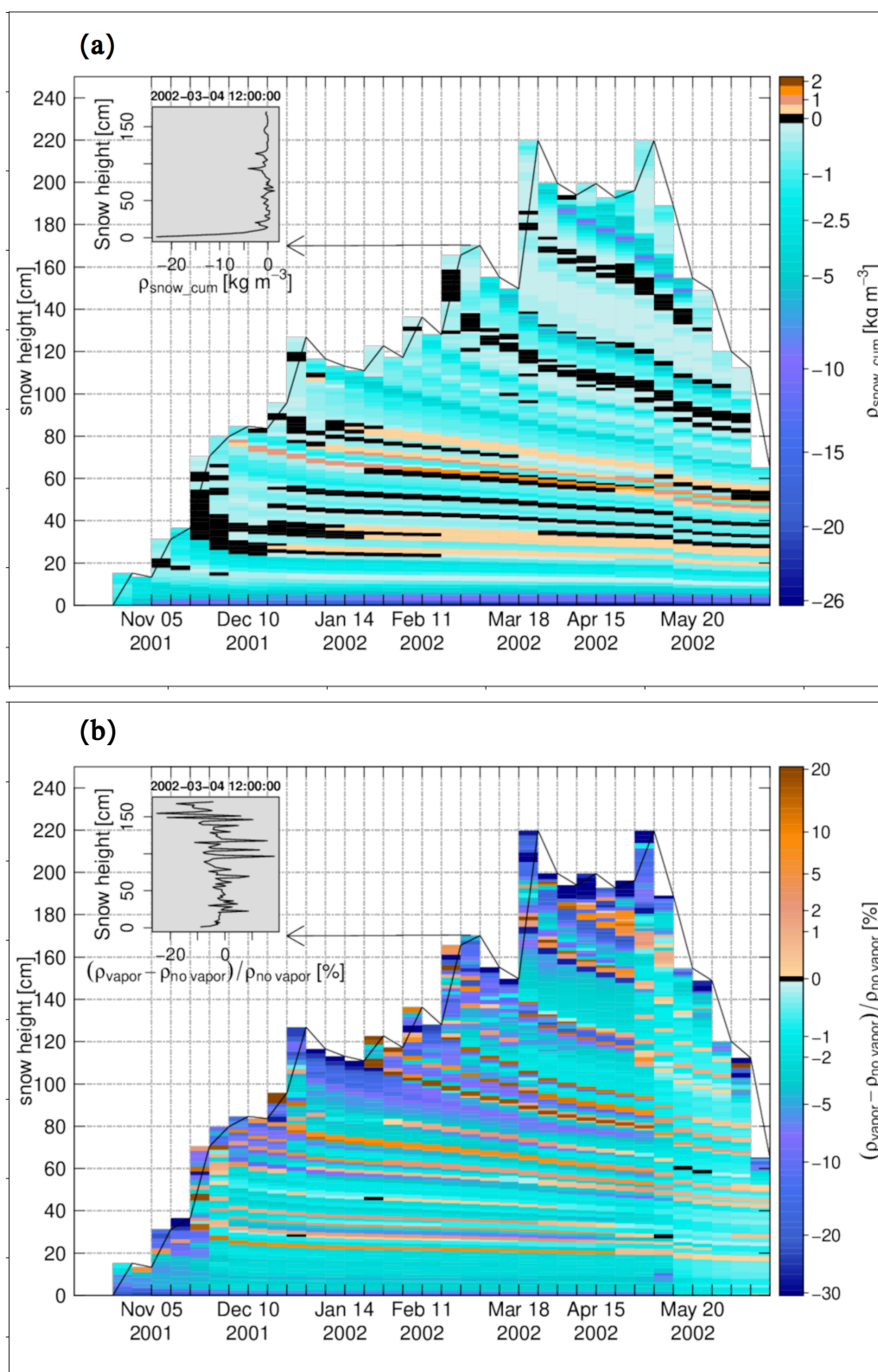
Figure 1.9: The weekly time series for Weissfluhjoch 2001-2002, (a) the cumulative density change, (b) the snow density difference in percentage between the case of vapor transport and the case without vapor transport. The insets in (a) and (b) show the vertical profiles on 4 March 2002 12:00:00. Black color refers to zero values.
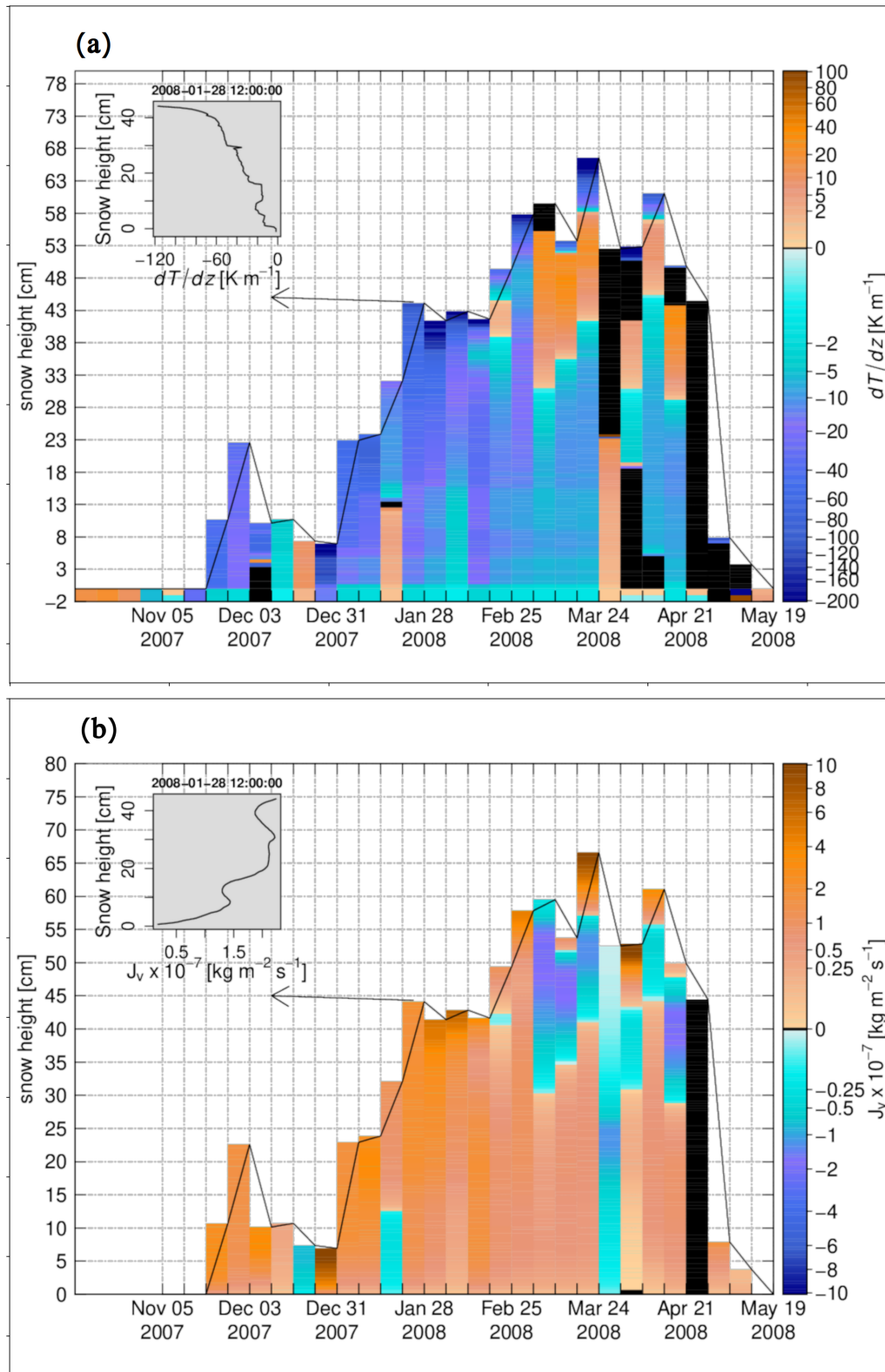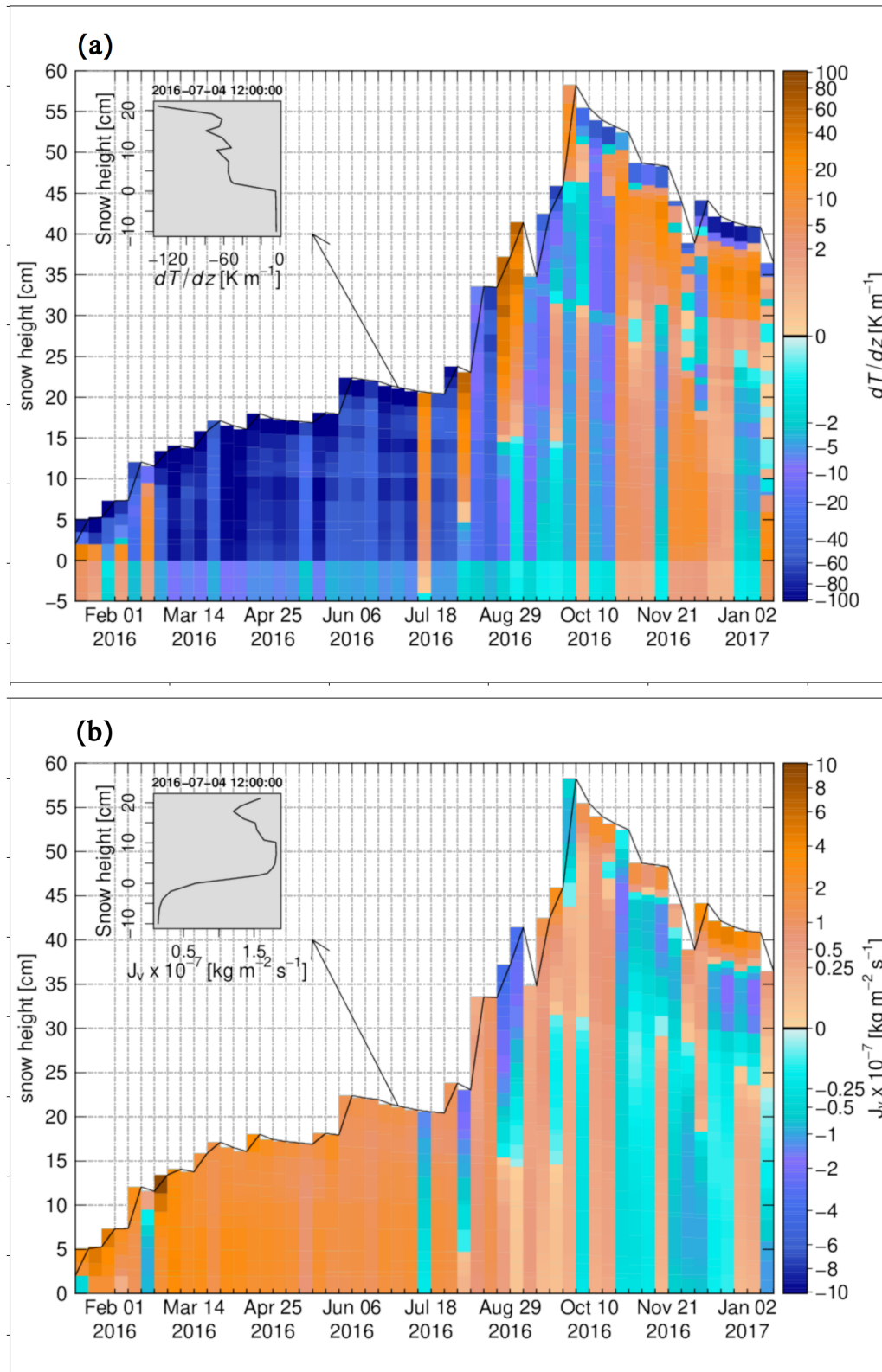
Figure 1.10: The weekly time series for Snow Buoy 2016S31, (a) the temperature gradient, (b) the diffusive water vapor flux. The insets in (a) and (b) show the vertical profiles on 4 July 2016 12:00:00. The zero-level height is the sea ice-snow inerface.
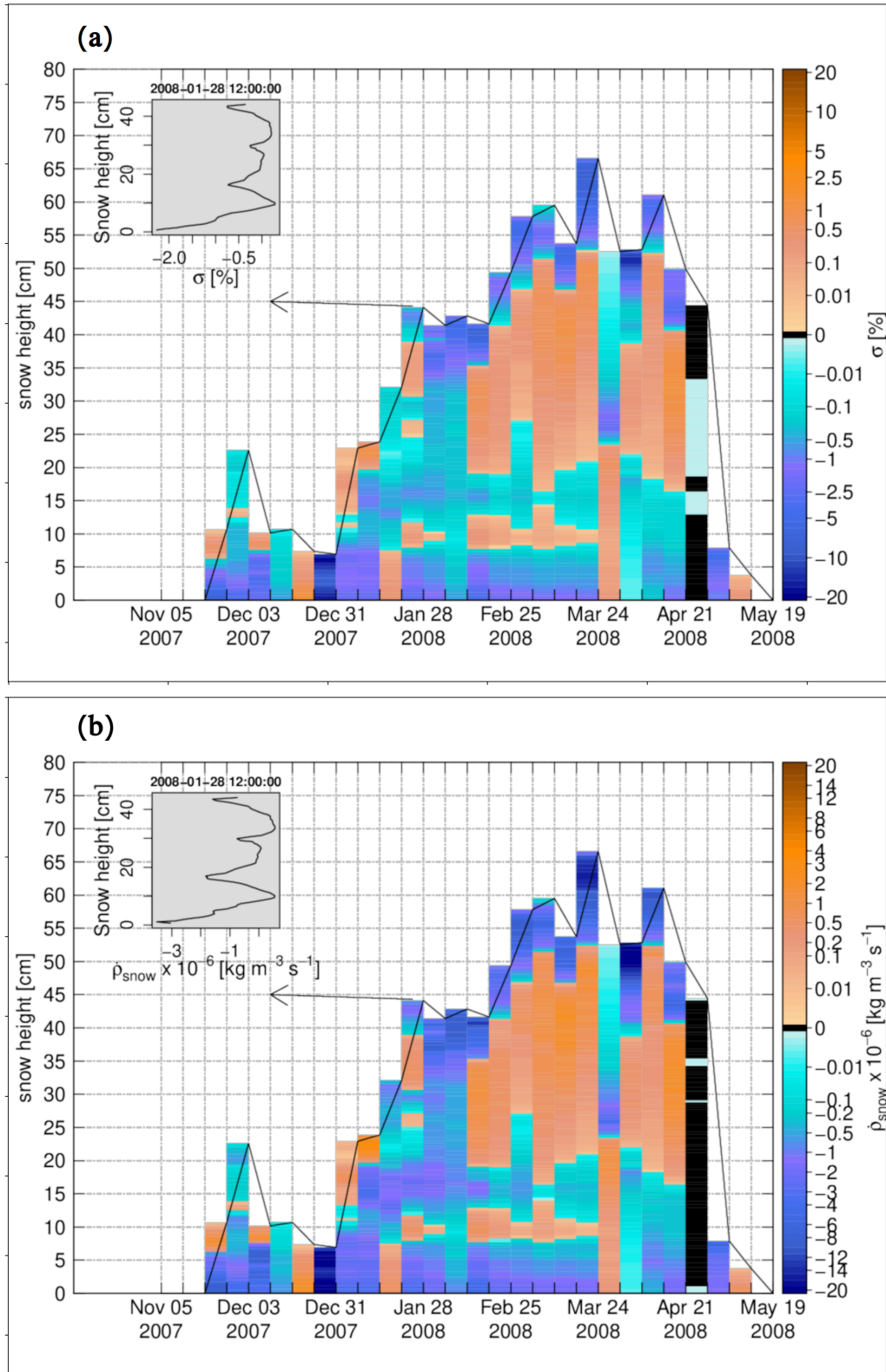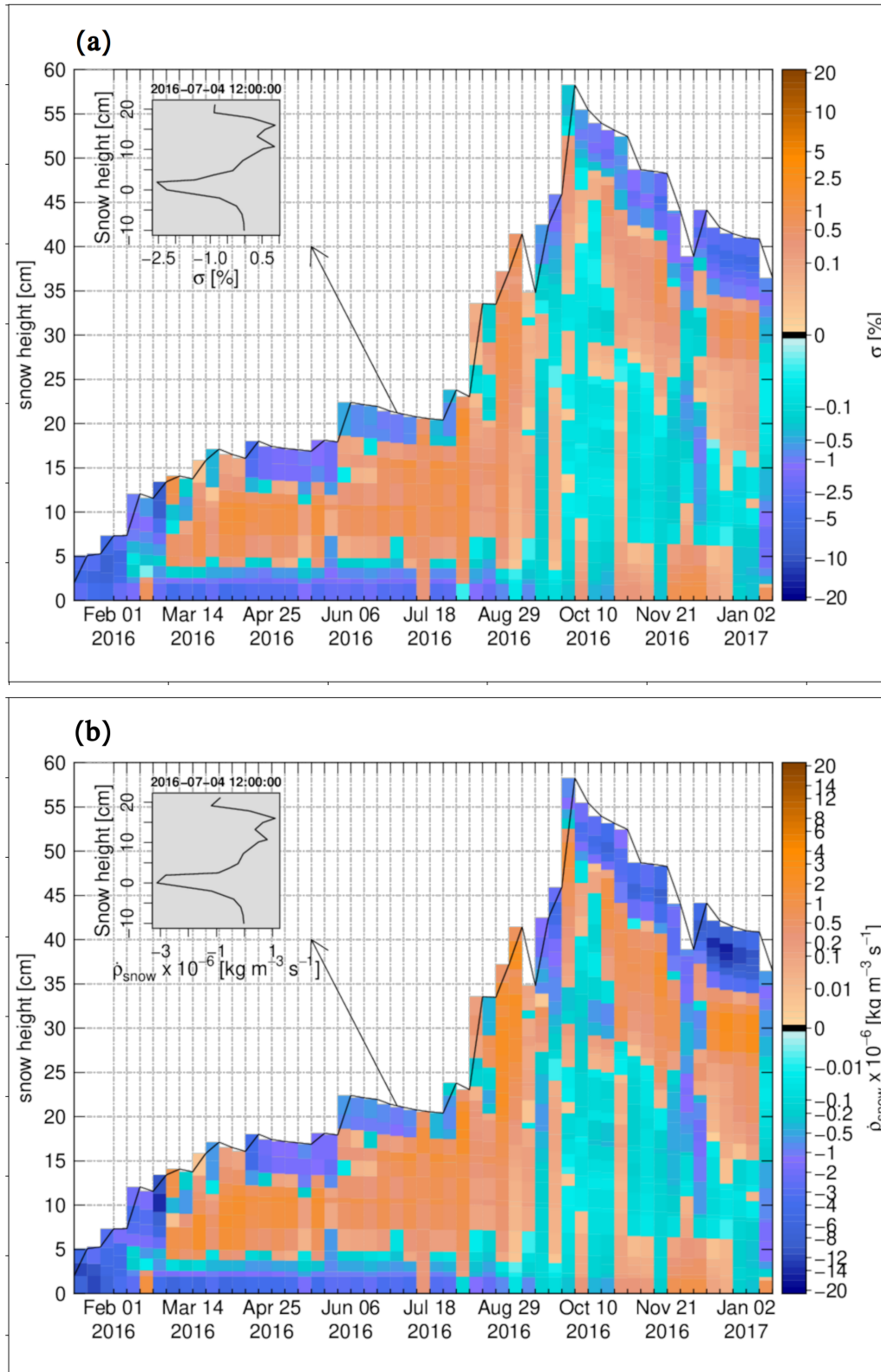
Figure 1.11: The weekly time series for Snow Buoy 2016S31, (a) the degree of undersaturation, (b) the snow density change rate due to water vapor transport. The insets in (a) and (b) show the vertical profiles on 4 July 2016 12:00:00. The zero-level height is the sea ice-snow inerface.
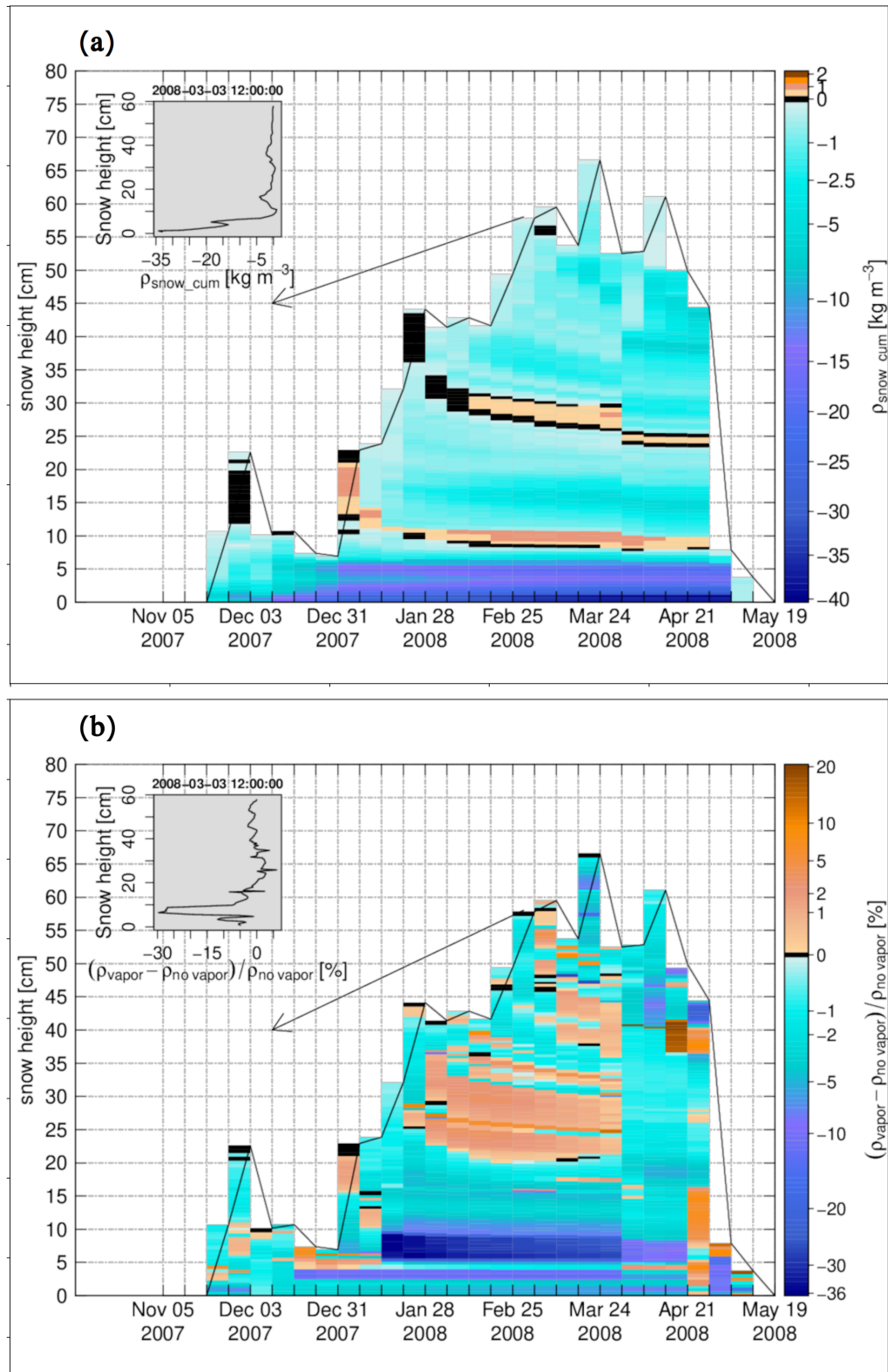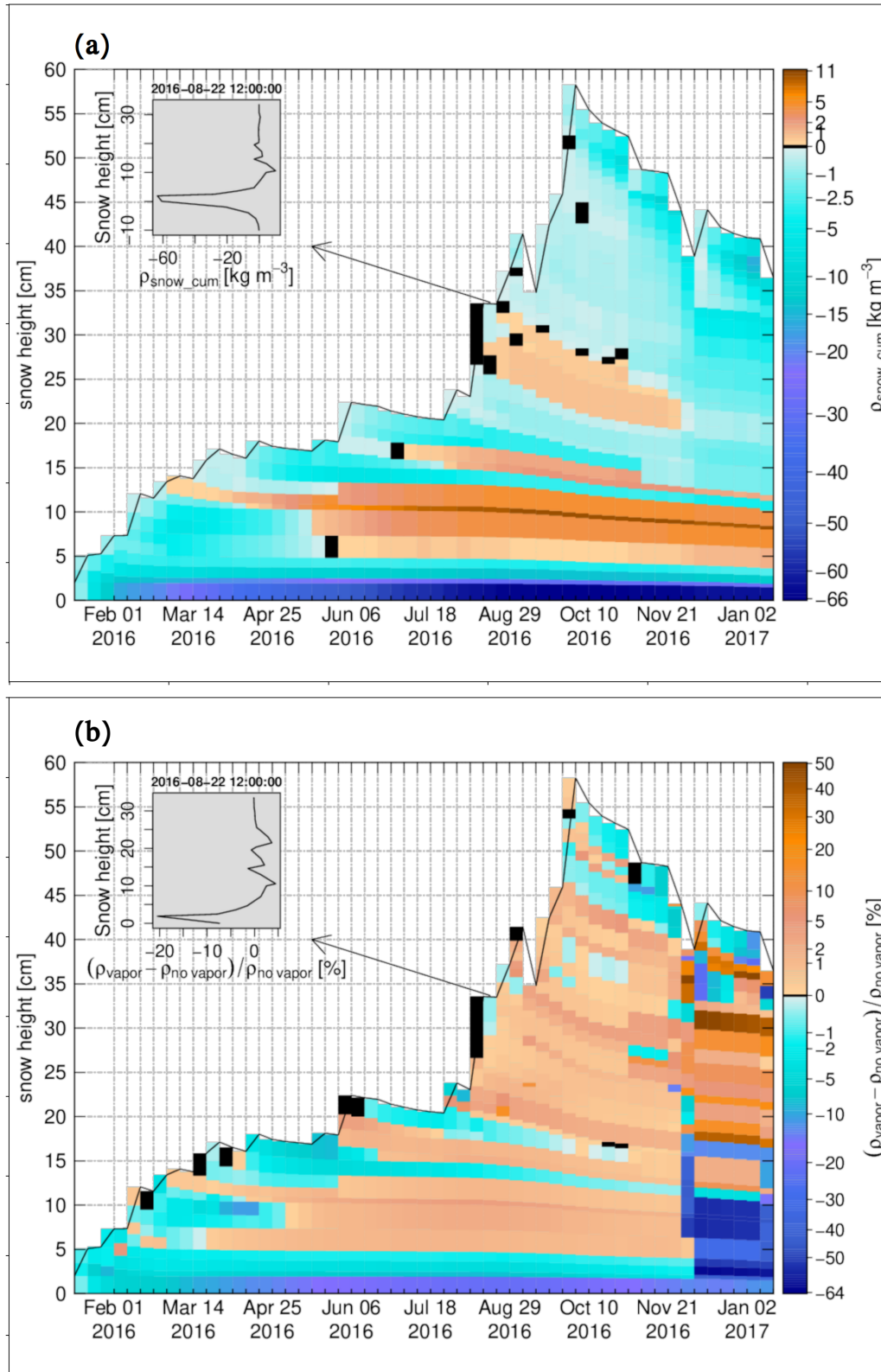
Figure 1.12: The weekly time series for Snow Buoy 2016S31, (a) the cumulative density change, (b) the snow density difference in percentage between the case of vapor transport and the case without vapor transport. The insets in (a) and (b) show the vertical profiles on 22 August 2016 12:00:00. Black color refers to zero values. The zero-level height is the sea ice-snow inerface.
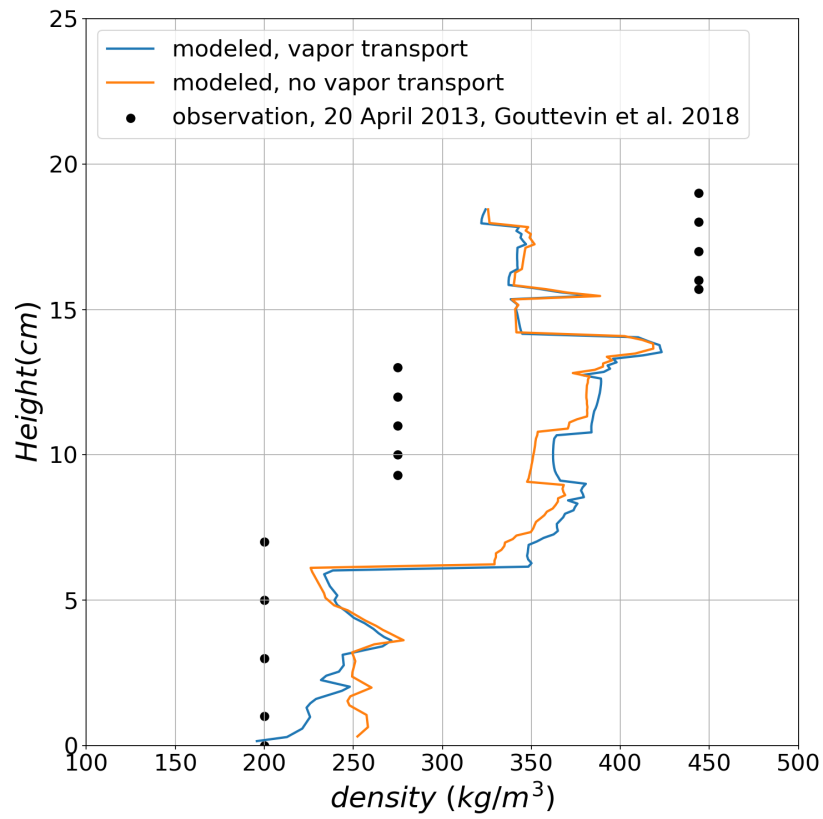
Figure 1.13: The comparison of simulated snow density profile with measured one for Samoylov on 20 April 2013.
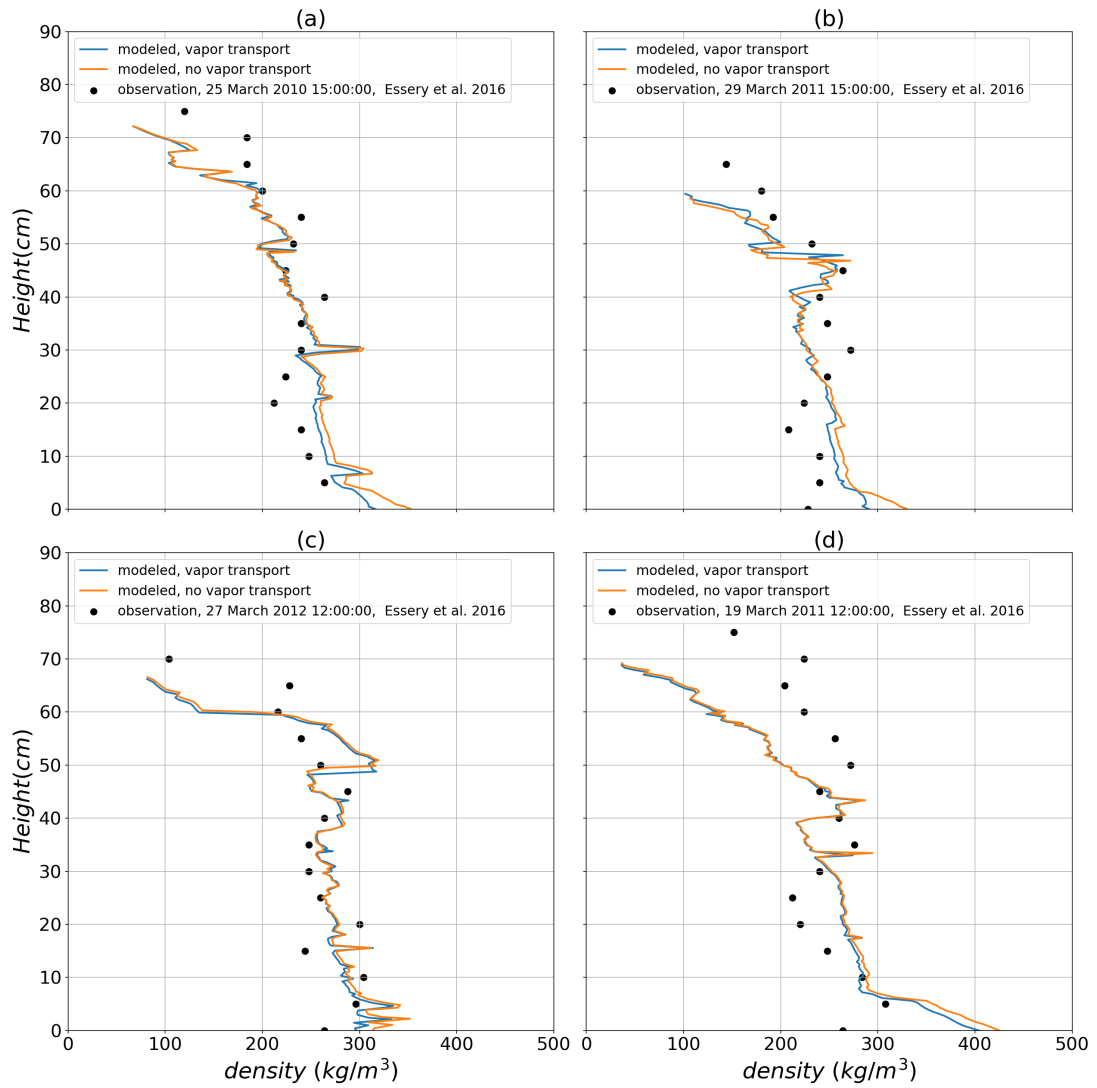
Figure 1.14: The comparison of simulated snow density profile with measured one for four winter seasons at Sodankylä, (a) on 25 March 2010, (b) on 29 March 2011, (c) on 27 March 2012, and (d) on 19 March 2013.

# 2 Convection of water vapor in snow-packs

This chapter is based on a postprint version of a published paper in the Journal of Fluid Mechanics as:

MJ started the project by implementing a new solver in OpneFOAM, performing the simulations, and analyzing the results. MJ prepared the manuscript with contributions from all co-authors.

## Abstract

This paper studies numerically the convection of water vapor in snowpacks using an Eulerian–Eulerian two-phase approach. The convective water vapor transport in snow and its effects on snow density are often invoked to explain observed density profiles e.g. of thin Arctic snow covers but this process has never been numerically simulated and analyzed in a systematic manner. Here, the impact of convection on the thermal and phase change regimes as a function of different snowpack depths, thermal boundary conditions and Rayleigh numbers is analyzed. We find considerable impact of the natural convection on the snow density distribution with a layer of significantly lower density at the bottom of the snowpack and a layer of higher density located higher in the snowpack or at the surface. We find that emergent heterogeneity in the snow porosity results in a feedback effect on the spatial organization of convection cells causing their horizontal displacement. Regions where the snowpack is most impacted by phase changes are found to be horizontally extended and vertically thin, "pancake" like layers at the top and bottom of the snowpack. We further demonstrate that among the parameters important for natural convection, the snowpack depth has the strongest influence on the heat and mass transfer. Despite our simplifying assumptions, our study represents a significant improvement over the state-of-the-art and a first step to accurately simulate snowpack dynamics in diverse regions of the cryosphere.

## 2.1  Introduction

Snow covers drastically modify the energy and water fluxes at or near the land surface (Groisman et al., 1994) even at long distances from the snow cover, and as a consequence, create significant feedback on the climate. They act as temporary water storage and control ground water recharge, making snow crucial to one-sixth of the world's population living in areas where solid precipitation dominates annual precipitation and runoff. The soil thermal properties and permafrost dynamics are dominated by the snow cover (Haberkorn et al., 2017; Bender et al., 2020). Precise modeling of the snow cover properties, especially snow density and depth, is therefore vital in many applications, e.g. as input and validation data for climate models, hydrological models for irrigation and hydroelectricity etc. Water vapor transport is a significant process in the snowpack in different aspects such as snow metamorphism (Sturm and Benson, 1997; Pfeffer and Mrugala, 2002), snowpack stability and avalanches (Woo, 2012; Pfeffer and Mrugala, 2002), and the thermal implications for climate applications (Slater et al., 2001; Callaghan et al., 2011). It has been demonstrated that current versions of 1-dimensional snow models cannot simulate Arctic snowpacks because they omit an accurate description of water vapor transport (Domine et al., 2019). For example, in the Arctic, observations by Trabant and Benson (1972); Sturm and Benson (1997); Domine et al. (2016b) suggest that the density of layers close to the ground in thin snow covers can decrease by more than 100 kg m$^{-3}$ due to water vapor flux.

It has been previously discussed in the literature that depending on the snowpack, soil, and

meteorological conditions, water vapor transport may occur through both diffusion and convection (Trabant and Benson, 1972; Johnson and Bens, 1987; Alley et al., 1990; Sturm and Johnson, 1991; Domine et al., 2016b, 2018). Jafari et al. (2020) discussed that diffusive water transport constitutes the lower limit for total water vapor transport and showed that diffusive vapor transport alone already reproduces lower densities at the base of the snowpack in some cases. However, in snowpacks under strong temperature gradients such as Arctic and sub-arctic ones, in which weak snow layers composed of depth hoar crystals are rapidly formed (Derksen et al., 2009; Sturm and Benson, 1997; Taillandier et al., 2006; Domine et al., 2015), water vapor transport is hypothesized to mainly be driven by natural convection. It has been concluded that significant convection must occur in snowpacks to explain the observations, namely: (1) the measured rates of densification and density changes for snow in Fairbanks by Trabant and Benson (1972), (2) significant horizontal thermal gradients and incoherent temporal variations of horizontal temperature patterns at their study site by Sturm and Johnson (1991), and (3) the near-total disappearance of basal depth hoar at Bylot Island by Domine et al. (2016b).

Snow - atmosphere coupling with high uncertainty in the magnitude of perturbation within the snow is another mechanism which may influence the heat and mass regime of the snowpack surface and if strong enough in deeper snow layers. Colbeck (1989) introduced three different such wind pumping or ventilation mechanisms namely barometric pressure variations, wind turbulence, and steady wind flow over topography and concluded the last one could be strong enough to induce significant air moving through snow. Waddington et al. (1996) concluded the dry deposition flux due to turbulent ventilation should be very small and that the air velocity through the snow surface by wind turbulence is on the order of 0.01 cm s$^{-1}$. Sokratov and Sato (2000) estimated the wind-induced horizontal air flux in the order of $10^{-2}$ m s$^{-1}$ while Albert and McGilvary (1992); Albert (1993) reported much larger values for air flux by wind pumping ranging from $10^{-7}$ to 0.1 m s$^{-1}$. Bartlett and Lehning (2011) in agreement with Colbeck (1989) and Waddington et al. (1996) concluded that ventilation should have a minimal impact on heat transfer under typical conditions. These studies suggest that measureable effects only occur to a small penetration depth (Colbeck, 1989; Waddington et al., 1996; Bartlett and Lehning, 2011).

Observations cannot distinguish between different types of vapor transport and represent a mixture of effects such as snow settling, vapor transport and wind compaction (Sommer et al., 2018). Therefore, a sound modeling of water vapor transport needs to take into account the natural convection as a possible mechanism of density change and observations need to be explained by modeling. As reviewed by Jafari et al. (2020), previous attempts to numerically study water vapor transport in snow and its effects on snow properties consider diffusion only. It is furthermore not possible to explicitly model convection with phase change in a one-dimensional snow model. Thus, in this work, the convective water vapor transport is numerically investigated in snowpacks, using a volume-averaged two-phase model in which each phase is treated separately and interactions between the phases are modeled. The numerical implementation is in a two-dimensional domain. Performance of the present model

for natural convection without mass transfer was validated by comparison with available numerical benchmarks. When including phase-change and the associated local density changes, a considerable impact of the natural convection on the snow density distribution with a layer of significantly lower density at the bottom of the snowpack and a layer of higher density located at the top is observed. This is consistent with measurements of Domine et al. (2016b), who find that the density increase for the wind slabs overlying the depth hoar may be attributed to upward water vapor transfer and its deposition.

## 2.2 Mathematical models

Whilst acknowledging but neglecting the effects of ventilation and snow compaction, to start with a tractable model and focus on the effect of convection, water vapor transport due to natural convection in idealized snowpacks is investigated numerically using an Eulerian–Eulerian two-phase approach. To do so, the volume averaging method is applied to the conservation of mass, momentum, and energy which are valid within each phase up to the interface between phases. In this paper, the snowpack is considered as a two-phase (humid air, ice) porous medium for which the phase change between the water vapor component in the gas mixture and ice is simulated. The detailed explanation, derivations, and operations constituting the volume averaging method can be found in (Whitaker, 1999; Faghri and Zhang, 2006). Note that, in this paper, all the phase properties presented as $\langle - \rangle^g$ and $\langle - \rangle^i$ are the intrinsic phase-averages for the gas and ice phases respectively while the extrinsic averages are shown as the operator $\langle - \rangle$.

### 2.2.1 Mass conservation

The volume-averaged mass conservation equations for the gas mixture (humid air), water vapor component, and ice phase are given respectively as:

$$\frac{\partial}{\partial t}(\epsilon_g \langle \rho_g \rangle^g) + \nabla \cdot (\langle \rho_g \rangle^g \langle \boldsymbol{U}_g \rangle) = \dot{m}_{iv} \tag{2.1}$$

$$\frac{\partial}{\partial t}(\epsilon_g \langle \rho_v \rangle^g) + \nabla \cdot (\langle \rho_v \rangle^g \langle \boldsymbol{U}_g \rangle) = \nabla \cdot (D_{\text{eff},s} \nabla \langle \rho_v \rangle^g) + \dot{m}_{iv} \tag{2.2}$$

$$\rho_i \frac{\partial \epsilon_i}{\partial t} = -\dot{m}_{iv} \tag{2.3}$$

where $\epsilon_g$ and $\epsilon_i$ are the volume fractions for the gas and ice phase respectively, $\langle \boldsymbol{U}_g \rangle$ is the bulk gas phase velocity vector (also known as superficial, extrinsic, filtration, Darcy or seepage velocity), $\langle \rho_g \rangle^g$ is the gas mixture density, $\langle \rho_v \rangle^g$ is the water vapor density, $\rho_i$ is the ice density, $\dot{m}_{iv}$ represents mass source (or sink) per unit volume due to the phase change

(subscript $iv$ refers to the mass transfer from ice to vapor while $vi$ from vapor to ice), and $D_{\text{eff},s}$ is the effective water vapor diffusivity in snow. A brief review on effective diffusivity and its enhancement in snow has been made in Jafari et al. (2020). Based on an analytical model developed first by Foslien (1994) and then extended by Hansen and Foslien (2015), the following parameterization for $D_{\text{eff},s}$ is used:

$$D_{\text{eff},s} = \epsilon_i \epsilon_g D_{v,a} + \epsilon_g \frac{k_i D_{v,a}}{\epsilon_i (k_a + L_{iv} D_{v,a} \frac{d\rho_{vs}}{dT}) + \epsilon_g k_i} \tag{2.4}$$

where $k_i$ and $k_a$ are the thermal conductivities for the air and ice component of snow respectively, $D_{v,a}$ is the water vapor diffusion coefficient in air, $\rho_{vs}$ is the saturation water vapor density calculated at the interface temperature between two phases, and $L_{iv}$ is the latent heat of sublimation. Following Albert and McGilvary (1992), $\dot{m}_{iv}$ may be evaluated as:

$$\dot{m}_{iv} = h_m a_s (\rho_{vs} - \langle \rho_v \rangle^g) \tag{2.5}$$

In equation (2.5), $h_m$ is the mass transfer coefficient, and $a_s = 6\epsilon_i / d_p$ is the specific surface area of snow with the optical grain diameter of $d_p$ (Calonne et al., 2012). Jafari et al. (2020) discussed that the entire specific surface area may be not active for mass transfer, and hence justified the choice of the formulation as $h_m = \rho_i / (\mathscr{B} \rho_{v,s})$ proposed respectively by Calonne et al. (2014) and Ebner et al. (2015). Here, the interface kinetic growth coefficient was found to be $\mathscr{B} = 9.7 \times 10^9$ s m$^{-1}$ from the experiments of sublimation and deposition on the ice structure with and without advective flows in snow. The degree of over- or under-saturation, $\sigma = (\langle \rho_v \rangle^g - \rho_{v,s}) / \rho_{v,s}$, is directly related to the phase change rate $\dot{m}_{iv}$ (the divergence of the vapor flux) (Jafari et al., 2020) and can be used as a diagnostic variable to quantify the intensity of the phase change rate. Hence, the phase change rate $\dot{m}_{iv}$ can be written as:

$$\dot{m}_{iv} = -\frac{6\epsilon_i \rho_i}{\mathscr{B} d_p} \sigma \tag{2.6}$$

### 2.2.2   Momentum

With the pore Reynolds number $Re_p = \rho_g |\langle \boldsymbol{U}_g \rangle| d_p / \mu$ (based of particle size, $d_p$) less than 10, the advective and inertial terms are negligible (Gray and O'Neill, 1976; Ganesan and Poirier, 1990; Faghri and Zhang, 2006; Nield and Bejan, 2017) and thus the volume-averaged momentum equation for gas flow through the snowpack as a porous medium with variable porosity can be simplified to the Darcy-Forchheimer equation (Ward, 1964; Faghri and Zhang, 2006; Nield and Bejan, 2017) as:

$$-\frac{\mu}{K}\langle \boldsymbol{U}_g\rangle - \frac{\langle \rho_g\rangle^g c_F}{\sqrt{K}}\left|\langle \boldsymbol{U}_g\rangle\right|\langle \boldsymbol{U}_g\rangle - \nabla\langle P_g\rangle^g + \langle \rho_g\rangle^g\,\boldsymbol{g} = 0 \qquad (2.7)$$

where $\mu$ is the dynamic viscosity of the air, $K$ is the intrinsic permeability of the porous medium, $c_F$ is a dimensionless form-drag constant, and $\langle P_g\rangle^g$ is the gas mixture pressure. In equation (2.7), the first and second terms refer to the Darcian relationship due to the viscous surface friction and the quadratic drag (or the nonlinear form drag) due to solid obstacles, respectively (Faghri and Zhang, 2006; Nield and Bejan, 2017). The quadratic drag is significant when $1 < Re_p < 10$ otherwise it is negligible compared to the Darcian term (Faghri and Zhang, 2006; Nield and Bejan, 2017). To extract the driving force associated with the gas density gradient in the momentum equation (2.7), the hydrostatic pressure contribution is separated from total gas pressure as $\langle P_g\rangle^g = \langle P_{g_d}\rangle^g - \langle \rho_g\rangle^g\,gz$. Hence, the momentum equation may be read equivalently as:

$$-\frac{\mu}{K}\langle \boldsymbol{U}_g\rangle - \frac{\langle \rho_g\rangle^g c_F}{\sqrt{K}}\left|\langle \boldsymbol{U}_g\rangle\right|\langle \boldsymbol{U}_g\rangle - \nabla\langle P_{g_d}\rangle^g + \nabla\langle \rho_g\rangle^g\left|gz\right| = 0 \qquad (2.8)$$

Using three-dimensional images of snow microstructure, Calonne et al. (2012) proposed the following regression for the snow permeability:

$$K = \frac{3}{4}d_p^2\,\exp\left(-0.013\rho_i\epsilon_i\right) \qquad (2.9)$$

Assuming Ergun's equation for momentum, the dimensionless form-drag constant can be evaluated by $c_F = \alpha\gamma^{-1/2}\epsilon_g^{-3/2}$ as an ad hoc procedure with $\alpha = 1.75$ and $\gamma = 150$ (Nield and Bejan, 2017).

### 2.2.3 Energy

Neglecting the effect of viscous dissipation on natural convection in a porous medium (Nield and Bejan, 2017), the intrinsic volume-averaged energy equations in terms of enthalpy $\langle h_g\rangle^g$ for the gas and $\langle h_i\rangle^i$ for ice phase with local thermal non-equilibrium (LTNE) are derived respectively as (Faghri and Zhang, 2006; Nield and Bejan, 2017):

$$\frac{\partial}{\partial t}(\epsilon_g\langle \rho_g\rangle^g\langle h_g\rangle^g) + \nabla\cdot(\langle \rho_g\rangle^g\langle h_g\rangle^g\langle \boldsymbol{U}_g\rangle) = -\nabla\cdot\left\langle \boldsymbol{q}_g''\right\rangle^g$$

$$-\nabla\cdot\left[\langle h_v\rangle^g\langle J_v\rangle + \langle h_a\rangle^g\langle J_a\rangle\right] + \epsilon_g\frac{\partial}{\partial t}\langle P_g\rangle^g + \langle \boldsymbol{U}_g\rangle\cdot\nabla\langle P_g\rangle^g$$

$$+\,\dot{m}_{iv}\langle h_{v,I}\rangle^g + \langle q_{I,g}\rangle \quad (2.10a)$$

$$\rho_i \frac{\partial}{\partial t} (\epsilon_i \langle h_i \rangle^i) = -\nabla \cdot \langle \boldsymbol{q}_i'' \rangle^i + \dot{m}_{vi} \langle h_{i,I} \rangle^i + \langle q_{I,i} \rangle \qquad (2.10b)$$

The subscripts $a$, and $v$ correspond to the dry air and water vapor component respectively. The first two terms on the right-hand side of equation (2.10a) represent the divergence of the conductive heat flux and the interdiffusional convection (the transfer of enthalpy with vapor and air diffusive fluxes as $\langle J_v \rangle$ and $\langle J_a \rangle$), respectively. The fourth term on the right-hand side of equation (2.10a) is the reversible rate of energy change per unit volume associated with compression. In equations (2.10), $\left\langle \boldsymbol{q}_g'' \right\rangle^g$ and $\langle \boldsymbol{q}_i'' \rangle^i$ are the conductive heat fluxes in the gas and ice phases respectively, $\langle q_{I,g} \rangle$ and $\langle q_{I,i} \rangle$ are the conductive heat transfer per unit volume from the interface to the related phases, and the terms $\dot{m}_{iv} \langle h_{v,I} \rangle^g$ and $\dot{m}_{vi} \langle h_{i,I} \rangle^g$ are the interphase enthalpy exchange due to phase change, in which $\langle h_{v,I} \rangle^g$ and $\langle h_{i,I} \rangle^i$ are the intrinsic volume-averaged enthalpies of the water vapor and ice, respectively, calculated at the interface temperature $T_I$. Assuming the humid air as being an ideal gas mixture and using the ideal gas equation of state for the water vapor and dry air components, the enthalpy $\langle h_g \rangle^g$, the specific heat capacity $\langle c_{pg} \rangle^g$, molecular mass $\langle M_g \rangle^g$, and the density of the gas mixture are evaluated as:

$$\langle h_g \rangle^g = \frac{\langle \rho_v \rangle^g \langle h_v \rangle^g + \langle \rho_a \rangle^g \langle h_a \rangle^g}{\langle \rho_g \rangle^g} \qquad (2.11a)$$

$$\langle c_{pg} \rangle^g = \frac{\langle \rho_v \rangle^g c_{pv} + \langle \rho_a \rangle^g c_{pa}}{\langle \rho_g \rangle^g} \qquad (2.11b)$$

$$\langle \rho_g \rangle^g = \langle \rho_v \rangle^g + \langle \rho_a \rangle^g = \frac{\langle P_g \rangle^g \langle M_g \rangle^g}{R_u \langle T_g \rangle^g} \qquad (2.11c)$$

$$\langle \rho_a \rangle^g = \frac{\langle P_a \rangle^g M_a}{R_u \langle T_g \rangle^g} \qquad (2.11d)$$

$$\langle \rho_v \rangle^g = \frac{\langle P_v \rangle^g M_v}{R_u \langle T_g \rangle^g} \qquad (2.11e)$$

$$\langle M_g \rangle^g = \frac{\langle \rho_g \rangle^g}{\langle \rho_a \rangle^g / M_a + \langle \rho_v \rangle^g / M_v} \qquad (2.11f)$$

In equation (2.11), $R_u$ is the universal gas constant, $M_v$ and $M_a$ are the molecular mass, $c_{pv}$ and $c_{pa}$ are the specific heat capacity, and finally $\langle P_v \rangle^g$, $\langle P_a \rangle^g$ are the partial pressure for the water vapor and dry air components respectively. The zero point of the enthalpy for the dry air and the liquid water is chosen at the reference temperature $T_{\text{ref}} = 273.15$ K. Therefore, the

enthalpies of the dry air, water vapor and ice are given as (Russo et al., 2014b):

$$\langle h_v \rangle^g = \langle h_v \rangle^g \, (T = T_{\text{ref}}) + c_{pv}(\langle T_g \rangle^g - T_{\text{ref}}) = L_{wv} + c_{pv}(\langle T_g \rangle^g - T_{\text{ref}}) \tag{2.12a}$$

$$\langle h_i \rangle^i = \langle h_i \rangle^i \, (T = T_{\text{ref}}) + c_{pi}(\langle T_i \rangle^i - T_{\text{ref}}) = -L_{iw} + c_{pi}(\langle T_i \rangle^i - T_{\text{ref}}) \tag{2.12b}$$

$$\langle h_a \rangle^g = c_{pa}(\langle T_g \rangle^g - T_{\text{ref}}) \tag{2.12c}$$

where $L_{iw}$ and $L_{wv}$ are the latent heat of fusion and evaporation respectively. Given that the interfacial energy terms associated with surface tension, the work done by pressure, and interfacial shear stress work (the conversion of mechanical to the thermal energy) are usually negligible with respect to the large energy exchange due to phase change, the energy balance at the interface can be written as (Ishii and Hibiki, 2010; Hugelius et al., 2014; Faghri and Zhang, 2006):

$$\dot{m}_{iv} \langle h_{v,I} \rangle^g + \langle q_{I,g} \rangle + \dot{m}_{vi} \langle h_{i,I} \rangle^i + \langle q_{I,i} \rangle = 0 \tag{2.13}$$

To obtain the heat transfer from the interface to the gas phase $\langle q_{I,g} \rangle$, Newton's law of cooling is used as follows:

$$\langle q_{I,g} \rangle = h_c a_s (T_I - \langle T_g \rangle^g) \tag{2.14}$$

where $h_c$ is the heat transfer coefficient and $a_s$ is the specific surface area of the porous medium. Substituting equation (2.14) into equation (2.13) with $\dot{m}_{vi} = -\dot{m}_{iv}$, the heat transfer from the interface to the ice phase $\langle q_{I,i} \rangle$, may be calculated as:

$$\langle q_{I,i} \rangle = -h_c a_s (\langle T_g \rangle^g - T_I) + \dot{m}_{iv}(\langle h_{i,I} \rangle^i - \langle h_{v,I} \rangle^g) \tag{2.15}$$

Based on the temporal term in the bulk heat transfer equation including both phases (homogeneous mixture model), the interface temperature $T_I$ may be evaluated as:

$$T_I = w_g \langle T_g \rangle^g + w_i \langle T_i \rangle^i \tag{2.16a}$$

$$w_g = \frac{\epsilon_g \langle \rho_g \rangle^g c_{pg}}{\epsilon_g \langle \rho_g \rangle^g c_{pg} + \epsilon_i \rho_i c_{pi}} \tag{2.16b}$$

$$w_i = \frac{\epsilon_i \rho_i c_{pi}}{\epsilon_g \langle \rho_g \rangle^g c_{pg} + \epsilon_i \rho_i c_{pi}} \tag{2.16c}$$

Based on analogies between heat and mass transfer (Bird et al., 1961; Faghri and Zhang, 2006; Bergman et al., 2011), it follows that the dimensionless temperature gradient expressed by the Nusselt number $Nu = h_c d_p / k_a = f(Re_p, Pr)$ and concentration gradient expressed by Sherwood number $Sh = h_m d_p / D_{v,a} = f(Re_p, Sc)$ are similar and we assume $Nu = Sh$. Where $Sc$ is the Schmidt number as the ratio of kinematic viscosity and mass diffusivity, and $Pr$ is the heat transfer equivalent of Schmidt number. For gases, $Sc$ and $Pr$ have similar values ($\approx 0.7$) and this is used as the basis for simple heat and mass transfer analogies. Therefore, the heat transfer coefficient $h_c$ may be related to the mass transfer coefficient $h_m$ as:

$$h_c = \frac{h_m k_a}{D_{v,a}} \tag{2.17}$$

Combining equations (2.11), (2.12), (2.14), (2.15), and (2.16) with equations (2.10), the energy equations in term of temperature for the gas and ice phases are derived as:

$$\frac{\partial}{\partial t}(\epsilon_g \langle \rho_g \rangle^g c_{pg} \langle T_g \rangle^g) + \nabla \cdot (\langle \rho_g \rangle^g c_{pg} \langle T_g \rangle^g \langle \boldsymbol{U}_g \rangle) = \nabla \cdot (\epsilon_g k_{\text{eff},g} \nabla \langle T_g \rangle^g)$$
$$+ \epsilon_g \frac{\partial}{\partial t} \langle P_g \rangle^g + \langle \boldsymbol{U}_g \rangle \cdot \nabla \langle P_g \rangle^g - \nabla \cdot \left[ \langle T_g \rangle^g (c_{pv} - c_{pa}) \langle J_v \rangle \right]$$
$$+ h_c a_s \left[ (\langle T_g \rangle^g (w_g - 1) - \langle T_i \rangle^i w_i) \right] + \dot{m}_{iv} c_{pv} \langle T_g \rangle^g \tag{2.18}$$

$$\rho_i c_{pi} \frac{\partial}{\partial t}(\epsilon_i \langle T_i \rangle^i) = \nabla \cdot (\epsilon_i k_{\text{eff},i} \nabla \langle T_i \rangle^i)$$
$$- h_c a_s \left[ (\langle T_g \rangle^g (w_g - 1) - \langle T_i \rangle^i w_i) \right]$$
$$- \dot{m}_{iv} c_{pv}(\langle T_g \rangle^g w_g + \langle T_i \rangle^i w_i) - \dot{m}_{iv}(c_{pi} - c_{pv}) T_{\text{ref}} - \dot{m}_{iv} L_{iv} \tag{2.19}$$

where $k_{\text{eff},g}$ and $k_{\text{eff},i}$ are, respectively, the effective thermal conductivity of the humid air and ice in snow. Using the definition of the effective thermal conductivity for snow $k_{\text{eff},s} = \epsilon_g k_{\text{eff},g} + \epsilon_i k_{\text{eff},i}$ (Calonne et al., 2012; Hansen and Foslien, 2015), one can extract $k_{\text{eff},g}$ and $k_{\text{eff},i}$ from the analytical parametrization derived for $k_{\text{eff},s}$ by Hansen and Foslien (2015) as:

$$k_{\text{eff},g} = \epsilon_i k_a + \frac{k_a k_i}{\epsilon_i (k_a + L_{iv} D_{v,a} \frac{d\rho_{vs}}{dT}) + \epsilon_g k_i} \tag{2.20a}$$

$$k_{\text{eff},i} = \epsilon_i k_i \qquad\qquad (2.20\text{b})$$

In equations (2.20), $k_i$ is the thermal conductivity of the ice.

The final set of the equations to be solved are equations (2.1), (2.2), and (2.3) for the mass conservation, equation (2.7) for the momentum, and equations (2.18) and (2.19) for the temperature-based energy equations.

Natural convection in a porous medium is triggered when buoyancy forces, driven by unstable fluid density gradients, are large enough to overcome viscous drag. Therefore, the ratio of buoyancy to viscous forces in a porous medium, expressed by the Rayleigh number, is used as an important non-dimensional parameter to analyze the convective heat and mass transfer in a porous medium:

$$Ra = \frac{\rho_{a_{\text{ref}}} \beta g \Delta T H K}{\mu k_{\text{eff},s}/(\rho_{a_{\text{ref}}} c_{pa})} \qquad\qquad (2.21)$$

where, $H$ is the depth of porous layer, and the air density $\rho_{a_{\text{ref}}}$, specific heat capacity $c_{pa}$, dynamic viscosity $\mu$, and thermal expansion coefficient $\beta$, all are used at the reference temperature $T_{\text{ref}} = 273.15$ K. The Rayleigh number can alternatively be interpreted as the ratio of convective to conductive velocity scales as $Ra = U_{conv}/U_{cond}$ (Hewitt et al., 2013a,b), in which the convective velocity scale is $U_{conv} = \rho_{a_{\text{ref}}} \beta \Delta T g K/\mu$ and the conductive velocity scale is $U_{cond} = k_{\text{eff},s}/(\rho_{a_{\text{ref}}} c_{pa} H)$.

## 2.3 Numerical scheme, solution procedure, and simulation setups

A direct numerical solver is developed to model convection of water vapor with phase change in snowpacks. This new solver, named as *snowpackBuoyantPimpleFoam* is based on the standard solver of *buoyantPimpleFoam* in the open-source fluid dynamics software, OpenFOAM 5.0 (www.openfoam.org). Using a finite volume approach, the governing equations are discretized on a collocated grid. PIMPLE as a combined PISO-SIMPLE algorithm (Moukalled et al., 2016) is used for the pressure-velocity coupling to solve the final set of equations described in section 2.2. For the solution procedure, the gas phase velocity obtained by the momentum equation is used to solve the water vapor density and the temperature for the gas and ice phases. Then, the gas mixture continuity equation including the mass source (or sink) term along with the semi-discretized momentum equation are used to solve the resulting pressure Poisson equation to obtain continuity-satisfying velocity and pressure fields (Moukalled et al., 2016). For the next time step, the heat and mass transfer coefficients are updated to repeat the solution procedure. To discretize the equations, the Gauss linear and Gauss linear corrected schemes, respectively, are used for the terms with gradient and diver-
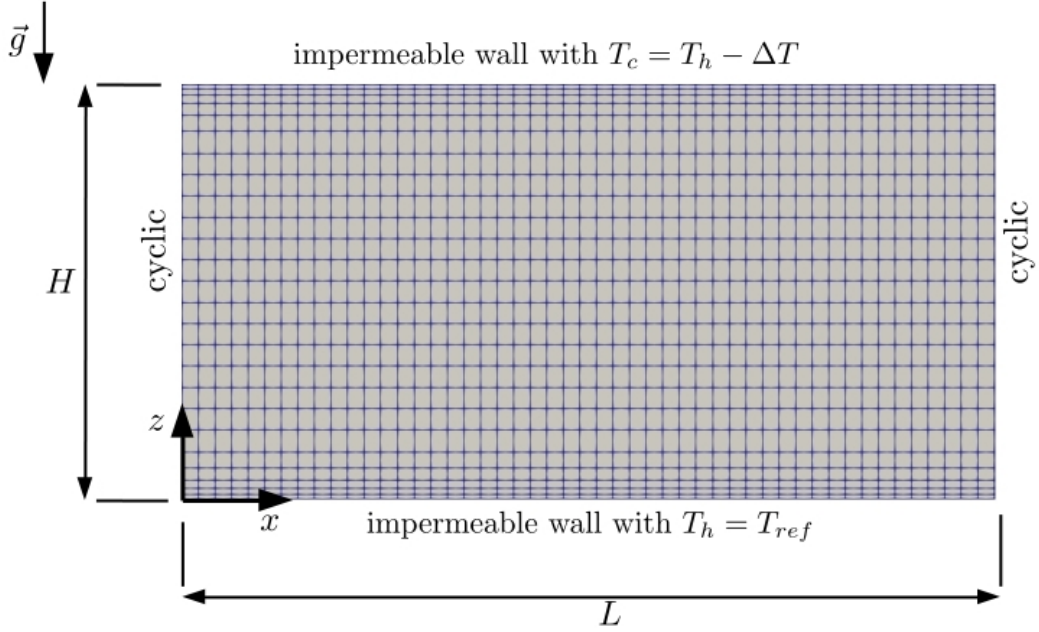
Figure 2.1: A sketch of two-dimensional domain with non-uniform mesh and prescribed boundary conditions.

gence operations and the Euler scheme is chosen for the discretization of the transient terms (Moukalled et al., 2016). The adjustable time step scheme with a limit on the Courant number was deployed to reduce the computational cost. The Courant number as the stability criterion is defined as $Co = |\langle \boldsymbol{U}_g \rangle| \Delta t / \Delta r$ where $\Delta t$ is the time step and $\Delta r$ is the distance between the computational cell centers.

The numerical simulation is performed for a natural convection flow in a two-dimensional snowpack of the depth $H$ and the length $L$. Figure 2.1 shows a sketch of the domain with the cyclic boundary conditions on lateral sides. The top and bottom boundaries are considered as impermeable walls with zero flux for the gas phase. For the heat transfer equations of both phases, the reference temperature is used as the bottom boundary condition, $T_h = T_{\text{ref}}$, whereas $T_c = T_{\text{ref}} - \Delta T$ is applied for the top boundary. The initial conditions are the reference temperature for both ice and gas phases and the saturation water vapor density as $\sigma = 0$. The sensitivity analysis has shown that the results are not sensitive to the choice of initial temperature and vapor distribution (figure A.1 in appendix A.1). A non-uniform mesh in the vertical direction is used to ensure that the grid size is small enough in the order of $Ra^{-1}$ to resolve the thin boundary layers (Hewitt et al., 2014). Note that in reality snow settling will counteract the density decrease caused by convection to a certain extent and prevent very low densities at the bottom. Since snow settling is not simulated in our model, we artificially limited the density decrease by the threshold of 95 % for the porosity above which the phase change is stopped. In general, the convective-diffusive heat and mass transfer with phase change in snowpacks are very slow processes and changes are small enough at each

| symbol | description | value | unit |
|--------|-------------|-------|------|
| $T_{\text{ref}}$ | reference temperature | 273.15 | K |
| $\rho_{a_{\text{ref}}}$ | reference air density | 1.293 | $\text{kg m}^{-3}$ |
| $\rho_{v s_{\text{ref}}}$ | reference saturation water vapor density | 0.005 | $\text{kg m}^{-3}$ |
| $\beta$ | thermal expansion coefficient of air | 0.00366 | $\text{K}^{-1}$ |
| $g$ | gravitational acceleration | 9.81 | $\text{m s}^{-2}$ |
| $\mu$ | dynamic viscosity of air | $17.29 \times 10^{-6}$ | $\text{kg m}^{-1}\,\text{s}^{-1}$ |
| $\rho_i$ | ice density | 273.15 | $\text{kg m}^{-3}$ |
| $c_{pa}$ | specific heat capacity of air | 1005 | $\text{J kg}^{-1}\,\text{s}^{-1}$ |
| $c_{pv}$ | specific heat capacity of water vapor | 1853 | $\text{J kg}^{-1}\,\text{s}^{-1}$ |
| $c_{pi}$ | specific heat capacity of ice | 2027 | $\text{J kg}^{-1}\,\text{s}^{-1}$ |
| $k_a$ | thermal conductivity of air | 0.02434 | $\text{W m}^{-1}\,\text{K}^{-1}$ |
| $k_i$ | thermal conductivity of ice | 2.25 | $\text{W m}^{-1}\,\text{K}^{-1}$ |
| $L_{wv}$ | latent heat of evaporation | $2.5008 \times 10^6$ | $\text{J kg}^{-1}$ |
| $L_{iw}$ | latent heat of fusion | $3.335 \times 10^5$ | $\text{J kg}^{-1}$ |
| $L_{iv}$ | latent heat of sublimation | $2.838 \times 10^5$ | $\text{J kg}^{-1}$ |
| $d_p$ | snow grain diameter | 0.001 | m |

Table 2.1: The thermal and physical properties of the gas and ice phases evaluated at the reference temperature.

time step to consider a quasi-steady state process especially when the convection cells are completely formed and only show small lateral movement (see below). This is due to the fact that convection cells form and reach a quasi-steady state in the order of a few hours (shown later in figure 2.3), the thermal boundary conditions are fixed, and that the order of magnitude for the porosity change is small at each time step. Scaling analysis of the ice mass conservation shows that for the minimum Rayleigh number studied, and assuming maximum mass transfer potential of $\sigma = 1$, the porosity change rate is small and in the order of $\partial \epsilon_i / \partial t \approx 10^{-9}\ \text{s}^{-1}$. Hence, the convection-diffusion terms (the net vapor divergence for sublimation and convergence for deposition) are almost equal to the mass source/sink term. Thus, the maximum Courant number of 200 with the outer PIMPLE loop of 50 and the residual control of $10^{-4}$ are used. Note that the sensitivity analysis performed shows that the results for the semi-steady state process are not changing for the maximum Courant number less than 200 as shown in figures A.2 and A.3 both in appendix A.3. In addition, changing the domain length $L$ from 5 m to 100 m did not change the results as it is shown in figure A.4 in appendix A.3. Hence, a domain length of 10 m was chosen for the simulations. The numerical setup also was validated comparing with available numerical benchmarks in section 2.4. The thermal and physical properties of the gas and ice phases used in the present numerical simulations are listed in table 2.1.

| Author | $\overline{Nu}$ | | | |
|---|---|---|---|---|
| | $Ra = 100$ | $Ra = 200$ | $Ra = 500$ | $Ra = 1000$ |
| Saeid and Pop (2004) | 3.002 | - | - | 13.726 |
| Horne (1975) | - | 4.89 | 8.78 | - |
| Walker and Homsy (1978) | 3.097 | 4.89 | 8.66 | 12.96 |
| present results | 3.062 | 4.81 | 8.52 | 13.20 |

Table 2.2: Comparison of the total Nusselt number $\overline{Nu}$ defined in equation (2.22b), at steady state with some previous numerical benchmarks.

## 2.4 Numerical validation

The numerical benchmarks for natural convection in a square porous medium with hot and cold impermeable boundaries on the sides and adiabatic and impermeable boundaries on the top and bottom are used to examine the performance of the solver developed. First, the results obtained by the present model are compared against the cases of thermal equilibrium. To that end, the local and total Nusselt numbers adapted for the thermal equilibrium should be used as (Saeid, 2004):

$$Nu(z) = \frac{H}{\Delta T(\epsilon_g k_{\text{eff},g} + \epsilon_i k_{\text{eff},i})}\left[\epsilon_g k_{\text{eff},g}\frac{d\langle T_g\rangle^g}{dz} + \epsilon_i k_{\text{eff},i}\frac{d\langle T_i\rangle^i}{dz}\right] \quad (2.22a)$$

$$\overline{Nu} = \frac{1}{H}\int_0^H Nu(z)\,dz \quad (2.22b)$$

Figure 2.2 shows the transient variation of the local Nusselt number with scaled time $\tau = k_{\text{eff},s}t/((\epsilon_g\rho_{a_{\text{ref}}}c_{pa} + \epsilon_i\rho_i c_{pi})H^2)$ for $Ra = 100$. The grid dependency analysis shows that the temporal variation of $Nu$ for the heights in the middle and upper parts of the domain is not changing with increasing the grid size and mostly the error is lest than 5 % while increasing the spatial resolution helps to decrease the error for the bottom region of the domain. However, in general, a good agreement between the present model and the numerical benchmark by Saeid and Pop (2004) can be seen for the transient behavior of the local heat transfer. In table 2.2, the resulting total Nusselt number for different Rayleigh numbers are compared with some available numerical benchmarks to verify the performance of the present solver. The larger variations of $Nu$ between different studies for higher $Ra$ is due to unstable and chaotic behavior of the flow which requires fine resolution dependent on $Ra$ as discussed in section 2.3.

Finally, a comparison was done with the results of local thermal non-equilibrium model by Baytas and Pop (2002) using the total Nusselt number defined separately for the gas and ice phases at cold and hot surfaces of the cavity as:
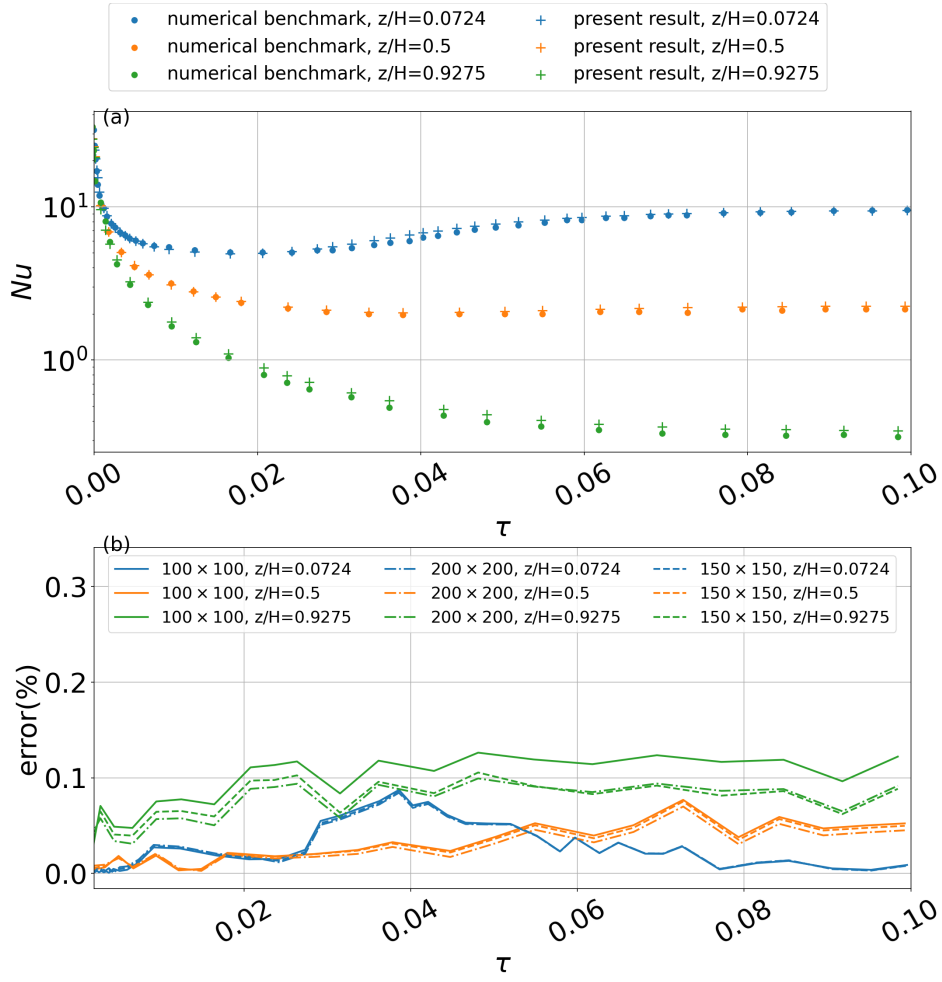
Figure 2.2: Comparison of present results with the numerical benchmark by Saeid and Pop (2004) (a) for the transient variation of the local Nusselt number with scaled time $\tau$ at three non-dimensional heights for the $Ra = 100$ and (b) the relative error for different grid sizes.

| $\frac{h_c H^2}{\epsilon_g k_{\text{eff},g}}$ | Baytas and Pop (2002) | | present results | |
|---|---|---|---|---|
| | $\overline{Nu_g}$ | $\overline{Nu_i}$ | $\overline{Nu_g}$ | $\overline{Nu_i}$ |
| 1 | 14.61 | 1.077 | 14.89 | 1.061 |
| 5 | 14.36 | 1.260 | 14.66 | 1.265 |
| 10 | 14.14 | 1.476 | 14.46 | 1.487 |
| 50 | 13.43 | 2.505 | 13.82 | 2.549 |
| 100 | 13.10 | 3.182 | 13.51 | 3.252 |

Table 2.3: Comparison of the total Nusselt numbers $\overline{Nu_g}$ and $\overline{Nu_i}$ for the case of local thermal non-equilibrium model with the fixed Rayleigh number $Ra = 500$ and $k_{\text{eff},g} = k_{\text{eff},i}$ but different heat transfer coefficients $h_c$.

$$\overline{Nu_g} = \frac{1}{\Delta T} \int_0^H \frac{d \langle T_g \rangle^g}{dz} dz \tag{2.23a}$$

$$\overline{Nu_i} = \frac{1}{\Delta T} \int_0^H \frac{d \langle T_i \rangle^i}{dz} dz \tag{2.23b}$$

Note that we have used the same term for the heat transfer between two phases as presented in Baytas and Pop (2002). From comparing the results in table 2.3, we found that the present results for $\overline{Nu_i}$ are very close to the numerical benchmark and that the maximum error for $\overline{Nu_g}$ compared to the benchmark is less than 3%.

## 2.5 Results and Discussion

To the best of our knowledge, we explore for the first time the convection of water vapor in a phase-changing snowpack and its effects on snow density change by looking at the thermal and phase change regimes for different snowpack conditions (vertical size, thermal boundary conditions, Rayleigh number). The conductive and convective velocity scales introduced in section 2.2.3 are the key measures to analyze the thermal and mass transfer in a snowpack and they are needed to show the differences in the phase change regime for different snowpack conditions. As the effective thermal conductivity and the intrinsic permeability of snow given respectively by equations (2.20) and (2.9) both are a function of porosity, for a specified Rayleigh number, the two parameters of interest are the snow height and the temperature difference (as the thermal boundary conditions) which define the conductive and convective velocity scales and will be discussed separately later.

In order to provide a context for our results, we want to summarize the main observations first: in section 2.5.1, the general thermal and phase change behavior in the snowpack is discussed and we find that (1) the thermal and phase change pattern in a convection cell is qualitatively

the same in all different snowpacks, (2) there is considerable impact of natural convection on the snow density distribution with a layer of significantly lower density at the bottom of the snowpack and a layer of higher density located at the top, and (3) as will be discussed in section 2.5.2, the horizontal displacement of the convection cells leads to a wider area of the top and bottom region to experience phase change processes, resulting in an almost uniformly increased snow density on the top mirroring the reduced density in the bottom region. Quantitatively, different phase change rates in snowpacks with various conditions (vertical size, thermal boundary conditions, Rayleigh number) are caused by the difference in the thermal and the flow regimes between their respective deposition and sublimation zones. With this respect, the heat and mass transfer will be compared between different snow heights $H$ in section 2.5.3 while the effect of the temperature difference, $\Delta T$ is investigated in section 2.5.4.

## 2.5.1   General thermal and phase change behavior

When the Rayleigh number is large enough such that convection cells form, the regime generally develops through three stages: (1) the pure conduction mode, (2) the transition mode when convection cells start to form, (3) the predominant convection mode when the convection cells are completely formed. As an example, figure 2.3 shows the evolution of the thermal regime through different stages, indicating also the flow directions. Both conduction heat transfer rate and the Rayleigh number determine how long stages 1 and 2 last. In figure 2.3a conduction is still the dominant mode. As the initial temperature is uniform and equal to the bottom warm boundary, at the start of simulation, there is considerable conduction heat transfer in the region close to the top boundary, cooling down that region (the stage 1 of the thermal regime). While the conduction leads to cooling of the bottom region, the convection starts to be active on the top region. This is shown in figure 2.3b as the stage 2 of the thermal regime. Figure 2.3c shows the transition between stages 2 and 3 when the convection cells fill almost the whole domain but they are not yet completely formed and stable. Finally, the convection mode with completely formed convection cells is shown in figure 2.3d as the last stage of the regime development. Figure 2.4 indicates the completely formed convection cells by streamlines. As shown in this figure, each convection cell is formed by neighboring upward and downward flows. Also, these cells can be split by the saturation line $\sigma = 0$ into the deposition zone (above the saturation line) and sublimation zone (below the saturation line).

It should be noted that the general thermal and phase change behavior in the upward and downward flows of a convection cell are qualitatively the same for snowpacks with different conditions (e.g. snow height, thermal boundary conditions, Rayleigh number). Hence, we analyze the heat and mass transfer regimes in different parts of a chosen convection cell after one week of the simulation for a sample case with snow height $H = 25$ cm, the temperature difference $\Delta T = 50$ K, and $Ra = 50$. Figure 2.5 shows profiles for the saturation degree, snow density change, saturation vapor density gradient, snow temperature gradient, and the air flow
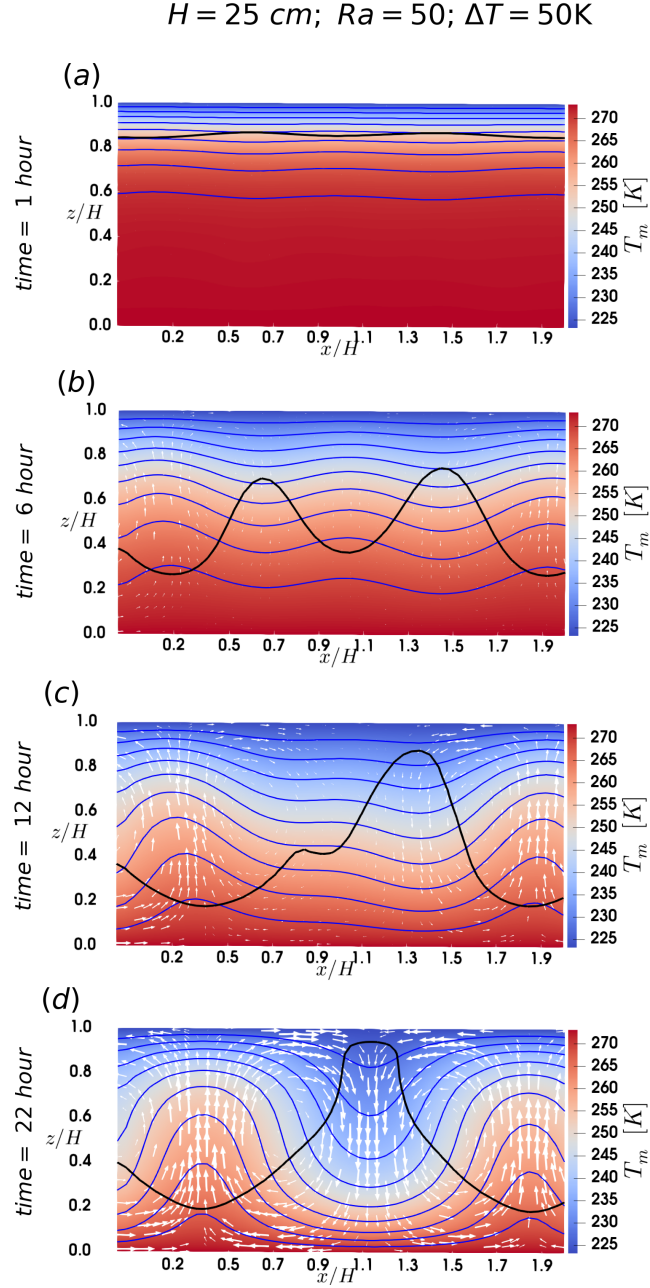
Figure 2.3: Evolution of the thermal regime through different stages, (a) the pure conduction mode at time = 1 hour, (b) transition mode when the convection starts to form on top at time = 6 hours, (c) transition mode when the convection cells fills almost the whole domain but not completely formed and stable at time = 12 hours, (d) the predominant convection mode with completely formed convection cells at time = 22 hours with maximum gas velocity of
$$3.1 \times 10^{-3} \text{ m s}^{-1}$$
. The white arrows shows the flow direction scaled by velocity magnitude. The black line refers to the saturation line where $\sigma = 0$. The isotherm lines for the snow temperature are in blue color which are equally spaced by 5 K.
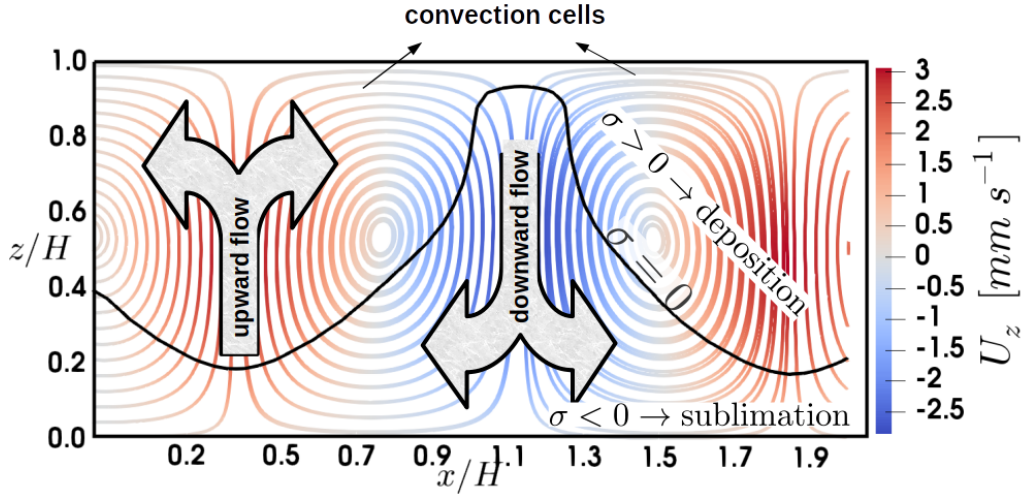
Figure 2.4: Streamlines for the completely formed convection cells. The black line refers to the saturation line $\sigma = 0$, above and under which there are the deposition and sublimation zones respectively.

velocity in the upward and downward flows of a convection cell for two scenarios i.e different snow heights and different temperature boundary conditions. Also, two-dimensional plots of the chosen convection cell for the sample case (snow height $H = 25$ cm, the temperature difference $\Delta T = 50$ K, and $Ra = 50$) are shown in figure 2.6. In these 2D plots, to highlight downward flows, the marker points p7, p1, p2, and p3 are used while for the upward flows the markers p4, p5, and p6 are used. In general, when convection is active, the downward convective flow stretches the top cold temperature towards the bottom hot boundary. As shown in figure 2.5a and figure 2.5n, this causes a smaller temperature gradient on top and larger temperature gradient in the bottom region. Oppositely, the upward convective flow stretches the bottom warm temperature towards the top resulting in a smaller temperature gradient at the bottom region and a larger gradient on the top because of the fixed top boundary temperature (figure 2.5i and figure 2.5s). Thus, compared to the pure conduction temperature profile, the region is colder in downward flow and warmer in upward flow. Also, in both upward and downward flows, the maximum stretching (the smallest temperature gradient) occurs where the gas flow velocity reaches maximum (compare figure 2.5n and figure 2.5o). For both regions close to and far enough from the boundaries, it will be discussed later that the effect of the convective stretching on the temperature profile in different snowpacks is determined by the Rayleigh number.

For the phase change regime in different parts of a chosen convection cell, we first analyze the downward flow from the saturation line. While the downward convective flow transports the water vapor towards the bottom (leading to less vapor content and smaller vapor gradient in the upper part), the sublimation phase change simultaneously counteracts the convection effect by adding vapor to the upper part. As discussed in appendix A.4, the phase change rate is dependent on both convective flow rate and the gradient of the saturation vapor density.
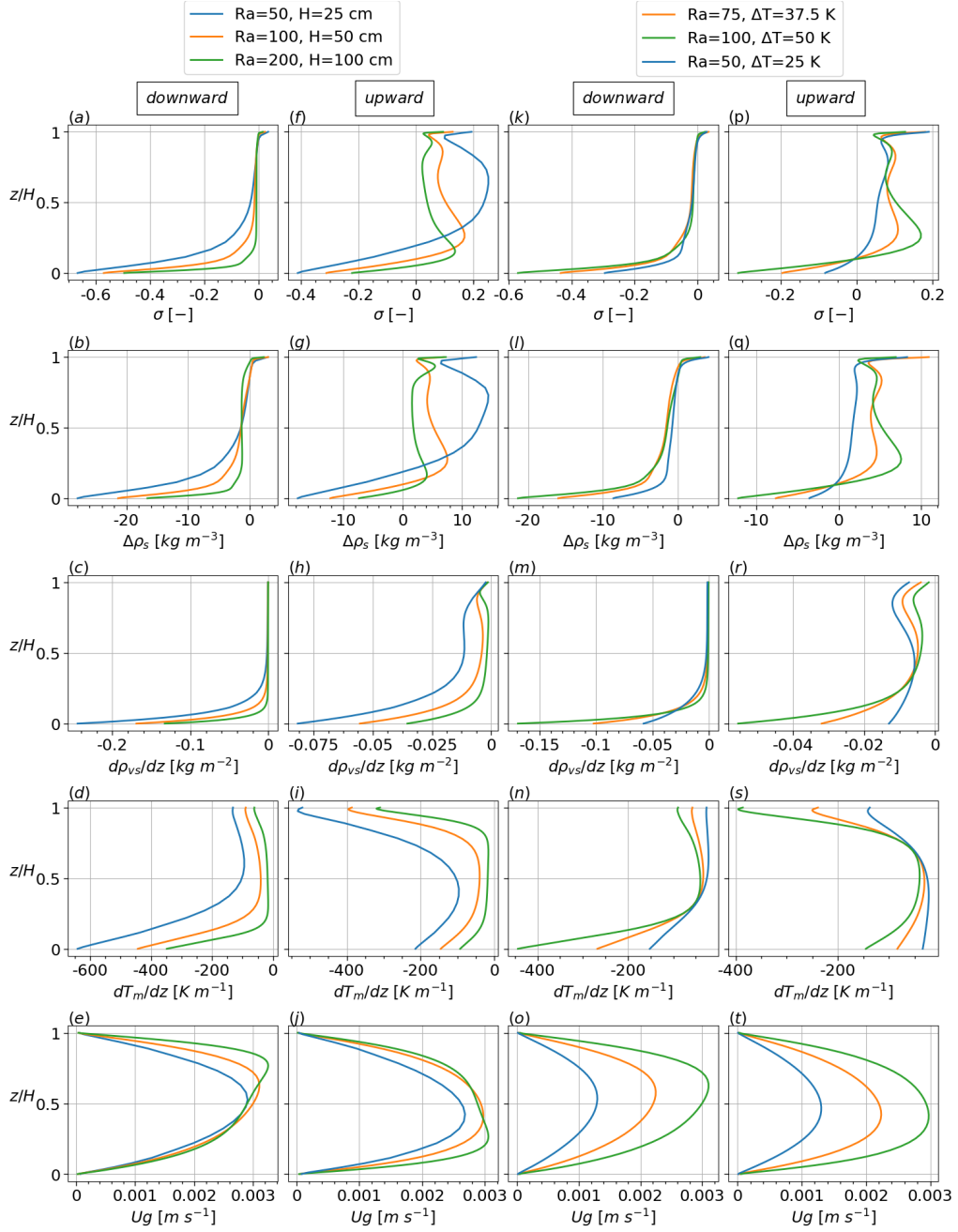
Figure 2.5: One-dimensional profiles of the saturation degree $\sigma$, the snow density change $\Delta\rho_s$, the gradient of saturation vapor density $d\rho_{vs}/dz$, the snow temperature gradient $dT_m/dz$, and the gas flow velocity $U_g$ at the location of downward and upward flows of a convection cell for different snow heights $H$, and the temperature difference $\Delta T$.
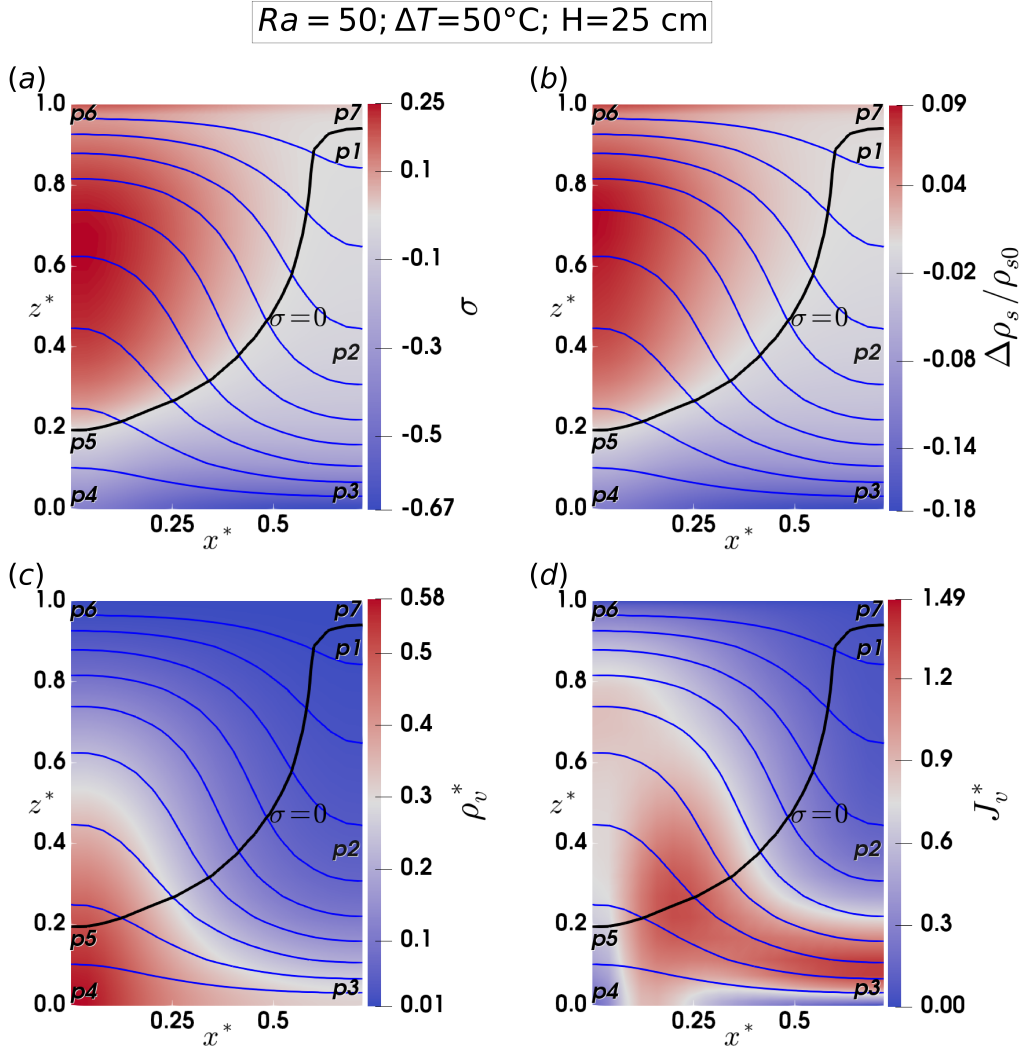
Figure 2.6: Simulated two-dimensional plots for the sample case with snow height $H = 25 cm$, the temperature difference $\Delta T = 50\,K$, and $Ra = 50$. (a) the saturation degree $\sigma$, (b) the snow density change $\Delta \rho_s / \rho_{so}$, (c) the water vapor density $\rho_v^* = \langle \rho_v \rangle^g / \rho_{v s_{\text{ref}}}$, and (d) diffusive water vapor flux $J_v^* = \langle J_v \rangle / (D_{va} \rho_{v s_{\text{ref}}} / H)$. The black line refers to the saturation line where $\sigma = 0$. The isotherm lines for the snow temperature are in blue color which are equally spaced by 5 K.
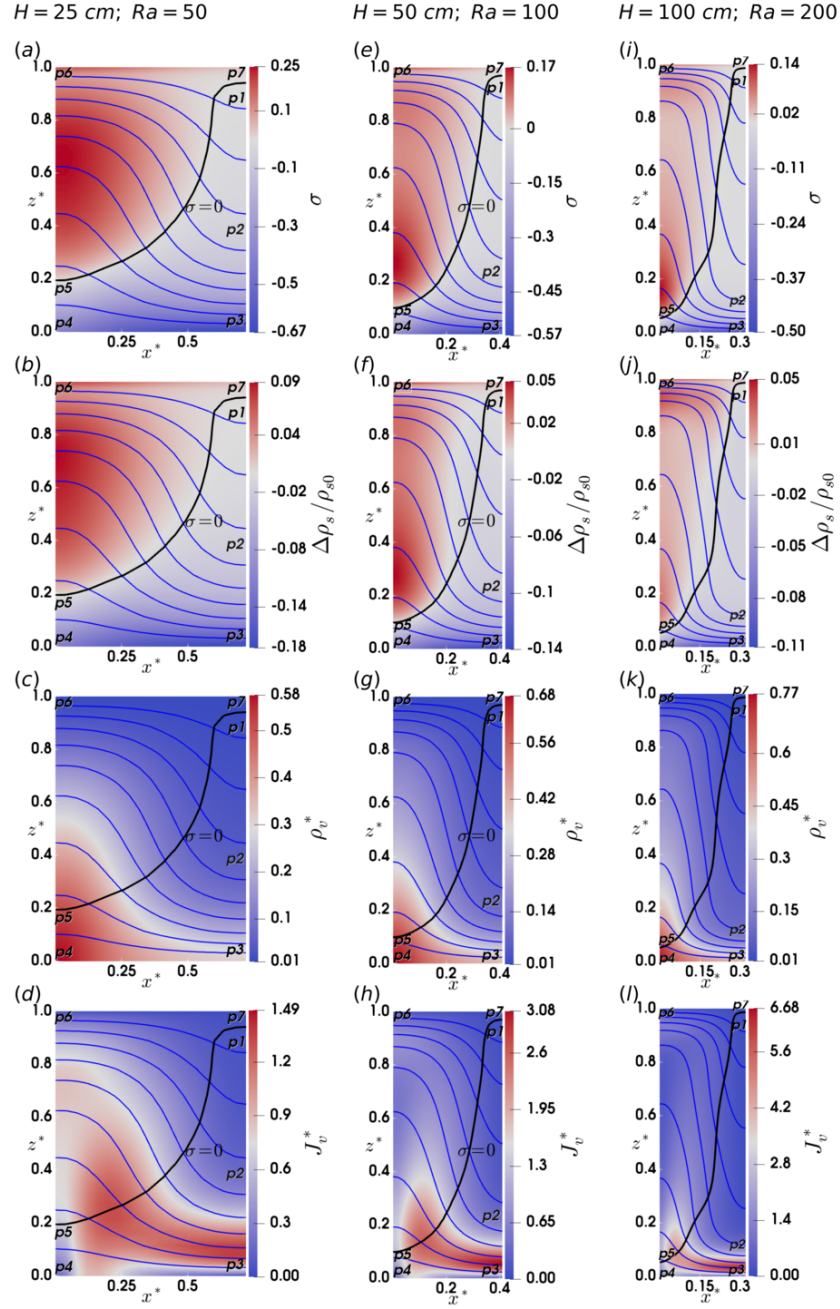
Figure 2.7: Simulated two-dimensional plots after a week of simulation for the saturation degree $\sigma$, the snow density change $\Delta\rho_s/\rho_{so}$, the water vapor density $\rho_v^* = \langle\rho_v\rangle^g/\rho_{vs_{\text{ref}}}$, and diffusive water vapor flux $J_v^* = \langle J_v\rangle/(D_{va}\rho_{vs_{\text{ref}}}/H)$ for three snow heights $H = 25\ cm\ (Ra = 50)$, $H = 50\ cm\ (Ra = 100)$, and $H = 100\ cm\ (Ra = 200)$. The black line refers to the saturation line where $\sigma = 0$. The isotherm lines for the snow temperature are in blue color which are equally spaced by 5 K.

With almost a constant convective flow velocity, the phase change rate mainly reacts on the saturation vapor density gradient, which itself is related to the temperature and temperature gradient, $d\rho_{v,s}/dz \propto \rho_{v,s} \times dT/dz$. In this respect, the sublimation zone is not vertically uniform in downward flow and may be split into three parts:

(i) for the cold region between p1 and p2, both temperature and its gradient are much smaller compared to the bottom region, resulting in much smaller phase change rate and thus a smaller value for oversaturation $\sigma$ just around -0.05 as shown in figure 2.6a.

(ii) the warmer region between p2 and p3, with a much larger temperature and temperature gradient than the first region (figure 2.5d), has a much larger sublimation rate as shown for the oversaturation $\sigma$ in figure 2.5a and for the snow density change $\Delta\rho_s$ in figure 2.5b. Also, it should be noted that the downward convective flow towards the bottom zero-flux boundary and also the large sublimation rate in the bottom region both cause a local concentration of the water vapor to increase the vapor density gradient. This is the reason of the larger upward diffusive flux in the bottom region as shown in figure 2.6d.

(iii) in the horizontal flow of the bottom region, from p2 and p3 to p4 and p5, the sublimation rate (represented by the saturation degree $\sigma$ and also the snow density change $\Delta\rho_s$ in figure 2.6) decreases as the saturation vapor density gradient decreases along with the temperature gradient. This can be seen by comparing the subplots of figure 2.5 at the bottom region between the downward and upward flows. It should be noted that the bottom region between p4 and p5, has the highest water vapor content shown in figure 2.6c. This is a result of flow advection and local sublimation.

Similarly, the phase change regime for the upward flow of the chosen convection cell is analyzed as follows:

(i) in the bottom region between p4 and p5, the convective flow transports and concentrates the vapor content upward, trying to reduce the vapor content and magnitude of its gradient in upstream flow, while the sublimation counteracts the convection effect by adding vapor content to upstream flow, causing a more linear vapor profile.

(ii) in the deposition zone between p5 and p6, the effect of the upward flow is to transport all the vapor towards the top, making the upstream flow devoid of vapor. But, this time, the deposition process counteracts the convection effect by removing water vapor from the upstream flow as can be seen from comparing the water vapor content shown in figure 2.6c. Finally, the opposite effects of the upward convection and deposition processes form an almost linear vapor profile with a negative slope. It should be noted that for the region close to the top boundary, because of the zero flux BCs, there is still a slight vapor density gradient and this causes an upward diffusive flux a bit larger in that region compared to the upstream flow in the middle of the domain (shown in figure 2.6d).

(iii) in the horizontal flow on the top region, as the flow goes from p6 to p7 and p1, the

saturation vapor density gradient decreases because both temperature and temperature gradient decrease, along with the fact that the magnitude of saturation degree decreases. This can be seen by comparing the subplots of figure 2.5. The deposition region of the downward flow has the minimum phase change rate (looking at figure 2.5a for the saturation degree $\sigma$ and also figure 2.5b for the snow density change $\Delta \rho_s$) due to the minimum saturation vapor density gradient in the convection cell shown in figure 2.5c. As the water vapor of the neighboring upward flows is constantly consumed to reach the deposition zone in the downward flow, this region has the lowest vapor content as shown in figure 2.6c.

We compare the deposition zone between p5 and p6 to the sublimation zone at the same non-dimensional heights. While both regions have more or less the same temperature gradient except for the regions close to the boundaries (comparing figure 2.5d with i), the deposition zone has a larger saturation vapor density gradient (comparing figure 2.5c with h) because of its higher temperature. This results in a larger magnitude for the phase change rate (comparing figure 2.5b with g), saturation degree (comparing figure 2.5a with f), and the saturation degree gradient in the deposition zone. However, compared to the bottom sublimation zone between p2 and p3, both the temperature and its gradient in deposition zone between p5 and p6 are much smaller. Thus, the phase change rate is higher in the sublimation zone. As shown in figure 2.6a for the saturation degree and also in figure 2.6b for the snow density change, this is the reason why there is a vertical effective deposition zone with a smaller saturation degree less than around 0.2 while the effective sublimation zone is horizontal in the bottom region with the saturation degree ranging from -0.05 to -0.9.

### 2.5.2 Horizontal displacement of convection cells

In natural convection without phase change in the porous medium, and with moderate Rayleigh number, the convection cells are fixed and are not moving horizontally in the domain. This is not the case when there is phase change and therefore density and porosity changes in the snowpack. This is because the convection cells induce heterogeneity in the snow porosity due to spatially varying phase change, which causes the momentum to be horizontally imbalanced. This temporary imbalance in momentum causes a displacement of the convection cells till the momentum again reaches a stable and balanced condition. The local phase change rate determines how fast the induced heterogeneity of the porosity grows in the domain and also how many times the horizontal displacement of the convection cell occurs during the snowpack life time. From what we observed numerically in different snowpacks, the displacement of the convection cells is large enough (in the order of a convection cell and snowpack height) to change locally the sign of both the phase change rate and the flow direction. For instance, a region which was already under the deposition process of an upward flow transforms into a region undergoing sublimation with a downward flow. For different snow heights, the convection cell displacement at four different time snapshots are shown in figure 2.7. At the first time-snapshot i.e. after a week of the simulation (subplots of a, e, and i in figure 2.7), a gray column is used between two neighbor cells as a fixed reference

position to compare the cell displacement between time snapshots. Considering the phase change pattern analyzed for a convection cell in section 2.5.1, the effects of the convection cell displacement are discussed as follows:

The region which was already under an upward flow: (i) the top region of the increased snow density, after the convection cell displacement, becomes the sublimation zone of a downward flow. As already discussed, the sublimation rate in this region is very small so that it barely reduces the snow density, (ii) the bottom region of the decreased snow density switches to sublimation in a downward flow which has the strongest phase change rate in a convection cell. This reduces the snow density of this region more than before. The region which was already in a downward flow: (i) the bottom region of the decreased snow density now becomes the sublimation zone of an upward flow. Still, the snow density in this region decreases but at a smaller rate than before, (ii) the top region of the almost constant snow density goes under the deposition zone of an upward flow. Obviously, the snow density increases in this region.

The conclusion of these four points is that the lateral displacement of the convection cells leads overall to an almost uniform higher snow density close to the surface and lower snow density at the bottom for the assumed temperature gradient of warmer temperatures at the bottom, which is the usual case in seasonal snow and on sea ice.

### 2.5.3 Effect of snow height, $H$

The three snowpack heights investigated in this section are of small ($H = 25\ cm$ and $Ra = 50$), medium ($H = 50\ cm$ and $Ra = 100$), and large ($H = 100\ cm$ and $Ra = 200$) sizes. With the same initial porosity $\epsilon_g = 0.8335$, the bottom thermal boundary condition of $T = 273.15\ K$, and the temperature difference $\Delta T = 50\ K$, the convective velocity scale, $U_{conv} = \rho \beta \Delta T g K / \mu$, is the same for all snow heights while the conductive velocity scale, $U_{cond} = k_{\mathrm{eff},s} / (\rho_{a_{\mathrm{ref}}} c_{pa} H)$, is different and smaller for the larger snowpack. To analyze the snow height effects on the convective vapor transport, we want to compare the temperature and its gradient, representing directly the saturation vapor density gradient as the main reason of the different phase change rates in snowpacks with the same convective flow velocity scales. The difference in the temperature and temperature gradient profiles between different snow heights is qualitatively discussed as:

(i) for the regions close to the boundaries, represented by the marker points p4, p6, p7 and p3 in figure 2.7: the small snowpack has the largest conductive velocity scale resulting in a more linear temperature profile and the smaller temperature gradient with respect to the non-dimensional snow height, $z^* = z/H$ (comparing the blue isothermal lines in all subplots of figure 2.7). However, in these regions, the smaller snowpack has a larger temperature gradient with respect to the dimensional height, ($dT/dz = 1/H \times dT/dz^*$) and thus as shown in figure 2.5d: $dT/dz|_{H=25cm} > dT/dz|_{H=50cm} > dT/dz|_{H=100cm}$.

(ii) the sublimation zone in the downward flow between markers p1 and p2 in figure 2.7: for

the larger snowpack, the conductive velocity scale is smaller and it has, therefore, a smaller effect against the convective heat transfer. Hence, the convective stretching effect on the temperature profile is stronger, resulting in a smaller - and overall less linear - temperature gradient with respect to both non-dimensional (comparing the blue isothermal lines in all subplots of figure 2.7) and dimensional heights (comparing three plots in figure 2.5d). This is the reason for a larger region with the smaller saturation vapor density gradient (figure 2.5c) and thus phase change rate (represented by snow density change in figure 2.5b). Note that this also refers to a smaller area between markers p2 and p3 (p3 is located where $|\sigma = 5\%|$) where the phase change rate is significant. In other words, the larger the snowpack, the smaller the area in which the saturation degree magnitude is greater than 5%, meaning that it has a smaller significant sublimation area in percentage compared to the smaller snowpacks (comparing the area size between p2 and p3 shown in all subplots of figure 2.7).

(iii) the deposition zone in the upward flow between markers p5 and p6 in figure 2.7: first, it should be noted that even though the larger snowpack has a smaller and less significant sublimation area, but due to its larger size, it has cumulatively more water vapor accumulated in the region between p4 and p5 (comparing the maximum value for the water vapor density in subplots c, g, and k in figure 2.7). This moves the saturation line (black line where $\sigma = 0$) closer to the bottom boundary for the larger snowpack, causing the sublimation zone between markers p4 and p5 to be smaller in a relative sense. For the deposition region above the marker p5 and far from the top boundary, the small snowpack has both a more linear temperature profile and thus a more uniform temperature gradient because of its reduced stretching (comparing the blue isothermal lines in all subplots of figure 2.7). This causes a more uniform saturation degree and phase change rate than for the larger snowpacks. On the contrary, the large snowpack has two peaks in the saturation degree with an almost saturated area in between (figure 2.7i). Its first peak is located in the lower half of the domain while the second one is located close to the top boundary. For the medium snowpack shown in figure 2.7e, the distance between these peaks is smaller, meaning that it has a smaller area of almost zero saturation degree compared to the large snowpack.

As introduced in section 2.5.2, convection cells move laterally due to changes in porosity distribution (induced heterogeneity) and its feedback on the flow. The process of breaking the symmetry in the system is first a continuous process responding to higher local phase change rate and then it relaxes to a steady state with a decreasing lateral movement of convection cells. A plausible explanation for these two stages is given as follows:

To support our hypothesis, the magnitude of different terms in momentum equation as well as the flow velocity are shown in figure 2.8 for eighteen days before the onset of lateral movement of convection cells. We follow a path between the marker points p1 - p7 (figure 2.3) first up, then right, then down and finally left within the cell. For the top region in the upward flow, comparing the case with phase change to the same case without phase change, the intrinsic permeability decreases exponentially with increase in snow density (equation (2.9)) leading to a higher viscous resistance factor i.e. $\mu/K$ while the viscous resistance force itself is almost
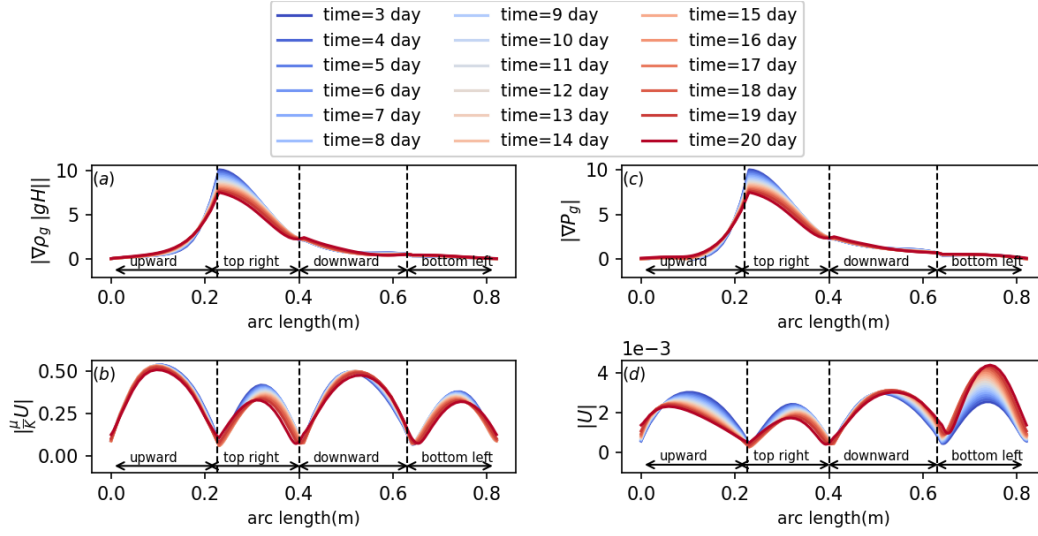
Figure 2.8: The magnitude of each term in momentum equation (2.8) as well as the flow velocity for eighteen days before lateral movement of convection cells along the path of a convection cell. Using the marker points introduced in section 2.5.1: upward between markers p4 and p6, top-right between markers p6 and p7, downward between markers p7 and p3, and bottom-left flow between markers p3 and p4.

unaltered (figure 2.8b for upward flow). This increased resistance factor causes a reduced flow velocity of approximately 25% before lateral movement of convection cells begins(figure 2.8d for upward flow). The reduced flow velocity has a direct feedback on the temperature gradient and thus both gas density gradient and dynamic pressure gradient forces are decreased also by 25% (figure 2.8a and c for upward and top-right flow). At the bottom reduced density causes almost 100% of velocity increase (figure 2.8d for bottom-left flow). The flow-blocking effect in upward flow (deposition zone) counteracts the significantly increased flow velocity at the bottom. The former tends to counteract the convection, while the latter tries to keep the convection cell at its location. However, for the lateral displacement of convection cells, this partially stable system needs a disturbance in the momentum (spatiotemporal chaos (Egolf et al., 2000)). The flow changes the path towards the lower density section on the top next to the initial deposition zone. This finally leads to the intuitive result that cells move laterally to avoid regions of higher density. The displacement decreases over time and a new symmetry in density distribution is established.

To indicate temporal variations in lateral displacement of convection cells through the two stages explained above, the time series of temperature for some fixed points are used as $T(t, \vec{r}_{\text{fp}})$. These fixed points with position $\vec{r}_{\text{fp}}$ are located on the peak of temperature $(T_c + T_h)/2$ (in the upward flow) for all convection cells formed in the system (the initial temperature is $(T_c + T_h)/2$). As the convection cells move laterally, the temperatures probed by these fixed points decreases, indicating how fast and large the cells are moving through phase 1 and 2. The average of these temperatures over all fixed points, $\overline{T} = \sum T(t, \vec{r}_{\text{fp}})/N_{\text{fp}}$, is shown in figure 2.9.

As shown in these plots, the smaller the snowpack, the faster transition from the stage 1 to stage 2 (from a continuous and persistent drift to a steady state with negligible convection cell movement) because of its larger snow density change. One more interesting point we found only for the small snowpack is that the convection cell size increases in accordance with stage 1 of convection cell movement (figure 2.10). From what we observed, during the stage 1 of the cell displacement, the neighboring convection cells are merging leading to a larger averaged cell sizes. This is because the convection cells are not moving laterally with the same rate direction. Each step change in the cells size for the small snowpack (figure 2.10) corresponds to merging a pair of neighbouring cells. For a medium snowpack, after a period of slow displacement of convection cells, we observe a sudden change in $\overline{T}$, meaning a fast transition from stage 1 to stage 2. For the larger snowpack, it has only a much longer stage 1 and its transition to stage 2 such that it keeps slowly moving the convection cell without reaching a complete new steady state and symmetry in porosity distribution.

For the range of moderate Rayleigh numbers when we have stable convection cells (Caltagirone, 1975), the number of convection cells and the average cell size is directly related to the Rayleigh number such that the higher the Rayleigh number, the more slender cells are formed in the domain (Holzbecher, 2019)) as shown in figure A.5 in appendix A.3. The sensitivity analysis shows the domain width has a small effect on the averaged cell size for the case without phase change. For the case with phase change, the convection cell size has more variation by changing the domain width (figure A.6 in appendix A.3). However, the laterally averaged snow density change is statistically the same and independent on the domain width as shown in figure A.4 in appendix A.3. It should be noted that the cell size is calculated as the distance between maximum of temperature level in upward flow and its minimum in the downward flow of a convection cell. Accordingly, the initial cell size after a week of simulation, for the small, medium, and large snowpacks is around $0.7H$, $0.4H$, and $0.3H$ as shown in figures 2.11a, e and i respectively. Given the fact discussed earlier that the small snowpack has a larger relative size (or extent) for the sublimation and deposition zones which are stronger than for the larger snowpacks, the induced heterogeneity occurs faster and earlier such that the initial convection cell (formed after a week shown in figure 2.11a) moves laterally around $0.8H$ during the first month of the simulation (comparing figure 2.11b and figure 2.11a). The horizontal displacement is about 14% greater than the initial cell size. For the medium snowpack during the first month, the convection cell moves laterally only around $0.15H$ (37.5% of its initial convection cell from comparing figure 2.11e and figure 2.11f). During the second month of the simulation, the small snowpack reaches an almost stable horizontal porosity distribution to have a small convection cell displacement around $0.1H$ (figure 2.11c compared to figure 2.11b) and also the convection cells are almost fixed till the end of the simulation (figure 2.11d compared to figure 2.11c). This is different for the medium snowpack as the induced heterogeneity gets large enough during the second month to trigger a significant displacement of around $0.6H$ (comparing figure 2.11g and figure 2.11f). Note that the convection cells are almost stable and fixed for the rest of simulation ( figure 2.11h compared to figure 2.11g). The large snowpack has the smallest and slowest convection cell displacement because of its
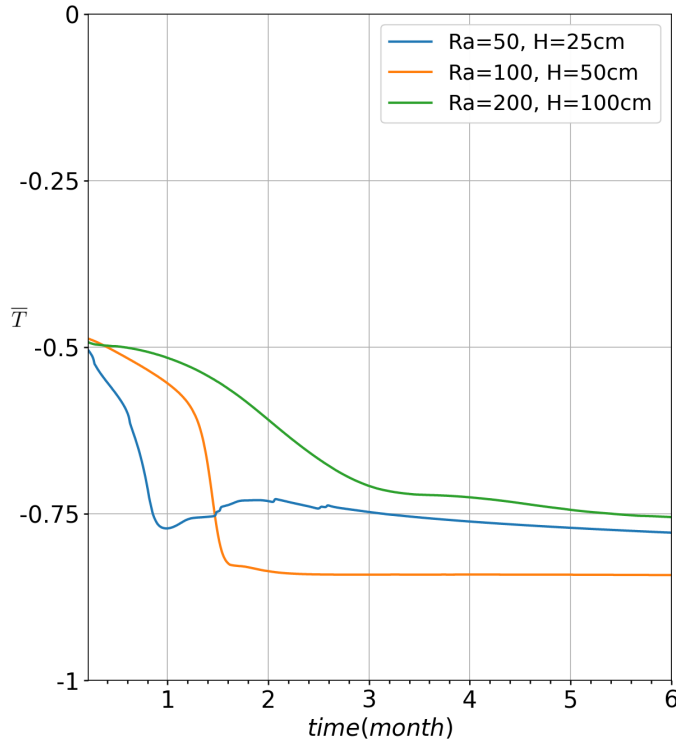
Figure 2.9: Temporal variations in lateral displacement of convection cells using the averaged probed temperature $\overline{T}$ as discussed in section 2.5.2 for different snow heights.

smaller and less significant phase change area (non-dimensional size) compared to the small and medium snowpacks. It has almost the same displacement around $0.05H$ during both the first and second month of the simulation (comparing figure 2.11i, j, k, and l).

For a general comparison of convective water vapor transport between different snow heights, the time-series of snow density change, the standard deviation of snow density change, snow temperature, and the saturation degree are shown in figure 2.12 based on a lateral average for each level of $z$. The non-dimensional thickness of the low density 'weak layer' at the bottom of snowpack, which has the minimum possible density (based on the threshold of 95 % set for the porosity above which the phase change is stopped) is around $0.2H$, $0.1H$ and $0.05H$ for small, medium and large snowpacks respectively. It takes 5, 7, and 11 weeks to reach for the first time the minimum snow density at the bottom for the small, medium, and large size snowpacks respectively. The small snowpack has a pronounced density change on top for which 46 % of its top region experienced a density increase of more than 25 %. However, only about 30 and 10 % of the top region experienced a density increase of more than 25% for the medium and large snowpacks, respectively. The maximum increase in density on top is 57% ($87 \, \text{kg} \, \text{m}^{-3}$), 47 % ($72 \, \text{kg} \, \text{m}^{-3}$), and 29% ($45 \, \text{kg} \, \text{m}^{-3}$) for small, medium and large snowpacks respectively. It is shown in figure 2.11d that through the upward flow within convection cells, a patch with minimum possible density (MPD patch) is formed in the weak layer. Such MPD
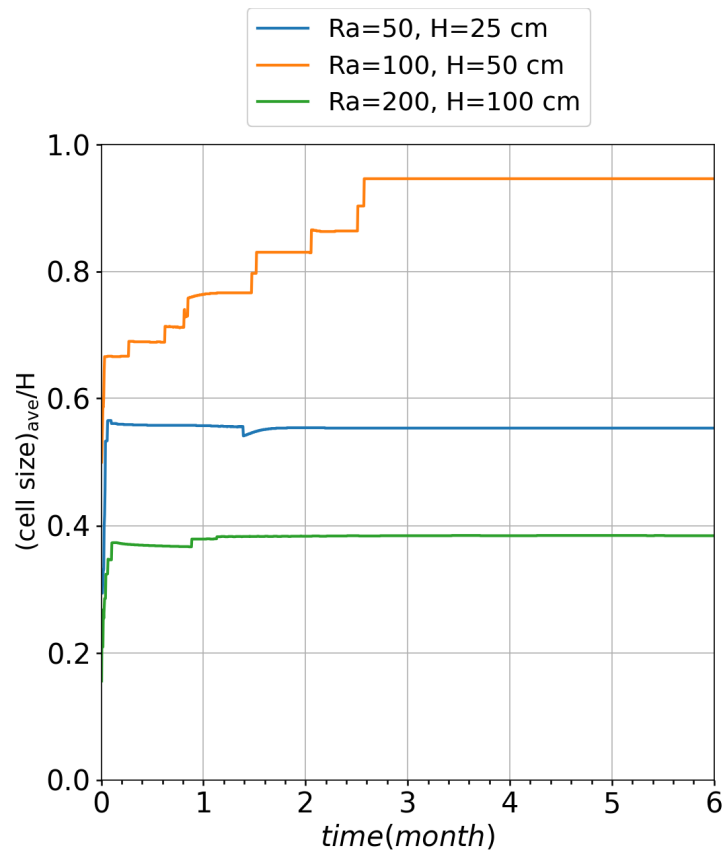
Figure 2.10: Comparison of the normalized convection cell size for different domain width for the case with phase change.
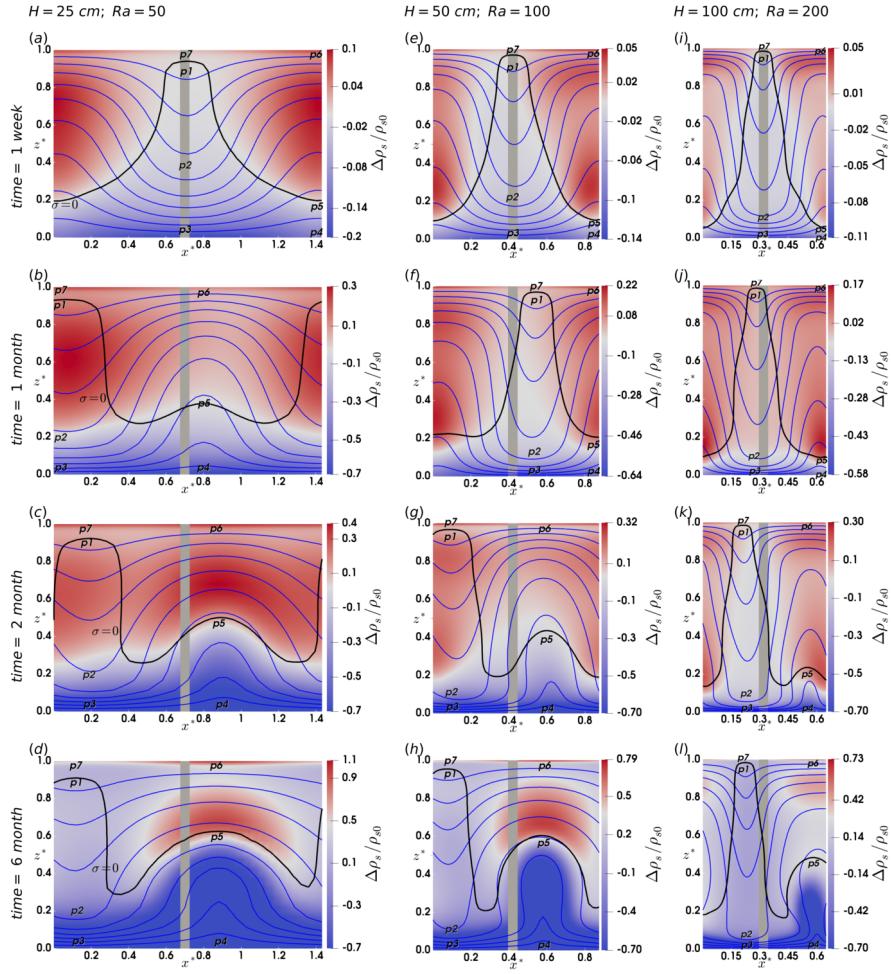
Figure 2.11: Simulated two-dimensional plots for snow density change $\Delta\rho_s$, showing the the horizontal displacement of the convection cells at four time snapshots for different snow heights. The gray column is used as the reference to measure the horizontal displacement between the different time snapshots. The black line refers to saturation line where $\sigma = 0$. The isotherm lines for the snow temperature are in blue color which is equally spaced by 5 K.
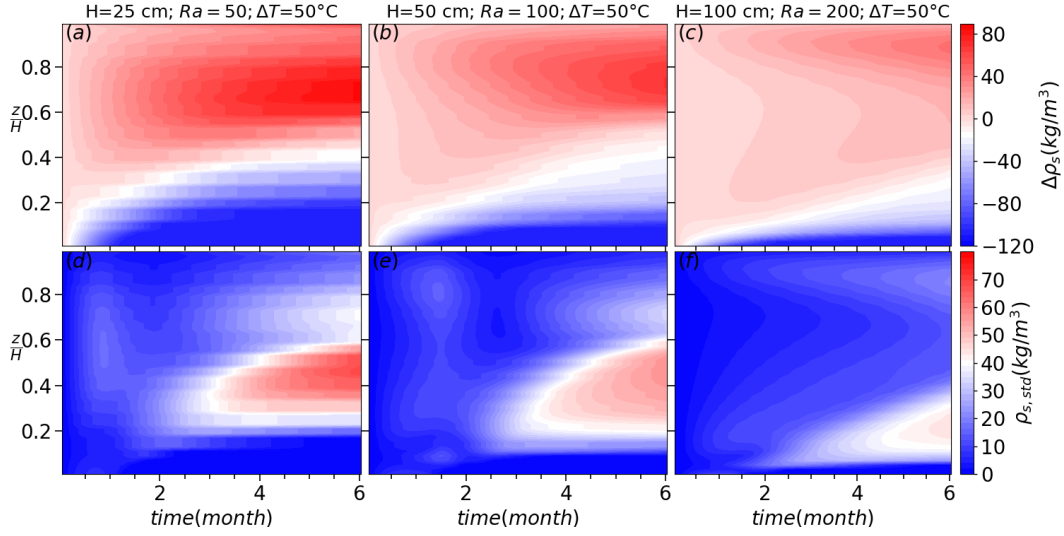
Figure 2.12: The time-series of snow density change $\Delta\rho_s$ and the standard deviation of snow density change $\rho_{s,std}$ for different snow heights.

patches are larger for the small snowpacks such that their vertical size may reach $0.5H$. As discussed earlier, this is due to the larger sublimation rate for the small snowpack that the weak layer at the bottom forms faster and it gets thicker at the end of simulation compared to the larger snowpacks. For the same reason, the small snowpack has the largest standard deviation of snow density change, which amounts to about $70 \text{ kg m}^{-3}$, while it is around 50 and $40 \text{ kg m}^{-3}$ for the medium and large snowpacks respectively.

### 2.5.4  Effect of the temperature difference, $\Delta T$

Setting the same initial porosity $\epsilon_g = 0.8335$, the bottom thermal boundary condition of $T = 273.15 \ K$, and the snow height of $H = 50 \ cm$, three cases with different temperature differences are investigated in this section as: the case of high $Ra$ ($\Delta T = 50$, $Ra = 100$), medium $Ra$ ($\Delta T = 37.15$, $Ra = 75$), and the low $Ra$ ($\Delta T = 25$, $Ra = 50$). In contrast to the previous section, here, the conductive velocity scale is almost the same in all cases while the larger $\Delta T$ (the higher $Ra$) leads to a larger convective velocity scale. Thus, both the saturation vapor density gradient and the convective flow velocity should be considered simultaneously when analyzing the difference in the snow density change:

(i) in the downward flow, the region from the top boundary to the non-dimensional height level of $z^* = 0.25$: even though the larger $\Delta T$ and $Ra$ favors more convective stretching and a smaller temperature gradient, the larger $\Delta T$ over the same snow height dominates to cause a larger temperature gradient (comparing three plots in figure 2.5n). Also, it is colder than the other cases with a smaller saturation vapor density gradient (figure 2.5m). Comparing the case of highest $Ra = 100$ with the lowest $Ra = 50$, we found that the highest $Ra$ has a larger snow density change as its convective flow velocity is higher (figure 2.5o). Moreover, the difference

in the snow density changes between two cases gets larger as the flow penetrates further down since the convective flow increases in strength. However, for the case of medium $Ra = 75$, the effect of the larger saturation density gradient compensates the effect of its lower convective flow velocity to have more or less the same snow density change compared to the case of higher $Ra$.

(ii) in the downward flow, the region close to the bottom boundary: the case of higher $Ra$ has a larger snow density change (figure 2.5l) because of its stronger saturation density gradient (figure 2.5m) and the higher convective flow velocity (figure 2.5o). Note that the larger convective temperature stretching and also the larger $\Delta T$ within the same snow height both lead to a stronger saturation vapor density gradient for the case of higher $Ra$.

(iii) in the upward flow, the region from the top boundary to the non-dimensional height level of $z^* = 0.25$: Similar to what was previously analyzed for the downward flow, even with a larger temperature gradient (figure 2.5s), the case of higher $Ra$ has a smaller saturation vapor density gradient (figure 2.5r) as it is colder in this region. However, its higher convective flow velocity causes a larger snow density change and saturation degree compared to the lowest $Ra$ case. Comparing to the medium $Ra$ case, the case of high $Ra$ has almost the same snow density change in the upper half of the domain while a larger snow density change in the lower half of the domain (figure 2.5q). This is because in the lower half of the domain, both the convective flow velocity (figure 2.5t) and the saturation vapor density gradient are larger in the high $Ra$ case.

(iv) in the upward flow, the region close to the bottom boundary: for the case of higher $Ra$, the larger temperature gradient because of larger $\Delta T$ over the same snow height and thus the stronger saturation vapor density gradient and also higher convective flow velocity all cause a larger snow density change compared to the lower $Ra$ cases.

The convection displacement at four different time snapshots are shown in figure 2.13. During the first month of the simulation, by comparing figure 2.13b with figure 2.13a for the low $Ra$ case and also figure 2.13e with figure 2.13f for the medium $Ra$ case, we found that for both low and medium $Ra$ cases, no convection displacement is observed while the case of high $Ra$ experiences a displacement of around $0.2H$ because of its larger snow density change (the larger heterogeneity) at the bottom and middle of snowpack (comparing figure 2.13j with figure 2.13i). During the second month of the simulation, the low $Ra$ case still has almost no convection displacement (figure 2.13c compared to figure 2.13b) while the medium $Ra$ case has a large enough heterogeneity in the snow density to have a displacement of around $0.2H$ (figure 2.13g compared to figure 2.13f). In this period, for the case of high $Ra$, the convection displacement of the cells gets even larger than during the first month (figure 2.13k compared to figure 2.13j) and the cells are almost fixed till the end of the simulation (figure 2.13l compared to figure 2.13k). For the cases of the low and medium $Ra$, large enough heterogeneity in the snow porosity is only achieved during the last four months of the simulation and triggers a significant convection cell displacement (comparing figure 2.13d with figure 2.13c for the low

$Ra$ case and also figure 2.13g with figure 2.13g for the medium $Ra$ case). Obviously, this is faster for the case of medium $Ra$ as its snow density change due to convective vapor transport is stronger than the case of low $Ra$.

The time-series of snow density change and the standard deviation of snow density change is shown in figure 2.14 for a general comparison of convective water vapor transport between three temperature differences. To reach for the first time the minimum snow density at the bottom, it takes 16.5, 8.5, and 6 weeks for the low, medium and high $Ra$ cases, respectively. After six months of the simulation, the non-dimensional thickness for the low density 'weak layer' with minimum possible density for all cases is around $0.1H$. However, above this weak layer, there is another low density layer till the non-dimensional height level of 0.2, 0.3, and 0.4 for the low, medium and high $Ra$ cases respectively, in which the density decreases almost linearly due to phase change from 15 % (at top of the second weak layer) to 70 % (at top of the first weak layer). The medium and high $Ra$ cases have almost the same pattern for an increase in density on top with maximum values of 42.8 % (65.4 kg m$^{-3}$) and 47.4% (72.3 kg m$^{-3}$) respectively. However, the low $Ra$ case has two peaks for the density increase of which the first one is only 23.8 % (36.38 kg m$^{-3}$) while the second peak is very close to the top boundary with the significant value of 44 % (67.4 kg m$^{-3}$).

### 2.5.5 Scaling and order of magnitude analyses

#### 2.5.5.1 Scaling argument

Non-dimensional governing equations and relevant scaling factors are introduced in detail in appendix A.6. As shown in normalized equations, the controlling parameters for heat and mass transfer are $Ra$ and $M = (6\epsilon_i Sh_{\text{ref}})/(d_p^{*2} RaLe_m)$. A complete scaling is achieved when the influence of initial and boundary condition disappears (Barenblatt, 1996). This would be the case with a system with only heat transfer (and no phase change) since the the thermal boundary conditions are mapped from $[T_c, T_h]$ to $[-1, 0]$. In this case, the bottom/top thermal boundary layer thickness is only scaled and dependent on Rayleigh number (the non-dimensional temperature and temperature gradient are completely scale-able and dependent on $Ra$). However, for the case with phase change, the scaling for water vapor distribution is not complete and it depends on both $Ra$ and bulk temperature difference. Using the Clausius-Clapeyron's law for $\rho_{vs} = \rho_{vs_{\text{ref}}} \exp [A(1/T_{\text{ref}} - 1/T)]$ where $A = L_{iv} m/(\rho_i k)$, $m$ is the mass of a water molecule and $k$ is the Boltzmann's constant, we show the dependency of $\rho_{vs}^*$ and $\nabla^* \rho_{vs}^*$ on $\Delta T$ and the reference temperature $T_{\text{ref}}$ as:

$$\rho_{vs}^* = \frac{\rho_{vs}}{\rho_{vs_{\text{ref}}}} = \exp \left[ A\Delta T \frac{T^*}{T_{\text{ref}}(T^* + T_{\text{ref}}/\Delta T)} \right] \tag{2.24a}$$

$$\nabla^* \rho_{vs}^* = \frac{\nabla \rho_{vs}}{\rho_{vs_{\text{ref}}}/H} = \frac{d\rho_{vs}/dT \, \nabla T}{\rho_{vs_{\text{ref}}}/H} = \rho_{vs}^* \nabla^* T^* \frac{A\Delta T}{(T^* + T_{\text{ref}}/\Delta T)^2} \tag{2.24b}$$

77
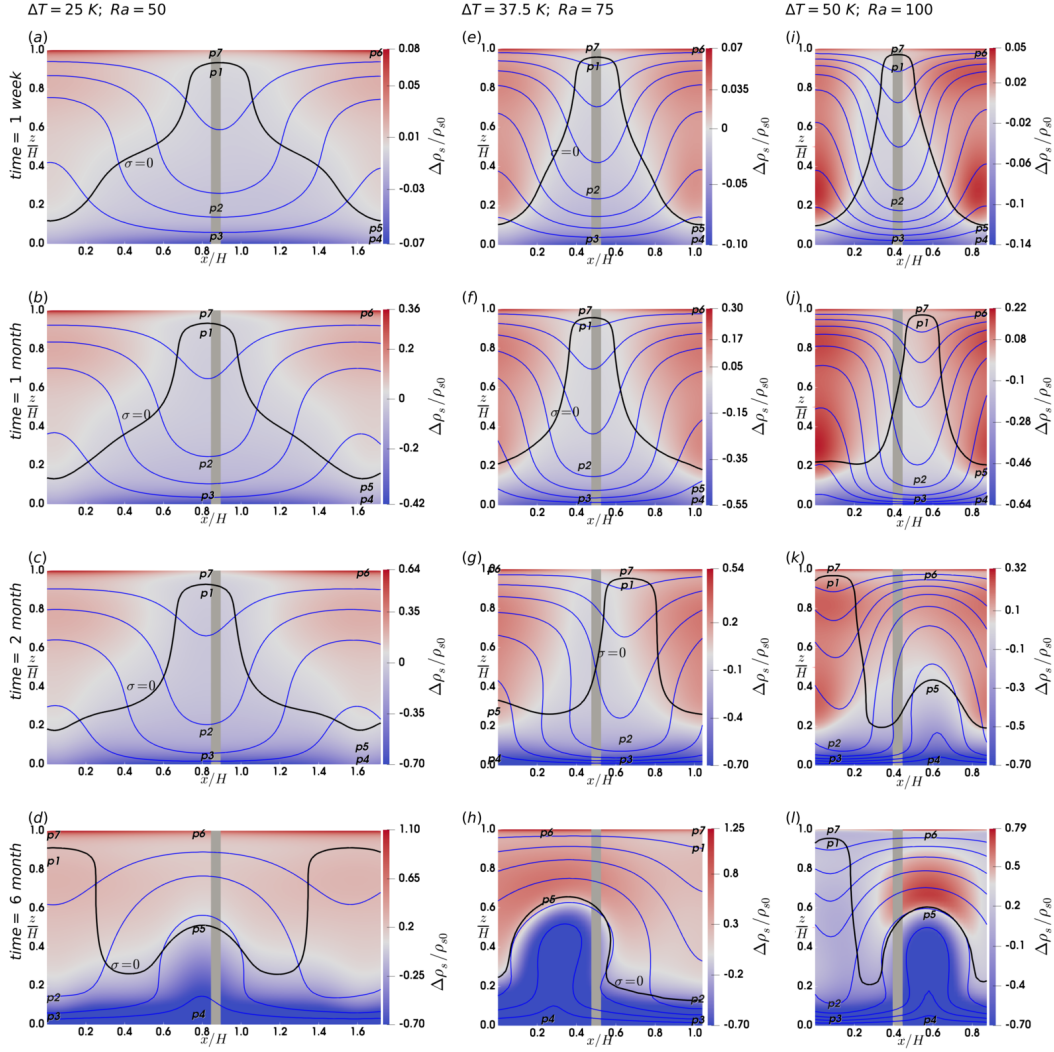
Figure 2.13: Simulated two-dimensional plots for snow density change $\Delta \rho_s$, showing the the horizontal displacement of the convection cells at four time snapshots for three temperature difference of $\Delta T = 25\ K$ ($Ra = 50$), $\Delta T = 37.5\ K$ ($Ra = 75$), and $\Delta T = 50\ K$ ($Ra = 100$). The gray column is used as the reference to measure the horizontal displacement between the different time snapshots. The black line refers to the saturation line where $\sigma = 0$. The isotherm lines for the snow temperature are in blue color which is equally spaced by 5 K.
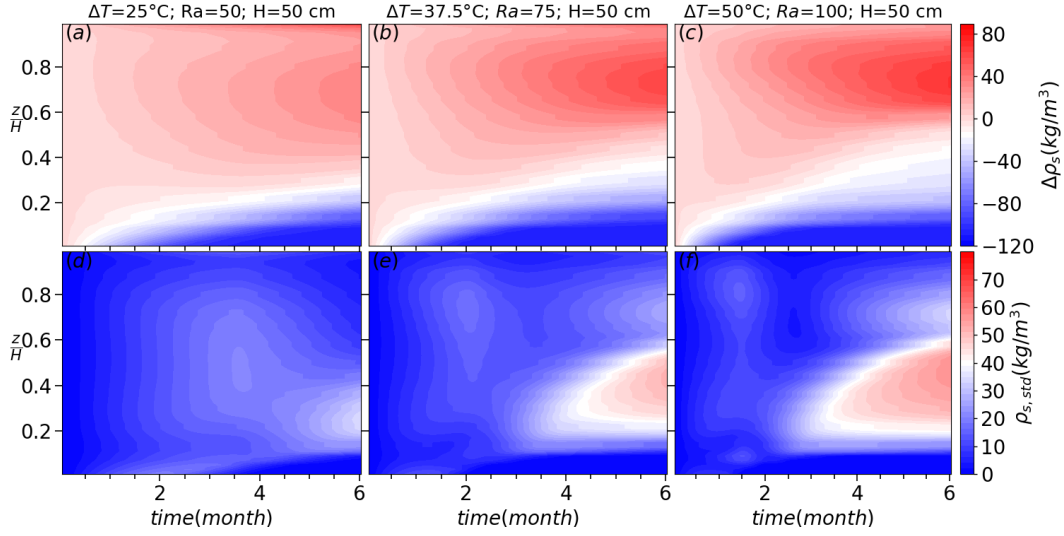
Figure 2.14: The time-series of snow density change $\Delta\rho_s$ and the standard deviation of snow density change $\rho_{s,std}$ for three temperature differences.

The equations (2.24) suggest that phase change behaviour (which is directly connected to the water vapor density gradient as discussed earlier) cannot be completely scaled only by $Ra$ and $M$. This may be shown by comparing two most similar cases for which both $Ra$ and $M$ are the same but the bulk temperature difference is different. As shown in figure 2.15, the non-dimensional porosity change rate and saturation degree are very different. For other cases in which the Rayleigh numbers are the same but with different $M$ (figure 2.17), the deviation and difference between cases is even larger, e.g. comparing figure 2.16 with figure 2.18 for non-dimensional temperature, temperature gradient, diffusive flux and flow velocity. Between the cases with same Rayleigh number, the smaller deviation in non-dimensional temperature(figure 2.17c and h) and temperature gradients (figure 2.17d and i) compared to deviation in diffusive water vapor density gradient (figure 2.17b and g) is directly linked to the relative contribution of phase change terms in energy and mass conservation equations, which will be discussed in the next section. Overall, it appears that $Ra$ is effective in partially but not completely collapsing the non-dimensional profiles.

### 2.5.5.2 Analysis of dominant terms

The contribution of each term in gas and ice energy equations (equations (2.18) and (2.19) respectively) are shown in figure 2.19 and figure 2.20 for the horizontally-averaged profiles and domain-averaged time-series respectively. For the gas energy, the dominant term is convection but comparable with the conduction term. Figure 2.20 shows the relative magnitude as the ratio of each term (magnitude) to the summation of magnitude for all terms. The relative magnitude of convection and conduction are 40% and 35% respectively (figure 2.20c). The heat transfer between phases is comparable to the net of convection and conduction term while it is quite well matched with the ice conduction term (figure 2.20a and c). Its relative
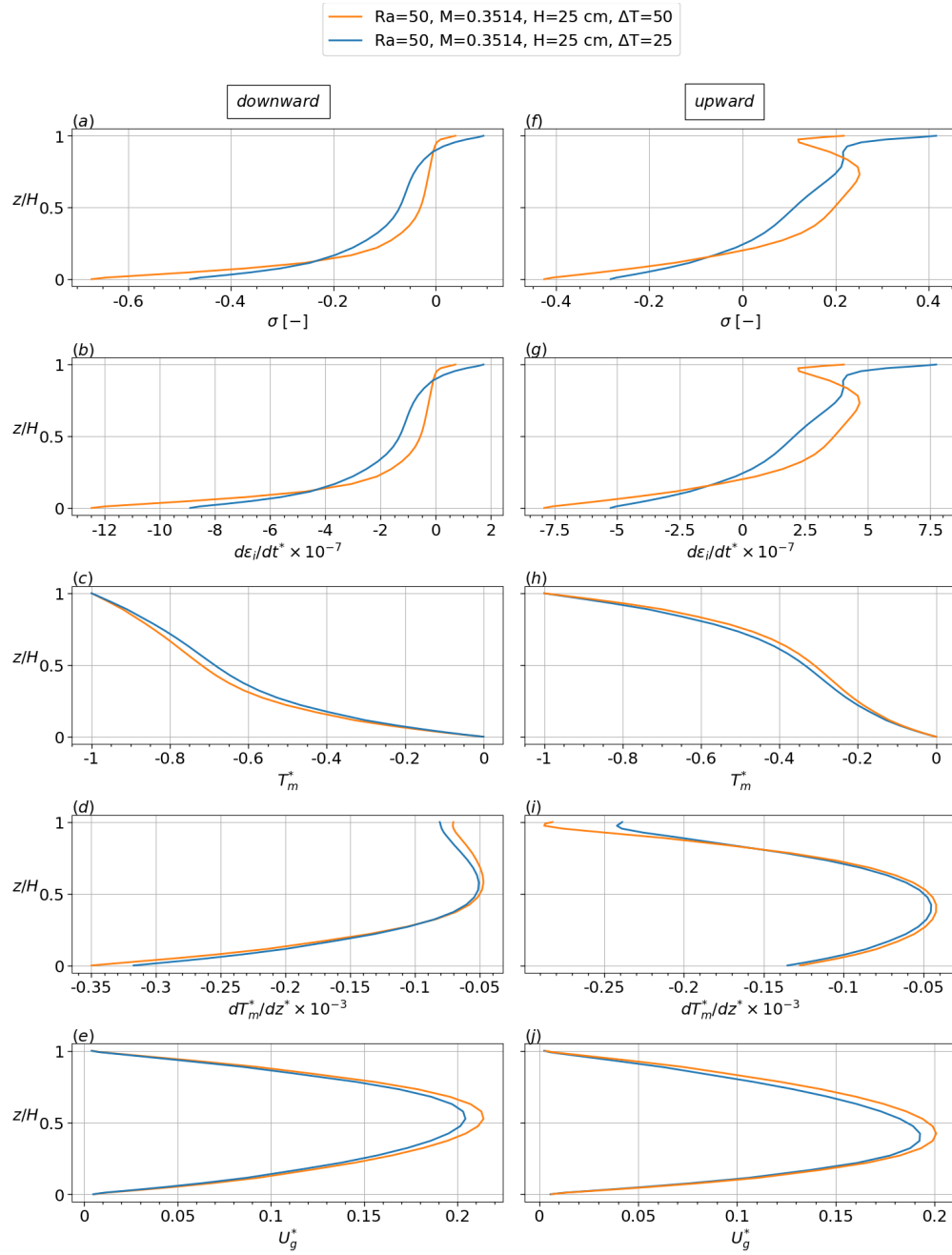
Figure 2.15: Non-dimensional results for two cases with same $Ra = 50$ and $M = 0.3514$ but different bulk temperature difference, $\Delta = 25$ K and $\Delta = 50$ K for: saturation degree $\sigma$, rate of change for ice volumetric content $d\epsilon_i/dt^*$, snow temperature $T_m^*$, snow temperature gradient $dT_m^*/dz^*$, and the gas flow velocity $U_g^*$.
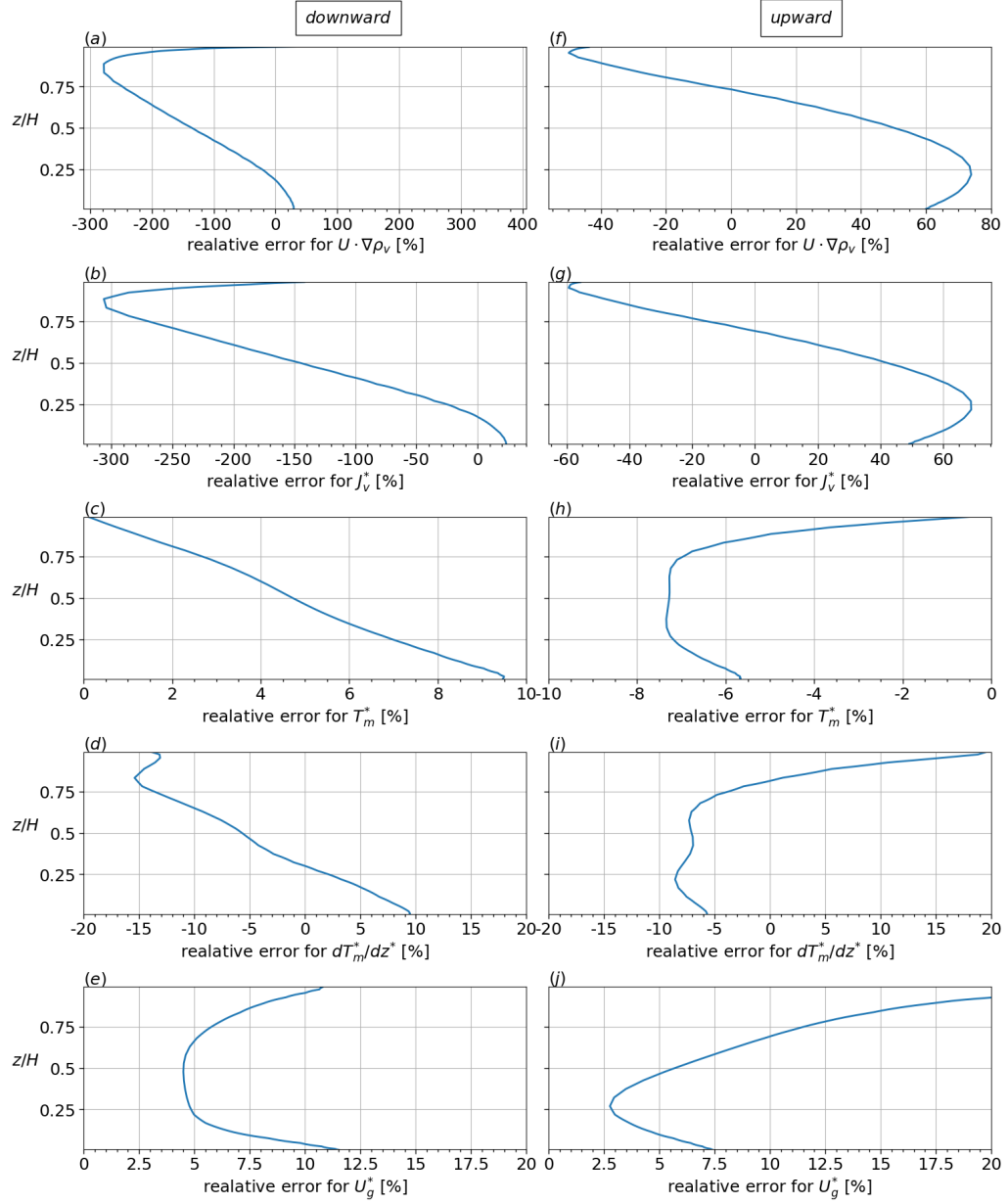
Figure 2.16: The relative error between two cases with same $Ra = 50$ and $M = 0.3514$ but different bulk temperature difference, $\Delta = 25$ K and $\Delta = 50$ K for the dimensionless results as: convective water vapor transport $\nabla^* \rho_v^* \cdot U_g^*$, diffusive water vapor flux $J_v^*$, snow temperature $T_m^*$, snow temperature gradient $dT_m^*/dz^*$, and the gas flow velocity $U_g^*$.
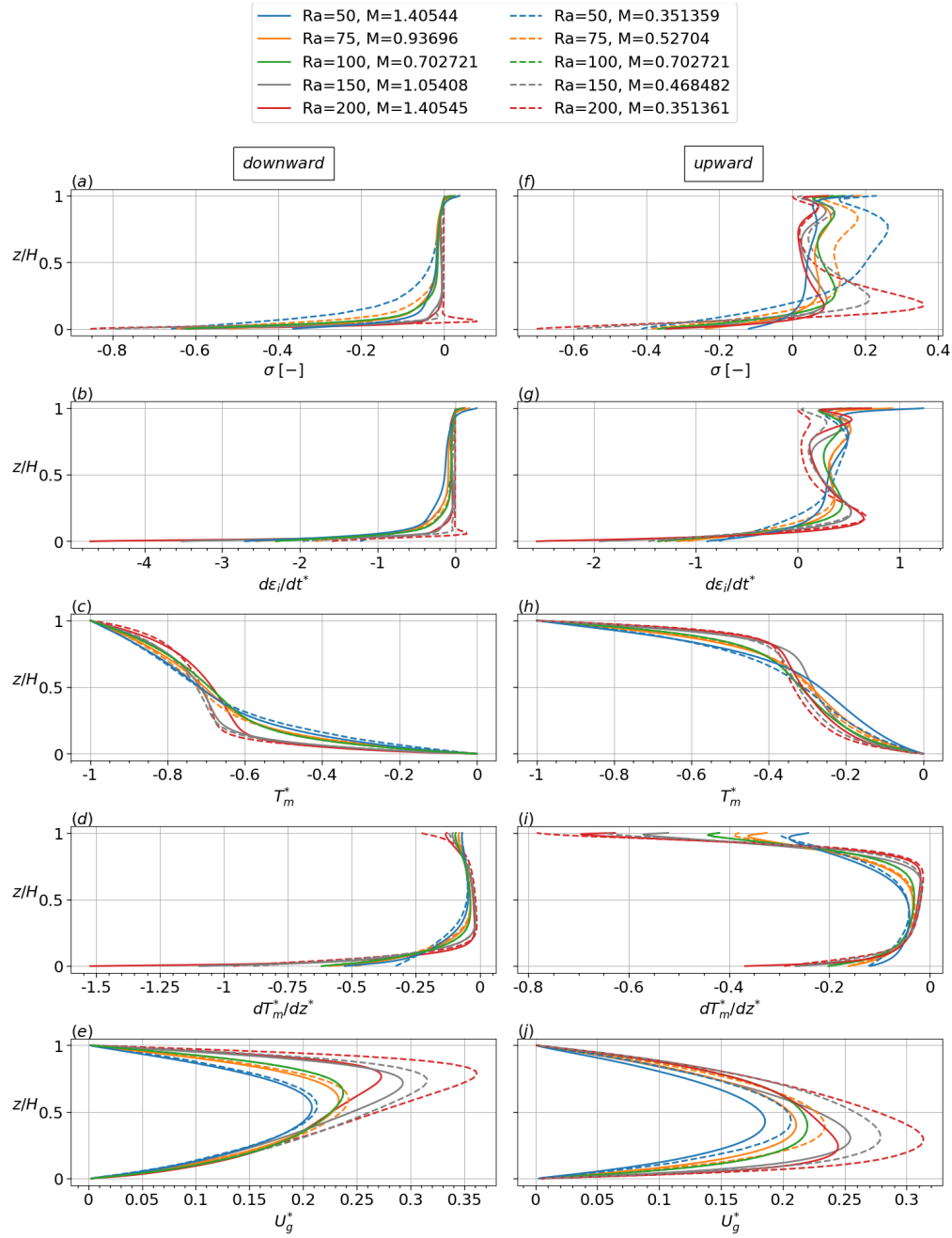
Figure 2.17: Non-dimensional results for saturation degree $\sigma$, rate of change for ice volumetric content $d\epsilon_i/dt^*$, snow temperature $T_m^*$, snow temperature gradient $dT_m^*/dz^*$, and the gas flow velocity $U_g^*$. The cases with the same $Ra$ have the same color in which the solid line is for larger $M$ and the dashed line is for the smaller $M$.
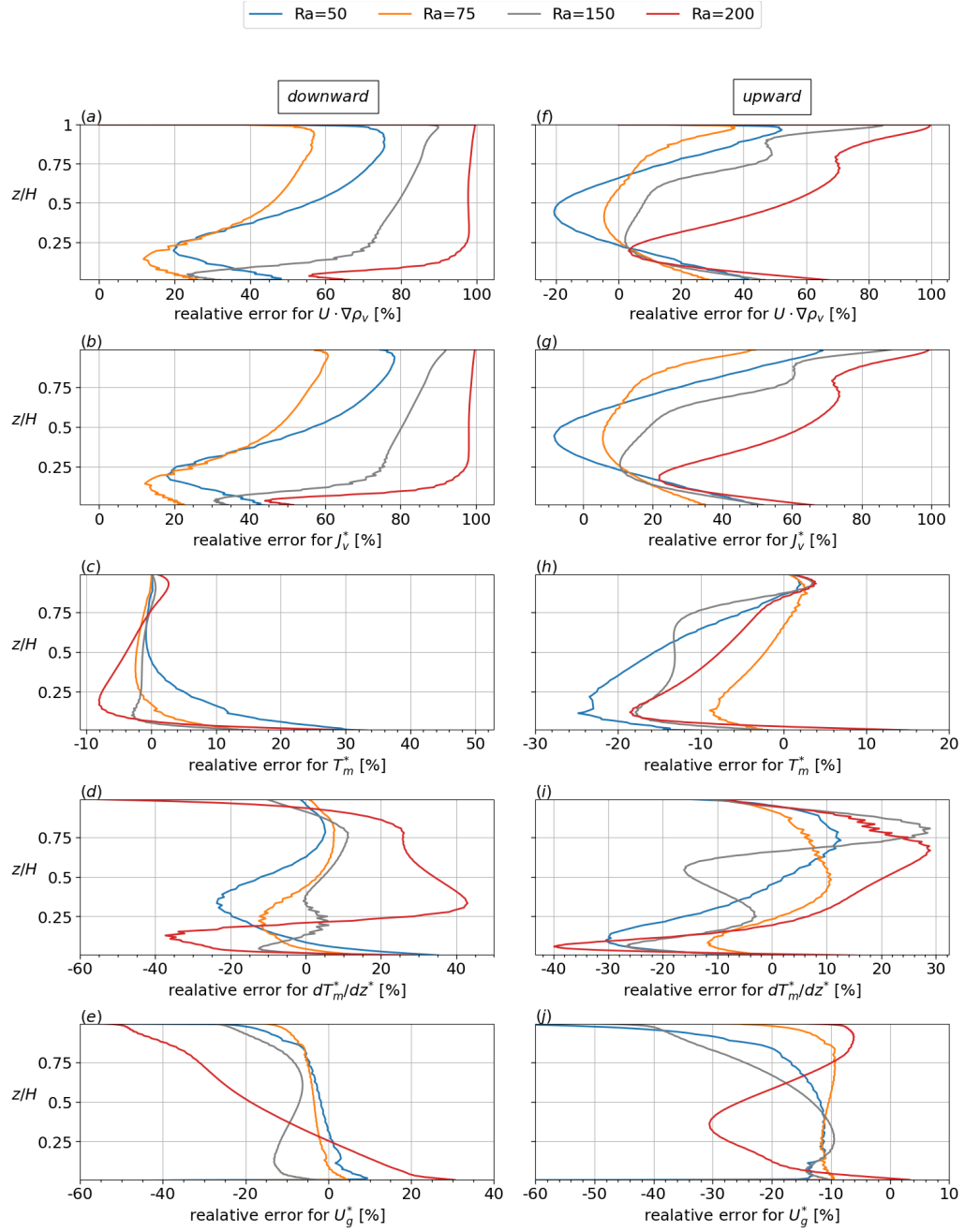
Figure 2.18: The relative error between two cases with the same $Ra$ but different $M$ = shown in figure 2.17 for the dimensionless results as: convective water vapor transport $\nabla^* \rho_v^* \cdot U_g^*$, diffusive water vapor flux $J_v^*$, snow temperature $T_m^*$, snow temperature gradient $dT_m^*/dz^*$, and the gas flow velocity $U_g^*$.
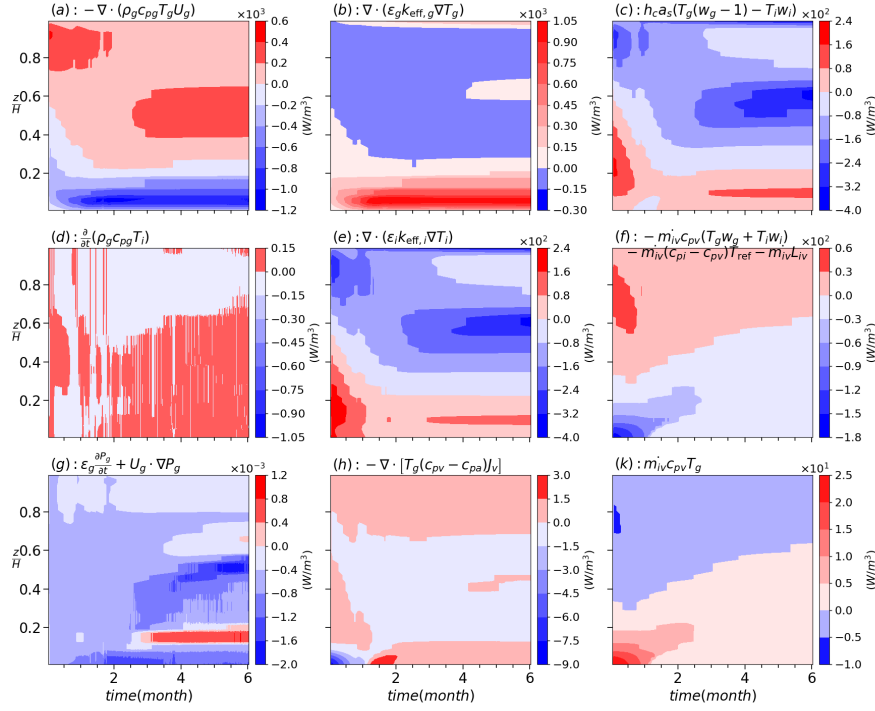
Figure 2.19: The horizontally-averaged time-series for the contribution of each term in equations (2.18) and (2.19) for gas and ice energy equations respectively.
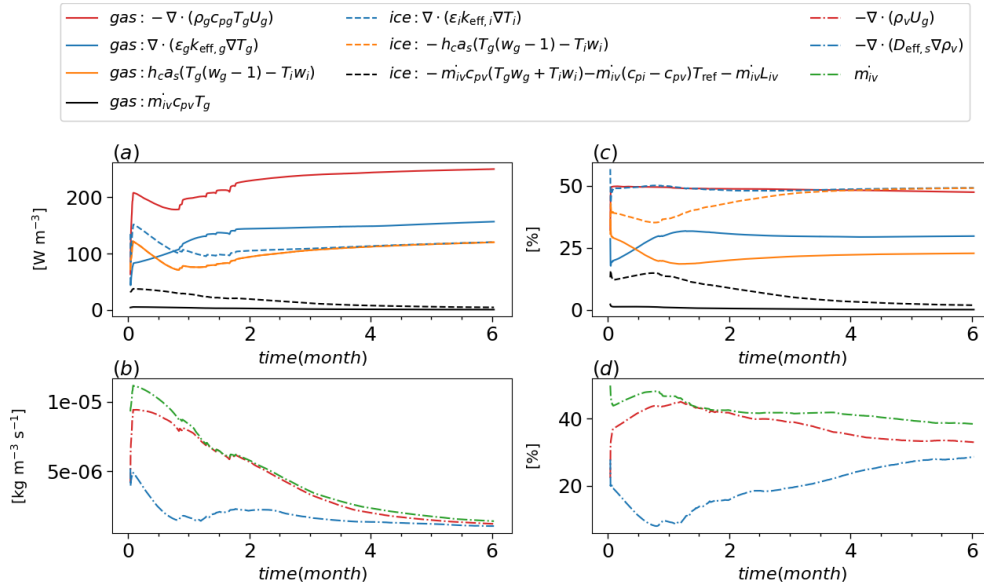


Figure 2.20: The domain-averaged time-series for the contribution and relative magnitude of each term respectively: (a) and (c) for gas and ice energy equations (equations (2.18) and (2.19) respectively), (b) and (d) for mass conservation of water vapor component, equation (2.2)
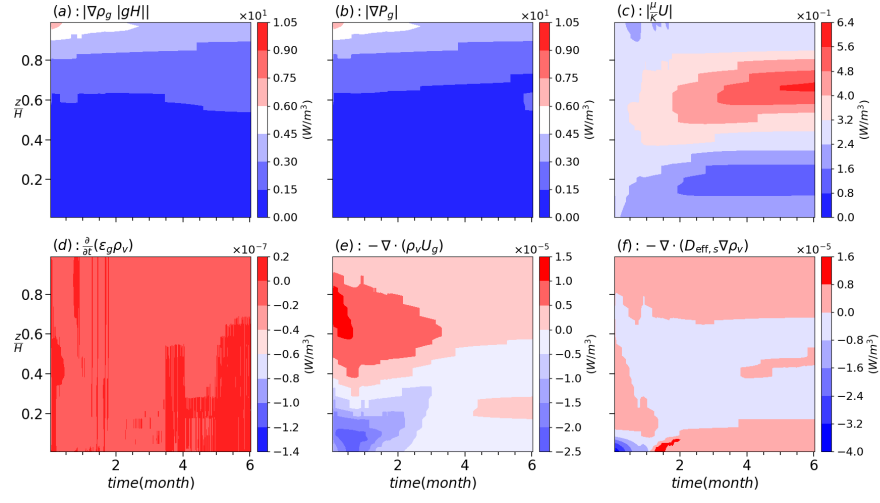
Figure 2.21: The horizontally-averaged time-series for the contribution of each term in equation (2.8) for momentum, and in equation (2.2) for mass conservation of water vapor component.
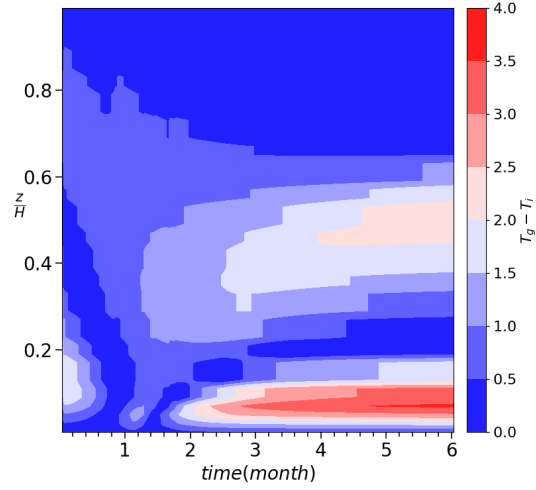


Figure 2.22: The horizontally-averaged time-series for the temperature difference between gas and ice phase.

magnitude in gas and ice energy equations are 20% and 40% respectively (figure 2.20c). This shows that we cannot neglect this term and this is the reason that the thermal equilibrium assumption is not valid. This is further shown in figure 2.22 for the temperature difference between gas and ice phases, in which the difference ranges from -5 K to 2 K. The phase change term in ice energy is much larger than the one in gas energy with the relative magnitude of 15% and 1%, respectively (figure 2.20c). However, the phase change term in ice energy is pronounced during the first month and later on it decreases gradually. Where the snow porosity increases laterally (at the bottom of snowpack) and vertically (in MPD patches at bottom), the flow velocity grows and consequently both convection and conduction terms grow (figure 2.19a and b). Later on, at the middle of snowpack, we observe that the convection term adds energy to the gas phase (figure 2.19a). This is because convection brings more energy through the MPD patches than the one leaving the deposition zone. This results in a convective energy flux convergence. We see that for the same area in the heat transfer term shown in figure 2.19c, the energy is negative. This means the convective energy is converted to the heat transfer between two phases. The term associated with the gas pressure change (figure 2.19g), energy transport by diffusive flux (figure 2.19h), and temporal term (figure 2.19d) are negligible and much smaller than other terms.

The relative magnitude and contribution of each term in equations (2.2) for the mass conservation of water vapor component are shown in figure 2.20 and figure 2.21. During the first week of simulation when the convection cells are forming (stage 1 to stage 3 of thermal behavior explained in section 2.5.1), the diffusion term is dominant at the bottom, while later the convection is dominant at the bottom and top of the snowpack (comparing figure 2.21e with figure 2.21f and also see figure 2.20d). At the bottom, once the porosity reaches the maximum possible value, the phase change stops and consequently both diffusion and convection balance each other. Also, on top, due to increase in snow density, the convection contribution decreases gradually by time (figure 2.21e, figure 2.20b, figure 2.20d). As shown in figure 2.20b and d, the dominant term in the mass conservation of water vapor component is the phase change term with a relative magnitude of 45 % early in simulation, which decreases gradually with time. The larger relative magnitude of the phase change term in the mass conservation equation around 45% compared to its contribution in the energy equation (approximately 15%), supports that non-dimensional temperature and temperature gradient are partially scaling with $Ra$ (within around 20% deviation) while this is not the case at all for the phase change rate. Finally, similar to the energy equation, the temporal term for mass conservation of water vapor component (figure 2.21d) is negligible and smaller than other terms by two orders of magnitude.

The gas density gradient term (last term in equation (2.8)) is always upward in vertical flows (upward and downward) and it has the same direction as lateral flow on top. However, the dynamic pressure gradient is always downward in vertical flows and it has an opposite direction of the lateral flows on top. Hence, for the upward flow and also lateral flows on top, the gas density gradient term is the driving force and the dynamic pressure gradient and viscous forces are the opposite forces. However, for downward flow and also lateral flow at

the bottom, the dynamic pressure gradient is larger and acts as driving force. As shown in figure 2.21a, the bouncy term is larger on top mainly because of $|gz|$. Also, because of the no flux condition, the dynamic pressure gradient must be the same with the gas density gradient term on top and bottom boundaries and its magnitude is larger on top, similar to the gas density gradient term. The viscous resistance force is two order of magnitude smaller than the other terms in the momentum equation. Moreover, we see that the viscous resistance force gradually increases on top while decreases at the bottom. The increase/decrease in snow density results in decrease/increase in both intrinsic permeability and flow velocity which has opposite effects in changing the viscous resistance force. However, the change in the intrinsic permeability is more pronounced than change in flow velocity and it is the reason for increasing the resistance force on top (deposition zone) and decreasing it at the bottom (sublimation zone). Note that since the pore Reynolds number is much smaller than 1, the second term in the momentum equation is neglected and not presented in our analysis.

## 2.6 Conclusions

In this paper, the effects of convective vapor transport for different snowpack conditions such as vertical size, thermal boundary conditions and Rayleigh number have been investigated numerically. To that end, a direct numerical solver based on the volume-averaged two-phase model has been implemented in the open-source fluid dynamics software, OpenFOAM 5.0 (www.openfoam.org).

Investigating the scaling behavior of our system, it is found that we do not have a complete scaling since heat and mass transfer are coupled by phase changes. It is discussed that we only have partially scaled results for interior temperature and its gradient but not for water vapor density and its gradient. We supported our argument by comparing the relative contribution of phase change terms in heat and mass transfer equations. Overall, it appears that $Ra$ is effective in partially but not completely collapsing the non-dimensional profiles.

Analyzing thermal and phase change regimes in detail, it is found that (1) the thermal and phase change behavior in the upward and downward flows of a convection cell are qualitatively the same for snowpacks with different conditions, (2) once convection cells are completely formed, compared to the pure conduction temperature profile, the region is colder in downward flow and warmer in upward flow, (3) phase change rate is very small for the cold region on top in downward flow and a very small value for oversaturation $\sigma$ of just around 0.05 is observed while for the warm region at the bottom, the sublimation rate is much larger, (4) the top region in downward flow has the lowest water vapor content while the bottom region in upward flow has the highest water vapor content, and (5) there is a vertical effective deposition zone with a smaller saturation degree less than around 0.2 while the effective sublimation zone is horizontal in the bottom region with the saturation degree ranging from -0.05 to -0.9, and (6) convection cells are not fixed and may have horizontal displacements due to horizontal heterogeneity induced in the snow porosity. This leads to an almost uniform higher snow

density close to the surface and a layer of significantly lower density at the bottom for the assumed temperature gradient of warmer temperatures at the bottom, which is the usual case in seasonal snow and on sea ice.

A significant influence of the snowpack size on the heat and mass transfer is observed: (1) for the sublimation zone in the downward flow, the larger the snowpack, the smaller the area in which the saturation degree magnitude is greater than 5%, meaning that it has a smaller significant sublimation area in percentage compared to the smaller snowpacks, (2) at the bottom of snowpack in the upward flow, the larger snowpack reaches the saturation line closer to the bottom boundary, resulting in a relatively smaller sublimation zone, (3) for the deposition region in the upward flow, while the small snowpack has more uniform and linear saturation degree and phase change rate, the large snowpack has two peaks in the saturation degree with a large saturation area in between, and (4) the induced heterogeneity in snow porosity occurs faster, earlier, and stronger for the small snowpack due to its larger relative size (or extent) for the sublimation and deposition zones. During the first month of the simulation, the convection cell displacement is around $0.8H$ for the small snowpack while it is only $0.15H$ for the medium snowpack.

Based on lateral averages for each level of $z$, it is observed for small, medium, and large snowpacks respectively that: (1) the weak layer at the bottom with the minimum possible density has the non-dimensional thickness of around $0.2H$, $0.1H$, and $0.05H$, (2) it takes 5, 7, and 11 weeks to reach for the first time the minimum snow density at the bottom, (3) after six month of the simulation, the portion of the top region with the density increase more than 25 % is around 46, 30 and 10 %, (4) the maximum increase in density on top is 57% ($87 \, \mathrm{kg \, m^{-3}}$), 47 % ($72 \, \mathrm{kg \, m^{-3}}$), and 29% ($45 \, \mathrm{kg \, m^{-3}}$), and (5) the MPD patches formed in the weak layer is larger for the small snowpack with the vertical size of around $0.5H$. As a result, the standard deviation for the snow density change is larger for the small snowpack around $70 \, \mathrm{kg \, m^{-3}}$ while it is around 50 and $40 \, \mathrm{kg \, m^{-3}}$ for the medium and large ones.

Results of different temperature differences indicate that (1) in both downward and upward flows far from the bottom boundary, the high $Ra$ case even with a smaller saturation vapor density gradient has a larger snow density change as its convective flow velocity is higher. However, it has almost the same snow density change compared to the medium $Ra$ case in the upper half of the domain while a larger snow density change in the lower half one, (2) in both downward and upward flows close to the bottom boundary, snow density change is larger for the case of higher $Ra$ because of its stronger saturation density gradient, (3) it takes 16.5, 8.5, and 6 weeks for the low, medium and high $Ra$ cases respectively, to reach the minimum snow density at the bottom, and (4) the maximum increase in density on top for medium and high $Ra$ cases is around 42.8 % ($65.4 \, \mathrm{kg \, m^{-3}}$) and 47.4% ($72.3 \, \mathrm{kg \, m^{-3}}$) respectively. The low $Ra$ case has two peaks for the density increase with a maximum one very close to the top boundary of 44 % ($67.4 \, \mathrm{kg \, m^{-3}}$).

The model system simulated and analyzed in this study is a considerably simplified repre-

sentation of a naturally occurring snowpack. A very important process, not considered here is the densification of snow due to metamorphism and overburden pressure arising from its own weight. Additionally the effect of wind pumping and the exchange of vapor with the the atmosphere is also neglected. This effect was tested in sensitivity simulations to verify and confirm that its effect is small (see figure A.8 in appendix A.5). Inspite of these simplifications, there are indeed vast areas of naturally-occurring snowpacks, such as those in the polar regions or on sea ice for which convection should be very important and likely needs to be considered (Appendix G). This study was motivated by the long standing debate in the cryospheric community about the relevance of vapor convection in snowpacks. There have been various field campaigns and reports that invoke vapor convection as the only plausible mechanism to explain observations of temperature and density distributions. This study was the first attempt to use a fluid dynamics based, numerical approach to investigate convection in snow. Our current and future work is to expand our numerical modelling to simulate more realistic scenarios where there is multi-scale heterogeneity, i.e realistic layering and lateral variations. The model system in this study, with its homogeneous boundary conditions and simple bottom geometry is in fact the most restrictive in triggering and sustaining convection. This study thus establishes the 'baseline' for future explorations. For example, there is long-standing evidence by Sturm and Johnson (1991) who reported implications of convective transport in natural snowpacks with Ra as low as 5. It is highly likely that in their and many other natural systems are heavily influenced by heterogeneity.

We demonstrated that the new model reproduces a low density layer and a high density layer respectively at the bottom and top of snow covers and especially for thin snow covers, the high density layer on top is often observed together with density decreases at the bottom. This has not been possible to reproduce with current snow models. While settling will partially counteract the generation of this low-density layer at the bottom, we note that the generation of asymmetric depth hoar crystals as a result of vapor transport allows for quite low density patches between chains of supporting depth hoar structures. The high porosity between such chains will help to keep convection going in real snow covers. For future work, the model developed in this paper for convective vapor transport will therefore be used to improve the one-dimensional physics-based multi-layer snow model by a tight coupling between Open-FOAM and SNOWPACK (Lehning et al., 1999a), in which lateral averages of the porosity change due to convective vapor transport will be feed into SNOWPACK.

## Acknowledgements

## Declaration of interests

The authors report no conflict of interest.

# 3 Convection of Snow: When and why does it happen?

**key points**

- in idealized snowpacks of plane-parallel layers, convection is unlikely to dominate vapor transport due to sub-critical Rayleigh numbers

- with lateral density variations, convection is shown to occur and lead to significant density changes for sub-critical Rayleigh numbers

- our work shows that for typical - not too thin - not too thick - Arctic snowpack convection may dominate vapor transport and density change

## Abstract

Convection of water vapor in snowpacks has not been directly measured and only recently been simulated. The analysis suggests that natural convection is not likely to happen in typical horizontally homogeneous Arctic or Alpine snow covers. This paper studies the potential impact of heterogeneity induced e.g. by shrubs on convection of water vapor. We find that natural convection triggered by the temperature gradient occurs even with sub-critical Rayleigh number as low as 5 due to heterogeneity in snow density. This leads to complementing contributions of diffusive and convective flux divergence on snow density changes. The strongest effect of convection is not for very thin or thick snow covers but for snow covers in between through convection cells with a scale of 0.5 m. Further work should address the additional effects of sub-snow lateral temperature variations and assess the effect of convective vapor fluxes on snow microstructure.

## Plain Language Summary

The typical density profile and microstructural properties of many - in particular Arctic - snow covers cannot be fully understood or explained with current models. They typically have a low-density base and a high density layer at the surface. A potential mechanism, which could explain such a profile is vapor transport via convection. We show that convection is more likely to happen in snow covers, which have low density patches close to the ground. These low density patches are known to exist due to shrubs or other roughness elements. This implies that the flow can move faster and easier through the snow intertwined with vegetation. Consequently, more water vapor transports from the snow base and results exactly in a reduction of density close to the ground and an increase of density closer to the surface. The strong vapor fluxes go along with the associated changes in microstructure and help to understand the important properties of Arctic and other snow covers.

## 3.1 Introduction

As temporary water storage, snow covers control ground water recharge and energy fluxes at or near the land surface (Groisman et al., 1994), making modeling of the snow cover properties crucial in many applications, e.g. for soil thermal properties and permafrost dynamics (Haberkorn et al., 2017; Bender et al., 2020), climate models, hydrological models for irrigation and hydroelectricity (Bavay et al., 2013), etc.. Water vapor transport is a dominant dynamical process in the snowpack for detailed modeling of snow cover properties and in particular influences snow density and microstructure. Water vapor fluxes are involved in snow metamorphism (Colbeck, 1983, 1987; Sturm and Benson, 1997; Pfeffer and Mrugala, 2002), snowpack stability and avalanches (Woo, 2012; Pfeffer and Mrugala, 2002), and thermal implications for climate studies (Slater et al., 2001; Callaghan et al., 2011). The basal density in thin Arctic snow cover can decrease by more than 100 kg m$^{-3}$ with water vapor flux as the only plausible explanation (Trabant and Benson, 1972; Sturm and Benson, 1997; Domine et al., 2016b). Domine et al. (2019) discussed that current versions of one-dimensional snow models lack an accurate description of water vapor transport and thus they cannot simulate Arctic snowpacks. At the same time, water vapor flux in snow has never been measured directly. Based on Palm and Tveitereid (1979); Powers et al. (1985), the critical Rayleigh number for the onset of convection ranges between 27 and 40 and it has been concluded that convection is unlikely in most natural snow covers, while Sturm and Johnson (1991) have postulated convection to occur for Rayleigh numbers as low as 4.

Earlier numerical studies of water vapor transport in snow focused exclusively on diffusion. However, convection may also occur depending on snowpack conditions (Trabant and Benson, 1972; Johnson and Bens, 1987; Alley et al., 1990; Sturm and Johnson, 1991; Domine et al., 2016b, 2018) and it is furthermore not possible to explicitly model convection with phase change in a one-dimensional snow model (Jafari et al., 2020, 2022). Jafari et al. (2022) developed the first model specifically for convection in snow and numerically studied the impact of convection on the thermal and phase change regimes. They investigated different snowpack depths, thermal boundary conditions and Rayleigh numbers, using a volume-averaged two-phase model in a two-dimensional domain. They observed a considerable and large impact of the natural convection on the snow density distribution, with a layer of significantly lower density at the bottom of the snowpack and a layer of higher density located at the top. However, the idealized snowpack used for demonstrating the effect may not be widespread enough to explain previous observations of density changes reported above.

Vegetation, e.g. shrubs and herbs, growing on Arctic tundra increases snow height, thermal insulating effect of the snowpack, and affects snow properties (Gouttevin et al., 2018; Domine et al., 2016a). In addition, snow often falls on terrain with a rough surface caused by rocks or pressure ridges on sea ice. As reviewed and pointed out by Domine et al. (2016a), as of yet, there is no extensive study of the impact of shrubs on snow physical properties. The important impacts of vegetation are their limited snow-holding capacity, mechanically reduced compaction, and enhanced grain growth (Gouttevin et al., 2018; Domine et al., 2016a). These

effects result in lower initial density due to the presence of vegetation after snowfall (Gouttevin et al., 2018). Since shrubs and other roughness elements have a rather random distribution in space, the resulting heterogeneity in initial snow density may influence convection and enhance the effects of water vapor transport on snow density change. In their Samoylov permafrost observation, Gouttevin et al. (2018) reported vegetation with a typical height of 15 to 20 cm. It got compressed by snow, reducing vegetation height to 7 to 10 cm. They chose a fresh snow density of 150 kg m$^3$ for the best match to end-of-season in-situ density observations. At Bylot Island in the Canadian high Arctic, Domine et al. (2016a) reported bushes of 20 to 40 cm high. They noticed that the network of stems limits snow compaction in shrubs, with observed densities as low as 125 kg m$^3$. To mimic the limited snow compaction, Domine et al. (2016a) increased the viscosity of dry snow in the presence of shrubs by a factor of 100 up to a snow height of 10 cm and by a factor of 10 to the top of the shrub. There are uncertainties relating to snow-holding capacity of vegetation after snowfall, the effective size of low density patches, and the distribution and coverage percentage of vegetation.

In addition to induced heterogeneity by vegetation in the initial snow density, there will in reality be thermal perturbations which lead to lateral temperature gradients in the soil due to presence of vegetation that might strengthen convection effects. Gouttevin et al. (2018) showed that in low-center polygons in permafrost terrain there are large temperature differences in the soil within a short distance, especially during freezing. This is because short-scale differences in soil moisture lead to different freezing dynamics and therefore temperature gradients. Differences in thermal regime between heterogeneity patches filled with vegetation and its neighbouring vegetation-free patches as well as the soil interface all lead to horizontal temperature gradients at the bottom boundary. This has been shown by the recent study Domine et al. (2022) for thermal bridging through shrub branches. They observe significant perturbations of the permafrost thermal regime by shrub branches. In this paper, we did not consider the thermal feedbacks from vegetation i.e modifying the thermal conductivity (considering vegetation as a component in porous material) or imposing a lateral-varying thermal boundary condition at the bottom since this would require simulations coupled with soil, which we consider beyond the scope of the current analysis.

Thus in this paper, we investigate numerically in how far density heterogeneity can influence convection. We hypothesize that it may facilitate onset and increase strength of convection cells. If the hypothesis can be confirmed, we have contributed to an increased understanding of snow dynamics. In particular, the current state of the art cannot explain the presumed role of convection in shaping typical Arctic density profiles. More frequent and stronger convection is required in our numerical model (Jafari et al., 2022) to achieve the desired effect. The following analysis tests the influence of lateral heterogeneity in that context.

## 3.2   Materials and Methods

Following the work done by Jafari et al. (2022), water vapor transport due to natural convection in idealized snowpacks is investigated numerically using an Eulerian–Eulerian two-phase approach. The snowpack is considered as a two-phase (humid air, ice) porous medium by neglecting the effects of ventilation and snow compaction to focus only on convection.

Applying the volume averaging method (Whitaker, 1999; Faghri and Zhang, 2006), the final set of the equations are mass conservation equations for the gas mixture (humid air), water vapor component, and ice phase, the momentum equation for the gas mixture, and finally the temperature-based energy equations for the gas and ice phases. These equations are solved to update the water vapor and air component densities as $\rho_v$ and $\rho_a$ respectively, the snow porosity as volumetric fraction of the gas phase $\epsilon_g$ and ice volumetric fraction $\epsilon_i = 1 - \epsilon_g$, the snow density $\rho_s = \epsilon_i \rho_i$, where $\rho_i$ is the ice density, the gas flow velocity $\boldsymbol{U}_g$, the diffusive water vapor flux $J_v = -D_{\text{eff}} \nabla \rho_v$ where $D_{\text{eff}}$ is the effective water vapor diffusivity, the phase change rate $\dot{m}_{iv}$ in which subscript $iv$ refers to the mass transfer from ice to vapor while $vi$ from vapor to ice, and finally the temperature for the gas and ice phases as $T_g$ and $T_i$, respectively. The detailed explanation, derivations, and model choices constituting the final set of equations can be found in Jafari et al. (2022). Note that the sensitivity of our results on different parameterizations for effective diffusivity and thermal conductivity (formulations by Hansen and Foslien (2015) compared with formulations by Fourteau et al. (2021)) is small and does not influence the conclusions.

Assuming that herbs and shrubs introduce heterogeneity in the initial snow density, the heterogeneity is modelled as half-circle patches of lower density. Size (radius) and spacing between patches are specified in our two-dimensional snowpack of the depth $H$ and the length $L$. Figure 3.1a shows a sketch of the domain including the heterogeneity patches with the cyclic boundary conditions on lateral sides and impermeable walls with zero flux for the gas phase on top and bottom boundaries. For the heat transfer equations of both phases, the reference temperature is used as the bottom warm boundary condition, $T_h = T_{\text{ref}}$, whereas $T_c = T_{\text{ref}} - \Delta T$ is applied for the top cold boundary. Here, $\Delta T$ is the temperature difference between top and bottom boundaries. The sensitivity analysis in Jafari et al. (2022) has shown that the results are not sensitive to the choice of initial temperature and vapor distribution. Thus, the initial conditions are the reference temperature for both ice and gas phases and the saturation water vapor density. Extended and fairly homogeneous patches of vegetation would indeed present a wider area of higher flow velocity to form convection cells than scattered shrubs studied in this study shown in Figure 3.1a. They would nonetheless lead to lateral heterogeneity because they will not have the same height everywhere.

As will be discussed later in section 3.3, to analyze the impact of heterogeneity on snow density change, we need to compare the contributions of convective and diffusive terms in the mass conservation of water vapor. As discussed in Jafari et al. (2022), the convective-diffusive heat and mass transfers with phase changes in snowpacks are very slow processes and changes

are small enough at each time step to consider a quasi-steady state process. Therefore, with the approximation for the convection term as $\nabla \cdot (\rho_v \boldsymbol{U}_g) \approx \boldsymbol{U}_g \cdot \nabla \rho_v$ (Jafari et al., 2022), the simplified mass conservation of the water vapor may be written as:

$$\boldsymbol{U}_g \cdot \nabla \rho_v + \nabla \cdot J_v = \dot{m}_{iv} \tag{3.1}$$

When buoyancy forces, driven by unstable fluid density gradients, are large enough to overcome viscous drag, natural convection in a porous medium is triggered. This can be evaluated by the Rayleigh number when it exceeds the critical value of $Ra_c = 4\pi^2 = 39.48$ (Lapwood, 1948). The Rayleigh number as the ratio of buoyancy to viscous forces in a porous medium is defined as:

$$Ra = \frac{\rho_{a_{\text{ref}}} \beta g \Delta T H K}{\mu k_{\text{eff},s}/(\rho_{a_{\text{ref}}} c_{pa})} \tag{3.2}$$

where, $H$ is the depth of porous layer, $k_{\text{eff},s}$ is the effective thermal conductivity of snow, $K$ is the intrinsic permeability of snow, and the air density $\rho_{a_{\text{ref}}}$, specific heat capacity $c_{pa}$, dynamic viscosity $\mu$, and thermal expansion coefficient $\beta$, all are used at the reference temperature $T_{\text{ref}} = 273.15$ K. The Rayleigh number can alternatively be interpreted as the ratio of convective to conductive velocity scales as $Ra = U_{conv}/U_{cond}$ (Hewitt et al., 2013a,b), in which the convective velocity scale is $U_{conv} = \rho_{a_{\text{ref}}} \beta \Delta T g K/\mu$ and the conductive velocity scale is $U_{cond} = k_{\text{eff},s}/(\rho_{a_{\text{ref}}} c_{pa} H)$. Note that in our analysis, heterogeneous low density patches shown in Figure 3.1a are excluded for calculation of Rayleigh number.

## 3.3  Results and Discussion

The three snow heights investigated in this section are $H = 30$ cm (thin), $H = 50$ cm (shallow) and $H = 75$ cm (thicker) with an initial snow density of 150 kg m$^3$ within the heterogeneity patches, which have a radius of 20 cm and spacing of 1 m based on Figure 3.1a. Also, a fixed grain diameter of 1 mm is used. For each snow height, four sub-critical Rayleigh numbers of 5, 10, 20 and 30 are considered with corresponding values for initial snow density, respectively, as 221, 188, 157, and 138 kg m$^{-3}$ for a thin, 272, 237, 204, and 184 kg m$^{-3}$ for a shallow, and finally 315, 278, 243, and 223 kg m$^{-3}$ for thicker snowpack. The specific surface area for all cases is 6.54 m$^2$ kg$^{-1}$. These values are in consistent with the sub-arctic snowpack, as e.g. in Sturm and Benson (1997). The typical snowpack properties for such snowpacks are a density of 200 kg m$^{-3}$ (Sturm and Benson, 1997), an SSA of 10 m$^2$ kg$^{-1}$ (Taillandier et al., 2006), a thermal conductivity around 0.05 W m$^{-1}$ K$^{-1}$ (Sturm and Johnson, 1992) and the permeability measured for such snowpacks is around 400 $\times$ 10$^{-10}$ m$^2$ (Domine et al., 2013).

Because of the dependency of $Ra$ on initial snow density (Jafari et al., 2022), the larger snowpack must have a larger initial snow density and thus smaller convective velocities. Given

the fact that both diffusive and convective terms in equation 3.1 depend mainly on the temperature gradient (Jafari et al., 2020, 2022), we consider the bulk temperature gradient to be the same for all cases as $\Delta T / H = 60$ K m$^{-1}$. This implies that for the cases with the same Rayleigh number, we expect the same non-dimensional temperature gradients. To investigate the impact of heterogeneity in the initial density, we need to analyze the difference between convective and diffusive fluxes as follows:

For the case without heterogeneity when Rayleigh number exceeds the critical value, i.e. $Ra > 39.48$, we see convection cells forming in the domain. The heat and mass transfer regimes in upward and downward flows of a convection cell have been discussed in detail by Jafari et al. (2022). In summary, for the downward flow of a convection cell, we observe mostly a weak sublimation region (almost at saturation water vapor density) except for the region close to the warm bottom boundary with strong sublimation. For the upward flow of a convection cell, after the strong sublimation zone at the bottom, there is a strong deposition zone. As discussed in Jafari et al. (2022), for each convection cell, we have a strong vertically extended deposition zone as well as a strong horizontally extended sublimation one.

The difference between the case with and without heterogeneity for the snow density, convective water vapor flux divergence, and diffusive water vapor flux divergence is shown in Figure 3.2, Figure 3.3, and Figure 3.4, respectively. Note that these quantities are laterally averaged for each level of $z$ excluding the heterogeneous low density patches. As shown in Figure 3.2 for the sub-critical Rayleigh numbers studied here, the snow density difference between the case with and without heterogeneity ranges from -30 to -75 kg m$^{-3}$ for the shallow snowpack $H = 50$ cm and thicker snowpack $H = 75$ cm. However, the snow density difference is small and less than 30 kg m$^{-3}$ for the thin snowpack $H = 30$ cm.

Once we introduce heterogeneity in the initial snow density as shown in Figure 3.1a, we observe convection cells are formed even with sub-critical $Ra$ as low as 5, e.g. Figure 3.1b. Obviously, a higher Rayleigh number results in a stronger convection cell with stronger temperature gradients (comparing isothermals between Figure 3.1c and b). Also, since the cold air on top is heavier, it helps the downward flow go mainly through the low density patches (see the downward flow through heterogeneity patches in Figure 3.1b, c , and d). This transports the water vapor through these patches, which subsequently leads towards the upward flow, which forms between two low density patches. As we have the same low density for the heterogeneous patches for all cases, the convective flow velocities are the same for cases with the same $Ra$. However, as soon as the flow goes through the domain of higher density (mainly horizontal flow close to the bottom boundary), depending on its snow density (convective flow velocity), the distribution of water vapor density becomes different. For the thicker snowpack $H = 75$ cm and for $Ra = 5$ (the lowest Rayleigh number), the flow cannot penetrate deep into the high density region and we have a higher concentration of water vapor compared to medium and small snowpacks. This leads to a higher vertical diffusive flux for larger snowpacks but smaller horizontal diffusive fluxes and flow velocity. This can be seen in Figure 3.3 comparing the fluxes between the shallow and thicker snowpacks. Note that as will be discussed later, for the

thin snowpack, the horizontal diffusive flux is smaller because more but weaker convection cells are formed between heterogeneity patches. Therefore, $\nabla \cdot J_v$ (Figure 3.4) is the dominant term compared to $\boldsymbol{U}_g \cdot \nabla \rho_v$ ( Figure 3.3) for larger snowpacks, favoring larger snow density changes for $Ra = 5$.

The water vapor distribution for $Ra = 10$ and $Ra = 5$ is the same except that for $Ra = 10$, the flow penetrates deeper into the region of larger density between two patches, resulting generally in a smaller vertical diffusive flux but larger horizontal diffusive flux close to low density patches. However, for $Ra = 10$, the flow still is not strong enough to transfer most of the water vapor far enough from the low density patches, horizontally and vertically, in order to have a larger horizontal diffusive flux relative to the vertical one (comparing the vapor distribution between $Ra = 30$ and $Ra = 5$ in Figure 3.1). This means that the increase in $\boldsymbol{U}_g \cdot \nabla \rho_v$ counteracts the decrease in $\nabla \cdot J_v$ for $Ra = 10$ such that the snow density change is smaller or at least the same compared to $Ra = 5$ (comparing subplots of Figure 3.2 for all snow heights between $Ra = 5$ and $Ra = 10$). For $Ra = 20$, the flow is strong enough to transport and accumulate the water vapor at the middle of the region of larger density between heterogeneous patches such that the horizontal diffusive flux is large enough close to the low density patches to have a dominant $\boldsymbol{U}_g \cdot \nabla \rho_v$ compared to $\nabla \cdot J_v$ (comparing related plots in Figure 3.3 and Figure 3.4 between different Rayleigh numbers). This is the reason for a larger snow density change for $Ra = 20$ and $Ra = 30$. For $Ra > 20$, comparing $H = 50$ cm and $H = 75$ cm, the impact of heterogeneity on snow density change is larger for $H = 50$ cm as a larger $U_g$ causes a larger horizontal diffusive flux and both together result in a larger $\boldsymbol{U}_g \cdot \nabla \rho_v$. However, unlike the reasoning for the shallow and thicker snowpacks, the snow density change is not increased for higher Rayleigh numbers ($Ra = 20$ and $Ra = 30$) in the thin snowpack $H = 30$ cm. This is because in a shallow snowpack, a larger number of less intensive convection cells is formed in the region between heterogeneity patches as shown in Figure 3.1d. This decreases the horizontal diffusive fluxes and results in a smaller $\boldsymbol{U}_g \cdot \nabla \rho_v$. Also, for the thin snowpack $H = 30$ and $Ra = 30$, even without heterogeneity in the initial snow density, the convection cells are formed since the initial density itself is small enough to trigger convection cells when the diffusive flux divergence reduces snow density at the bottom of the snowpack.

Spacing between and size of heterogeneity patches (shown in Figure 3.1a) mainly has effects on the number of convection cells formed in the domain as for higher Rayleigh numbers and also smaller snowpacks, more slender cells may be potentially formed. For example, for a larger spacing of 2 m, the water vapor distribution is shown in Figure 3.5 for the shallow snowpack $H = 50$ cm with different Rayleigh numbers. For $Ra = 5$, two large convection cells are formed (Figure 3.5a) while for $Ra = 10$ two smaller cells are added between the two large cells (Figure 3.5b). However, they are not strong enough to split the vapor distribution into two peaks as it is the case for higher Rayleigh numbers such as Ra=20 and Ra=30 (Figure 3.5c and d respectively). Comparing Ra=30 (Figure 3.5d) with Ra=20 (Figure 3.5c), the flow is stronger in the former and pushes water vapor further away from low density patches. However, a higher number of cells for the larger spacing of 2 m results in decreased lateral vapor fluxes

and this is the reason for smaller effects of convection on snow density change for $H = 50$ cm ($Ra = 20$ and $Ra = 30$) compared to the ones for the smaller spacing of 1 m (comparing Figure 3.2h and Figure 3.2k for spacing of 1 m with Figure 3.6h and Figure 3.6k for spacing of 2 m respectively). As discussed earlier, for different heterogeneity configurations (spacing and radius), the number of convection cells and the flow strength determine the contribution of diffusion and convection for snow density change influenced by vertical and lateral vapor fluxes respectively.

## 3.4 Conclusions

In this paper, a numerical solver based on a volume-averaged two-phase model as previously implemented (Jafari et al., 2022) in the open-source fluid dynamics software, OpenFOAM 5.0 (www.openfoam.org) has been used to investigate the role of initial snow density heterogeneity on convection of water vapor in snowbanks for different snow depths. Parameters such as Rayleigh number and the length scale of the heterogeneity have been varied in the investigation.

The study has been motivated by the observation that convection in rather shallow (Arctic) snow covers needs to be stronger than previously predicted by a numerical model. We tested the hypothesis that density variations as e.g. caused by vegetation may help to trigger convection and lead to stronger vapor fluxes.

We observe that due to heterogeneity convection cells form even with sub-critical Rayleigh number as low as 5. The hypothesis could clearly be confirmed. We find further that the relative importance of diffusive versus convective contributions to snow density change is governed by highly non-linear feed backs: Depending on the flow strength coming from low density patches and penetrating into the region of larger density, the diffusive and convective flux divergences have different contributions for snow density change. For lower Rayleigh numbers, the vertical diffusive flux and its divergence is more dominant while for higher Rayleigh numbers the convective vapor flux divergence is the dominant term because of both higher convective flow velocity and horizontal diffusive flux. For very thin snow covers, a higher number of smaller and therefore weaker convection cells formed between low density patches, splits the accumulation of water vapor into multiple peaks and brings the accumulation peaks closer to the low density patches. This results in a smaller horizontal diffusive flux and finally a smaller convective vapor flux divergence and thus a smaller change in snow density. The results analyzed here show significant impacts of heterogeneity on the snow density change, overall enhancing the contribution of convection. Hence, future work that aims to improve the one-dimensional physics-based multi-layer snow model by a tight coupling between OpenFOAM and SNOWPACK (Lehning et al., 1999a) should take into account impacts of heterogeneity on the snow density change.

This study demonstrates some important interactions of vapor transport in snow covers. It is, however, still idealized with respect to the numerical set-up and physical assumptions.
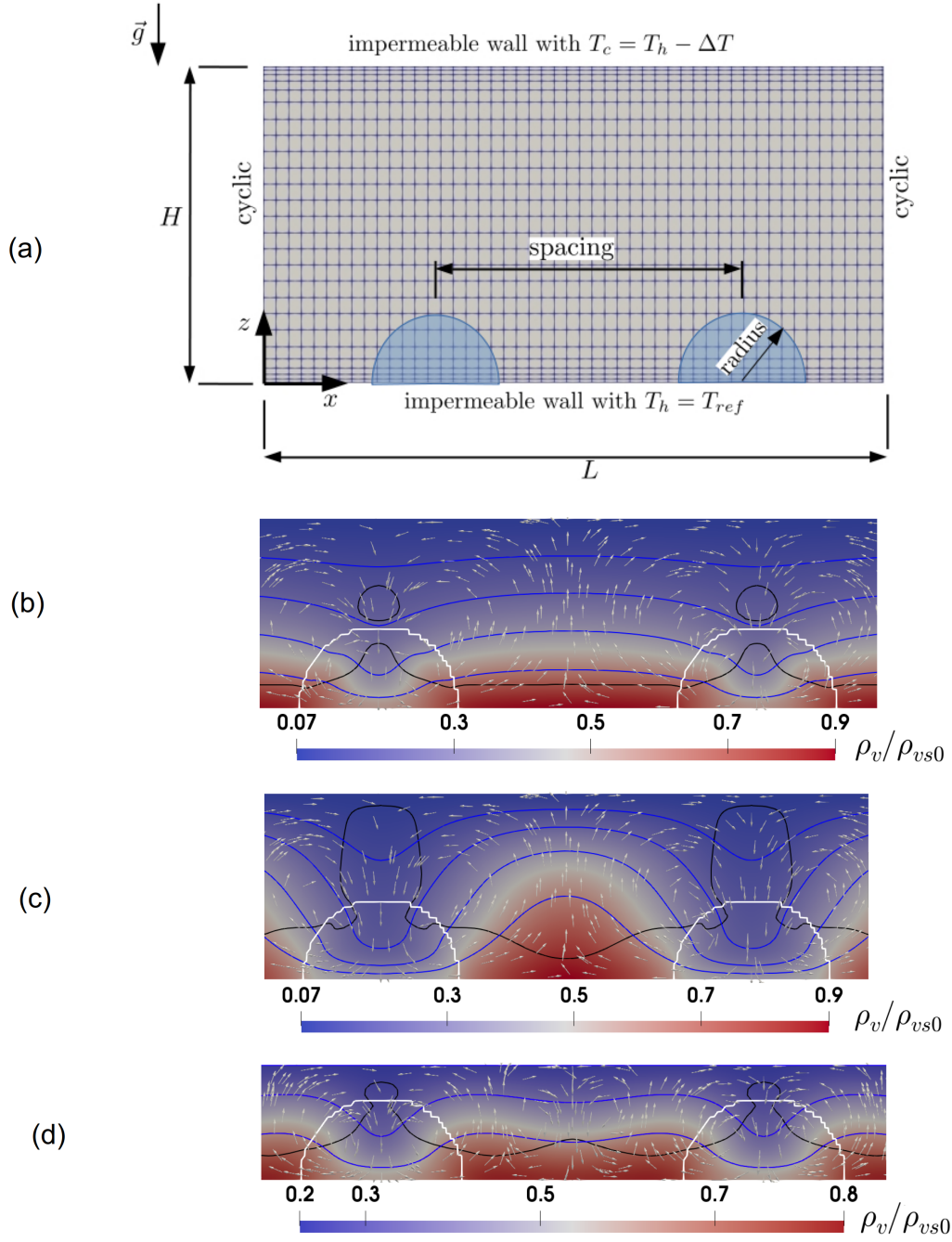
Figure 3.1: A sketch of two-dimensional domain with non-uniform mesh and prescribed boundary conditions shown in subplot (a) and the convection cells, the flow direction, and normalized water vapor distribution between two heterogeneity patches with radius size of 20 cm and spacing of 1 m after a week of simulation for (b) $H = 50$ cm, $Ra = 5$, (c) $H = 50$ cm, $Ra = 30$, and (d) $H = 30$ cm, $Ra = 30$. The white arrows show the flow direction scaled by velocity magnitude. The black line refers to the saturation line where $\rho_v = \rho_{vs}$. The isotherm lines for the snow temperature are in blue color and are equally spaced by $5K$.

Figure 3.2: The snow density difference between the case with and without heterogeneity for different snow heights and Rayleigh numbers for the setup as shown in Figure 3.1 with the heterogeneity radius of 20 cm and spacing of 1 m.
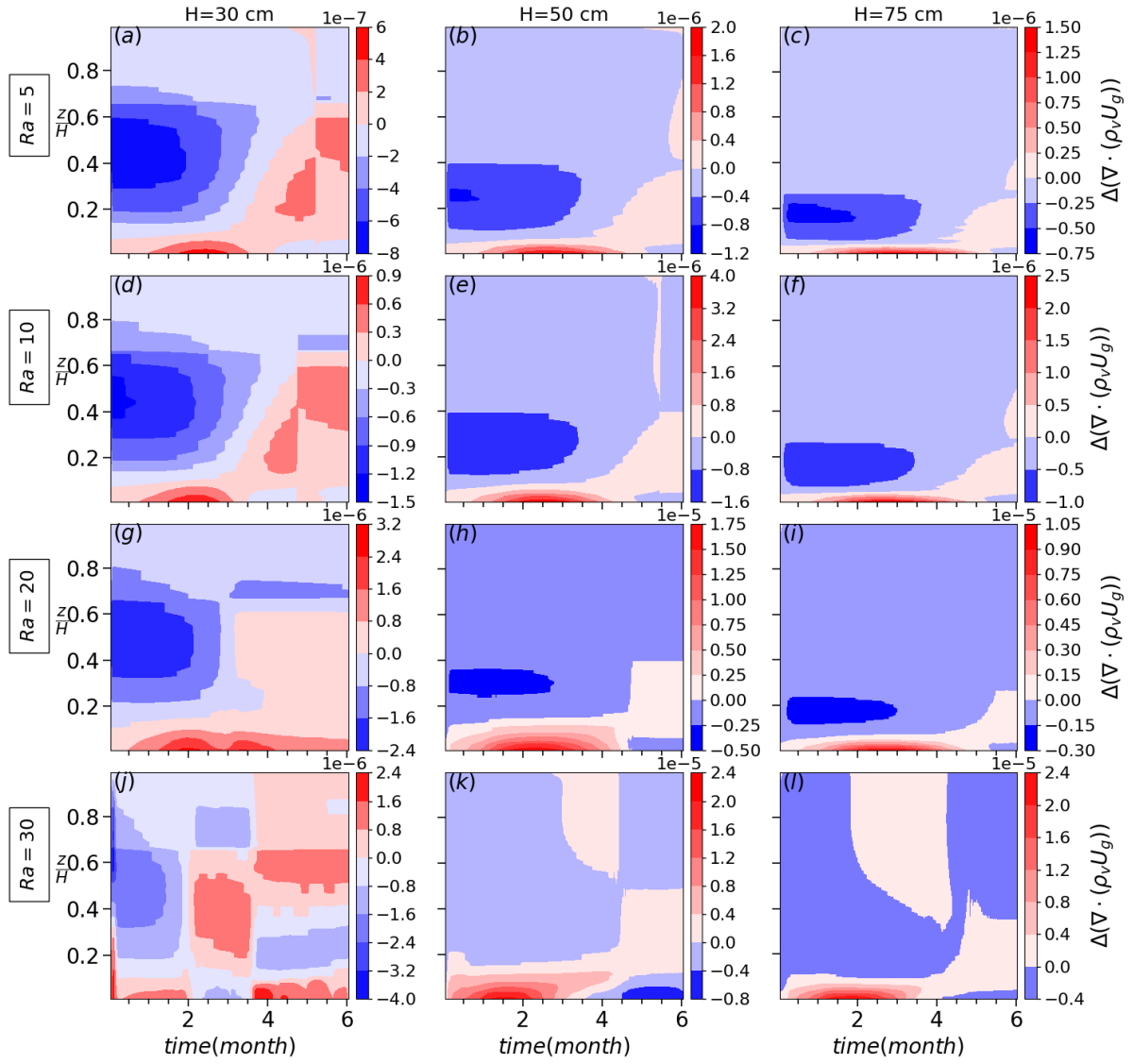
Figure 3.3: The difference in convective flux divergence $\nabla \cdot (\rho_v \boldsymbol{U}_g)$ between the case with and without heterogeneity for different snow heights and Rayleigh numbers with the heterogeneity radius of 20 cm and spacing of 1 m.
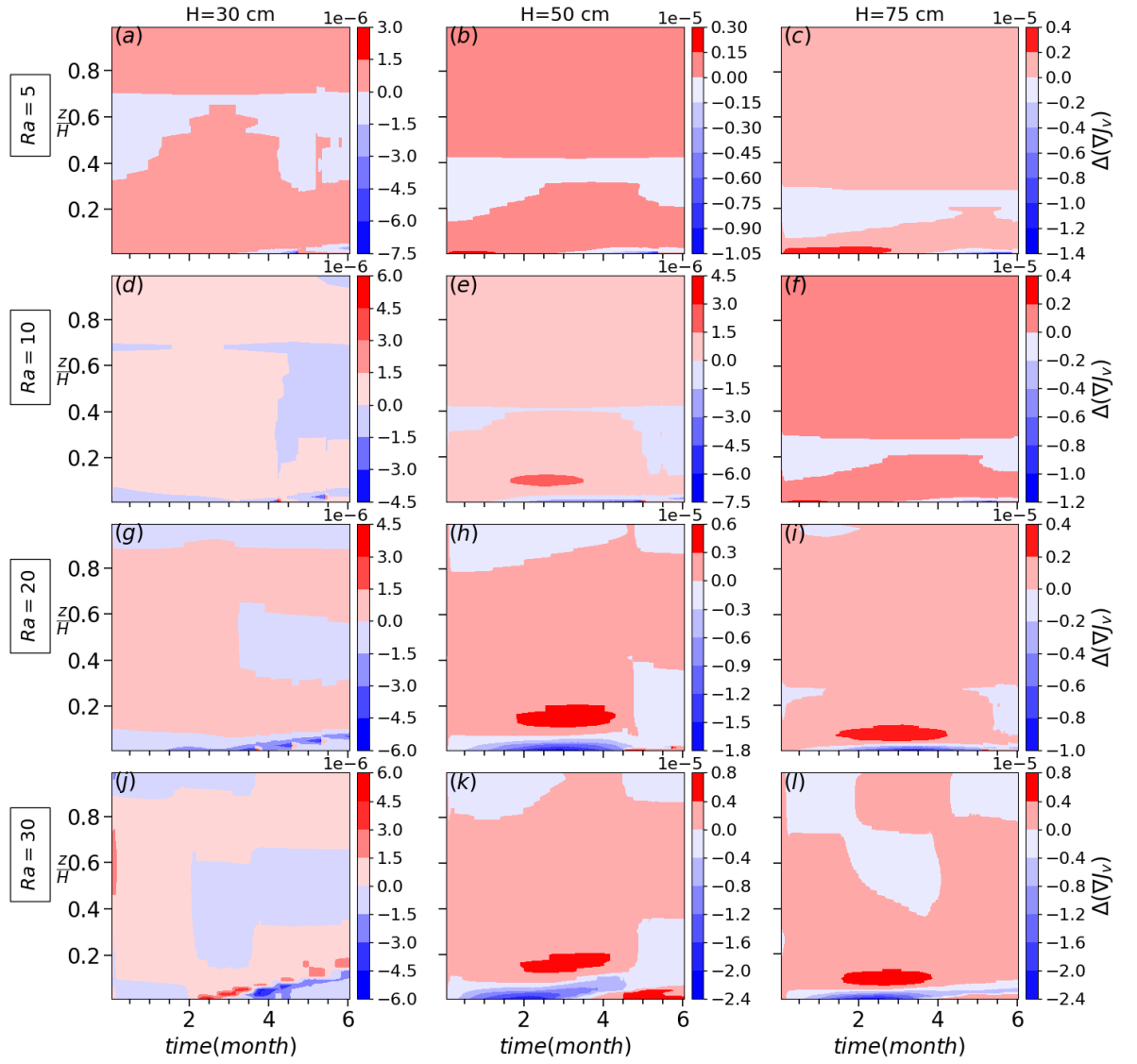
Figure 3.4: The difference in diffusive flux divergence $\nabla \cdot J_v$ between the case with and without heterogeneity for different snow heights and Rayleigh numbers with the heterogeneity radius of 20 cm and spacing of 1 m.
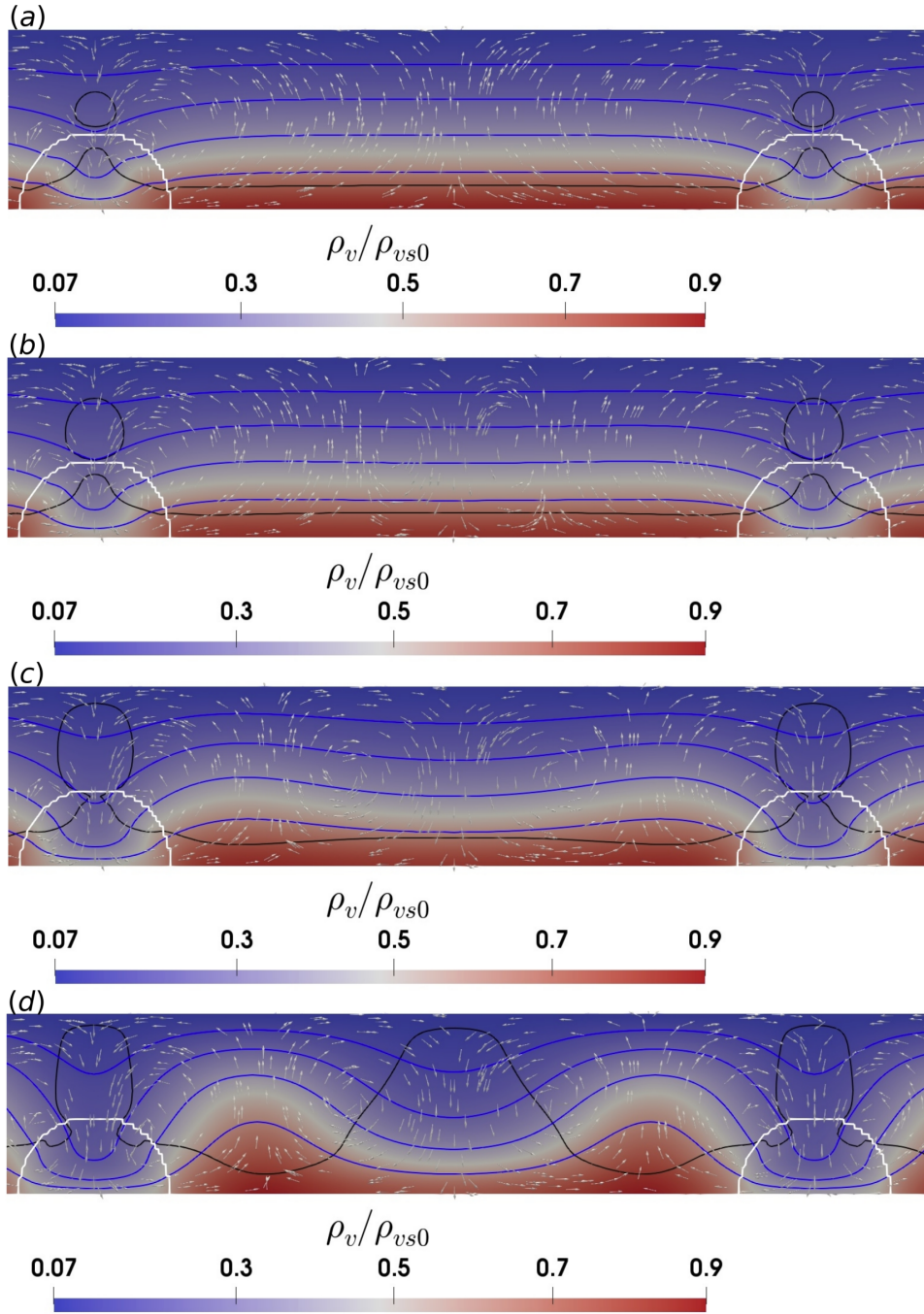
Figure 3.5: The convection cells, flow direction, and normalized water vapor distribution between two heterogeneity patches with radius size of 20 cm and spacing of 2 m after a week of simulation for the shallow snowpack $H = 50$ cm (a) $Ra = 5$, (b) $Ra = 10$, (c) $Ra = 20$, and (d) $Ra = 30$. The arrows show the flow direction but not scaled by velocity magnitude. The black line refers to the saturation line where $\rho_v = \rho_{vs}$. The isotherm lines for the snow temperature are in blue color and are equally spaced by $5K$.
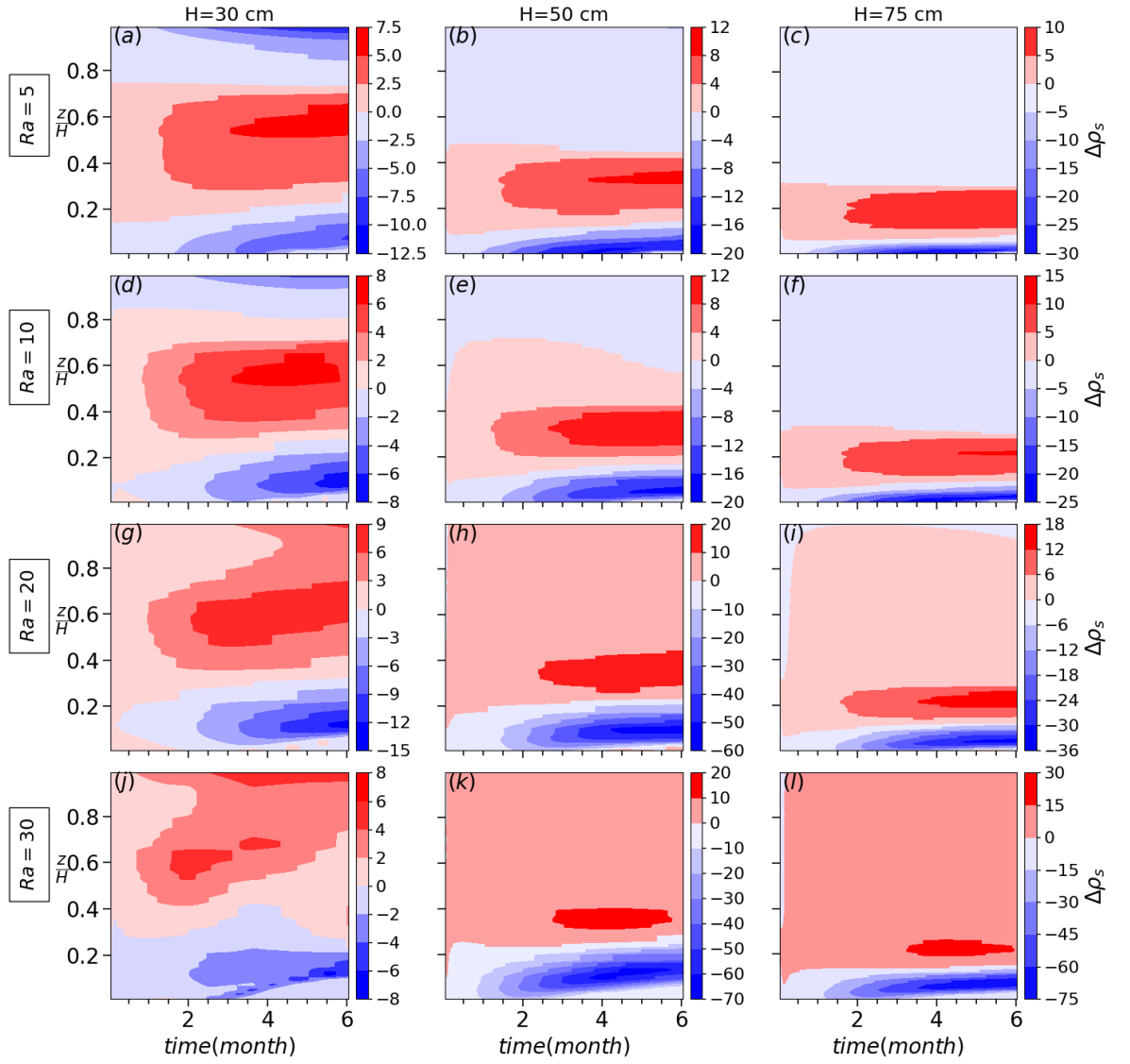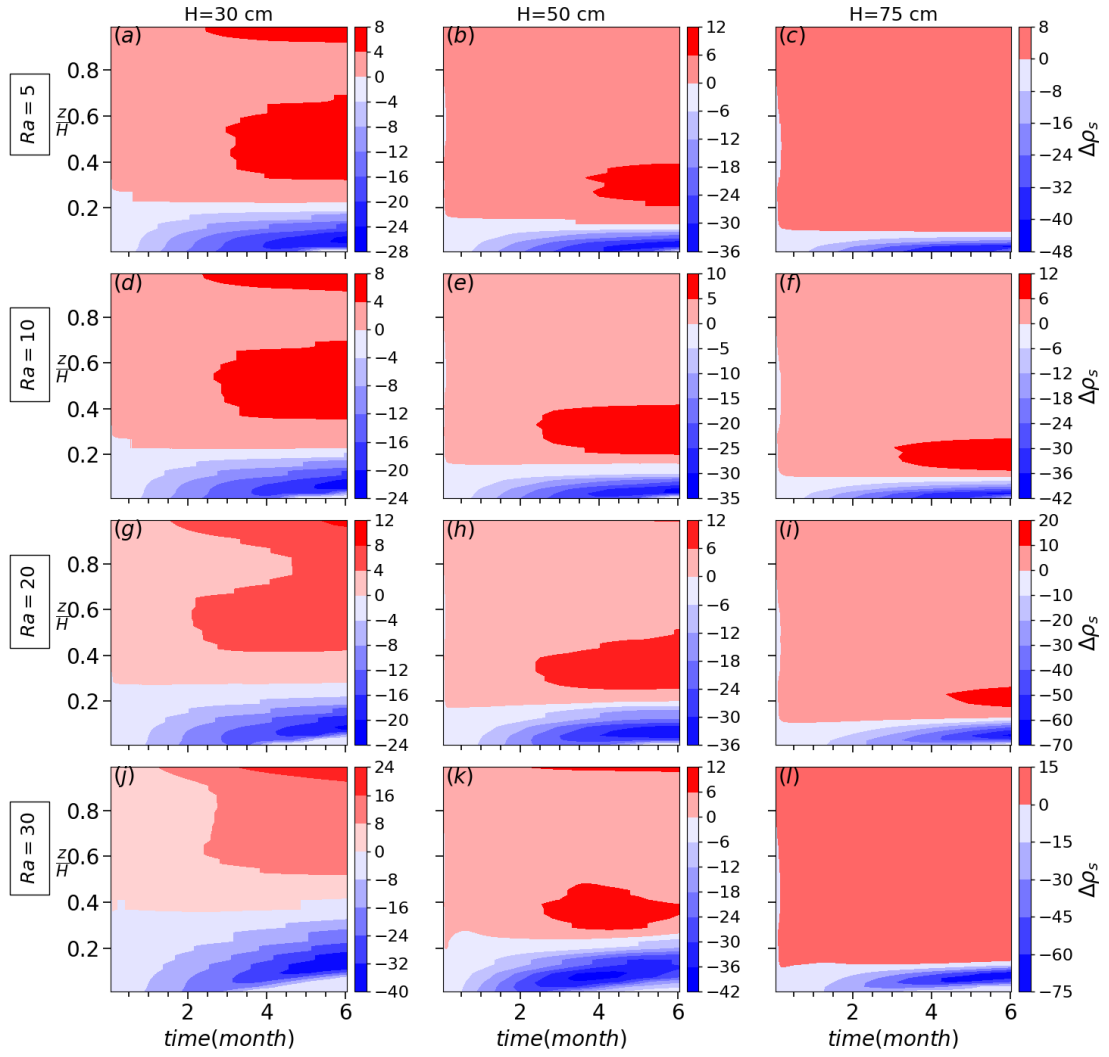
Figure 3.6: The snow density difference between the case with and without heterogeneity for different snow heights and Rayleigh numbers for the setup as shown in Figure 3.1 with the heterogeneity radius of 20 cm and spacing of 2 m.

Limitations of the work are therefore associated with the two dimensional model used as a basis. It is not given that a fully three-dimensional treatment would give the same quantitative results. A further limitation is the assumption of "no settling" and the non-consideration of laterally varying thermal boundary conditions. Future work should therefore attempt to model the system in three-dimensions and to allow for snow settling. A potential way to address 1) compaction and 2) laterally varying thermal boundary conditions coming from the soil is the coupling with existing snow cover models, which we will attempt as a next step.

## Open Research

The source code used in this paper is *snowpackBuoyantPimpleFoam* which is available in the EnviDat repository (Jafari and Lehning, 2021).

## Acknowledgements

# 4 SNOWPACK-OpenFOAM coupling to investigate natural convection in real snow covers

## 4.1   Introduction

Jafari et al. (2020) studied the effects of diffusive water vapor transport on snow density for different snow covers by implementing vapor diffusion in SNOWPACK. However, the combined effects of convection and diffusion for water vapor transport have never been numerically investigated in real snow covers. Recently, in their study of a two-dimensional idealized snowpack, Jafari et al. (2022) (presented in chapter 2) employed a new physical model implemented in OpenFOAM to analyze how convection of water vapor can significantly change the snow structure laterally and vertically. Since modelling convection in one-dimensional snow models is not possible, a direct solution to take into account the effects of convection for real snow covers is to couple SNOWPACK with OpenFOAM. The work presented in this chapter brings us valuable insights: (1) the details in flow velocity, thermal, and phase change regimes can be analyzed as a basis for future parametrizations of convection in one-dimensional snow models with no need to directly use OpenFOAM, (2) the effects of convection, do not only substantially change the snow density vertically, but also induce a considerable and transient lateral heterogeneity in snow structure, (3) the induced lateral heterogeneity due to convection has a direct feedback on snow properties linked on the snow density such as the effective thermal conductivity, snow viscosity, and compaction, (4) the large difference between the temperature profiles in the upward and downward flow of a convection cell causes the temperature-dependent processes such as metamorphism and melting-refreezing to vary laterally in the snowpack.

## 4.2   Materials and Methods

As a straightforward solution to improve the one-dimensional physics-based multi-layer snow model, a C++ interface (dynamic library) is implemented for a tight coupling between SNOWPACK and OpenFOAM. As presented in Figure 4.1, the coupling procedure works as: (1) first, the new time step of SNOWPACK is solved taking into account all important processes such as settling, metamorphism, and melting-refreezing, (Lehning et al., 1999b; Bartelt and Lehning, 2002; Lehning et al., 2002d,b), (2) the snow height in OpenFOAM is dynamically synchronized with the new snow height from the SNOWPACK solution. Note that the dynamic mesh strategy used in the OpenFOAM solution is adding or removing layers only from the top. The minimum and maximum layer thicknesses are the thresholds given by the user to control the process for removing and adding a layer. Since the changes in both ice and water contents due to processes such as settling, water transport, and melting-refreezing are updated from the SNOWPACK solution, there is no need to change the size of internal elements in the OpenFOAM, (3) the snow density change will be interpolated from the SNOWPACK solution to the OpenFOAM domain uniformly in the lateral direction as will be explained later in item (i), (4) after the information exchange between the two solvers, the two-dimensional natural convection is solved by OpenFOAM to update the snow density change due to vapor transport. Note that the detailed explanation, derivations, and model choices constituting the final set of equations can be found in Jafari et al. (2022), and (5) finally, the horizontal average of the

snow density change rate in OpenFOAM is interpolated for each element of SNOWPACK. The assumptions and limitations considered for SNOWPACK-OpenFOAM coupling are explained as follows:

(i) for new snow elements in the OpenFOAM domain, all the snow parameters are directly interpolated from the SNOWPACK output with uniform distribution in the lateral direction. For previously formed snow elements in the OpenFOAM domain, the snow density change due to snow compaction (settling), water transport, and melting-refreezing process from the SNOWPACK solution is considered as: (1) In the OpenFOAM domain, the cumulative changes in both ice and water volumetric contents due to vapor transport are stored as $\Delta\theta_{i,cum_{vap},OF}$ and $\Delta\theta_{w,cum_{vap},OF}$ respectively, (2) the absolute changes in both ice and water volumetric contents due to vapor transport in the SNOWPACK solution (already given form the OpenFOAM solution) are stored as $\Delta\theta_{i,vap,SN}$ and $\Delta\theta_{w,vap,SN}$ respectively, (3) then, these absolute and cumulative changes due to vapor transport are subtracted from the new ice and water content calculated in SNOWPACK as $\theta_{i,SN}$ and $\theta_{w,SN}$ respectively, (4) finally, after the SNOWPACK solution, the new ice and water content in the OpenFOAM domain may be calculated as $\theta_{i,OF} = \theta_{i,SN} - \Delta\theta_{i,vap,SN} + \Delta\theta_{i,cum_{vap},OF}$ and $\theta_{w,OF} = \theta_{w,SN} - \Delta\theta_{w,vap,SN} + \Delta\theta_{w,cum_{vap},OF}$ repressively. Note that the subscript *SN* refers to the SNOWPACK solution while *OF* refers to the OpenFOAM domain. Note further that for any required quantities for the information exchange between the SNOWPACK and OpenFOAM domains, the interpolation process is done by comparing the height of an element in OpenFOAM with element heights in SNOWPACK. This implies that the interpolation from the SNOWPACK solution is done uniformly in the lateral direction into the OpenFOAM domain. Adding or removing layers is governed by criterion of minimum and maximum layer thicknesses, chosen as 0.005 m and 0.01 m, respectively. These values are consistent with a chosen value of 0.0075 mm for the height of a new element in SNOWPACK to have almost the same number of elements in both SNOWPACK and OpenFOAM, which is important to preserve layer properties in the profiles when interpolating between SNOWPACK and OpenFOAM.

(ii) the only feedback from OpenFOAM to SNOWPACK is laterally-averaged snow density change rate due to water vapor transport. However, because of convection effects, laterally-averaged temperature profiles would be different from the SNOWPACK solution. In the future, (1) the averaged temperature profiles from the OpenFOAM solution can be used as an initial temperature profile for the next time step of SNOWPACK, and (2) the interpolated density change rate due to vapor transport from the OpenFOAM solution will be used for the metamorphism calculation in SNOWPACK. Note that thermal boundary conditions in OpenFOAM for the top and bottom boundaries will be set from the SNOWPACK solution. It is worth mentioning that it is practically possible to use several parallel SNOWPACK solutions in the lateral direction in the OpenFOAM domain. Because of lateral heterogeneity in snow density (as discussed later in section 4.3), the

snow compaction is different and this would result in different snow heights for each SNOWPACK solution. This makes a discontinuity on the top boundary and avoids to use the same dynamic mesh strategy in OpenFOAM used in this chapter only for one SNOWPACK solution for the whole OpenFOAM domain. To address this problem for the future work, from the numerical modeling perspective in OpenFOAM it is possible for each SNOWPACK domain to have its own mesh which is disconnected from the neighbouring meshes (the neighbouring SNOWPACK domains). However, careful attention needs to be made (1) to meaningfully set up the thermal and flow boundary conditions at the discontinuity patches on top, and (2) for the information exchange between neighbouring meshes (each SNOWPACK solution) in the OpenFOAM domain. Note that in the SNOWPACK-OpenFOAM coupling, the soil part is only considered in SNOWPACK as convection is unlikely to occur in the soil. However, later with using several parallel SNOWPACK solutions in the lateral direction of the OpenFOAM domain, it is possible to represent the lateral thermal variations at the bottom of snowpack for the OpenFOAM solution as referred to in chapter 3.

(iii) in case of melting-refreezing and water transport, (1) the water transport is only modelled by SNOWPACK, (2) the phase change calculation for melting-refreezing process in SNOWPACK is treated explicitly and therefore the temperature is forced to be the melting temperature in SNOWPACK, (3) however, in OpenFOAM, thermal equilibrium is assumed between the ice and water while the local thermal non-equilibrium model is still considered between the ice-water mixture and the gas phase. Note that in case the short wave radiation is large enough to increase the ice temperature in OpenFOAM, we limit it by the melting temperature (as it is explicitly done in SNOWPACK for melting-refreezing process) and therefore we do not directly use the heat source/sink term from melting-refreezing in OpenFOAM. The heat transfer equations for the ice-water mixture and the gas phase are similar to those presented in Jafari et al. (2022) (chapter 2) except for the changes due to presence of water and the heat source/sink term from shortwave radiation absorption. The energy equations with above mentioned changes compared to ones in Jafari et al. (2022) (chapter 2) in terms of temperature for the gas phase and ice-water mixture are presented as:

$$
\frac{\partial}{\partial t}(\epsilon_g \langle \rho_g \rangle^g c_{pg} \langle T_g \rangle^g) + \nabla \cdot (\langle \rho_g \rangle^g c_{pg} \langle T_g \rangle^g \langle \boldsymbol{U}_g \rangle) = \nabla \cdot (\epsilon_g k_{\text{eff},g} \nabla \langle T_g \rangle^g)
$$

$$
+ \epsilon_g \frac{\partial}{\partial t} \langle P_g \rangle^g + \langle \boldsymbol{U}_g \rangle \cdot \nabla \langle P_g \rangle^g - \nabla \cdot \left[ \langle T_g \rangle^g (c_{pv} - c_{pa}) \langle J_v \rangle \right]
$$

$$
+ h_c a_s \left[ (\langle T_g \rangle^g (w_g - 1) - \langle T_i \rangle^i w_i) \right] + (\dot{m}_{iv} + \dot{m}_{wv}) c_{pv} \langle T_g \rangle^g \quad (4.1)
$$

$$\frac{\partial}{\partial t}(\rho_i c_{pi}\epsilon_i\langle T_i\rangle^i + \rho_w c_{pw}\epsilon_w\langle T_i\rangle^i) = \nabla\cdot(\epsilon_i k_{\text{eff},i}\nabla\langle T_i\rangle^i + \epsilon_w k_{\text{eff},w}\nabla\langle T_i\rangle^i)$$

$$-h_c a_s\left[(\langle T_g\rangle^g(w_g-1)-\langle T_i\rangle^i w_i)\right]$$

$$-\dot{m}_{iv}c_{pv}(\langle T_g\rangle^g w_g + \langle T_i\rangle^i w_i) - \dot{m}_{iv}(c_{pi}-c_{pv})T_{\text{ref}} - \dot{m}_{iv}L_{iv}$$

$$-\dot{m}_{wv}c_{pv}(\langle T_g\rangle^g w_g + \langle T_i\rangle^i w_i) - \dot{m}_{wv}(c_{pw}-c_{pv})T_{\text{ref}} - \dot{m}_{wv}L_{wv}$$

$$+Q_{swr} \quad (4.2)$$

In the above equations, respectively, $\epsilon_i$, $\epsilon_w$, $\epsilon_g$ are the volume fractions for ice, water, and gas phase, $\dot{m}_{wv}$ and $\dot{m}_{iv}$ are the rates of phase change from water to vapor and from ice to vapor, $\rho_i$, $\rho_w$, $\rho_g$ are the densities for ice, water, and gas phase, $c_{pi}$, $c_{pw}$, and $c_{pg}$ are the specific heat capacities for ice, water, and gas phase, $\langle T_i\rangle^i$ is the temperature of water-ice mixture and it is the ice temperature if the water is absent, $k_{\text{eff},i}$, $k_{\text{eff},w}$, and $k_{\text{eff},g}$ are the effective thermal conductivities of ice, water, and the gas phase in snow, $\langle \boldsymbol{U}_g\rangle$ is the bulk gas-phase velocity vector, $\langle P_g\rangle^g$ is the gas pressure, $h_c$ is the heat transfer coefficient, $a_s$ is the specific surface area, $T_{\text{ref}} = 273.15$ K is the reference temperature, and finally $Q_{swr}$ is the heat source due to shortwave radiation absorption. Many of the parameters defined here are the same as presented in Jafari et al. (2022). Note that (1) the thermal conductivities are calculated by a parametrization presented in Lehning et al. (2002d) and used in SNOWPACK and they are indeed extracted from the definition of the effective thermal conductivity of snow as $k_{\text{eff},s} = \epsilon_i k_{\text{eff},i} + \epsilon_w k_{\text{eff},w} + \epsilon_g k_{\text{eff},g}$ (Calonne et al., 2012; Hansen and Foslien, 2015), (2) the calculation of the mass transfer coefficient between ice and vapor, introduced as $h_m$ in Jafari et al. (2022), is also assumed the same between water and vapor, and (3) the specific surface area $a_s$ is calculated as explained in Jafari et al. (2020) when both water and ice are present.

(iv) For the calculation of all parameters dependent on the grain diameter such as specific surface area, the pore Reynolds number and snow permeability, we use the "classical" grain size not the optical grain diameter. SNOWPACK provides both the classical (heuristic) grain size as $r_g$ and optical grain size as $r_{osg}$ which is directly linked to the specific surface area (Calonne et al., 2012) but only a parameterized quantity in SNOWPACK. Based on the simulations in this chapter, the values for $r_{osg}$ are often smaller in particular at the bottom of snowpack by a factor of two. This means using $r_{osg}$ compared to $r_{osg}$ induces smaller permeability and flow velocity (pore Reynolds number). In this chapter, we use $r_g$ and have therefore more convection than if we used $r_{osg}$. Obviously, a smaller flow velocity obtained by using optical grain size implies that the effects of convection would be more limited. The sensitivity on grain size parameterization could be explored in future work.

(v) Within one time step of SNOWPACK (15 min is chosen in this chapter), OpenFOAM integrates over several smaller adjustable time steps based on the maximum Courant number of 5. Note that it is possible to use the PIMPLE algorithm for higher values of the

maximum Courant number in OpenFOAM as employed in Jafari et al. (2022) (chapter 2), but as the thermal boundary condition is changing through the SNOWPACK solution and therefore there is a transient thermal process, it is faster to use the smaller maximum Courant number of 5 (numerically stable) with the PISO algorithm (Moukalled et al., 2016). Note that within a 15 min time interval for coupling, for the first few minutes in OpenFOAM there are transient changes for the thermal regime and the flow velocity and after that it will be often (not always) a steady-state process till the end of 15 min time interval. Therefore, to avoid computational cost, it is possible to freeze the thermal and flow calculation in OpenFOAM for the steady-state part of a 15 min time interval and only update the snow density change due to vapor transport. We call this strategy as "flow-freezing" time integration and in this chapter we use the threshold of 60 sec after which the thermal and flow calculation in OpenFOAM is stopped till the end of 15 min time interval. We performed simulations with full transient time integration and compared it to "flow freezing" for only the first two months of a winter season in Bylot herb tundra. We found that (1) it takes 21 hours (with four MPI processors) of computer runtime while it takes only 5 hours with "flow-freezing" and (2) the averaged cumulative density changes have shown acceptably small differences. We point out, however, that the snow density change rate and flow velocity are similar only for moderate convection events and they are quite different for the strong convection events observed at the end of the second month in the winter season. These values are smaller for "flow-freezing" again in particular at the bottom of the snowpack (smaller by a factor of two), where strong grain growth leads to stronger convection. This implies that we may underestimate the effects of convection when using "flow-freezing". Again, further sensitivity studies are needed to explore this effect together with the grain size representation. It is further important to mention that the calculated snow density change rate due to vapor transport from OpenFOAM to SNOWPACK is chosen at the end of 15 min time interval and not averaged over 15 min, based on the same assumption that a steady state situation is attained. Time averaged snow density change rates over 15 min time interval in OpenFOAM would be a better choice if transient effects within the 15 minutes master time step are important.

(vi) Thermal dispersion and hydrodynamic dispersion (for mass transfer) are not considered in this study. Thermal and hydrodynamic dispersion coefficients are often considered as an additional tensorial term added to the effective thermal conductivity and vapor diffusivity, respectively. These coefficients are important for strong advection and convection, i.e. when the pore Péclet number $Pe_p = ScRe_p > 1$ with $Sc$ as the Schmidt number and $Re_p$ as the pore Reynolds number (Bear, 1961, 1988; Calonne et al., 2015). For convection in idealized snowpacks as reported by Jafari et al. (2022), the pore Reynolds number and consequently Péclet number are smaller than 1. However, based on the results in this chapter for convection in real snowpacks (Bylot herb tundra), for the first few centimeters in downward flow at bottom of the snowpack and only when convection forms low density patches there, the pore Péclet number can reach values up to 10 depending on the convection strength. Note that as mentioned in item (iv), these results are based on the classical grain size which often induces larger snow permeability and flow velocity.

```
          ╱─────────────────────────────────────╱
         ╱      Start of time integration        ╱
        ╱─────────────────────────────────────╱
                          │
                          ▼
            ┌───────────────────────────┐
            │     SNOWPACK solution      │
            └───────────────────────────┘
                          │
                          ▼
     ┌─────────────────────────────────────────┐
     │  SNOWPACK-OpenFOAM mesh synchronization  │
     └─────────────────────────────────────────┘
                          │
                          ▼
     ┌─────────────────────────────────────────┐
     │  SNOWPACK to OpenFOAM interpolation      │
     └─────────────────────────────────────────┘
                          │
                          ▼
            ┌───────────────────────────┐
            │     OpenFOAM solution      │
            └───────────────────────────┘
                          │
                          ▼
     ┌─────────────────────────────────────────┐
     │  OpenFOAM to SNOWPACK interpolation      │
     └─────────────────────────────────────────┘
                          │
                          ▼
          ╱─────────────────────────────────────╱
         ╱      End of time integration          ╱
        ╱─────────────────────────────────────╱
```
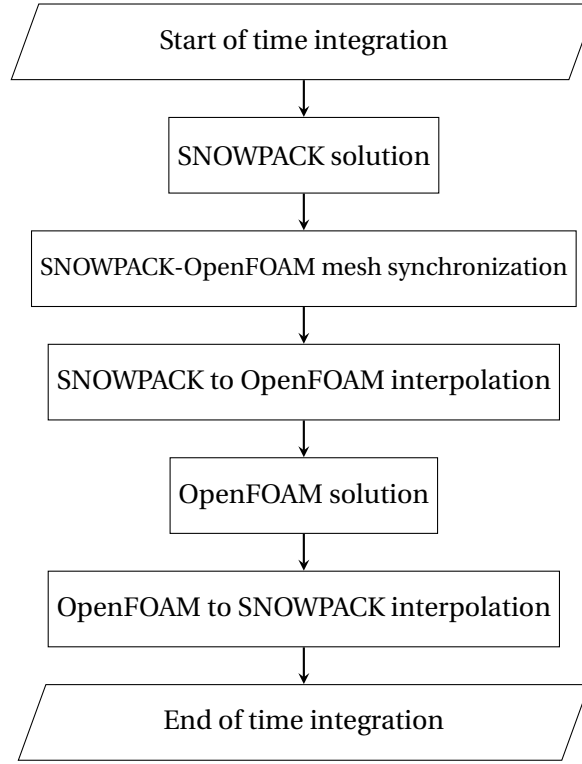
Figure 4.1: The coupling procedure between SNOWPACK and OpenFOAM.

Using the optical grain size (lower snow permeability and flow velocity), the pore Péclet number would remain smaller up to 2.8. For the gas flow in the porous medium with randomly packed spheres based on Delgado (2007), the ratio of hydrodynamic dispersivity to diffusivity is on the order of the Péclet number for $1 < Pe_p < 10$. Thus, effects of dispersion could be locally important and should further be explored. Nield and Bejan (2017); Kvernvold and Tyvand (1980) discuss that thermal dispersion does not affect the critical Rayleigh number which is based of effective molecular diffusivity but it can influence the flow structure in a convection cell (Nield and Bejan, 2017; Wen et al., 2018; Fahs et al., 2020).

In summary, for the OpenFOAM solution as presented in detail in Jafari et al. (2022), an Eulerian–Eulerian two-phase approach is used to solve mass conservation equations for the gas mixture (humid air), water vapor component, and ice phase, the momentum equation for the gas mixture, and finally the temperature-based energy equations for the gas and ice phases. Therefore, the numerical output from OpenFOAM solver provides solutions for water vapor and air component densities, snow porosity and density, the gas flow velocity, the diffusive water vapor flux, the phase change rate between ice and vapor, and finally the temperature for the gas and ice phases.

## 4.3   Results and Discussion

For thick snow covers (e.g. Alpine and sub-arctic), no convection of water vapor has been observed in our numerical analysis because of both insufficient temperature gradients and high snow density. However, for a herb tundra permafrost, situated at Bylot Island, Canadian high Arctic, conditions to trigger convection are at least partially fulfilled. Forcing data from observations for snow depth and surface temperature (Domine et al., 2021) are used to drive the SNOWPACK model. The following results presented for Bylot herb tundra are based on assumptions and limitations explained in section section 4.2. As mentioned in item (iv) of section 4.2, the normal grain size from SNOWPACK is used, which is often larger than the optical grain size. Obviously, using the optical grain size would induce lower flow velocities and the results will be quantitatively different. Also, we used the measured snow heights and surface temperatures to drive the SNOWPACK model. Using the precipitation and heat fluxes to drive SNOWPACK often leads to much colder temperature regimes.

Here, we analyse the effects of convective water vapor transport at Bylot over tundra permafrost for three winter seasons. The time series for the temperature profiles due to only diffusive vapor transport from SNOWPACK simulations are shown in figure 4.2. As can be seen in this figure, there are several persistent cold events, some of which have been active for a few months. For instance, during the winter season 2017-2018, there were three main cold events, the second of which began on December 15 and lasted for three months and a half with almost no change in the snow height.
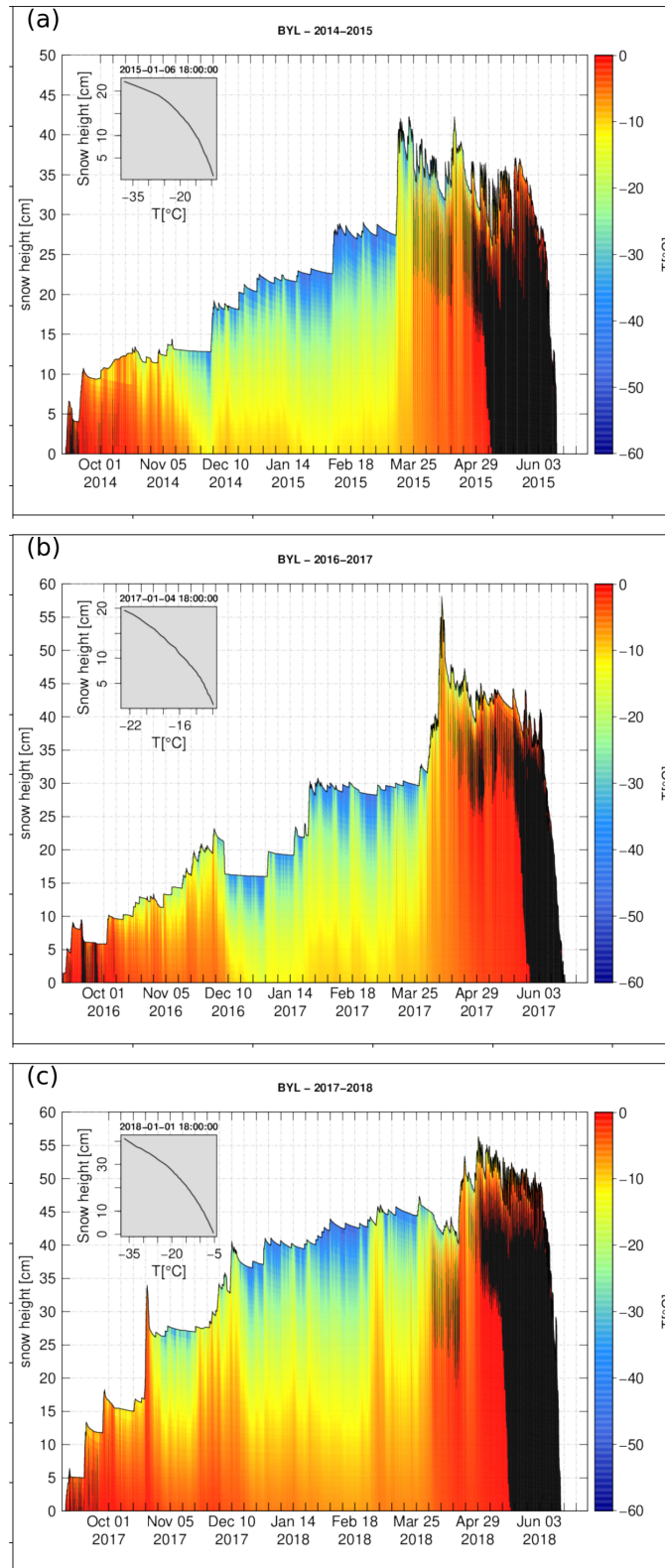
Figure 4.2: The time series of snow temperature from SNOWPACK simulation with only diffusion in Bylot herb tundra for (a) winter season 2014-2015, (b) winter season 2016-2017, and (c) winter season 2017-2018. The insets show the vertical profiles on early January for all three years. Black color refers to zero values.

115

SNOWPACK simulations with only diffusion are compared to those with convection from SNOWPACK-OpenFOAM simulations, as shown in figure 4.3 and figure 4.4 for cumulative density change and also in figure 4.5 and figure 4.6 for snow density change rate due to water vapor transport. At Bylot, a large enough temperature difference and low enough snow density fulfill the conditions for significant and persistent convection events that are well synchronized with cold events. For example, during these cold events, SNOWPACK-OpenFOAM simulations show higher values of snow density change rate compared to SNOWPACK simulations (comparing figure 4.5a with figure 4.5b for winter season 2016-2017, and figure 4.6a with figure 4.6b for winter season 2017-2018). This also shows a meaningful difference in snow density change when compared to diffusion from SNOWPACK simulations, particularly for the snow density increase in the deposition zone. For example, the cumulative snow density change is increased by 35 kg m$^{-3}$ in the winter season 2017-2018 whereas the increase by diffusion from SNOW-PACK simulations is small and around 5 kg m$^{-3}$ (comparing figure 4.4a to figure 4.4b). This would be even larger and around 55 kg m$^{-3}$ for local cumulative density change as is shown in figure 4.9f for two-dimensional profiles.

A higher decrease in cumulative density change with a different profile is also observed from SNOWPACK-OpenFOAM results compared to diffusion from SNOWPACK simulations. This can be seen by comparing the subplots of figure 4.3 for winter season 2016-2017 and figure 4.4 for winter season 2017-2018. Moreover, an effective depth of about 10-20 cm is observed for decreased snow density by convective vapor transport (figure 4.7a and e) while for diffusive vapor transport, the reduced snow density is mainly observed for a thin layer close to the ground (figure 4.7a, c and e). Similarly, the density profiles observed before the melt season from SNOWPACK-OpenFOAM simulations, have an obvious shift and decrease compared to diffusion-only results (figure 4.7b, d and f). This decrease is not limited only to layers close to the ground and it can be seen almost through the whole snow column, in the range between 20 to 40 kg m$^{-3}$ for the winter season 2014-2015 (figure 4.7b), 20 to 100 kg m$^{-3}$ for the winter season 2016-2017 (figure 4.7d), and finally 20-80 kg m$^{-3}$ for the winter season 2017-2018 (figure 4.7f).

Figure 4.3: The time series of cumulative density change for winter 2016-2017 in Bylot herb tundra, (a) SNOWPACK simulation with diffusion and (b) SNOWPACK-OpenFOAM simulation with convection. The insets in (a) and (b) show the vertical profiles on 4 January 2017 18:00:00. Black color refers to zero values.
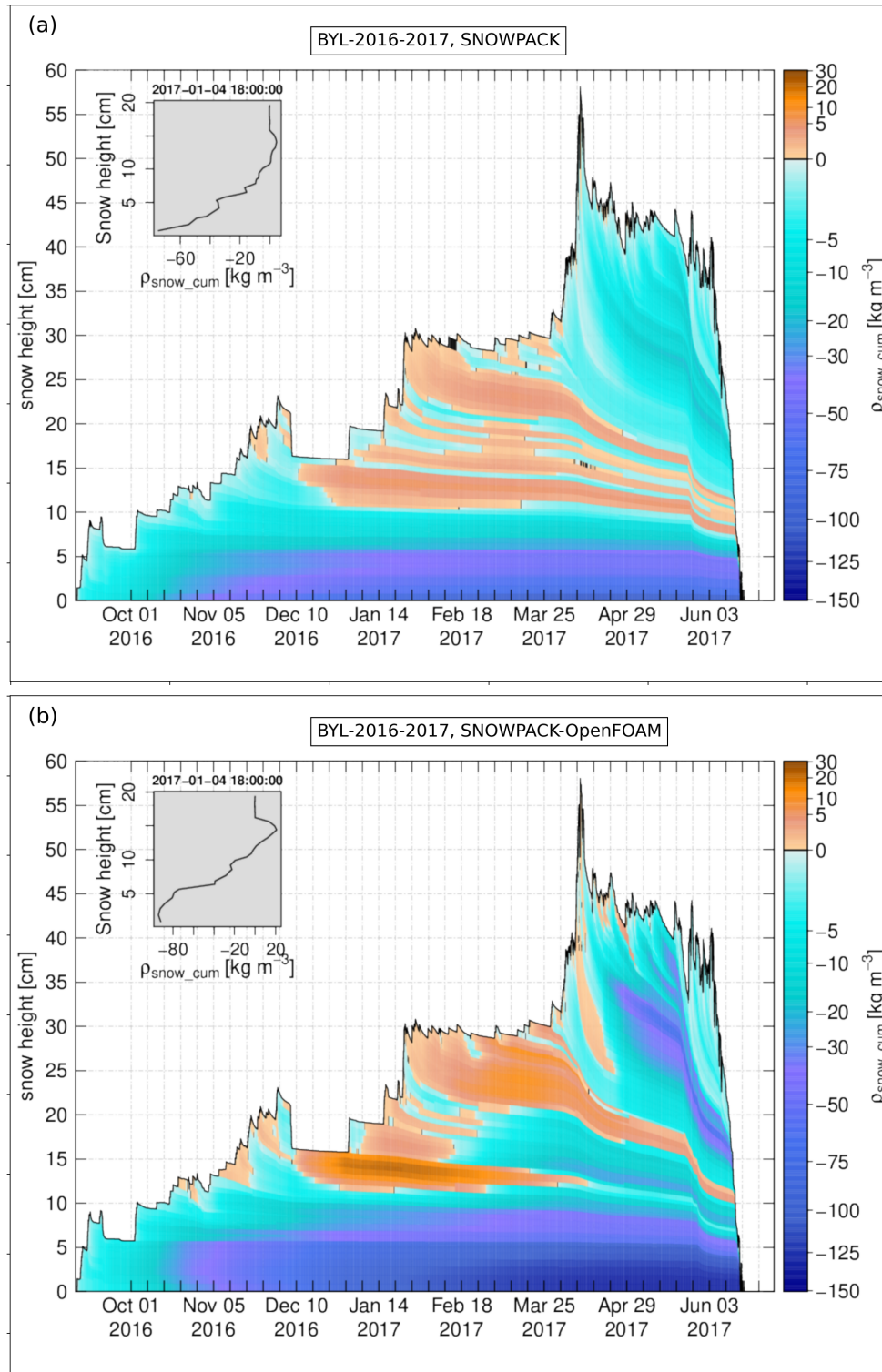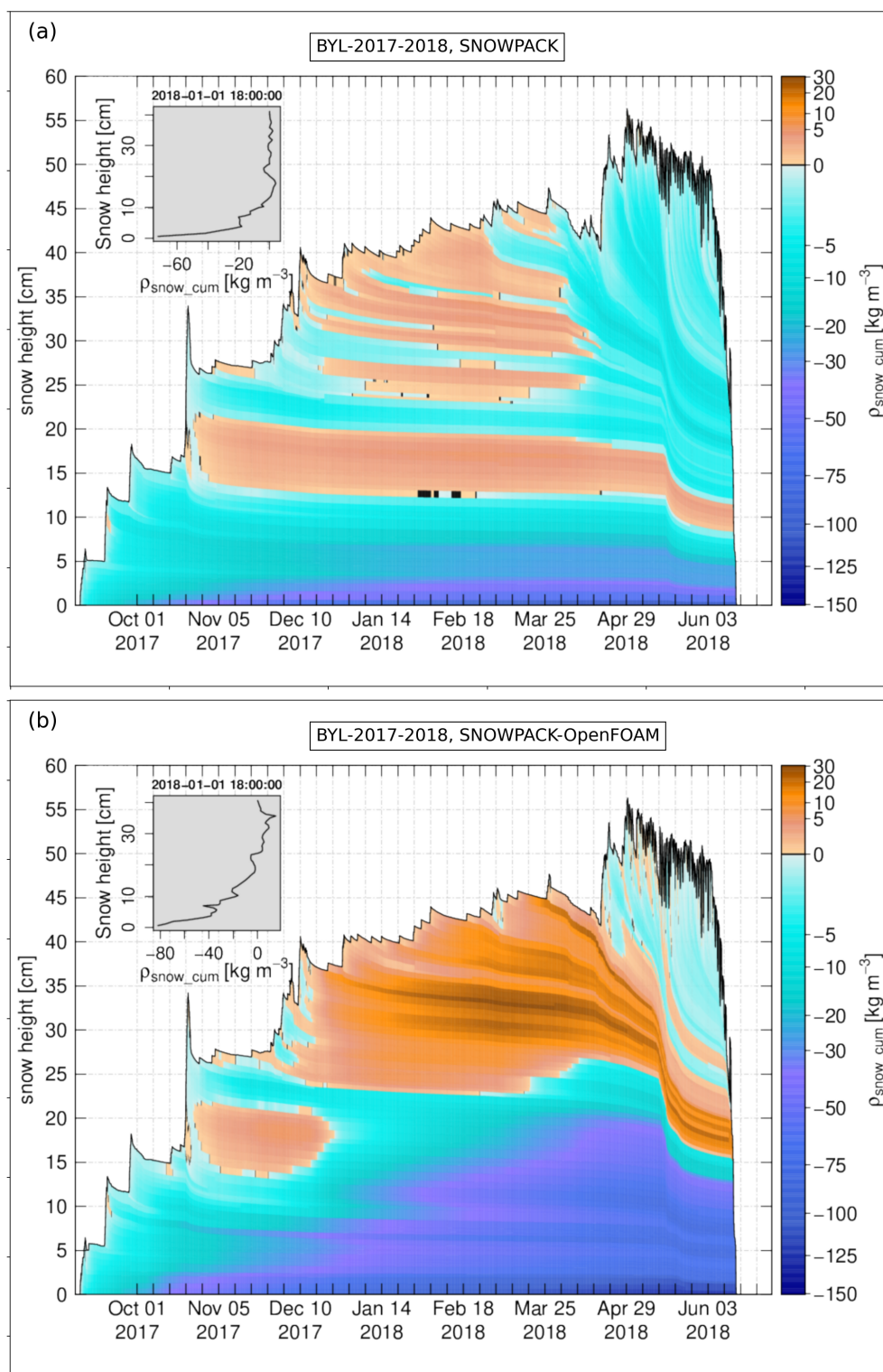
Figure 4.4: The time series of cumulative density change for winter 2017-2018 in Bylot herb tundra, (a) SNOWPACK simulation with diffusion and (b) SNOWPACK-OpenFOAM simulation with convection. The insets in (a) and (b) show the vertical profiles on 1 January 2018 18:00:00. Black color refers to zero values.
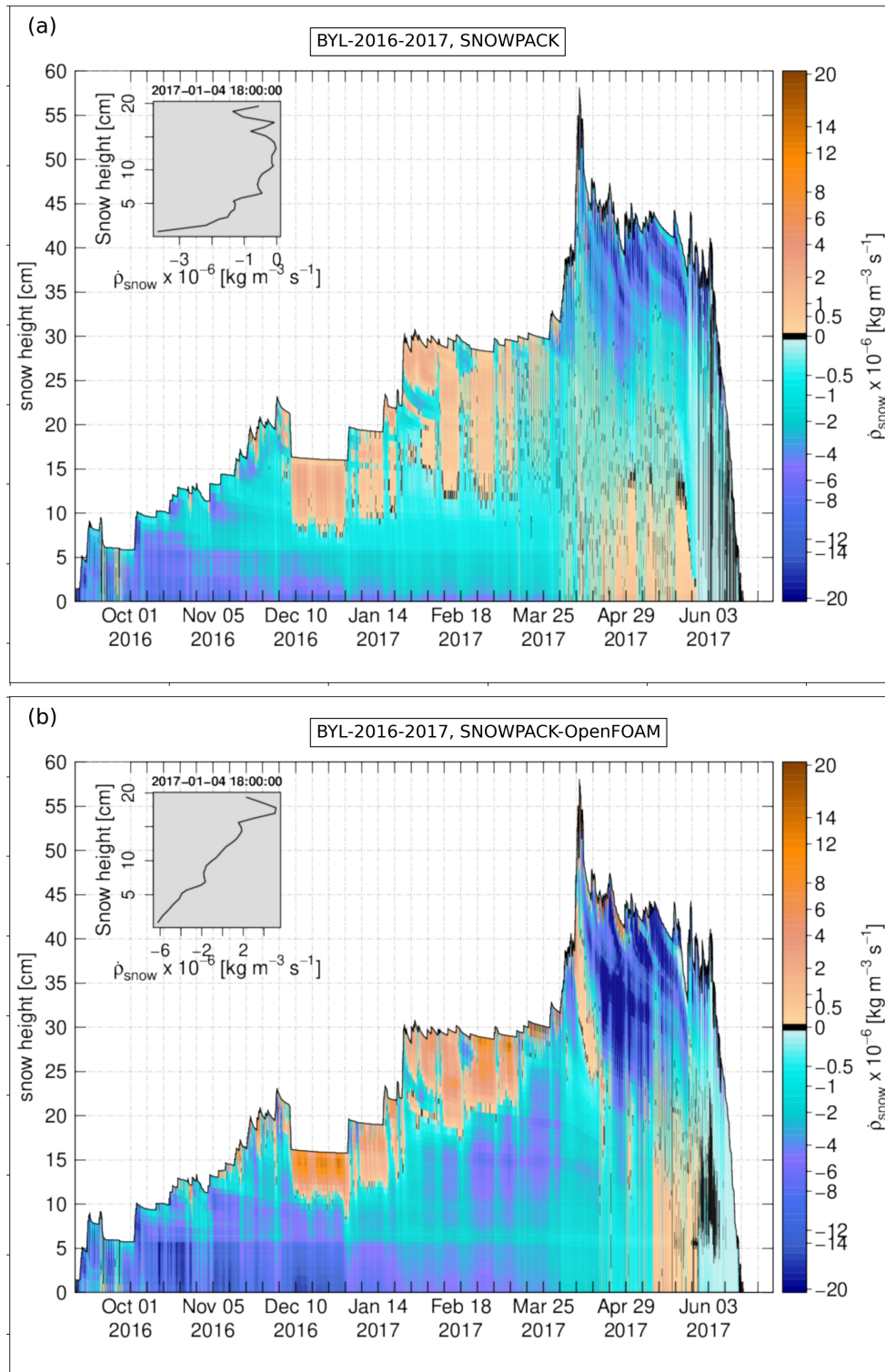
Figure 4.5: The time series of snow density change rate due to vapor transport for winter 2016-2017 in Bylot herb tundra, (a) SNOWPACK simulation with diffusion and (b) SNOWPACK-OpenFOAM simulation with convection. The insets in (a) and (b) show the vertical profiles on 4 January 2017 18:00:00. Black color refers to zero values.

Figure 4.6: The time series of snow density change rate due to vapor transport for winter 2017-2018 in Bylot herb tundra, (a) SNOWPACK simulation with diffusion and (b) SNOWPACK-OpenFOAM simulation with convection. The insets in (a) and (b) show the vertical profiles on 1 January 2018 18:00:00. Black color refers to zero values.
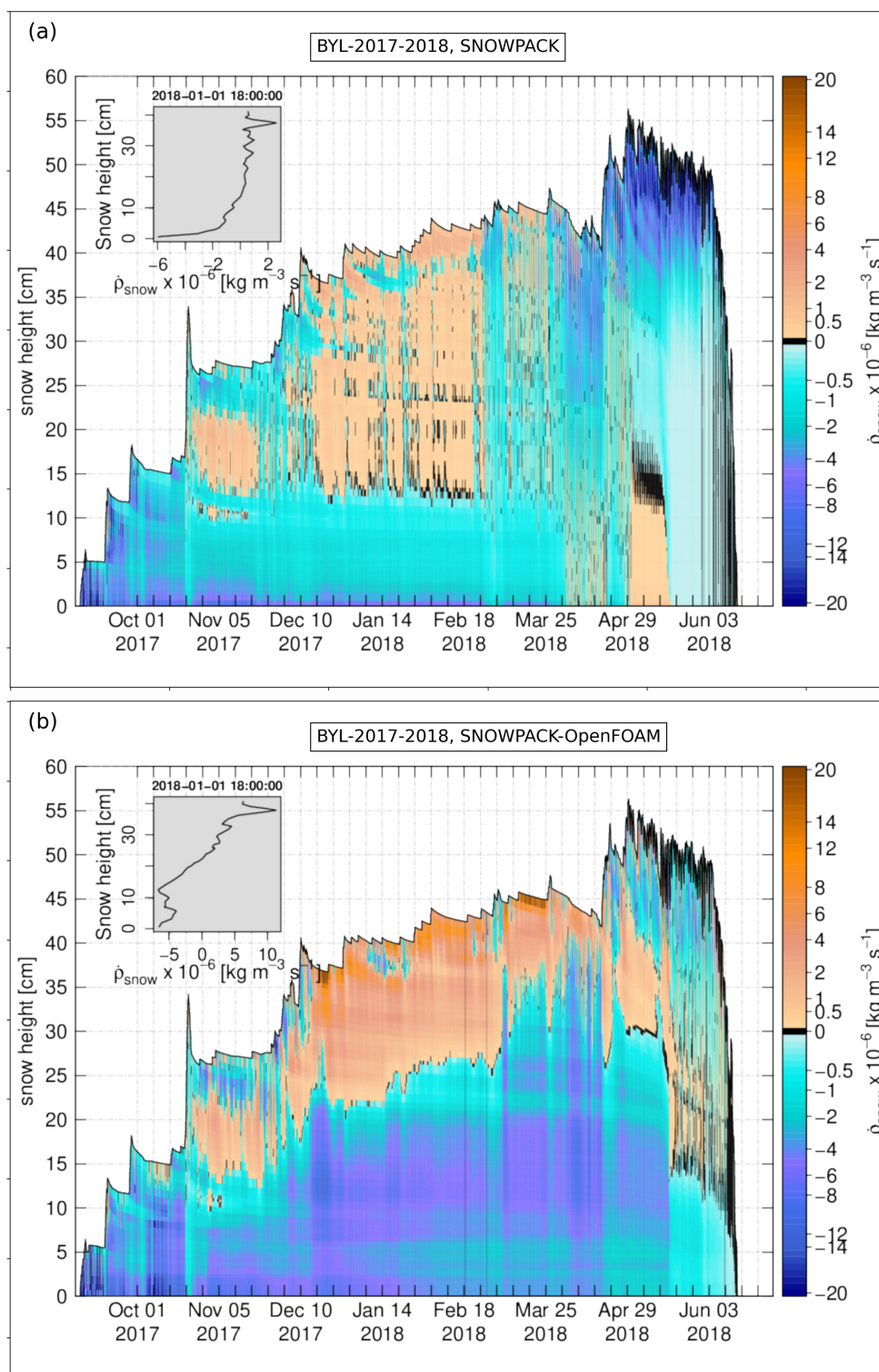
As an example, here we focus on the winter season 2017-2018 to explore the effects of convection on the thermal and phase change regimes and how it laterally and vertically changes the snow density and temperature. To do this, the two-dimensional profiles for snow density are shown in figure 4.8 at the end of second cold event on March 11. As can be seen, the convection cells have the same pattern for shaping the snowpack structure but they are different in size with smallest width as 40 cm and the largest one as 85 cm (figure 4.8).

Time snapshots to show the evolution in snow density due to convective water vapor transport for the beginning (December 14), middle (January 26), and end (March 11) of the second cold event are shown in figure 4.9. For the first snapshot, we do not see a large footprint of convection in the snow density (figure 4.9a) but we can observe the changes in the cumulative snow density change (figure 4.9d). As indicated in figure 4.9 for phase change rate from ice to vapor, for all three snapshots, we can see that sublimation is significant for the whole downward flow and not only for the layer close to the ground. This is different from what we observed for the effective sublimation zone in idealized snowpacks discussed in Jafari et al. (2022). For the second time snapshot (middle of the second cold event on December 14), the sublimation can already create a vertical low density path through the downward flow to consequently have increased flow velocity in the whole downward flow. This process continues till the end of the second cold event such that the convection cells gets stronger and more stable over time and stay at their initial location. Here, we do not see the lateral displacement of the convection cells, which is again different from what we indicated for idealized snowpacks in Jafari et al. (2022).

One more different observation for convection in real snow covers from the one in idealized snowpacks is that the deposition zone often expected to be on top in the upward flow is distorted toward the top between main downward and upward flows for convection in real snow covers. This is interesting because although the convection cells do not migrate laterally, but the flow-blocking process in upward flow due to deposition may still distort the deposition zone toward the region on top between downward and upward flows (figure 4.9l).

Furthermore, as can also be seen from figure 4.10, significant lateral variations within a convection cell are present on OpenFOAM-SNOWPACK coupling for snow density, cumulative snow density change, and snow temperature. In figure 4.10, these profiles are plotted over three different vertical lines (as drawn in figure 4.9c) i.e. line 1 for upward flow, line 2 between upward and downward flows, and finally line 3 for downward flow. For example, lateral differences up to $80 \text{ kg m}^{-3}$ (90%) are observed for snow density (figure 4.10b and c) and up to 6.5 K (32%) for snow temperature (figure 4.10f and g) at the end (March 10) of the second cold event in the winter season 2017-2018.

## 4.4   Conclusions, Limitations and Outlook

In this chapter, convective vapor transport in more realistic snow covers and its effects on snowpack structure have been investigated numerically. To that end, a C++ interface has been
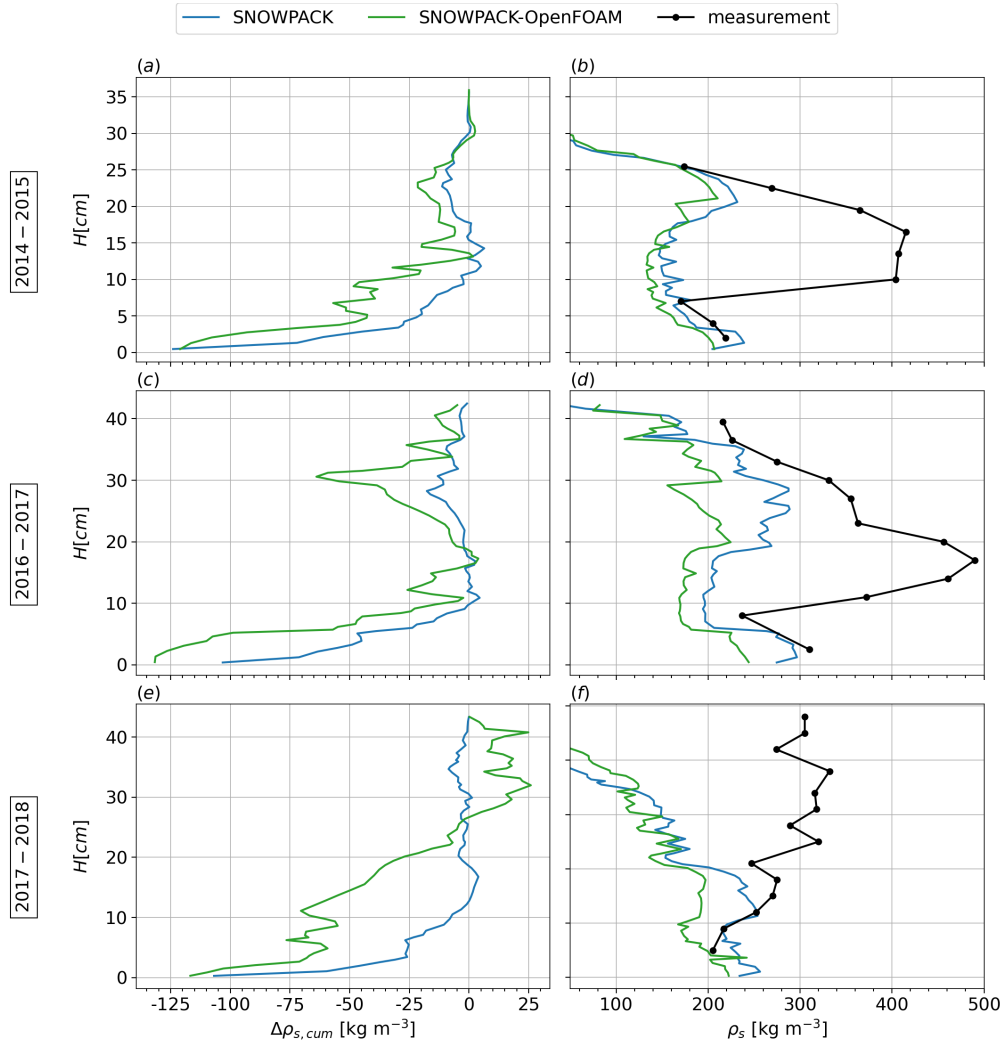
Figure 4.7: Comparison between diffusion from SNOWPACK simulation and convection from SNOWPACK-OpenFOAM simulation for cumulative snow density change and snow density profiles on 12 April 2015 12:00:00 for winter season 2014-2015, 13 May 2017 12:00:00 for winter season 2016-2017, and 14 April 2018 12:00:00 for winter season 2017-2018.
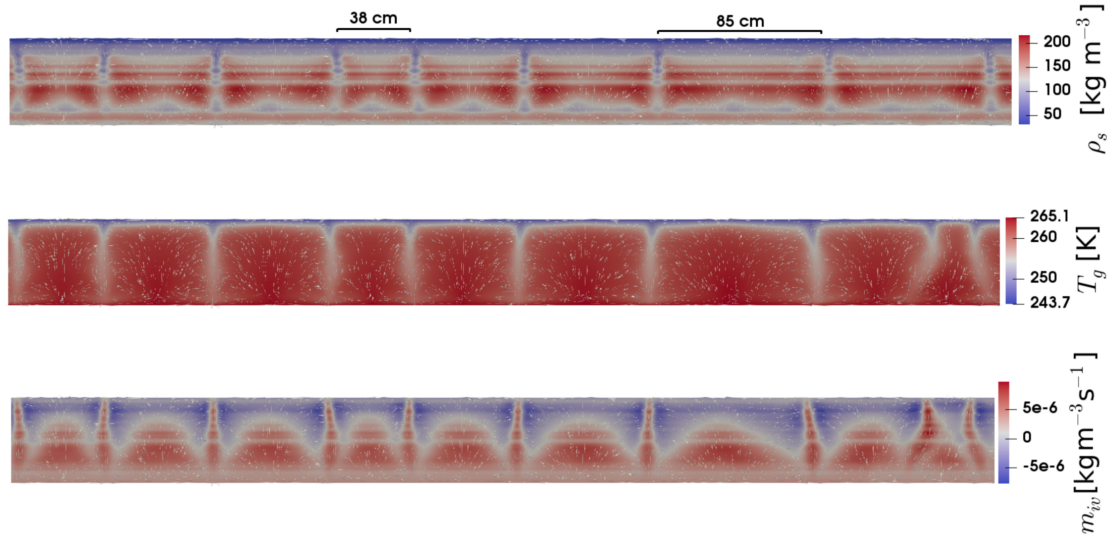
Figure 4.8: Simulated two-dimensional plots from SNOWPACK-OpenFOAM coupling on 11 March 2018 12:00:00 for (a) snow density, (b) the gas phase temperature, and (c) the phase change rate from ice to vapor.
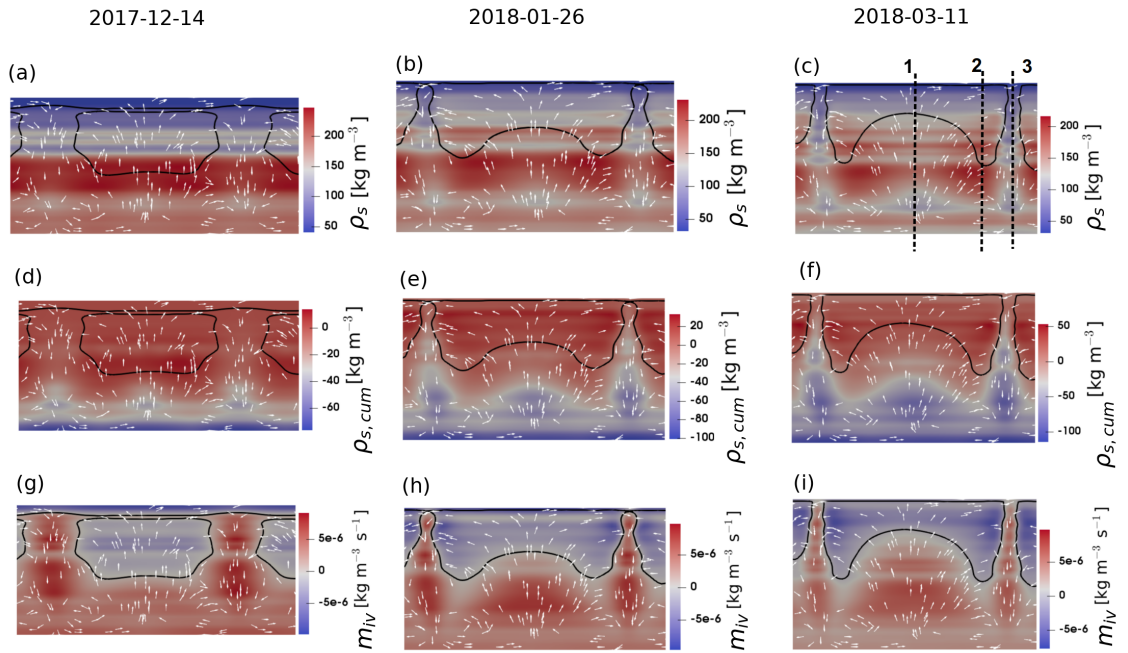


Figure 4.9: Evolution of snow density, cumulative snow density change, and phase change rate from ice to vapor for different dates as December 14, January 26, and March 11 in the winter season 2017-2018. The white arrows show the flow direction and are not scaled with the velocity magnitude.

123
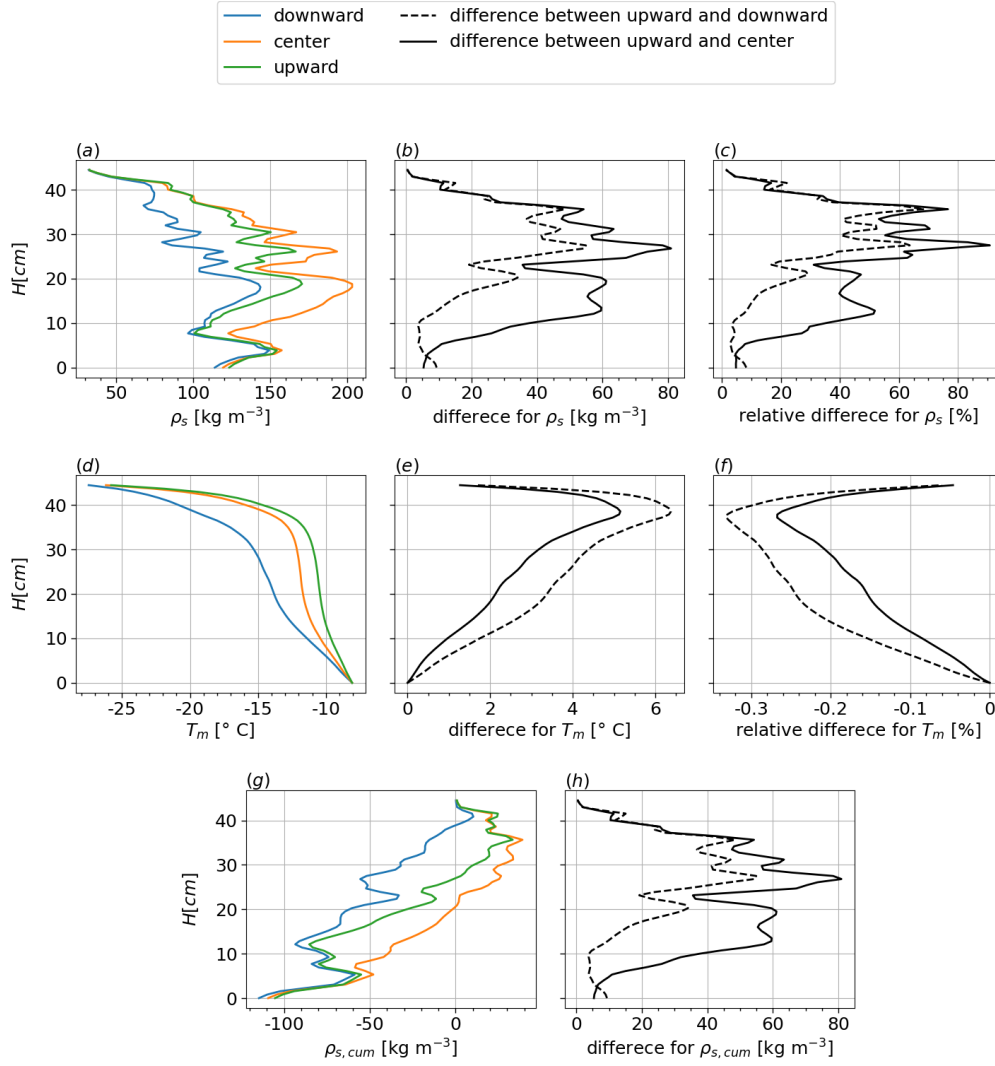
Figure 4.10: Lateral variations in a convection cell for the snow density, temperature, and cumulative snow density change due to water vapor transport. These profiles are plotted over three vertical lines as drawn in figure 4.9c on March 11 in winter seasons 2017-2018.

implemented for a tight coupling between SNOWPACK and OpenFOAM.

Looking at time series of temperature profiles, it is found that strong snow density change rates due to sustained convection are strongly linked to persistent cold events observed for Bylot herb tundra. Compared to diffusion results, a larger increase in cumulative snow density change up to 55 kg m$^{-3}$ is observed close to the snow surface. Furthermore, it is shown that a significant decrease in snow density due to convective vapor transport (e.g. 20 to 100 kg m$^{-3}$ for the winter season 2016-2017) is not limited only to a small layer at the base but it has an effective depth of about 10-20 cm, which corresponds better to observations.

Investigating lateral and vertical effects of convection on the thermal and phase change regimes for Bylot, it is found that convection cells qualitatively have the same footprint on the snowpack structure but with different lateral sizes, from about 40 to 85 cm. Different from what observed for convection in idealized snowpacks, it is further found that (1) sublimation is significant for the whole downward flow not only for the layer close to the ground, (2) the convection cells become more stable over time and do not move laterally, and (3) flow-blocking process due to deposition may still move the deposition zone toward the region on top between downward and upward flows. Lateral variations up to 80 kg m$^{-3}$ (90%) for snow density and up to 6.5 K (32%) for snow temperature indicate major gradients within a convection cell, which may substantially influence secondary processes such as metamorphism and melt-refreeze to laterally vary in the snowpack.

By using SNOWPACK-OpenFOAM coupling, we tested the hypothesis that one-dimensional snow models need to take into account water vapor transport to better capture snow profiles often observed for Arctic snowpacks (i.e. high density on top and lower density in the bottom). The model system simulated in this study leads to a better understanding of the potential impacts of convection in snow covers and how it changes the snow structure, as earlier reported in this chapter. However, results show a significant difference between observed snow density profiles and simulated ones even when the effects of convection are included (figure 4.7b, d and f). This shows that the snow model itself needs to be adjusted for Arctic snow covers by further improvements of other important processes shaping the snow profiles such as snow settling and wind compaction. For Samoylov as discussed in chapter 1, some adjustments for these processes have been already used to have a better representation of snow profiles. Therefore, we need to make the cautionary remark that a realistic high snow density on top - if simulated correctly - could prevent convection, which is a clear limitation of the results discussed above. It needs to be subject of further research, which is not easy as the dynamics of wind compaction are not fully understood and no physics-based model exists, apart from parameterizations as in Gouttevin et al. (2018). As for the Arctic site situated at Samoylov Island, Russia, if we include the effects of wind compaction by using this tailor-made parametrization for new snow density, a layer of high density forms on top. In this case, numerical analysis by SNOWPACK-OpenFOAM coupling shows that if convection occurs, the cells are formed only in the bottom and as a result the the effects of convection are almost negligible. This coupling model only makes sense if tuning and adjustments for these processes (e.g snow settling and

wind compaction) do not already include the effects of convection otherwise these effects would be accounted for twice. In this respect, we acknowledge that the results presented in this chapter may show the upper limit for the effects of convection since (1) the classical grain size is used which induces higher flow velocities than using the optical grain size, (2) the dispersion effects on the thermal and mass transport regimes are not considered which may be important for the bottom of snowpack where the Péclet number is locally greater than 1, and (3) the effects of wind compaction is not considered as discussed above. In any case, future work should address these problems and the current work may serve as a first step into this uncharted land.

# Conclusions

This thesis presents an in-depth treatment of water vapor transport in snowpacks and its impacts on snow structure. First, a transient-diffusion equation for soil and snow has been implemented in SNOWPACK to explore the diffusive water vapor transport for different snow covers. For natural convection that may occur in snowpack, an Eulerian–Eulerian two-phase method has been developed and then used to comprehensively analyze the thermal and phase change regimes in an idealized snowpack. Furthermore, the potential impact of heterogeneity induced e.g. by shrubs or rocks on convection and diffusion of water vapor has been investigated using the model developed previously for natural convection in the snowpack. Finally, SNOWPACK has been coupled with OpenFOAM in a master-slave way to simulate the combined effects of convection and diffusion of water vapor in natural snow covers.

The diffusive water vapor transport itself shows a significant influence on snow density for shallow Arctic snowpacks and also snow on sea ice from Antarctica, due to very low surface temperatures that generate large temperature gradients through snow in both cases. Our simulations indicate that diffusive vapor transport may generate locally a low density at the base but it is not a sufficient mechanism to explain the observed low density at the base in Arctic snow covers. In particular, diffusion would not create low densities over as much of the snow profile as observed.

Numerical modeling for convection of water vapor in an idealized snowpack brings us new insights about how convection cells influence the heat and mass transfer regimes and how they evolve the snow structure and its properties, in particular the snow density. We observe that once the convection cells are formed, the phase change regime is spilt into the deposition zone on top in the upward flow and sublimation zone in the downward flow extending to the zone of the beginning upward flow. We find that the major part of the sublimation zone is horizontally extended at the base. It is stronger than the deposition zone which is located on top. We also find that because of (1) the reduced snow density at the base by sublimation and consequently the increased gas flow velocity and (2) the flow blocking caused by increased snow density due to deposition on top, the convection cells migrate laterally in the snowpack. This allows a larger area at the bottom and on top to experience sublimation and deposition, respectively. As a result, this changes the initial uniform snow density to "pancake like" layers, with a lower density at the base and larger density on top. It is discussed that, based on non-dimensional equations, the scaling is not complete for normalized water vapor density

as well as the phase change rate. However, for the temperature and its gradient the system is partially scaled with Rayleigh number. It is argued that this is because the contribution of the phase change rate in the mass continuity of water vapor is much larger that the one in heat transfer equations. Also, we show that the contribution of the phase change term in heat transfer equation (particularly for ice phase) cannot be neglected and also the thermal equilibrium assumption is not valid.

Numerical simulations with coupled SNOWPACK-OpenFOAM show that for thick (e.g. Alpine and sub-arctic) snow covers, the large snow density and also small temperature gradients prevent convection and thus diffusion is the only effective mechanism for water vapor transport. With heterogeneity induced e.g. by shrubs in the initial snow density, we observe that convection may be triggered even with sub-critical Rayleigh number as low as 5. We find that depending on the flow strength through the heterogeneity patches, the contributions of convection and diffusion for water vapor transport may be different. We show that for the medium-depth snowpack, e.g. not too thin, not too thick Arctic snowpack, convective vapor transport has the strongest effect on snow density change. For this case, a snow density difference of about 72 kg m$^{-3}$ is observed between the case with and without heterogeneity. The results analyzed here show significant impacts of heterogeneity on the snow density change, overall enhancing the contribution of convection.

By coupling SNOWPACK with OpenFOAM, the upper limits for the impacts of water vapor transport on thermal regimes and mass redistribution are investigated in a herb tundra snowpack, where conditions to trigger convection are satisfied. The findings of this study can be summarized as: (1) significant sublimation is shown for the whole downward flow and not just at the bottom, (2) distortion of deposition is observed from top in upward flow to the top region close to downward flow, and (3) strong lateral gradients in snow density and temperature are caused by convection cells e.g. up to 80 kg m$^{-3}$ (90%) and up to 6.5 K (32%) respectively. Incomplete agreement with measured snow profiles suggests that further investigations for other processes in snow models such as snow settling and wind compaction are needed for accurately modelling Arctic snow covers. In particular, the effect of the ubiquitous wind slab in Arctic environments will limit convection and has to be further investigated. In particular in the coupled simulations, we had to make a number of assumptions and simplifications related to grain size representation, neglect of dispersive effects and regarding flow evolution. Most of these simplifications would rather lead to an overestimation of the effect of convection. For all theses assumptions, sensitivity analyses need to performed to see how much the results will be quantitatively and qualitatively different from the current results, which may show the upper limit for the effects of convection. Moreover, to draw a comprehensive conclusion, the SNOWPACK-OpenFOAM coupling framework needs to be applied for a range of snowpacks that can fulfill the conditions to trigger convection similar to what is observed in a herb tundra snowpack. Based on the current simulations, it is concluded that when convection occurs in real snowpacks (low enough snow densities in addition to large enough temperature gradients), the flow and thermal regimes are expected to be strongly depended on the choice of grain size.

This work has only been possible with assuming simplifications and making assumptions on some settings and quantities. In the following, we present a discussion on assumptions made. Jafari et al. (2022) (chapter 2) report that the pore Reynolds number (fixed grain diameter of 1 mm) for convection in idealized snowpacks is smaller than 1 and therefore the quadratic drag in the momentum equation is negligible compared to the Darcian term. Note that for convection in idealized snowpacks in chapters 2 and 3, the fixed grain diameter of 1 mm is used. For the intrinsic permeability of snow, Calonne et al. (2012) show that their formulation is in good agreement with values obtained by both Zermatten et al. (2011) (if they use the specific surface area per unit of ice volume) and the Carman-Kozeny equation. Therefore, if we revisit the quadratic drag term in the momentum equation, the dimensionless form-drag constant $c_F$ used in this thesis (as an ad hoc procedure by assuming Ergun's equation for momentum which based on Carman-Kozeny equation (Nield and Bejan, 2017)) would be often larger with an average relative error of 90 % compared to the values obtained by Zermatten et al. (2011) using pore scale simulations. This implies that using $c_F$ by Zermatten et al. (2011) would induce less quadratic drag resistance and consequently higher flow velocities than what has been found in this thesis.

In both Eulerian–Lagrangian and Eulerian–Eulerian methods for dilute gas–solid flow modeling, the heat and mass transfer coefficients obtained for a single sphere may be used as e.g. in Sharma et al. (2021) (Eulerian-Eulerian snow transport model), Sharma et al. (2018) (Eulerian-Lagrangian snow transport model), and Russo et al. (2014a) (Eulerian–Lagrangian method for water droplet condensation and evaporation). However, this is not the case for snowpack (dense pack of snow grains) since the bulk heat and mass transfer coefficient is much more limited than the one for a single sphere as discussed in detail in chapter 1. In our work, we assume the mass transfer coefficient to be a material property and rely on the two only available experiments (Neumann et al., 2009; Ebner et al., 2015). The experiments suggest that the mass transfer coefficient in snowpacks is limited. And, it is the formulation by Ebner et al. (2015) that leads to the best match against numerical benchmark as shown in chapter 2 otherwise using larger values for heat and mass transfer coefficients in particular the one for a single sphere would be very different from the numerical benchmark for temporal thermal variations. Note that our theoretical framework allows to investigate different magnitudes of assumed transfer coefficients and numerically stable solutions are found for a large range of such values. Note further that Calonne et al. (2014) also state that larger values of $\beta = 10^9$ s m$^{-1}$ (inversely linked to the mass transfer coefficient) must be used to match the experiment by Neumann et al. (2009). This value is similar to the one measured by Ebner et al. (2015) as $\beta = 8.7 \times 10^9$ s m$^{-1}$ but still one order of magnitude smaller. This apparent discrepancy between bulk mass transfer coefficient and the one for a single sphere has been clearly referred to in the text books in Kunii and Levenspiel (1991); Crowe (2005). However, in studies for the pore scale vapor transport between snow grains (Kaempfer and Plapp, 2009; Krol and Löwe, 2018; Fourteau et al., 2021) higher values for local mass transfer coefficient on ice surfaces are used or assumed. We note that local values may differ from bulk values needed in this work. Thus, it would be interesting to show how a numerically integrated bulk mass transfer

## Conclusions

coefficient based on the works of Kaempfer and Plapp (2009); Krol and Löwe (2018); Fourteau et al. (2021) would compare to the ones used here. Using or indicating a higher value for local mass transfer coefficient on the ice surface does not mean that the bulk mass transfer coefficient for the whole pack of snow grains is not limited compared to the values for a single sphere. For the infinitely fast surface kinetics assumption (very large value for local mass transfer coefficient on ice surface) used in Fourteau et al. (2021), it can be seen from their Figure 3 for vapor flux that sublimated vapor will be all or partly redeposited directly on the neighboring ice grain. This has been discussed by Fourteau et al. (2021) that the vapor flux does not need to go around the ice grain and is rather moving from ice grain to ice grain, in agreement with the suggestion of Yosida et al. (1955) and the numerical simulations of Pinzer et al. (2012). This results in the fact that the net mass transfer between ice and air for a large number of grains as assumed in a bulk approach cannot be compared to the theoretical value for a single sphere that has one-way mass transfer. A single grain maintains a uniform vapor concentration on its interface inside a large air domain with a different vapor concentration and this is in agreement with our argument that the entire specific surface area may not be active for mass transfer in a dense porous medium inducing much lower estimations of the bulk mass transfer coefficient. However, this needs to be confirmed by pore scale simulations in future work and it remains to be seen, how much grain-to-grain mass transfer together with local saturation can reduce the bulk mass transfer coefficient. It is still uncertain how fast surface kinetics really are.

For the effective water vapor diffusivity in snow, the formulation by Hansen and Foslien (2015) is used in this thesis. It shows an enhancement in water vapor diffusivity in snow over that in air. It should be noted that governing equations (energy and mass continuity) used by Hansen and Foslien (2015) to derive the diffusion coefficient in snow are based on representative volume elements (RVE) and they are indeed derived from the volume-averaging approach. A brief review on effective diffusivity and its enhancement in snow has been made in Jafari et al. (2020). More recently, Fourteau et al. (2021) conclude that water vapor diffusion is not enhanced in snow and that studies showing enhancement for diffusivity in snow are not stringent. It should be noted that both formulations by Fourteau et al. (2021) and Hansen and Foslien (2015) suggest similar values for effective thermal conductivities and the relative deviation between these formulations is less than 3% for the the range of snow densities studied in chapter 3. It may still have some significant effect on vapor diffusion and generate notable density differences. However, as discussed in Jafari et al. (2022) (chapter 2), the relative magnitude of diffusion if convection is present is small even with enhancement of diffusivity.

This thesis was motivated by the long-standing debate in the cryospheric community about the relevance of (convective) vapor transport in snowpacks. Acknowledging the lack of appropriate model developments for water vapor transport in the snow literature, the focus of this thesis on computational and physical insights to explore the impact of such a complex process on the snow structure represents a significant improvement over the state-of-the-art. This study was the first step in effectively modeling snowpack dynamics in different cryosphere regions using a fluid dynamics-based computational approach.

Our convection model relies on some debated parametrizations for effective water vapor diffusivity, effective thermal conductivity, and mass transfer coefficient. However, the sensitivity of our results on those parameterizations is small and does not influence the conclusions. Future work may include pore scale simulations for water vapor transport between snow grains. The front tracking method - which is successfully applied for multi-fluid flows - may be used to accurately capture the grain surface evolution due to phase change. This would cast light on our understanding of the local heat and mass transfer and how the potential of mass transfer would be reduced and limited for a pack of particles. This would also be a solid basis for re-evaluating heat and mass transfer coefficient as well as effective vapor diffusivity in snow.

# A  Convection of water vapor in snowpacks

## A.1   Results of the sensitivity analysis for the initial values

The sensitivity analysis for the initial temperature and vapor distribution is shown in figure A.1.

## A.2   Results of the sensitivity analysis for the maximum Courant number

The sensitivity analysis for the maximum Courant number after a month and six months of simulation are shown in figure A.2 and figure A.3 respectively.

## A.3   Results of the sensitivity analysis for the domain width

The sensitivity analysis of the domain width for the normalized snow density is shown in figure A.4. Also, comparison of the normalized convection cell size for different domain width for the case without and with phase change are shown in figure A.5 and figure A.6 respectively.

## A.4   Qualitative analysis of the phase change rate

To analyze the local mass transfer regime, we rely on the qualitative dependency of the phase change rate (or saturation degree) on both convective flow rate and the gradient of the saturation vapor density. Extending the convection term of the steady state continuity equations for the air component and gas mixture and also neglecting the diffusion term due to its small relative contribution compared to convection, we have the following equations respectively:

$$\langle \rho_g \rangle^g \, \nabla \cdot \langle \boldsymbol{U}_g \rangle + \langle \boldsymbol{U}_g \rangle \cdot \nabla \langle \rho_g \rangle^g = \dot{m}_{iv} \tag{A.1}$$
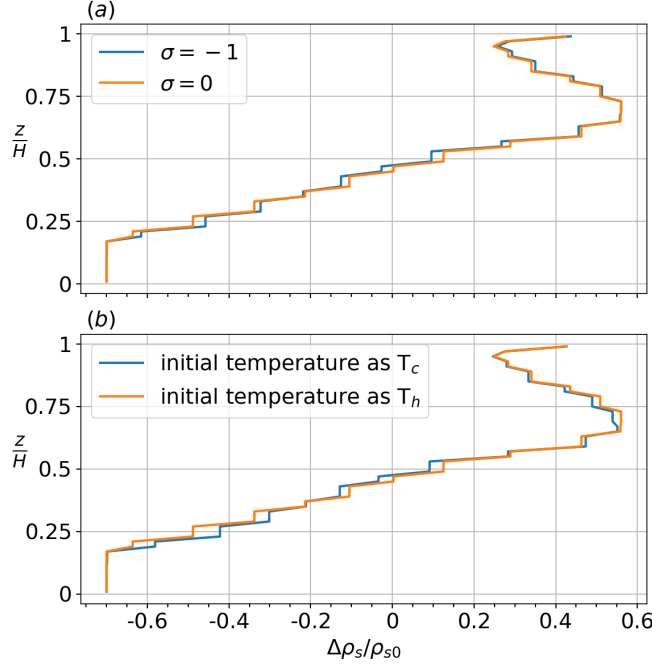
Figure A.1: Comparison of the results for two different initial values. (a) dry snowpack $\sigma = -1$ compared to the saturation vapor density $\sigma = 0$, (b) the initial temperatures of $T_c$ and $T_h$ are compared.

$$\langle \rho_a \rangle^g \nabla \cdot \langle \boldsymbol{U}_g \rangle = - \langle \boldsymbol{U}_g \rangle \cdot \nabla \langle \rho_a \rangle^g \tag{A.2}$$

Using the approximation $\langle \rho_g \rangle^g \approx \langle \rho_a \rangle^g$ in the first term of equation (A.1) and then replacing it with the term on the right hand side of equation (A.2) and simplifying, we have finally the driving force for the mass transfer as:

$$\langle \boldsymbol{U}_g \rangle \cdot \nabla \langle \rho_v \rangle^g = \dot{m}_{iv} \tag{A.3}$$

Note that in equation (A.3), for the qualitative analysis, the water vapor density gradient may be approximated by the gradient of saturation vapor density. As shown in figure A.7, this is because $\rho_v = (1 + \sigma)\rho_{vs}$ means that the vapor density is directly correlated to saturation vapor density.

## A.5   A test case for the wind pumping effect

We performed a test case for different snow heights to investigate the wind pumping effect when natural convection is active in the system. To this end, the perturbation by wind turbulence is randomly sampled by the normal Gaussian distribution as wind-turbulent
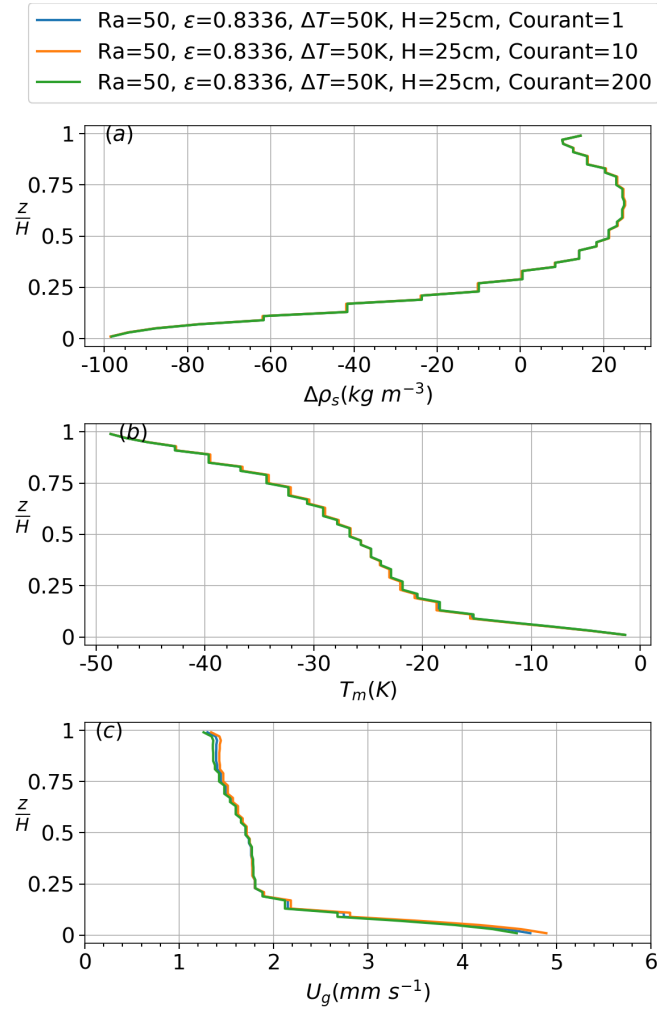
Figure A.2: Comparison of the results for different maximum Courant numbers after a month days of simulation. (a) the snow density change, (b) the snow temperature, and (c) the gas flow velocity.
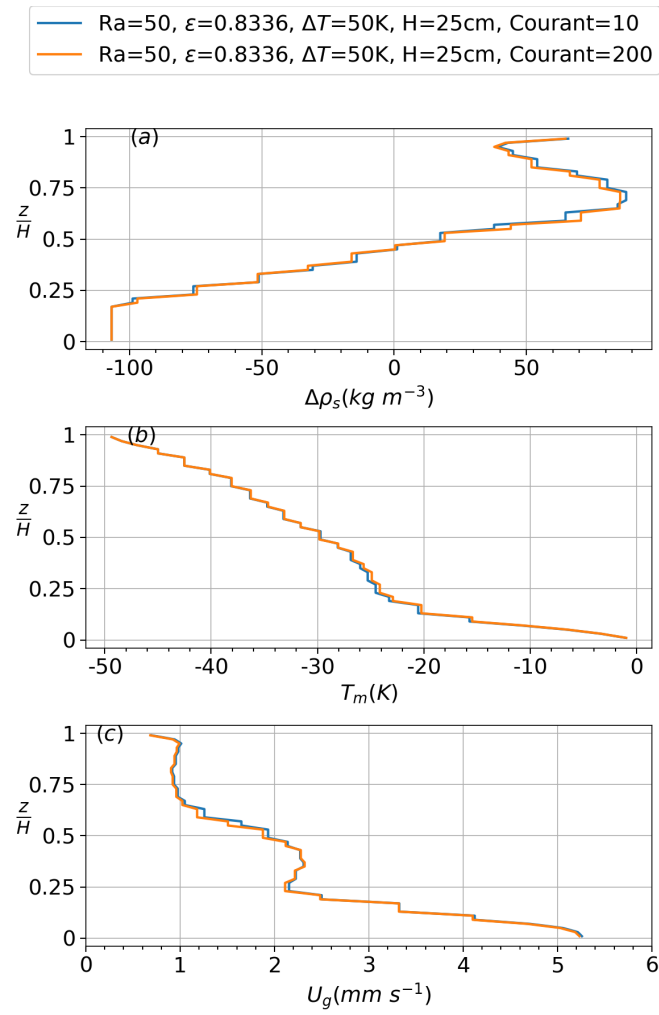
Figure A.3: Comparison of the results for different maximum Courant numbers after 6 month of simulation.
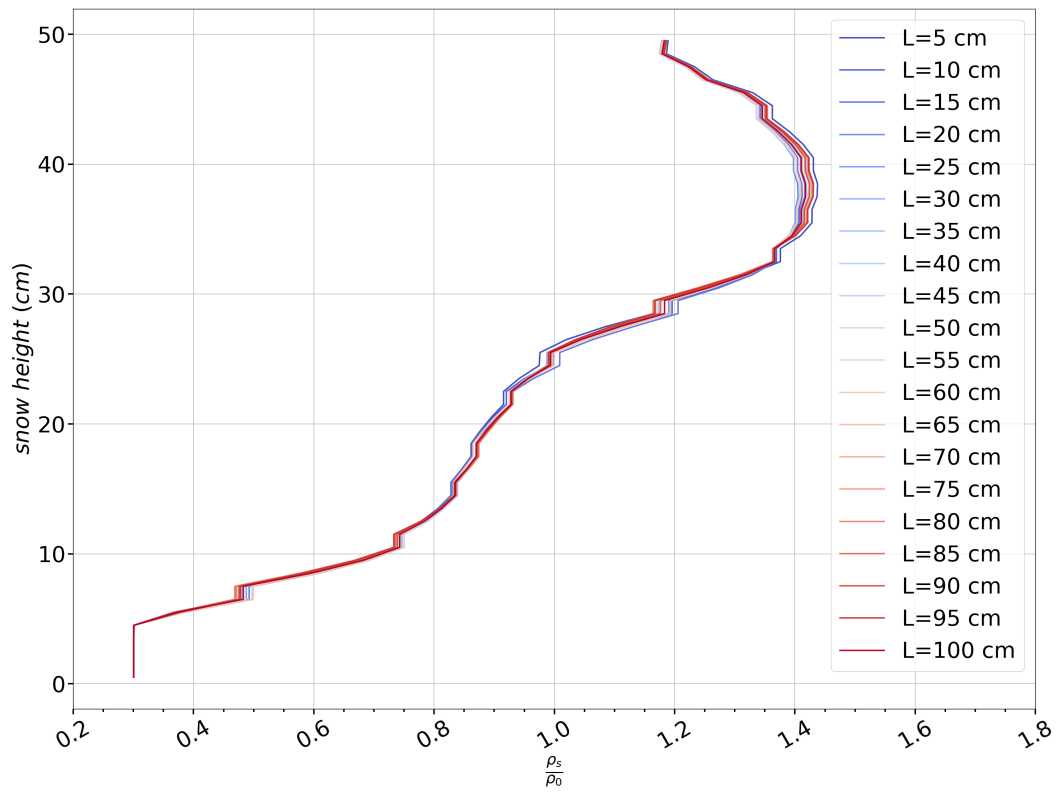
Figure A.4: Comparison of the normalized snow density for different domain length with $Ra = 100$, $H = 50$ cm, and $\Delta T = 50$ $K$.
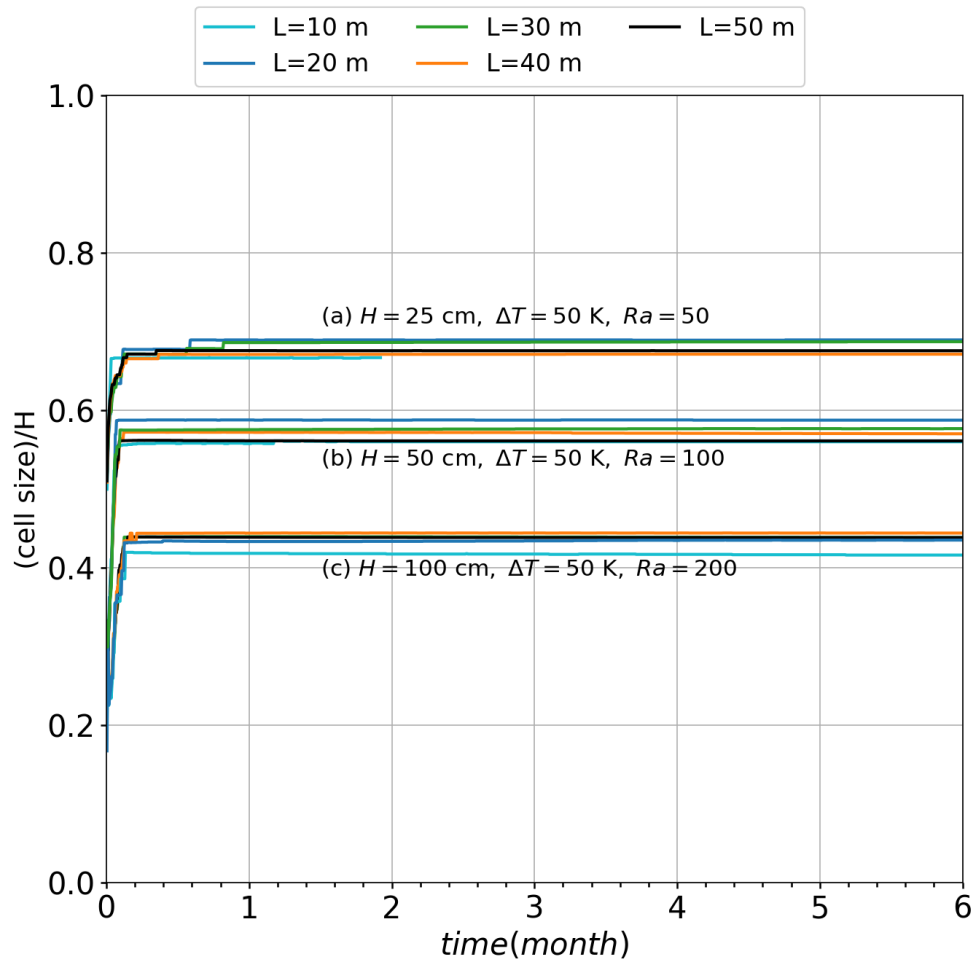
Figure A.5: Comparison of the normalized convection cell size for different domain width for the case without phase change.
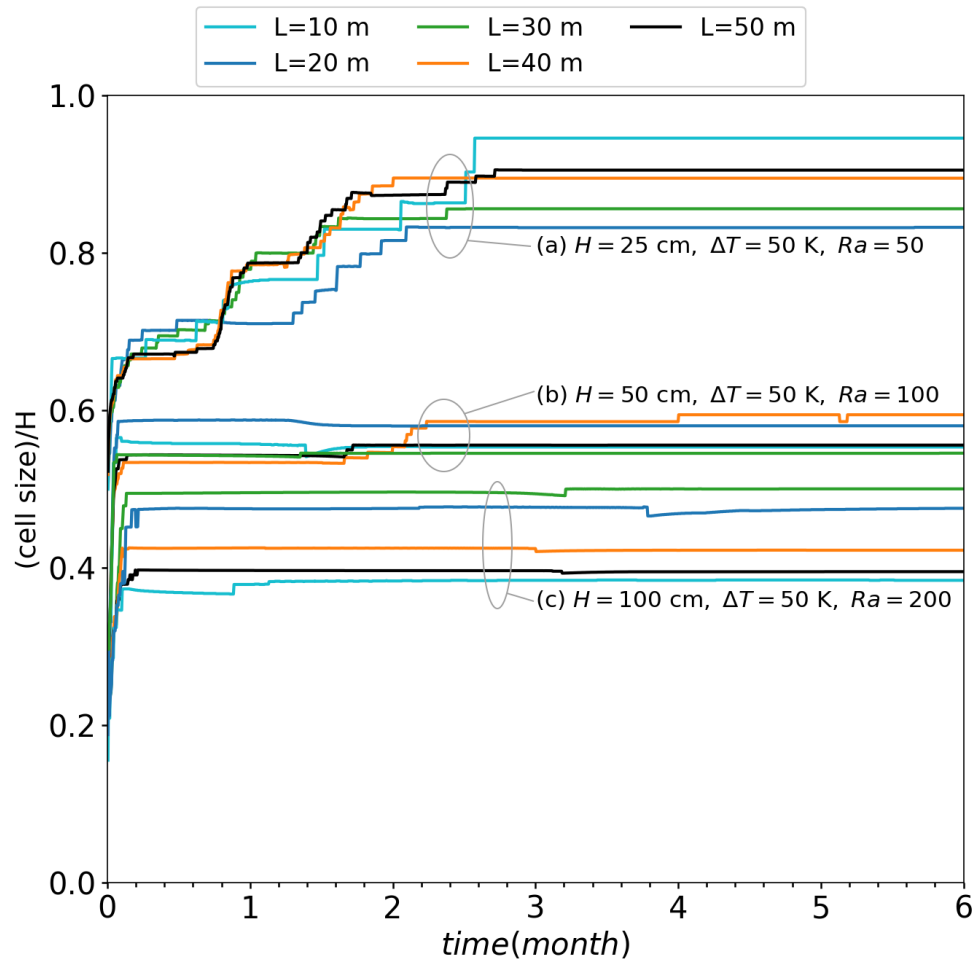
Figure A.6: Comparison of the normalized convection cell size for different domain width for the case with phase change.
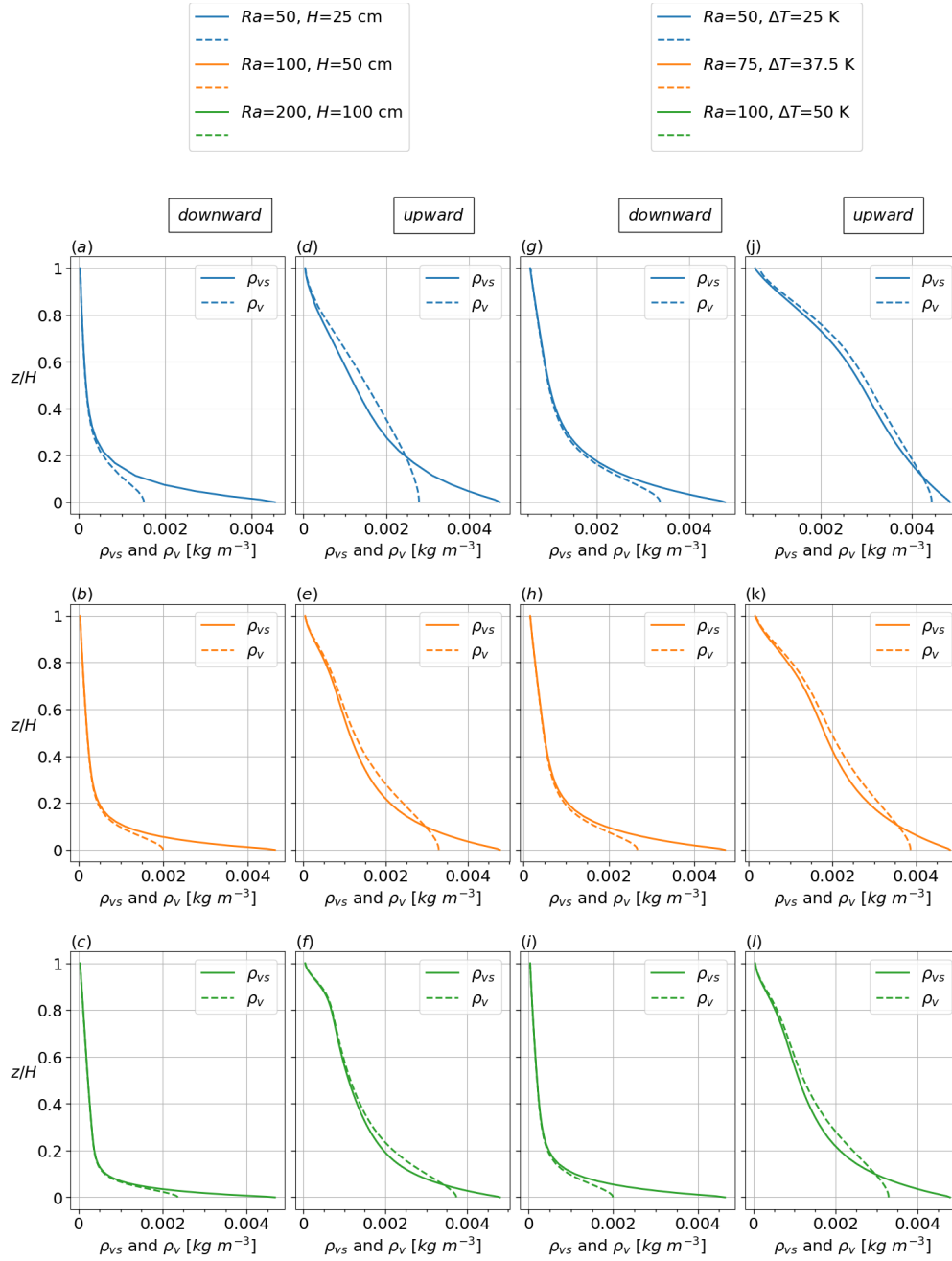
Figure A.7: One-dimensional profiles of the saturation vapor density $\rho_{vs}$ and vapor density $\rho_v$ at the location of downward and upward flows of a convection cell for different snow heights $H$, and the temperature difference $\Delta T$, all after a week of simulation.

ventilation is a high-frequency phenomenon. In the sampling distribution with the standard deviation of 1, the mean ventilation velocity is considered as $0.05 \text{ cm s}^{-1}$ which is reported by (Colbeck, 1989; Waddington et al., 1996). Since for each cell face on the top boundary the ventilation velocity is sampled randomly, we modified the resulting sampled velocities to guarantee that the net air flux on top boundary is zero due to air mass conservation in the whole system. Note that in spite of zero net gas (air and vapor) flux, there is still a non-zero vapor flux, both locally and globally and thus, the system is 'open' for water vapor. Comparing the cases with and without ventilation, we found almost no difference in laterally averaged snow density change profile as shown in figure A.8. Note that this was expected since the ventilation velocity of $0.05 \text{ cm s}^{-1}$ is almost one order of magnitude smaller than the convective velocity scale $U_{\text{conv}}$. Obviously, larger ventilation velocities might lead to a stronger disturbance in convection cells and if strong enough it may stop and shut down the convection in snowpack. Moreover, in many Arctic snow covers and for snow on sea ice, a hard crust or wind slab frequently develops at the surface. With such a hard surface, our assumption is less unrealistic.

## A.6    Non-dimensional governing equations:

The scaling factors for the length, pressure, and density gradient are selected as $H$, $\rho_{a,\text{ref}} \beta \Delta T g H$, and $\rho \beta \Delta T / H$ respectively. Note that, $\rho_{a,\text{ref}}$ is used for the gas mixture density whereas $\rho_{vs_{\text{ref}}}$ (saturation vapor density at $T_{\text{ref}}$) is used for the water vapor density as scaling factor. The effective thermal conductivities and the intrinsic permeability all are scaled based on the initial porosity as $k_{\text{eff},s0}$ and $K_0$ respectively. Since convection is the dominant transport mechanism, the reference velocity and time scales are chosen as $U_{\text{conv}}$ and $H/U_{\text{conv}}$ respectively. The dimensionless variables with the superscript asterisk shown as follows:

$$t^* = \frac{t}{H/U_{\text{conv}}}; \qquad x^* = \frac{x}{H}; \qquad z^* = \frac{z}{H}; \qquad \nabla^* = \frac{\nabla}{H} \tag{A.4}$$

$$\left\langle T_g^* \right\rangle^g = \frac{\left\langle T_g \right\rangle^g - T_h}{T_h - T_c}; \qquad \left\langle T_i^* \right\rangle^i = \frac{\left\langle T_i \right\rangle^i - T_h}{T_h - T_c} \tag{A.5}$$

$$\left\langle \rho_g^* \right\rangle^g = \frac{\left\langle \rho_g \right\rangle^g}{\rho_{a_{\text{ref}}}}; \qquad \left\langle \rho_v^* \right\rangle^g = \frac{\left\langle \rho_v \right\rangle^g}{\rho_{vs_{\text{ref}}}}; \qquad \left\langle \rho_a^* \right\rangle^g = \frac{\left\langle \rho_a \right\rangle^g}{\rho_{a_{\text{ref}}}}; \qquad \left\langle J_v^* \right\rangle = \frac{\left\langle J_v \right\rangle}{D_{va} \rho_{vs_{\text{ref}}}/H} \tag{A.6}$$

$$\left\langle U_g^* \right\rangle = \frac{\left\langle U_g \right\rangle}{U_{\text{conv}}}; \qquad \left\langle P_g^* \right\rangle^g = \frac{\left\langle P_g \right\rangle^g}{\rho_{a_{\text{ref}}} \beta \Delta T g H}; \qquad \nabla^* \left\langle \rho_g^* \right\rangle^g = \frac{\nabla \left\langle \rho_g \right\rangle^g}{\rho_{a_{\text{ref}}} \beta \Delta T / H} \tag{A.7}$$

$$D_{\text{eff},s}^* = \frac{D_{\text{eff},s}}{D_{va}}; \qquad k_{\text{eff},g}^* = \frac{k_{\text{eff},g}}{k_{\text{eff},s0}}; \qquad k_{\text{eff},i}^* = \frac{k_{\text{eff},i}}{k_{\text{eff},s0}}; \qquad c_{pg}^* = \frac{c_{pg}}{c_{pa}}; \qquad d_p^* = \frac{d_p}{H} \tag{A.8}$$

Using the defined scaling factors and dimensionless variables, the final set of the equations (2.1), (2.2), and (2.3) for the mass conservation, equation (2.8) for the momentum,
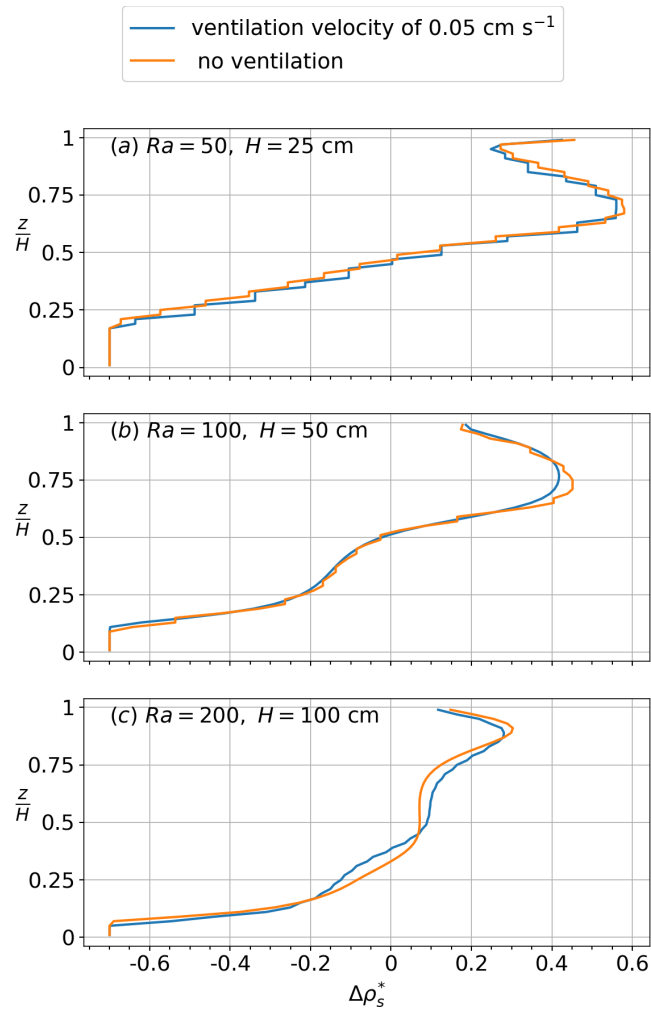
Figure A.8: Comparison of the results for a case without wind pumping and a case with the ventilation velocity of $0.05$ cm s$^{-1}$.

and equations (2.18) and (2.19) for the temperature-based energy equations are normalized respectively as follows to extract the group of non-dimensional numbers important for the convection of water vapor in snowpack:

$$\frac{\partial}{\partial t^*}(\epsilon_g \langle \rho_g^* \rangle^g) + \nabla^* \cdot (\langle \rho_g^* \rangle^g \langle \boldsymbol{U}_g^* \rangle) = - \left[ \frac{\rho_{vs_{\mathrm{ref}}}}{\rho_{a_{\mathrm{ref}}}} \frac{6\epsilon_i Sh_{\mathrm{ref}}}{d_p^{*2} RaLe_m} \right] \sigma \tag{A.9}$$

$$\frac{\partial}{\partial t^*}(\epsilon_g \langle \rho_v^* \rangle^g) + \nabla^* \cdot (\langle \rho_v^* \rangle^g \langle \boldsymbol{U}_g^* \rangle) = \left[ \frac{1}{RaLe_m} \right] \nabla^* \cdot (D_{\mathrm{eff},s}^* \nabla^* \langle \rho_v^* \rangle^g) - \left[ \frac{6\epsilon_i Sh_{\mathrm{ref}}}{d_p^{*2} RaLe_m} \right] \sigma \tag{A.10}$$

$$\frac{\partial \epsilon_i}{\partial t^*} = \left[ \frac{\rho_{vs_{\mathrm{ref}}}}{\rho_i} \frac{6\epsilon_i Sh_{\mathrm{ref}}}{d_p^{*2} RaLe_m} \right] \sigma \tag{A.11}$$

$$-\frac{\langle \boldsymbol{U}_g^* \rangle}{K^*} - \frac{\langle \rho_g^* \rangle^g c_F}{\sqrt{K^*}} \left| \langle \boldsymbol{U}_g^* \rangle \right| \langle \boldsymbol{U}_g^* \rangle \left[ \frac{Ra\sqrt{Da}}{Pr_m} \right] - \nabla^* \langle P_g^* \rangle^g + \nabla^* \langle \rho_g^* \rangle^g z^* = 0 \tag{A.12}$$

$$\frac{\partial}{\partial t^*}(\epsilon_g \langle \rho_g^* \rangle^g c_{pg}^* \langle T_g^* \rangle^g) + \nabla^* \cdot (\langle \rho_g^* \rangle^g c_{pg}^* \langle T_g^* \rangle^g \langle \boldsymbol{U}_g^* \rangle) =$$
$$\left[ \frac{1}{Ra} \right] \nabla^* \cdot (\epsilon_g k_{\mathrm{eff},g}^* \nabla^* \langle T_g^* \rangle^g)$$
$$+ [Ge]\, (\epsilon_g \frac{\partial}{\partial t^*} \langle P_g^* \rangle^g + \langle \boldsymbol{U}_g^* \rangle \cdot \nabla^* \langle P_g^* \rangle^g)$$
$$- \left[ \frac{\rho_{vs_{\mathrm{ref}}}(c_{pv} - c_{pa})}{\rho_{a_{\mathrm{ref}}} c_{pa}} \frac{1}{RaLe_m} \right] \nabla^* \cdot (\langle T_g^* \rangle^g \langle J_v^* \rangle)$$
$$+ \left[ \frac{6\epsilon_i Sh_{\mathrm{ref}} Le_{\mathrm{ref}}}{d_p^{*2} \rho_{vs}^* RaLe_m} \right] (\langle T_g^* \rangle^g (w_g - 1) + \langle T_i^* \rangle^i w_i)$$
$$- \left[ \frac{\rho_{vs_{\mathrm{ref}}} c_{pv}}{\rho_{a_{\mathrm{ref}}} c_{pa}} \frac{6\epsilon_i Sh_{\mathrm{ref}}}{d_p^{*2} RaLe_m} \right] \sigma \langle T_g^* \rangle^g \tag{A.13}$$

$$\frac{\partial}{\partial t^*}(\epsilon_i \langle T_i^* \rangle^i) = \left[ \frac{\rho_{a_{\text{ref}}} c_{pa}}{\rho_i c_{pi}} \frac{1}{Ra} \right] \nabla^* \cdot (\epsilon_i k_{\text{eff},i}^* \nabla^* \langle T_i^* \rangle^i)$$

$$- \left[ \frac{\rho_{a_{\text{ref}}} c_{pa}}{\rho_i c_{pi}} \frac{6\epsilon_i Sh_{\text{ref}} Le_{\text{ref}}}{d_p^{*2} \rho_{vs}^* Ra Le_m} \right] (\langle T_g^* \rangle^g (w_g - 1) + \langle T_i^* \rangle^i w_i)$$

$$+ \left[ \frac{\rho_{vs_{\text{ref}}} c_{pv}}{\rho_i c_{pi}} \frac{6\epsilon_i Sh_{\text{ref}}}{d_p^{*2} Ra Le_m} \right] \sigma(\langle T_g^* \rangle^g w_g + \langle T_i^* \rangle^i w_i)$$

$$+ \left[ \frac{\rho_{vs_{\text{ref}}} (c_{pi} - c_{pv}) T_{\text{ref}}}{\rho_i c_{pi} \Delta T} \frac{6\epsilon_i Sh_{\text{ref}}}{d_p^{*2} Ra Le_m} \right] \sigma$$

$$+ \left[ \frac{\rho_{vs_{\text{ref}}} L_{iv}}{\rho_i c_{pi} \Delta T} \frac{6\epsilon_i Sh_{\text{ref}}}{d_p^{*2} Ra Le_m} \right] \sigma \quad \text{(A.14)}$$

In the above set of equations, groups of non-dimensional numbers are put inside the brackets. Also, for the sake of convenience, the group of non-dimensional numbers on the right hand side of equation (A.10) is named as $M = (6\epsilon_i Sh_{\text{ref}})/(d_p^{*2} Ra Le_m)$, which appears in other terms. The other non-dimensional numbers in the above equations include Sherwood number, the Lewis number, the reference Lewis number, the Prandtl number, the Darcy number, and finally the Gebhart number which all shown as follows:

$$Sh_{\text{ref}} = \frac{\rho_i d_p}{\mathscr{B} \rho_{vs_{\text{ref}}} D_{va}} \quad \text{(A.15)}$$

$$Le_m = \frac{k_{\text{eff},s0}}{\rho_{a,\text{ref}} c_{pa} D_{va}}; \qquad Le_{\text{ref}} = \frac{k_a}{\rho_{a,\text{ref}} c_{pa} D_{va}} \quad \text{(A.16)}$$

$$Pr_m = \frac{\mu/\rho_{a,\text{ref}}}{k_{\text{eff},s0}/(\rho_{a,\text{ref}} c_{pa})} \quad \text{(A.17)}$$

$$Da = \frac{K_0}{H^2} \quad \text{(A.18)}$$

$$Ge = \frac{\beta g H}{c_{pa}} \quad \text{(A.19)}$$

As shown in these normalized equation, for both heat and mass transfer, the controlling parameters are $Ra$, $Le_m$, and $d_p^*$ (as they appear in the parameter $M$), meaning that the mass transfer regime cannot be abstracted only by $Ra$. The term $M$ can be interpreted as the dimensionless mass transfer coefficient and $\sigma$ as the potential or driving force for the mass transfer. By expanding parameter $M$, one can show that for a specified porosity and grain size, $M$ is indeed a function of the inverse characteristic temperature gradient $\Delta T/H$.

## A.7  Model system and real-world analogs

The conditions, which we assume in our idealized set-up are realistic and can be found in snowpacks in the polar regions, and especially for snow on sea ice, where the temperature at the bottom remains always close to melting if the ice is thin and the surface can get very cold. But also in other snow covers, conditions can be found, which are close to our idealized set-up. We discuss this now in more detail and provide the references as:

- **Snow Density**: there are many areas in the cryosphere that are subjected to perhaps only a few snowfall events during the entire winter period. Examples include vast expanses of Siberia and the Arctic (Gouttevin et al., 2018; Jafari et al., 2020), or, for instance Tibet. In many of these areas, a singular snow fall event with new snow densities well below 100 kg m$^{-3}$ can be found and low densities can persist for multiple months. In the polar regions in particular, absence of solar radiation and persistent low temperatures through out the winter months helps to limit settling in these conditions. Thus even the very idealized case in this study has many real-world analogs.

- **Temperature gradients**: Temperature gradients of the $\mathcal{O}$ (100) K m$^{-1}$ are quite common in snowpacks. For example, our own previous work on vapor diffusion (Jafari et al., 2020) discusses data from Samoylov, shown in figure 1a of Jafari et al. (2020). In Samoylov, we can see persistent negative temperature gradients of 100-200 K m$^{-1}$ over a period of 4-5 months interrupted only by the onset of spring (figure 1a of Jafari et al. (2020)).

- **Bottom thermal boundary at 0 °C**: For snow on sea ice, where the temperature at the bottom remains always close to melting if the ice is thin and the surface can get very cold (Nicolaus and Schwegmann, 2017; Wever et al., 2020).

# Bibliography

Akitaya, E. (1974). Studies on depth hoar. *Contributions from the Institute of Low Temperature Science*, 26:1–67.

Albert, M. (1993). Some numerical experiments on firn ventilation with heat transfer. *Annals of Glaciology*, 18:161–165.

Albert, M., Shuman, C., Courville, Z., Bauer, R., Fahnestock, M., and Scambos, T. (2004). Extreme firn metamorphism: impact of decades of vapor transport on near-surface firn at a low-accumulation glazed site on the east antarctic plateau. *Annals of Glaciology*, 39:73–78, DOI: 10.3189/172756404781814041.

Albert, M. R. and McGilvary, W. R. (1992). Thermal effects due to air flow and vapor transport in dry snow. *Journal of Glaciology*, 38(129):273–281, DOI: 10.3189/S0022143000003683.

Alley, R., Saltzman, E., Cuffey, K., and Fitzpatrick, J. (1990). Summertime formation of depth hoar in central greenland. *Geophysical Research Letters*, 17(13):2393–2396.

Barenblatt, G. I. (1996). *Scaling, Self-similarity, and Intermediate Asymptotics: Dimensional Analysis and Intermediate Asymptotics*. Cambridge Texts in Applied Mathematics. Cambridge University Press, DOI: 10.1017/CBO9781107050242.

Barrere, M., Domine, F., Decharme, B., Morin, S., Vionnet, V., and Lafaysse, M. (2017). Evaluating the performance of coupled snow–soil models in surfexv8 to simulate the permafrost thermal regime at a high arctic site. *Geoscientific Model Development*, 10(9):3461–3479.

Bartelt, P., Buser, O., and Sokratov, S. A. (2004). A nonequilibrium treatment of heat and mass transfer in alpine snowcovers. *Cold Regions Science and Technology*, 39(2):219 – 242, DOI: https://doi.org/10.1016/j.coldregions.2004.04.005, http://www.sciencedirect.com/science/article/pii/S0165232X0400045X. Snow And Avalanches: Papers Presented At The European Geophysical Union Conference, Nice, April 2003. Dedicated To The Avalanche Dynamics Pioneer Dr. B. Salm.

Bartelt, P. and Lehning, M. (2002). A physical snowpack model for the swiss avalanche warning: Part i: numerical model. *Cold Regions Science and Technology*, 35:123–145, DOI: 10.1016/S0165-232X(02)00074-5.

## Bibliography

Bartlett, S. and Lehning, M. (2011). A theoretical assessment of heat transfer by ventilation in homogeneous snowpacks. *Water Resources Research*, 47(4).

Bavay, M., Grünewald, T., and Lehning, M. (2013). Response of snow cover and runoff to climate change in high alpine catchments of eastern switzerland. *Advances in Water Resources*, 55:4–16, DOI: https://doi.org/10.1016/j.advwatres.2012.12.009, https://www.sciencedirect.com/science/article/pii/S0309170812003193. Snow–Atmosphere Interactions and Hydrological Consequences.

Baytas, A. and Pop, I. (2002). Free convection in a square porous cavity using a thermal nonequilibrium model. *International Journal of Thermal Sciences*, 41(9):861 – 870, DOI: https://doi.org/10.1016/S1290-0729(02)01379-0, http://www.sciencedirect.com/science/article/pii/S1290072902013790.

Bear, J. (1961). On the tensor form of dispersion in porous media. *Journal of Geophysical Research*, 66(4):1185–1197.

Bear, J. (1988). *Dynamics of fluids in porous media.* Courier Corporation.

Bender, E., Lehning, M., and Fiddes, J. (2020). Changes in climatology, snow cover, and ground temperatures at high alpine locations. *Frontiers in Earth Science*, 8:100, DOI: 10.3389/feart.2020.00100, https://www.frontiersin.org/article/10.3389/feart.2020.00100.

Bergman, T., Incropera, F., DeWitt, D., and Lavine, A. (2011). *Fundamentals of Heat and Mass Transfer.* Wiley, ISBN: 9780470501979, https://books.google.ch/books?id=vvyIoXEywMoC.

Bird, R. B., Stewart, W. E., and Lightfoot, E. N. (1961). Transport phenomena, john wiley and sons, inc., new york (1960). 780 pages. \$11.50. *AIChE Journal*, 7(2):5J–6J, DOI: 10.1002/aic.690070245, https://aiche.onlinelibrary.wiley.com/doi/abs/10.1002/aic.690070245.

Birkeland, K. W. (1998). Terminology and predominant processes associated with the formation of weak layers of near-surface faceted crystals in the mountain snowpack. *Arctic and Alpine Research*, 30(2):193–199, DOI: 10.1080/00040851.1998.12002891, https://www.tandfonline.com/doi/abs/10.1080/00040851.1998.12002891.

Birkeland, K. W., Johnson, R. F., and Schmidt, D. S. (1998). Near-surface faceted crystals formed by diurnal recrystallization: A case study of weak layer formation in the mountain snowpack and its contribution to snow avalanches. *Arctic and Alpine Research*, 30(2):200–204, DOI: 10.1080/00040851.1998.12002892, https://www.tandfonline.com/doi/abs/10.1080/00040851.1998.12002892.

Boike, J., Kattenstroth, B., Abramova, K., Bornemann, N., Chetverova, A., Fedorova, I., Fröb, K., Grigoriev, M., Grüber, M., Kutzbach, L., Langer, M., Minke, M., Muster, S., Piel, K., Pfeiffer, E. M., Stoof, G., Westermann, S., Wischnewski, K., Wille, C., and Hubberten, H. W. (2013). Baseline characteristics of climate, permafrost and land cover from a new permafrost

observatory in the Lena River Delta, Siberia (1998-2011). *Biogeosciences*, 10(3):2105–2128, DOI: 10.5194/bg-10-2105-2013.

Boike, J., Nitzbon, J., Anders, K., Grigoriev, M., Bolshiyanov, D., Langer, M., Lange, S., Bornemann, N., Morgenstern, A., Schreiber, P., Wille, C., Chadburn, S., Gouttevin, I., and Kutzbach, L. (2018). A 16-year record (2002–2017) of permafrost, active layer, and meteorological conditions at the samoylov island arctic permafrost research site, lena river delta, northern siberia: an opportunity to validate remote sensing data and land surface, snow, and permafrost models. *Earth System Science Data Discussions*, 2018:1–77, DOI: 10.5194/essd-2018-82, https://www.earth-syst-sci-data-discuss.net/essd-2018-82/.

Callaghan, T. V., Johansson, M., Brown, R. D., Groisman, P. Y., Labba, N., Radionov, V., Bradley, R. S., Blangy, S., Bulygina, O. N., Christensen, T. R., Colman, J. E., Essery, R. L. H., Forbes, B. C., Forchhammer, M. C., Golubev, V. N., Honrath, R. E., Juday, G. P., Meshcherskaya, A. V., Phoenix, G. K., Pomeroy, J., Rautio, A., Robinson, D. A., Schmidt, N. M., Serreze, M. C., Shevchenko, V. P., Shiklomanov, A. I., Shmakin, A. B., Sköld, P., Sturm, M., Woo, M.-k., and Wood, E. F. (2011). Multiple effects of changes in arctic snow cover. *AMBIO*, 40(1):32–45, DOI: 10.1007/s13280-011-0213-x, https://doi.org/10.1007/s13280-011-0213-x.

Calonne, N., Geindreau, C., and Flin, F. (2014). Macroscopic modeling for heat and water vapor transfer in dry snow by homogenization. *The Journal of Physical Chemistry B*, 118(47):13393–13403, DOI: 10.1021/jp5052535, https://doi.org/10.1021/jp5052535. PMID: 25011981.

Calonne, N., Geindreau, C., and Flin, F. (2015). Macroscopic modeling of heat and water vapor transfer with phase change in dry snow based on an upscaling method: Influence of air convection. *Journal of Geophysical Research: Earth Surface*, 120(12):2476–2497, DOI: https://doi.org/10.1002/2015JF003605, https://agupubs.onlinelibrary.wiley.com/doi/abs/10.1002/2015JF003605.

Calonne, N., Geindreau, C., Flin, F., Morin, S., Lesaffre, B., Rolland du Roscoat, S., and Charrier, P. (2012). 3-d image-based numerical computations of snow permeability: links to specific surface area, density, and microstructural anisotropy. *The Cryosphere*, 6(5):939–951, DOI: 10.5194/tc-6-939-2012, https://www.the-cryosphere.net/6/939/2012/.

Caltagirone, J. P. (1975). Thermoconvective instabilities in a horizontal porous layer. *Journal of Fluid Mechanics*, 72(2):269–287, DOI: 10.1017/S0022112075003345.

Christon, M., Burns, P. J., and Sommerfeld, R. A. (1994). Quasi-steady temperature gradient metamorphism in idealized, dry snow. *Numerical Heat Transfer, Part A: Applications*, 25(3):259–278, DOI: 10.1080/10407789408955948, https://doi.org/10.1080/10407789408955948.

Colbeck, S. (1989). Air movement in snow due to windpumping. *Journal of Glaciology*, 35(120):209–213.

# Bibliography

Colbeck, S. C. (1983). Theory of metamorphism of dry snow. *Journal of Geophysical Research: Oceans*, 88(C9):5475–5482, DOI: https://doi.org/10.1029/JC088iC09p05475, https://agupubs.onlinelibrary.wiley.com/doi/abs/10.1029/JC088iC09p05475.

Colbeck, S. C. (1987). *Snow Metamorphism and Classification*, pages 1–35. Springer Netherlands, Dordrecht, ISBN: 978-94-009-3947-9, DOI: 10.1007/978-94-009-3947-9_1, https://doi.org/10.1007/978-94-009-3947-9_1.

Colbeck, S. C. (1993). The vapor diffusion coefficient for snow. *Water Resources Research*, 29(1):109–115, DOI: 10.1029/92WR02301, https://agupubs.onlinelibrary.wiley.com/doi/abs/10.1029/92WR02301.

Courant, R., Friedrichs, K., and Lewy, H. (1928). über die partiellen Differenzengleichungen der mathematischen Physik. *Math. Ann.*, 100(32):32–74, DOI: 10.1007/BF01448839. In German.

Crowe, C. T. (2005). *Multiphase flow handbook*. CRC press, Boca Raton.

Delgado, J. (2007). Longitudinal and transverse dispersion in porous media. *Chemical Engineering Research and Design*, 85(9):1245–1252.

Derksen, C., Silis, A., Sturm, M., Holmgren, J., Liston, G. E., Huntington, H., and Solie, D. (2009). Northwest territories and nunavut snow characteristics from a subarctic traverse: Implications for passive microwave remote sensing. *Journal of Hydrometeorology*, 10(2):448–463.

Domine, F., Barrere, M., and Morin, S. (2016a). The growth of shrubs on high arctic tundra at bylot island: impact on snow physical properties and permafrost thermal regime. *Biogeosciences*, 13(23):6471–6486, DOI: 10.5194/bg-13-6471-2016, https://bg.copernicus.org/articles/13/6471/2016/.

Domine, F., Barrere, M., and Sarrazin, D. (2016b). Seasonal evolution of the effective thermal conductivity of the snow and the soil in high arctic herb tundra at bylot island, canada. *The Cryosphere*, 10(6):2573.

Domine, F., Barrere, M., Sarrazin, D., Morin, S., and Arnaud, L. (2015). Automatic monitoring of the effective thermal conductivity of snow in a low-arctic shrub tundra. *The Cryosphere*, 9(3):1265–1276.

Domine, F., BELKE-BREA, M., SARRAZIN, D., ARNAUD, L., BARRERE, M., and POIRIER, M. (2018). Soil moisture, wind speed and depth hoar formation in the arctic snowpack. *Journal of Glaciology*, 64(248):990–1002, DOI: 10.1017/jog.2018.89.

Domine, F., Fourteau, K., Picard, G., Lackner, G., Sarrazin, D., and Poirier, M. (2022). *Nature Portfolio*, DOI: 10.21203/rs.3.rs-679013/v1, https://doi.org/10.21203/rs.3.rs-679013/v1.

Domine, F., Lackner, G., Sarrazin, D., Poirier, M., and Belke-Brea, M. (2021). Meteorological, snow and soil data (2013–2019) from a herb tundra permafrost site at bylot island, canadian high arctic, for driving and testing snow and land surface models. *Earth System Science Data*, 13(9):4331–4348, DOI: 10.5194/essd-13-4331-2021, https://essd.copernicus.org/articles/13/4331/2021/.

Domine, F., Morin, S., Brun, E., Lafaysse, M., and Carmagnola, C. (2013). Seasonal evolution of snow permeability under equi-temperature and temperature-gradient conditions. *The Cryosphere*, 7(6):1915–1929.

Domine, F., Picard, G., Morin, S., Barrere, M., Madore, J.-B., and Langlois, A. (2019). Major issues in simulating some arctic snowpack properties using current detailed snow physics models: Consequences for the thermal regime and water budget of permafrost. *Journal of Advances in Modeling Earth Systems*, 11(0):34–44, DOI: 10.1029/2018MS001445, https://agupubs.onlinelibrary.wiley.com/doi/abs/10.1029/2018MS001445.

Ebner, P., Steen-Larsen, H. C., Stenni, B., Schneebeli, M., and Steinfeld, A. (2017). Experimental observation of transient $\delta^{18}o$ interaction between snow and advective airflow under various temperature gradient conditions. *The Cryosphere Discussions*, 11:1733–1743.

Ebner, P. P., Andreoli, C., Schneebeli, M., and Steinfeld, A. (2015). Tomography-based characterization of ice-air interface dynamics of temperature gradient snow metamorphism under advective conditions. *Journal of Geophysical Research: Earth Surface*, 120(12):2437–2451, DOI: 10.1002/2015JF003648, https://agupubs.onlinelibrary.wiley.com/doi/abs/10.1002/2015JF003648.

Egolf, D. A., Melnikov, I. V., Pesch, W., and Ecke, R. E. (2000). Mechanisms of extensive spatiotemporal chaos in rayleigh–bénard convection. *Nature*, 404(6779):733–736.

Enescu, I. I., Plattner, G.-K., Pernas, L. E., Haas-Artho, D., Bischof, S., Lehning, M., and Steffen, K. (2018). The envidat concept for an institutional environmental data portal. *Data Science Journal*, 17:28.

Essery, R., Kontu, A., Lemmetyinen, J., Dumont, M., and Ménard, C. B. (2016). A 7-year dataset for driving and evaluating snow models at an Arctic site (Sodankylä, Finland). *Geosci. Instrum. Method. Data Syst*, 5:219–227, DOI: 10.5194/gi-5-219-2016, www.geosci-instrum-method-data-syst.net/5/219/2016/.

Faghri, A. and Zhang, Y. (2006). *Transport Phenomena in Multiphase Systems*. Elsevier Science, ISBN: 9780080547688, https://books.google.ch/books?id=bxndY2KSuQsC.

Fahs, M., Graf, T., Tran, T. V., Ataie-Ashtiani, B., Simmons, C., Younes, A., et al. (2020). Study of the effect of thermal dispersion on internal natural convection in porous media using fourier series. *Transport in Porous Media*, 131(2):537–568.

Foslien, W. E. (1994). A modern mixture theory applied to heat and mass transfer in snow. *MS thesis, University of Wyoming, Laramie, WY, USA, 1994.*

151

## Bibliography

Fourteau, K., Domine, F., and Hagenmuller, P. (2021). Macroscopic water vapor diffusion is not enhanced in snow. *The Cryosphere*, 15(1):389–406, DOI: 10.5194/tc-15-389-2021, https://tc.copernicus.org/articles/15/389/2021/.

Gallet, J.-C., Domine, F., and Dumont, M. (2014). Measuring the specific surface area of wet snow using 1310 nm reflectance. *The Cryosphere*, 8(4):1139–1148, DOI: 10.5194/tc-8-1139-2014, https://www.the-cryosphere.net/8/1139/2014/.

Ganesan, S. and Poirier, D. R. (1990). Conservation of mass and momentum for the flow of interdendritic liquid during solidification. *Metallurgical Transactions B*, 21(1):173.

Gouttevin, I., Langer, M., Löwe, H., Boike, J., Proksch, M., and Schneebeli, M. (2018). Observation and modelling of snow at a polygonal tundra permafrost site: spatial variability and thermal implications. *The Cryosphere*, 12(11):3693–3717, DOI: 10.5194/tc-12-3693-2018, https://www.the-cryosphere.net/12/3693/2018/.

Gouttevin, I., Menegoz, M., Dominé, F., Krinner, G., Koven, C., Ciais, P., Tarnocai, C., and Boike, J. (2012). How the insulating properties of snow affect soil carbon distribution in the continental pan-arctic area. *Journal of Geophysical Research: Biogeosciences*, 117(G2), DOI: 10.1029/2011JG001916, https://agupubs.onlinelibrary.wiley.com/doi/abs/10.1029/2011JG001916.

Gray, W. G. and O'Neill, K. (1976). On the general equations for flow in porous media and their reduction to darcy's law. *Water Resources Research*, 12(2):148–154.

Groisman, P. Y., Karl, T. R., and Knight, R. W. (1994). Observed impact of snow cover on the heat balance and the rise of continental spring temperatures. *Science*, 263(5144):198–200, DOI: 10.1126/science.263.5144.198, http://science.sciencemag.org/content/263/5144/198.

Gubler, H. (1985). Model for dry snow metamorphism by interparticle vapor flux. *Journal of Geophysical Research: Atmospheres*, 90(D5):8081–8092.

Guennebaud, G., Jacob, B., et al. (2010). Eigen v3.

Haberkorn, A., Wever, N., Hoelzle, M., Phillips, M., Kenner, R., Bavay, M., and Lehning, M. (2017). Distributed snow and rock temperature modelling in steep rock walls using alpine3d. *The Cryosphere*, 11(1):585–607, DOI: 10.5194/tc-11-585-2017, https://tc.copernicus.org/articles/11/585/2017/.

Hansen, A. C. and Foslien, W. E. (2015). A macroscale mixture theory analysis of deposition and sublimation rates during heat and mass transfer in dry snow. *The Cryosphere*, 9(5):1857–1878, DOI: 10.5194/tc-9-1857-2015, https://www.the-cryosphere.net/9/1857/2015/.

Hewitt, D., Neufeld, J., and Lister, J. (2014). High rayleigh number convection in a three-dimensional porous medium. *Journal of Fluid Mechanics*, 748:879–895, DOI: 10.1017/jfm.2014.216.

Hewitt, D. R., Neufeld, J. A., and Lister, J. R. (2013a). Convective shutdown in a porous medium at high rayleigh number. *Journal of Fluid Mechanics*, 719:551–586, DOI: 10.1017/jfm.2013.23.

Hewitt, D. R., Neufeld, J. A., and Lister, J. R. (2013b). Stability of columnar convection in a porous medium. *Journal of Fluid Mechanics*, 737:205–231, DOI: 10.1017/jfm.2013.559.

Ho, C. K. and Webb, S. W. (1998). Review of porous media enhanced vapor-phase diffusion mechanisms, models, and data—does enhanced vapor-phase diffusion exist? *Journal of porous media*, 1(1):71–92.

Holzbecher, E. (2019). Convection pattern formation in a domain with a horizontal interface. *Physics of Fluids*, 31(5):056602, DOI: 10.1063/1.5094402, https://doi.org/10.1063/1.5094402.

Horne, R. N. (1975). *Transient effects in geothermal convective systems*. PhD thesis, Citeseer.

Hugelius, G., Strauss, J., Zubrzycki, S., Harden, J. W., Schuur, E., Ping, C.-L., Schirrmeister, L., Grosse, G., Michaelson, G. J., Koven, C. D., et al. (2014). Estimated stocks of circumpolar permafrost carbon with quantified uncertainty ranges and identified data gaps. *Biogeosciences*, 11(23):6573–6593.

Ishii, M. and Hibiki, T. (2010). *Thermo-Fluid Dynamics of Two-Phase Flow*. SpringerLink : Bücher. Springer New York, ISBN: 9781441979858, https://books.google.ch/books?id= K9LP5omwjQcC.

Jafari, M., Gouttevin, I., Couttet, M., Wever, N., Michel, A., Sharma, V., Rossmann, L., Maass, N., Nicolaus, M., and Lehning, M. (2020). The impact of diffusive water vapor transport on snow profiles in deep and shallow snow covers and on sea ice. *Frontiers in Earth Science*, 8:249, DOI: 10.3389/feart.2020.00249, https://www.frontiersin.org/article/10.3389/feart. 2020.00249.

Jafari, M. and Lehning, M. (2021). snowpackbuoyantpimplefoam: an openfoam eulerian–eulerian two-phase solver for modelling convection of water vapor in snowpacks. EnviDat. DOI: http://dx.doi.org/10.16904/envidat.265. https://www.envidat.ch/dataset/ convection-in-snow.

Jafari, M., Sharma, V., and Lehning, M. (2022). Convection of water vapour in snowpacks. *Journal of Fluid Mechanics*, 934:A38, DOI: 10.1017/jfm.2021.1146.

Johnson, J.B., M. S. D. P. and Bens, C. (1987). Field observations of thermal convection in a subarctic snow cover. *International Association of Hydrological Sciences Pulblication*, 162:105–118.

Jordan, R. (1991). A one-dimensional temperature model for a snow cover: Technical documentation for sntherm. 89. Technical report, Cold Regions Research and Engineering Lab Hanover NH.

## Bibliography

Kaempfer, T. U. and Plapp, M. (2009). Phase-field modeling of dry snow metamorphism. *Phys. Rev. E*, 79:031502, DOI: 10.1103/PhysRevE.79.031502, https://link.aps.org/doi/10.1103/PhysRevE.79.031502.

Klever, N. (1985). Air and water-vapour convection in snow. *Annals of Glaciology*, 6:39–42, DOI: 10.3189/1985AoG6-1-39-42.

Krol, Q. and Löwe, H. (2018). Upscaling ice crystal growth dynamics in snow: Rigorous modeling and comparison to 4d x-ray tomography data. *Acta Materialia*, 151:478–487, DOI: https://doi.org/10.1016/j.actamat.2018.03.010, https://www.sciencedirect.com/science/article/pii/S1359645418301897.

Kunii, D. and Levenspiel, O. (1991). Chapter 11 - particle-to-gas mass and heat transfer. In Kunii, D. and Levenspiel, O., editors, *Fluidization Engineering (Second Edition)*, pages 257 – 276. Butterworth-Heinemann, Boston, second edition edition, ISBN: 978-0-08-050664-7, DOI: https://doi.org/10.1016/B978-0-08-050664-7.50017-2, http://www.sciencedirect.com/science/article/pii/B9780080506647500172.

Kvernvold, O. and Tyvand, P. A. (1980). Dispersion effects on thermal convection in porous media. *Journal of Fluid Mechanics*, 99(4):673–686, DOI: 10.1017/S0022112080000821.

Lapwood, E. R. (1948). Convection of a fluid in a porous medium. *Mathematical Proceedings of the Cambridge Philosophical Society*, 44(4):508–521, DOI: 10.1017/S030500410002452X.

Lehning, M., Bartelt, P., Brown, B., and Fierz, C. (2002a). A physical snowpack model for the swiss avalanche warning: Part iii: Meteorological forcing, thin layer formation and evaluation. *Cold Regions Science and Technology*, 35(3):169–184.

Lehning, M., Bartelt, P., Brown, B., and Fierz, C. (2002b). A physical snowpack model for the swiss avalanche warning part iii: Meteorological forcing, thin layer formation and evaluation. *Cold Regions Science and Technology*, 35:169–184, DOI: 10.1016/S0165-232X(02)00072-1.

Lehning, M., Bartelt, P., Brown, B., Fierz, C., and Satyawali, P. (2002c). A physical snowpack model for the swiss avalanche warning: Part ii. snow microstructure. *Cold regions science and technology*, 35(3):147–167.

Lehning, M., Bartelt, P., Brown, B., Fierz, C., and Satyawali, P. (2002d). A physical snowpack model for the swiss avalanche warning: Part ii. snow microstructure. *Cold regions science and technology*, 35(3):147–167.

Lehning, M., Bartelt, P., Brown, B., Russi, T., Stöckli, U., and Zimmerli, M. (1999a). Snowpack model calculations for avalanche warning based upon a new network of weather and snow stations. *Cold Regions Science and Technology*, 30(1):145–157.

Lehning, M., Bartelt, P., Brown, B., Russi, T., Stöckli, U., and Zimmerli, M. (1999b). Snowpack model calculations for avalanche warning based upon a network of weather and snow stations. *Cold Regions Science and Technology*, 30:145–157, DOI: 10.1016/S0165-232X(99)00022-1.

Loewe, H., Riche, F., and Schneebeli, M. (2013). A general treatment of snow microstructure exemplified by an improved relation for thermal conductivity. *The Cryosphere*, 7(5):1473–1480, DOI: 10.5194/tc-7-1473-2013, https://www.the-cryosphere.net/7/1473/2013/.

Millington, R. J. and Quirk, J. P. (1961). Transport in porous media (in soil science). *Trans. Int. Congr. Soil Sci.*, 7:97–106.

Moukalled, F., Mangani, L., Darwish, M., et al. (2016). *The finite volume method in computational fluid dynamics*, volume 6. Springer.

Neumann, T. A., Albert, M. R., Engel, C., Courville, Z., and Perron, F. (2009). Sublimation rate and the mass-transfer coefficient for snow sublimation. *International Journal of Heat and Mass Transfer*, 52(1):309 – 315, DOI: https://doi.org/10.1016/j.ijheatmasstransfer.2008.06.003, http://www.sciencedirect.com/science/article/pii/S0017931008003475.

Nicolaus, M. and Schwegmann, S. (2017). Snow height on sea ice and sea ice drift from autonomous measurements from buoy 2014s9, deployed during polarstern cruise ps82 (ant-xxix/9). PANGAEA, DOI: 10.1594/PANGAEA.875273, https://doi.org/10.1594/PANGAEA.875273. In: Nicolaus, Marcel; Hoppmann, Mario; Arndt, Stefanie; Hendricks, Stefan; Katlein, Christian; König-Langlo, Gert; Nicolaus, Anja; Rossmann, Leonard; Schiller, Martin; Schwegmann, Sandra; Langevin, Danielle; Bartsch, Annekathrin (2017): Snow height and air temperature on sea ice from Snow Buoy measurements. Alfred Wegener Institute, Helmholtz Center for Polar and Marine Research, Bremerhaven, PANGAEA, https://doi.org/10.1594/PANGAEA.875638.

Nield, D. and Bejan, A. (2017). *Convection in Porous Media*. Springer International Publishing, ISBN: 9783319495620, https://books.google.ch/books?id=WptcDgAAQBAJ.

Palm, E. and Tveitereid, M. (1979). On heat and mass flux through dry snow. *Journal of Geophysical Research: Oceans*, 84(C2):745–749, DOI: 10.1029/JC084iC02p00745, https://agupubs.onlinelibrary.wiley.com/doi/abs/10.1029/JC084iC02p00745.

Pfeffer, W. T. and Mrugala, R. (2002). Temperature gradient and initial snow density as controlling factors in the formation and structure of hard depth hoar. *Journal of Glaciology*, 48(163):485–494, DOI: 10.3189/172756502781831098.

Pinzer, B. R., Schneebeli, M., and Kaempfer, T. U. (2012). Vapor flux and recrystallization during dry snow metamorphism under a steady temperature gradient as observed by time-lapse micro-tomography. *The Cryosphere*, 6(5):1141–1155, DOI: 10.5194/tc-6-1141-2012, https://www.the-cryosphere.net/6/1141/2012/.

Powers, D., O'Neill, K., and Colbeck, S. C. (1985). Theory of natural convection in snow. *Journal of Geophysical Research: Atmospheres*, 90(D6):10641–10649, DOI: 10.1029/JD090iD06p10641, https://agupubs.onlinelibrary.wiley.com/doi/abs/10.1029/JD090iD06p10641.

# Bibliography

Proksch, M., Rutter, N., Fierz, C., and Schneebeli, M. (2016). Intercomparison of snow density measurements: bias, precision, and vertical resolution. *The Cryosphere*, 10:371–384.

Richards, L. A. (1931). Capillary conduction of liquids through porous mediums. *Journal of Applied Physics*, 1(5):318–333, DOI: 10.1063/1.1745010.

Russo, E., Kuerten, J., van der Geld, C., and Geurts, B. (2014a). Water droplet condensation and evaporation in turbulent channel flow. *Journal of Fluid Mechanics*, 749:666–700, DOI: 10.1017/jfm.2014.239.

Russo, E., Kuerten, J. G., Van Der Geld, C., and Geurts, B. J. (2014b). Water droplet condensation and evaporation in turbulent channel flow. *Journal of fluid mechanics*, 749:666–700.

Saeid, N. H. (2004). Analysis of mixed convection in a vertical porous layer using non-equilibrium model. *International Journal of Heat and Mass Transfer*, 47(26):5619 – 5627, DOI: https://doi.org/10.1016/j.ijheatmasstransfer.2004.07.033, http://www.sciencedirect.com/science/article/pii/S0017931004003333.

Saeid, N. H. and Pop, I. (2004). Transient free convection in a square cavity filled with a porous medium. *International Journal of Heat and Mass Transfer*, 47(8):1917 – 1924, DOI: https://doi.org/10.1016/j.ijheatmasstransfer.2003.10.014, http://www.sciencedirect.com/science/article/pii/S0017931003006057.

Schneider von Deimling, T., Meinshausen, M., Levermann, A., Huber, V., Frieler, K., Lawrence, D. M., and Brovkin, V. (2012). Estimating the near-surface permafrost-carbon feedback on global warming. *Biogeosciences*, 9(2):649–665, DOI: 10.5194/bg-9-649-2012, https://www.biogeosciences.net/9/649/2012/.

Sharma, V., Comola, F., and Lehning, M. (2018). On the suitability of the thorpe–mason model for calculating sublimation of saltating snow. *The Cryosphere*, 12(11):3499–3509, DOI: 10.5194/tc-12-3499-2018, https://tc.copernicus.org/articles/12/3499/2018/.

Sharma, V., Gerber, F., and Lehning, M. (2021). Introducing cryowrf v1.0: Multiscale atmospheric flow simulations with advanced snow cover modelling. *Geoscientific Model Development Discussions*, 2021:1–46, DOI: 10.5194/gmd-2021-231, https://gmd.copernicus.org/preprints/gmd-2021-231/.

Shokri, N., Lehmann, P., and Or, D. (2009). Critical evaluation of enhancement factors for vapor transport through unsaturated porous media. *Water resources research*, 45(10).

Slater, A. G., Schlosser, C. A., Desborough, C., Pitman, A., Henderson-Sellers, A., Robock, A., Vinnikov, K. Y., Entin, J., Mitchell, K., Chen, F., et al. (2001). The representation of snow in land surface schemes: Results from pilps 2 (d). *Journal of Hydrometeorology*, 2(1):7–25.

Sokratov, S. and Sato, A. (2000). Wind propagation to snow observed in laboratory. *Annals of Glaciology*, 31:427–433.

Sokratov, S. A. and Maeno, N. (2000). Effective water vapor diffusion coefficient of snow under a temperature gradient. *Water Resources Research*, 36(5):1269–1276, DOI: 10.1029/2000WR900014, https://agupubs.onlinelibrary.wiley.com/doi/abs/10.1029/2000WR900014.

Sommer, C. G., Lehning, M., and Fierz, C. (2018). Wind tunnel experiments: Influence of erosion and deposition on wind-packing of new snow. *Frontiers in Earth Science*, 6:4, DOI: 10.3389/feart.2018.00004, https://www.frontiersin.org/article/10.3389/feart.2018.00004.

Sommerfeld, R. A., Friedman, I., and Nilles, M. (1987). The fractionation of natural isotopes during temperature gradient metamorphism of snow. In Jones, H. G. and Orville-Thomas, W. J., editors, *Seasonal Snowcovers: Physics, Chemistry, Hydrology*, pages 95–105. Springer, Dordrecht.

Sturm, M. and Benson, I. C. S. (1997). Vapor transport, grain growth and depth-hoar development in the subarctic snow. *Journal of Glaciology*, 43(143):42.

Sturm, M. and Johnson, J. B. (1991). Natural convection in the subarctic snow cover. *Journal of Geophysical Research: Solid Earth*, 96(B7):11657–11671, DOI: 10.1029/91JB00895, https://doi.org/10.1029/91JB00895.

Sturm, M. and Johnson, J. B. (1992). Thermal conductivity measurements of depth hoar. *Journal of Geophysical Research: Solid Earth*, 97(B2):2129–2139.

Taillandier, A.-S., Domine, F., Simpson, W. R., Sturm, M., Douglas, T. A., and Severin, K. (2006). Evolution of the snow area index of the subarctic snowpack in central alaska over a whole season. consequences for the air to snow transfer of pollutants. *Environmental science & technology*, 40(24):7521–7527.

Thorpe, A. D. and Mason, B. J. (1966). The evaporation of ice spheres and ice crystals. *British Journal of Applied Physics*, 17(4):541–548, DOI: 10.1088/0508-3443/17/4/316, https://doi.org/10.1088%2F0508-3443%2F17%2F4%2F316.

Touzeau, A., Landais, A., Morin, S., Arnaud, L., and Picard, G. (2018). Numerical experiments on vapor diffusion in polar snow and firn and its impact on isotopes using the multi-layer energy balance model crocus in surfex v8.0. *Geoscientific Model Development*, 11(6):2393–2418, DOI: 10.5194/gmd-11-2393-2018, https://www.geosci-model-dev.net/11/2393/2018/.

Trabant, D. and Benson, C. (1972). Field experiments on the development of depth hoar. *Geological Society of America Memoirs*, 135:309–322.

Waddington, E., Cunningham, J., and Harder, S. (1996). The effects of snow ventilation on chemical concentrations. In *Chemical Exchange between the atmosphere and polar snow*, pages 403–451. Springer.

Walker, K. L. and Homsy, G. M. (1978). Convection in a porous cavity. *Journal of Fluid Mechanics*, 87(3):449–474, DOI: 10.1017/S0022112078001718.

# Bibliography

Ward, J. (1964). Turbulent flow in porous media. *Journal of the hydraulics division*, 90(5):1–12.

Wen, B., Chang, K. W., and Hesse, M. A. (2018). Rayleigh-darcy convection with hydrodynamic dispersion. *Physical Review Fluids*, 3(12):123801.

Wever, N., Fierz, C., Mitterer, C., Hirashima, H., and Lehning, M. (2014). Solving Richards Equation for snow improves snowpack meltwater runoff estimations in detailed multi-layer snowpack model. *Cryosphere*, 8(1):257–274, DOI: 10.5194/tc-8-257-2014.

Wever, N., Rossmann, L., Maaß, N., Leonard, K. C., Kaleschke, L., Nicolaus, M., and Lehning, M. (2020). Version 1 of a sea ice module for the physics-based, detailed, multi-layer SNOWPACK model. *Geosci. Model Dev.*, 13(1):99–119, DOI: 10.5194/gmd-13-99-2020, https://www.geosci-model-dev.net/13/99/2020/.

Wever, N., Schmid, L., Heilig, A., Eisen, O., Fierz, C., and Lehning, M. (2015). Verification of the multi-layer snowpack model with different water transport schemes. *Cryosphere*, 9(6):2271–2293, DOI: 10.5194/tc-9-2271-2015, https://www.the-cryosphere.net/9/2271/2015/.

Whitaker, S. (1999). Theory and applications of transport in porous media: The method of volume averaging. *The Netherlands: Kluwer Academic Publishers*.

Woo, M.-k. (2012). *Permafrost hydrology*. Springer Science & Business Media, Berlin.

Yosida, Z., Oura, H., Kuroiwa, D., Huzioka, T., Kojima, K., Aoki, S.-i., and Kinoshita, S. (1955). Physical studies on deposited snow. .; thermal properties. *Contributions from the Institute of Low Temperature Science*, 7:19–74.

Zermatten, E., Haussener, S., Schneebeli, M., and Steinfeld, A. (2011). Tomography-based determination of permeability and dupuit–forchheimer coefficient of characteristic snow samples. *Journal of Glaciology*, 57(205):811–816, DOI: 10.3189/002214311798043799.

Zhang, T., Osterkamp, T. E., and Stamnes, K. (1996). Influence of the depth hoar layer of the seasonal snow cover on the ground thermal regime. *Water Resources Research*, 32(7):2075–2086.

## PERSONAL INFORMATION

**Mahdi Jafari**

📍 Chemin du Suchet 10, 1024 Ecublens VD, Switzerland

📍 Office: GR A0 434 (Bâtiment GR) Station 2,  EPFL ENAC IIE CRYOS.

📱 +41 786686523  ✉ mahdi.jafari@epfl.ch, jafari90@aut.ac.ir, mahdijafari.135@gmail.com

Sex Male | Date of birth 16/09/1988 | Nationality Iranian

## EDUCATION

| | |
|---|---|
| 2017 – 2022 JAN | **PhD in Mechanical Engineering, CRYOS, School of Architecture, Civil and Environmental Engineering, EPFL, Lausanne, Switzerland.** |
| | ■ ***Thesis:*** Water vapor transport in snowpacks. |
| *2016 | ***Chosen as a Brilliant Talent and an Academic award winner by Iran's National Elites Foundation (INEF).** |
| 2011 – 2013 | **MSc in Mechanical Engineering, Energy Conversion, Amirkabir University of Technology, Tehran, Iran, GPA = 18.16/20** |
| | ■ **Thesis:** *Study of solid phase effect on stratified smooth liquid- gas flow in natural gas pipe line.* |
| 2007 – 2011 | ***BSc in Mechanical Engineering, Amirkabir University of Technology, Tehran, Iran, GPA = 17.56/20** |
| | **Thesis:** *Analytical and numerical solution of pressure drop for laminar flow in noncircular ducts.* |
| *2009 | ***Chosen as a top talented student and allowed to study two BSc degrees simultaneously in 2009.** |
| 2007 – 2014 | ***BSc in Marine Engineering, Amirkabir University of Technology, Tehran, Iran, GPA = 17.42/20** |
| | **Thesis:** *Numerical investigation of the injection timing in a diesel engine.* |

## SKILLS

**Technical**
- ■ Computational fluid dynamics (CFD)
- ■ Eulerian-Lagrangian multiscale simulation
- ■ Eulerian-Eulerian two fluid simulation for heat and mass transfer in porous media
- ■ LES and turbulent multiphase flow and spray
- ■ Multi-fluid flow (bubbly flow, deformable droplet) using VOF and  front tracking method
- ■ fluid structure interaction (FSI) and immersed boundary method (IBM)
- ■ Parallel processing methods in numerical Analysis
- ■ Numerical optimization methods and machine learning
- ■ Turbomachinery CFD and Cumbustion modelling

**Advanced Computer**
- ■ Programming : **FORTRAN, C, C++,  python,** and Linux **shell scripting**
- ■ Parallel processing: **OpenMP,  MPI**
- ■ Open-source CFD: **OpenFOAM**
- ■ Commercial CFD: **AVLFire,  Advanced ANSYS FLUENT (dynamic mesh, combustion, ICE, turbomachinary), CFX**
- ■ mesh geration: **Gambit, Ansys mesher, ICEM CFD,  cfMesh**
- ■ Optimization: **ANSYS** (**DesignXplorer**), **modeFRONTIER**
- ■ Machine learning and data analysis: **PyTorch, TensorFlow, scikit-learn**
- ■ Post processing: **TECPLOT, ParaView, PyVista, PyFoam**…
- ■ Engineering: **AutoCAD,  EES**
- ■ OS: **Windows, Linux**
- ■ Other: **Office**, and other tool boxes

**Languages**
- ■ **English**: fluent
- ■ **Persian**: Native

## DETAILS

**Industrial and academic experience**
- ■ **Industrial projects:**
  - □ Using turbomachinery CFD to numerically obtain the performance chart of  the compressor (CFX or Fluent), combustion chamber (Fluent) , and  turbine (CFX or Fluent).

159

- ☐ Finding matching (operating) point of the gas turbine using performance charts by genetic algorithm optimization method.
- ☐ Modeling internal combustion engines to optimize the first and second low efficiency using AVLFire, ANSYS Fluent and OpenFOAM .
- ☐ Modeling static and dynamic aerodynamic coefficients of bluff bodies using Ansys Fluent(different dynamic mesh strategis) and OpenFOAM (overset mesh method or IBM)
- ☐ teaching advanced Ansys Fluent and OpenFOAM (implementing new libraries)

■ **Academic work experience::**
- ☐ Teaching assistant for "Advanced Radiation Heat Transfer", 2016 and for the "Advanced thermodynamics for the foreign students", 2016 both graduate course in Amirkabir University of Technology, Tehran, Iran.
- ☐ Teaching assistant for two semesters in "Physics and Hydrology of Snow" graduate course at EPFL.
- ☐ Supervision of master students and internships in CRYOS laboratory at EPFL.

■ **Developing OpenFOAM libraries and solvers:**
- ☐ **SNOWPACKFoam:** a solver based on tight (master/slave) coupling between SNOWPACK and OpenFOAM.
- ☐ **snowpackBuoyantPimpleFoam:** an OpenFOAM Eulerian-Eulerian two-phase solver for modeling convection of water vapor in snowpacks.
  For more information, check the link: http://dx.doi.org/10.16904/envidat.265
- ☐ **snowBedFoam:** an OpenFOAM Eulerian-Lagrangian solver for modeling snow transport.
  For more information, check the link: http://dx.doi.org/10.16904/envidat.223
- ☐ **Improving the Intermediate library of OpenFOAM 2.3.0**:
  Some important parts were added to this library to be able for simulating the four-way coupling gas- solid flows.
- ☐ **Implementing front tracking method in OpenFOAM 2.3.0:**
  This new library is called intermediateFrontTracking, and its related solver (interFTFoam) both have been separately developed using the standard intermediate library and interFoam solver respectively.

**PUBLICATIONS**

ISI Journal papers

■ Jafari, M., Lehining, M., & Sharma, V. (2022). Convection of water vapor in snowpacks, Journal of Fluid Mechanics, 934:A38, DOI: 10.1017/jfm.2021.1146.

■ Jafari, M., Hames, O., Wagner, D. N., Raphael, I., Clemens-Sewall, D., Polashenski, C., Shupe, M. D., Schneebeli, M., and Lehning, M.: Modelling the small-scale deposition of snow onto structured Arct``ic sea ice during a MOSAiC storm using snowBedFoam 1.0., Geosci. Model Dev. Discuss. [preprint], https://doi.org/10.5194/gmd-2021-254, in review, 2021.

■ Jafari, M., Gouttevin, I., Couttet, M., Wever, N., Michel, A., Sharma, V., and Lehning, M. (2020).
The impact of diffusive water vapor transport on snow profiles in deep and shallow snow covers and on sea ice. Frontiers in Earth Science,8, 249. Retrieved from https://www.frontiersin.org/article/10.3389/

■ M. Jafari, M.J. Parhizkar, E. Amani, H. Naderan, "Inclusion of entropy generation minimization in multi-objective CFD optimization of diesel engines", *Energy* 114 (2016) 526-541.

■ M. Jafari, Z. Mansoori , M. Saffar Avval , G. Ahmadi, " The effects of wall roughness on erosion rate in gas–solid turbulent annular pipe flow", Powder Technology 271 (2015) 248–254.

■ M. Jafari, Z. Mansoori, M. Saffar Avval, G. Ahmadi, A. Ebadi, "Modelling and numerical investigation of erosion for turbulent gas-solid two phase flow in a horizontal pipe", Powder Technology 271 (2015) 248–254.

■ M. Jafari, Z. Mansoori, M. Saffar Avval, G. Ahmadi, A. Ebadi, "Numerical Investigation of the Effect of Solid Particles on Liquid Holdup in Stratified Wavy Gas-Liquid Flow in Natural Gas Pipelines", Proceedings of the ASME 2014 4th Joint US-European Fluids Engineering Division Summer Meeting FEDSM-2014 August 3-7, 2014, Chicago, Illinois, USA.

Annexes     References, recommendation letters and transcript of records would be provided upon request.

160